Robust Control Schemes for a Pediatric Gait Exoskeleton System in Passive-assist and Active-assist Mode

A thesis submitted in partial fulfillment of the requirements for the degree of

Doctor of Philosophy

by

Jyotindra Narayan
Roll No: 176103009

DEPARTMENT OF MECHANICAL ENGINEERING
INDIAN INSTITUTE OF TECHNOLOGY GUWAHATI

Guwahati-781039
INDIA

January 2023

Declaration

I declare that this thesis entitled " Robust Control Schemes for a Pediatric Gait Exoskeleton System in Passive-assist and Active-assist Mode", submitted by me is a presentation of my original research work done under the guidance of Dr. Santosha K. Dwivedy, Professor, Department of Mechanical Engineering, Indian Institute of Technology Guwahati. This work has not been submitted elsewhere for the award of any degree and diploma in this institute or any other university or institution of higher learning.

Jyotindra Narayan
Research Scholar,
Department of Mechanical Engineering,
Indian Institute of Technology Guwahati,
Guwahati, Assam, INDIA 781039,
Email: *jyoti176103009@iitg.ac.in, n.jyotindra@gmail.com*

Place: IIT Guwahati

Certificate

This is to certify that this thesis entitled "Robust Control Schemes for a Pediatric Gait Exoskeleton System in Passive-assist and Active-assist Mode", submitted by "Jyotindra Narayan", in partial fulfilment of the requirements for the award of the degree of Doctor of Philosophy, to the Indian Institute of Technology Guwahati, Assam, India, is a record of the *bona fide* research work carried out by him under my guidance and supervision at the Department of Mechanical Engineering, Indian Institute of Technology Guwahati, Assam, India. To the best of my knowledge, no part of the work reported in this thesis has been presented for the award of any degree and diploma in this institute or any other university or institution of higher learning.

Dr. Santosha K. Dwivedy
Department of Mechanical Engineering,
Indian Institute of Technology Guwahati,
Guwahati, Assam, INDIA 781039,
Email:*dwivedy@iitg.ac.in*

Place: IIT Guwahati

Dedicated to

my grandparents

Late Ram Gobind Tiwary

and

Late Samrajo Devi

for their infinite love, support, motivation and guidance.

Acknowledgements

It gives me immense pleasure to thank each individual who supported directly or indirectly towards completion of this journey. At first, I would like to express my wholehearted gratitude to my supervisor Prof. Santosha K. Dwivedy for his exceptional support and guidance throughout my doctoral work. Moreover, his dedication towards his duties and research always inspire me. I would always be indebted to him for several thought provoking ideas and the academic freedom he has given to me.

I would like to thank my doctoral committee members namely, Prof. Subramani Kanagaraj, Prof. Shyamanta M. Hazarika, and Prof. Shivashankar B. Nair for their constructive suggestions towards shaping my research goals as well as the entire thesis. I extend my sincere thanks to Prof. Shyamanta M. Hazarika for the various research discussions and his valuable suggestions during my progress. Further, I am grateful to Prof. Sachin Singh Gautam for his collaborations on the deep learning which enriched my knowledge base in domain of neural networks.

I humbly thank to Mr. Monuranjan Dowarah for his kind help while conducting the simulation runs and experiments in Mechatronics and Robotics Laboratory. I extend my special thank to Mr. Arunjyoti Borgohain, Director of Yantrabot Technologies, for his critical suggestions during manufacturing of the exoskeleton systems. I am thankful to Mr. Nandan Das for helping out in fabricating experimental setups in mechanical workshop. I would also like to thank Dr. Bhaben Kalita for his amiable collaborations and helpful discussions. I am grateful to Dr. Durgesh Kumar for introducing and helping me with research writing in Latex interface.

Fortunately, I have met with a few great friends during my doctoral journey whom I have spent the quality time. I am privileged to mention Dr. Arun Kadian, Mr. Subhash Pratap Singh, and Mr. Santosh Kumar as long time peers who supported my journey in several perspectives. I would also like to thank my friends from other institutes, especially, Mr. Sumit Mehta, Mr. Ishan Chawla, and Ms. Sapna Rajoria who who have always motivated me in my tough times. I extend my deepest acknowledgements to Mr. Mohamed Abbas for all the research collaborations and constructive feedbacks on my progress. I would like to acknowledge Mr. Rajan Kumar, Mr. Sachit Narayan Pandey, Mr. Bhavik Patel, and Mr. Rahul Ranjan Bharti for their rigorous discussions. My thesis would not have been completed without their effective support. I am grateful to Mr. Rajesh Rajan from my early

days of this journey who has constantly motivated me to carry out the prospective research.

My family members have played a crucial role throughout my academic carrier. Their constant support, love, motivation, and faith in me help me bounce back at different phases of my life. From the core of my heart, I would like to thank my parents, my brother, and my sister-in-law for showering immense love and moral support. Finally, I would like to thank my fiancé Ms. Shivali for all her patience and having faith in my academic carrier.

Jyotindra Narayan
Department of Mechanical Engineering,
Indian Institute of Technology Guwahati,
Guwahati, Assam, INDIA 781039,
IIT Guwahati

Abstract

Over the years, a significant rise in neurological disorders has been observed for different age groups, such as stroke, spinal cord injury (SCI), and cerebral palsy (CP). Many pediatric subjects face dyskinesia and muscle atrophy in their lower limbs. In the last few years, the proliferation of exoskeleton technology has enabled the therapy process to be less cumbersome and more sustainable. However, there are minimal exoskeleton devices available for pediatric gait rehabilitation. Moreover, the control design to achieve the desired gait training in different therapy modes is still open to research and a benchmark problem statement due to significant parametric perturbations and external disturbances (PPED) in pediatric exoskeleton systems. Therefore, this thesis proposes a few robust control schemes for a newly designed pediatric exoskeleton in passive- and active-assist rehabilitation mode.

Primarily, the design and prototype development of a 6-DOFs (3-DOF/limb) low-cost stand-aided hip-knee-ankle foot exoskeleton is carried out for pediatric gait rehabilitation in two phases. In first phase, the athropometric parameters of five healthy pediatric participants (8-12 years, 25-40kg, 115-125cm) are considered to design and model the preliminary version (LLES$v1$) of the gait exoskeleton. Thereafter, in second phase, considering the athropometric parameters of 11 healthy participants (8-12 years, 25-40kg, 128-132cm), the previous version is modified (LLES$v2$) for better structural strength, actuators' placement, adaptability, and maneuverability. The maximum joint's range of motion (ROM) for the exoskeleton systems is estimated using a NI-LabView motion capture setup. The static structural analysis for both designs are carried out for reaction period and double support phase over a gait cycle. Invoking Euler-Lagrange principle, the dynamic modeling is derived for passive-assist and active-assist training mode. The proof-of-concept prototype for both versions are presented with required actuators' for hip, and knee, and ankle joint.

Two intelligent controllers, i.e., robust LQR-based neural fuzzy (RLQR-NF) and Neural-Fuzzy compensated PID (NF-CPID) control schemes, are investigated for the passive-assist gait tracking of the coupled human-exoskeleton system. In first study, a robust dataset based on LQR gain and output is formed by perturbing the masses of coupled system and a NF architecture is trained with the dataset in offline mode. In another study, an online adaptation of NF weights are considered to compensate both the parametric uncertainties and external disturbances which

are unaccounted by conventional PID control. The initial values of weights in online mode are found using an inverse model based offline trained NF architecture. The stability of the NF-CPID control scheme is ensured using the Lyapunov theory. The RLQR-NF outperforms the another robust control named exponential reaching law-based sliding mode control for passive-assist gait tracking. The simulation runs show that NF-CPID has outperformed the RLQR-NF against PPED and unperformed against the PP only. The experiments with the proposed control schemes are carried out with a child dummy coupled to LLES$v1$.

To avoid the computational complexity of selecting NF hyperparameters and improve the gait tracking, a robust adaptive backstepping (RABS) control is proposed to dealt the presence of PPED. The well-known problem of 'overparameterization' and the 'explosion of terms' are avoided through the implicit Lyapunov-based design of RABS. The simulation results are compared with NF-CPID and found to be promising in passive-assit gait tracking against PPED. The experimental validations are also carried out for a pediatric subject with GMFCS-Level III coupled to LLES$v2$ which confirms the robustness of the proposed RABS control.

Furthermore, an adaptive backstepping sliding mode-based subject cooperative control (ABSM-SCC) is proposed to include the subject-exoskeleton interaction during active-assist gait training. A neural-fuzzy-based variable admittance control (VAC) is designed to incorporate a realistic subject-exoskeleton interaction and consider the active participation of the subject. A robust ABSM control with rapid reaching law (RRL) is utilized to deal with parametric uncertainties and external disturbances. The stability of the proposed position control is addressed using Lyapunov theory. The effectiveness of the proposed cooperative control scheme is compared with an adaptive backstepping-fixed admittance control (AB-FAC) for two different therapeutic cases, i.e., regular active-assist mode and active-assist mode with the effect of sudden reflex. Based on the several simulation runs, the proposed cooperative controller has shown a promising tracking behavior, appropriate safe and compliant interaction, in active-assist gait training.

The ABSM-SCC is further extended for finite-time and fast convergence of error states by presenting an adaptive backstepping integral-aided singularity-free fast terminal sliding mode-based subject cooperative control (ABISFFTSM-SCC). Reducing the computational complexity, a fixed admittance model has been considered in the outer loop control to regulate the interaction forces. The sliding function has shown the potential of proposed cooperative control to converge the error states in finite-time as compared to ABSM-SCC.

Contents

List of Figures

List of Tables

Abbreviations

a/a	Abduction/Adduction
AA	Active-Assist
ABC	Adaptive Backstepping Control
AB-FAC	Adaptive Backstepping-Fixed Admittance Control
RRL	Rapid Reaching Law
ABISFFTSM	Adaptive Backstepping Integral-aided Singularity Free Fast Terminal Sliding Mode
ABSMC	Adaptive Backstepping Sliding Mode Control
VAC	Variable Admittance Control
AD	Axiomatic Design
ADC	Analog-Digital Conversion
ADL	Activities of Daily Living
AFO	Ankle-Foot Orthosis
AGoRA	Adaptable Robotic Platform for Gait rehabilitation and Assistance
ALEX	Active Leg Exoskeleton
ANFIS	Adaptive Neuro-Fuzzy Inference System
BC	Backstepping Control
BLEEX	Berkeley Lower Extremity Exoskeleton
CAD	Computer Aided Design
CI	Chattering Indicator
CP	Cerebral Palsy
d/p	Dorsi/Plantar Flexion
DL	Defuzzification Layer
DOF	Degrees of Freedom
DP	Domain Parameters
EEG	Electroencephalogram
EHS	End Heel Strike
EICoSI	Exoskeleton Intelligently Communicating and Sensitive to Intention
EMG	Electromyography

ERL-SM	Exponential Reaching Law-Sliding Mode
EXPOS	Exoskeleton for Patients and The Old by The Sogang University
ExRoLEG	Exoskeleton Robotic Leg
f/e	Flexion/Extension
FA	Feet Adjacent
FEA	Finite Element Analysis
FSM	Finite State Machine
FSR	Force Sensing Resistors
GMFCS	Gross Motor Function Classification System
GRF	Ground Reaction Force
HAL	Hybrid Assitive Limb
HK	Hip-Knee
HKAF	Hip-Knee-Ankle Foot
HLC	High Level Control
HOSM	High Order Sliding Mode
HR	Heel Rise
i/e	Intra/Extra Rotation
IHS	Initial Heel Strike
IMU	Inertial Measurement Unit
INR	Indian Rupee
IR	Infrared Sensor
ISFFTSM	Integral Singularity Free Fast Terminal Sliding Mode
ISS	Input to State Stability
FMA	Fugl-Meyer Assessment
ITSMC	Integral Terminal Sliding Mode Control
KAF	Knee-Ankle Foot
LLC	Lower Level Control
LLES$v1$	Lower Limb Exoskeleton System-Version First
LLES$v2$	Lower Limb Exoskeleton System-Version Second
LOPES	Lower Extremity Powered Exoskeleton
LQR	Linear Quadratic Regulator
LRF	Laser Range Finder
LSO	Lumbar Sacral Orthosis
MD	Muscular Dystrophies
MF	Membership Function
MHRI	Multimodal Human-Robot Interface
MIMO	Multi-Input Multi-Output
ML	Membership Layer

MOCAP	Motion Capture
MS	Microsoft
NF	Neural-Fuzzy
NF-CPID	Neural-Fuzzy Compensated PID
NL	Node Layer
NN	Neural Networks
OL	Output Layer
PA	Passive-Assist
PAM	Penumatic Artifical Muscle
PI	Performance Index
PID	Propotional-Integral-Derivative
SMC	Sliding Mode Control
pHRI	Physical Human-Robot Interaction
PPED	Paramteric Perturbations and External Disturbances
P-LEGS	paediatric Lower-Extremity Gait System
PWM	Pulse Width Modulation
RABS	Robust Adaptive Backstepping
RL	Rule Layer
RLQR-NF	Robust Linear Quadratic Regulator-based Neural-Fuzzy
RMSE	Root Mean Square Error
RMST	Root Mean Square Torque
RMSV	Root Mean Square Voltage
ROM	Range of Motion
RSEA	Rotary Series Elastic Actuator
SC	Supervisory Control
SCI	Spinal Cord Injury
SCPE	Surveillance of Cerebral Palsy in Europe
SDK	Software Development Kit
SEA	Series Elastic Actuator
SFFTSMC	Singularity Free Fast Terminal Sliding Mode Control
SMA	Spinal Muscular Atrophy
THKAF	Trunk-Hip-Knee-Ankle Foot
TLSO	thoracic lumbar sacral orthosis
TO	Toe Off
ULC	Upper Level Control
USD	United State Dollar
WWH	Wearable Walking Helper

Symbols

$(a,\ b,\ c)$	body joint triples
q_j	joint angle from skeleton data
d_E	Euclidean distance
$(M,\ N,\ O)$	Euclidean distance for each pair in join triples
x_a, y_a	Cartesian coordinate of body joint a
x_b, y_b	Cartesian coordinate of body joint b
x_c, y_c	Cartesian coordinate of body joint c
$K_{(h,e)}$	kinetic energy of the human-exoskeleton system
$P_{(h,e)}$	potential energy of the human-exoskeleton system
$\tau_{j(h,e)}$	joint torque in coupled human-exoskeleton system
$q_{j(h,e)}$	joint angle of coupled human-exoskeleton system
$q_{j,e}$	joint angle of exoskeleton system
$q_{j,h}$	desired joint angle of human subject
$\dot{q}_{j(h,e)}$	joint angular speed of human-exoskeleton system
$\ddot{q}_{j(h,e)}$	joint angular acceleration of human-exoskeleton system
$m_{i(h,e)}$	mass of the coupled link
$I_{i(h,e)}$	rotational moment of inertia of the coupled link
$l_{i(h,e)}$	rotational moment of inertia of the coupled link
$\mathcal{M}_{h,e}(q_{j,e})$	inertia matrix of the coupled system
$\mathcal{C}_{h,e}(q_{j,e}, \dot{q}_{j,e})$	Coriolis/centrifugal matrix of the coupled system
$\mathcal{G}_{h,e}(q_{j,e})$	gravity matrix of the coupled system
τ_{eth}	interaction torque from exoskeleton to human
τ_{hte}	interaction torque from human to exoskeleton
$\tau_{j,int}$	cooperative interaction torque
$f_{j,int}$	cooperative interaction force
$x_{i,h},\ \dot{x}_{i,h}$	position and velocity of the human's contact point
$x_{i,e},\ \dot{x}_{i,e}$	position and velocity of the exoskeleton's contact point
c	damping of the bracing strap

k	spring coefficient of the bracing strap
J	Jacobian
$\tau_{ja(h,e)}$	joint actuator torque in coupled system
l_s	numerical parameter
F_t	thrust force by leadscrew actuator
p_r	pitch of the leadscrew
q_{22e}	rotary movement of leadscrew actuator
q_s	constant geometrical parameter in degrees
o_{12}	constant geometrical length
l_{12e}	leadscrew translation
$k_t,\ n_c$	fixed design parameters per subject
n	order of the dynamical model
p	total number of inputs and outputs
x	state vector
Ψ	smooth vector field
v	control input vector
y_i	control output vector
Λ_i	smooth non-linear function
Γ_i	another smooth vector field
$L^i_\Psi \Lambda_j$	Lie derivatives of $\Lambda_j(x)$ in the direction of Ψ
$L^i_\Gamma \Lambda_j$	Lie derivatives of $\Lambda_j(x)$ in the direction of Γ
d_p	relative degree
d	total relative degree
z	transformed state vector
$\mathcal{A},\ \mathcal{B},\ \mathcal{C}$	state-weight factor matrices
$\sigma(x)$	invertible matrix of order $p \times p$
$\delta(x)$	decoupling matrix of the coupled system
u	input vector in linearized model
$\mathcal{O}^1_j$	node output for the first ANFIS layer
$\mathcal{O}^2_j$	node output for the second ANFIS layer
$\mathcal{O}^3_j$	node output for the third ANFIS layer
$\mathcal{O}^4_j$	node output for the fourth ANFIS layer
$\mathcal{O}^5_j$	node output for the fifth ANFIS layer
$\omega_{A_j}(\mathrm{x}),\ \omega_{B_j}(\mathrm{y})$	membership weightage of respective input variables
$A_j,\ B_j$	type of membership function
a_j	width parameter of the bell MF
b_j	shape parameter of the bell MF
c_j	center position of the bell MF

m_j	firing strength
$\bar{m}_j$	normalized firing strength
$\bar{m}_j$	fuzzy rule weight matrix
$\mathcal{Q},\ \mathcal{R}$	user-defined state weighing matrices
$\mathcal{K}$	optimal state gain matrix
$\mathcal{P}$	answer of the Riccati equation
E	error vector in LQR control
S_d	dataset
S_{rd}	robust dataset
ξ_1	joint angular error in passive-assist mode
K_p	proportional gain
K_i	integral gain
K_d	derivative gain
τ_{PID}	PID controller output
τ_{NCP}	neuro-fuzzy compensated PID controller output
τ_{NF}	neuro-fuzzy controller output
$\mathcal{M}_{oe}(q_{j,e})$	nominal inertia matrix of the coupled system
$\mathcal{C}_{oe}(q_{j,e}, \dot{q}_{j,e})$	nominal centrifugal matrix of the coupled system
$\mathcal{G}_{oe}(q_{j,e})$	nominal gravity matrix of the coupled system
ρ	lumped form of PPED
δ_s	uncertain scaling factor
τ_d	external disturbance
$\mathcal{F}_{\dot{q}_{j,e}}$	friction model
C_f	Coloumb friction
$\mathcal{V}_f$	viscous friction
σ_v	velocity factor
$\mathcal{E}$	error vector in NF-CPID control
$\bar{\angle}^*$	optimal weight matrices of the ANFIS architecture
$\bar{\angle}$	actual weight matrices of the ANFIS architecture
c_j	centre distance from the origin in Gaussian MF
σ_{wj}	curve width in Gaussian MF
k_p	positive constant
$\mathbb{M}_g$	normalized firing strength matrix with Gaussian MF
$\mathcal{W}$	constraint set
V	Lyapunov function
$\tilde{a}_1,\ \tilde{a}_2$	positive constants
$r_1,\ r_2$	state vectors in RABS control
ζ	virtual control law in RABS control

ξ_2	second gait tracking error variable in RABS control
$\epsilon_1,\ \epsilon_2$	positive diagonal matrices
Φ	regression matrix
Ω	unknown nonlinear parameters
$\tilde{\Omega}$	estimation error of unknown parameters
$\sqcap$	arbitrary selected positive definite matrix
ρ_d	belongs to a class of kappa functions
$\lambda_{min},\ \lambda_{max}$	minimum and maximum eigen values
M_a	inertia admittance parameter
C_a	damping admittance parameter
K_a	stiffness admittance parameter
$\acute{\tau}_{1,int},\ \acute{\tau}_{2,int},\ \acute{\tau}_{3,int}$	interaction torque input vectors to the ANFIS architecture
$\acute{C}_a$	damping output vector in ANFIS architecture
$\acute{K}_a$	stiffness output vector in ANFIS architecture
$r_1a,\ r_2a$	state vectors in ABSM-SCC
ζ_a	virtual control law in ABSM-SCC
$\xi_{1a},\ \xi_{2a}$	first and second gait tracking error variable in ABSM-SCC
$q_{j,\alpha}$	reference gait trajectory
s	sliding surface in ABSM-SCC
λ_p	positive definite diagonal matrix
$\kappa_1,\ \kappa_2$	positive constant parameter
ε	positive constant parameter
μ	positive even number
$\beta_1(s)$	designed nonlinear function
$\beta_2(s)$	piecewise defined function
t_a	approaching time
$\nu,\ h$	positive definite diagonal matrix
$\hat{\rho}$	estimation of lumped form of PPED
$\tilde{\rho}$	estimation error of lumped form of PPED in ABSM-SCC
N	total number of data points
p_v	performance value
τ_s^{int}	sudden interaction torque
F_s^{int}	sudden reflex force
A_int	amplitude of the modeled reflex
t_s^{int}	starting time interval of sudden forces
t_e^{int}	ending time interval of sudden forces
ξ_a	gait tracking error variable in ABISFFTSM-SCC
$k_{1m},\ k_{2m}$	positive definite diagonal matrix

$p_o,\ q_o$	positive odd numbers
s_1	sliding surface in ABISFFTSM-SCC
$\S_1,\ \S_2,\ \S_3$	positive design parameter
$\vartheta_1,\ \vartheta_2,\ \vartheta_3$	modified coordinates
d_c	user defined constant
$\mathbb{o}_1,\ \mathbb{o}_2$	virtual control law
∇	inertia-aided lumped form of PPED
$\mathbb{r}$	upper bound relation with lumped form of PPED
$\hat{\mathbb{r}}$	upper bound estimation of $\mathbb{r}$

Chapter 1

Introduction

1.1 Background

Mobility is one of the most fundamental and vital characteristics of human beings which allows them to perform activities of daily living (ADLs) at an independent level. Human locomotion is defined as the ability to utilize and regulate body movements based on the interaction between neuromuscular and musculoskeletal systems [1]. Any disparity from the natural body movements may lead to mobility disorder and hamper the different ADLs such as sitting, standing, walking, and running. Around one billion individuals (15% of the total population) across the globe are experiencing some form of disabilities like muscle weakness, partial or full paralysis, and loss of assistance in the lower extremities [2]. As age increases, aggravating muscle weakness and nerve-related issues lead to major prolonged chronic diseases, viz., stroke and spinal cord injury. As reported by World Health Organization [3], Stroke is found to be the second principal reason for the death of more than 5 million people during 2000-2016 and the third leading source of disability worldwide. Spinal Cord Injury (SCI) is another severely disabling disease that affects the sensory, motor, and autonomic functions of patients. The incidence of non-traumatic spinal cord injury in developed countries is higher than that of traumatic spinal cord injury, with a rate of 9.3 per million inhabitants per year [4]. On the other hand, abnormal damage, considered as pediatric stroke, to the brain of the child in the womb or just after birth leads to cerebral palsy (CP). The stroke incidence for the pediatric group is recorded as 2.5-13 per 100,000/year [5]. In a recent study by Chauhan et al. [6], the prevalence of CP per 1000 children in India was recorded as 2.95. Kopyta et al. [7] found in a study that arterial

ischemic stroke (AIS) is more prevalent in male children and adolescents rather than female ones as shown in Figure 1.1.

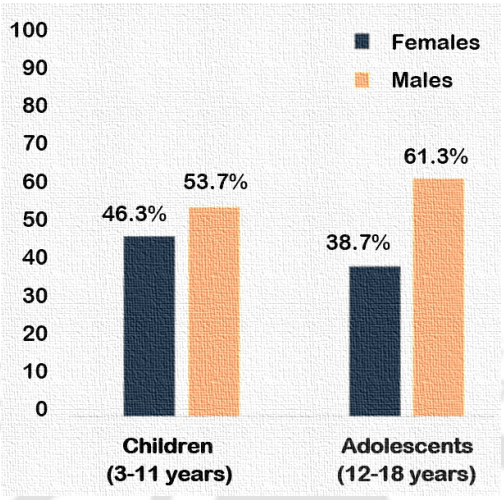

FIGURE 1.1: Gender-based AIS distribution for pediatric age group [7]

1.2 Motivation

Many people suffering from stroke, SCI, and CP experience dyskinesia in their lower limbs as a result of partial or complete paralytic conditions and feel incapable to move from one place to another without any external assistance. For motion assistance and augmenting mobility, various conventional means have been extensively exploited for more than three decades such as wheelchairs, supporting canes, and stands. However, the conventional approaches have some limitations such as limited mobility, additional in-person assistance, and more dependency on physical therapists for limb rehabilitation. Nowadays, more teenagers start using wheelchairs at an early age and they become dependent on them throughout their growth. This engenders the long sitting associated problems that worsen their physical capabilities and brings more complications such as bowel and bladder issues, respiratory difficulties, obesity, and upper body muscle fatigue/weakness. Moreover, the use of wheelchairs at an early age has bad implications for their mental health due to the absence of eye-to-eye communication, and reduced self-acceptance. Most of the patients are recommended to practice manual physical rehabilitation to improve their motor functions and minimize the onset of secondary injuries. It has been shown that motor function of the lower limbs can be significantly improved using the appropriate and repetitive process of rehabilitation training carried out by physical therapists [8, 9]. However, as the cases of

patients are increasing, the manual process becomes cumbersome, involves skilled labor, delivers less sustainability, and brings fatigue to the therapists. Moreover, the significant benefits of manual therapy get lost if ever the process is withdrawn for a short period of time [10]. Therefore, to address the limitations of conventional methods, the proliferation of exoskeleton technology has been observed for the lower-limb rehabilitation [11–15]

The present work dedicates to the design of robust control schemes for pediatric gait exoskeletons in different rehabilitation modes. To understand the control architecture required for pediatric exoskeletons, an in-depth study of the existing exoskeleton systems is required. A great deal of work has been done to demonstrate the effectiveness of robotic exoskeletons compared with manual therapy in patients suffering from neurological disorders. The robotic equipment for gait training, termed as lower limb exoskeleton, is formed with an external structure that supports and encompasses the majority of the human's lower extremity. The gait exoskeleton system is an active mechanical wearable device that is anthropomorphic in nature to support the lower-body [16]. The significant feature of the exoskeleton device is that the anatomy of the human limb maps very closely with the kinematic of the device.

In late 1960, two researcher groups from the United States and Yugoslavia had started the first study about the lower limb exoskeleton systems to provide motion assistance in the field of military and rehabilitation purposes, respectively [17]. Thereafter, the research on exoskeleton systems has been started with distinct mechanical structures, actuators, and control interfaces. In 2008, Dollar and Herr [17] summarized the design of the actuation mode, hardware, sensory, and different control strategies for the exoskeleton systems. In another work, Herr [18] classified the exoskeleton systems based on parallel and series arrangement with the human lower limb. These exoskeletons exhibited a physical and cognitive interface with the individuals by providing movement support and received the user mobility information [19]. The exoskeleton systems are mainly used for various applications by strengthening the weak muscle of the user to recover the locomotion capability. Some systems like Berkeley Lower Extremity Exoskeleton (BLEEX) [20], Sarcos Exoskeleton [21], MIT Exoskeleton [22] is used for the power augmentation of the healthy people to carry heavy loads. The exoskeleton systems are engaged in providing further capacity for walking and climbing stairs for elderly people (Cyberdyne's hybrid assistive limb exoskeleton [23], Wearable Walking Helper (WWH) [24]). Lower Extremity Powered Exoskeleton (LOPES) [25] are used for rehabilitation purposes by physiotherapists to avoid repetitive work for a long

time. Some other exoskeletons, for example, ANKUR-LL II [26], ATLAS [27], ExoRoboWalker [28] are used for the paraplegic or quadriplegic subjects to assist in the locomotion.

There are a very limited number of exoskeleton systems available for pediatric rehabilitation. Therefore, the design and related implications of such exoskeleton systems are a very crucial and exciting topic to explore for the benefits of motion assistance and gait rehabilitation of the pediatric age group. The following Section 1.3 presents the detailed literature of locomotion diseases, biomechanics of human gait, and state-of-the-art gait exoskeleton systems. The design, actuation methods, control scheme, and development stages are extensively reviewed, with a focus on pediatric gait exoskeletons. Based on the review, potential research gaps are identified in Section 1.4 which motivates to carry out the present research work. Thereafter, the objectives of the present work are enlisted in Section 1.5 Finally, the organization of the complete thesis work is outlined in Section 1.6.

1.3 Literature Review

This section presents the state-of-the-art research available related to the lower-limb exoskeleton systems. At first, locomotion diseases and biomechanics of human gait are explained. Thereafter, the design, actuation methods, control scheme, and development details of the lower-limb exoskeleton systems are extensively presented.

1.3.1 Locomotion diseases

The lower-limb impairment is caused by damage to the nervous system after an illness or a shock. Figure 1.2 shows the most common diseases for different age groups which cause mobility disorders. Diseases can be primarily categorized as accidental ones and congenital diseases. The first category is represented by SCI and Stroke, and the second category includes CP and Muscular dystrophy. In the forthcoming sections, a brief description of these diseases is given which includes a general definition, the physical symptoms which affect the lower limb, the impact of the disease, the rehabilitation management methods, and the rehabilitation costs.

Stroke

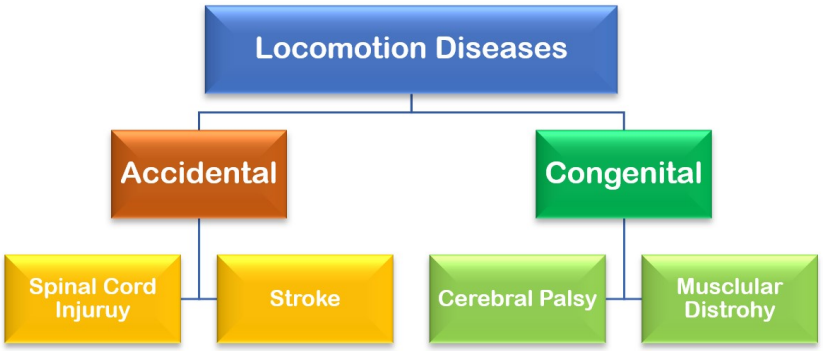

FIGURE 1.2: Classification of the mobility diseases

Stroke is a loss of brain function due to a block in the blood vessels. When this occurs, the affected person usually has one or more limbs paralyzed on one side of the body because the contralateral affected area on the brain can no longer function. Stroke causes a greater range of disabilities than any other condition and can affect lower limbs in most of cases [29]. For stroke survivors, it often requires long-term rehabilitation before can regain their independence while some of them never fully recover.

Spinal Cord Injury

A spinal cord injury represents damage to any part of the spinal cord or nerves at the end of the spinal canal. It can cause permanent changes to different body extremities depending upon the location of the injury. Spinal cord injuries are classified into a number of levels [30]. The first one is the primary level of the injury. It is classified as tetraplegia or quadriplegia which affects the arms and legs and paraplegia where the injury affects only the lower body. Secondary-level injuries include bed sores, spasticity, respiratory dysfunction, osteoporosis, and pressure ulcers. It is very frequent among adolescents and young adults rather than pediatric groups [31].

Cerebral Palsy

Cerebral palsy "CP" is caused by damage that occurs to the immature, developing brain most often before birth or in early childhood [32]. People suffering from cerebral palsy may suffer a reduced range of motion at various joints of their bodies due to muscle stiffness. Since CP is a heterogeneous condition rather than a single disease, a group of classification systems is required to better understand the interventions; motor type, topography, gross motor function, and gait patterns [33, 34].

Based on motor-type, the CP is further sub-classified as spastic, dyskinetic, ataxic, and hybrid [35]. In the case of spastic motor type, the subject shows the symptoms of tight leg muscles (hypertonia) that lead to the toe-walk. The dyskinetic CP is characterized by unwanted and erratic gait postures. The ataxic type manifests the loss of muscular coordination and leads to abnormal motions. The hybrid one is the combination of all three types. Around 30% of CP-affected children show a heterogeneous behavior of motor-type disorders. The hybrid motor-types are more complex to analyze as compared to the classical ones [35].

Following the topographical distribution shown in Figure 1.3, Surveillance of Cerebral Palsy in Europe (SCPE) has divided CP into two categories [36,37]: first one, Unilateral where either side of the body is impaired (monoplegia and hemiplegia) and the second one, Bilateral where both sides of the body are impaired (diplegia, tetraplegia, and quadriplegia). In most of the bilateral cases, the lower-limbs are more majorly affected than the upper limbs [38]. Moreover, motor-type and topographical classifications are very generic and show low reliability [35].

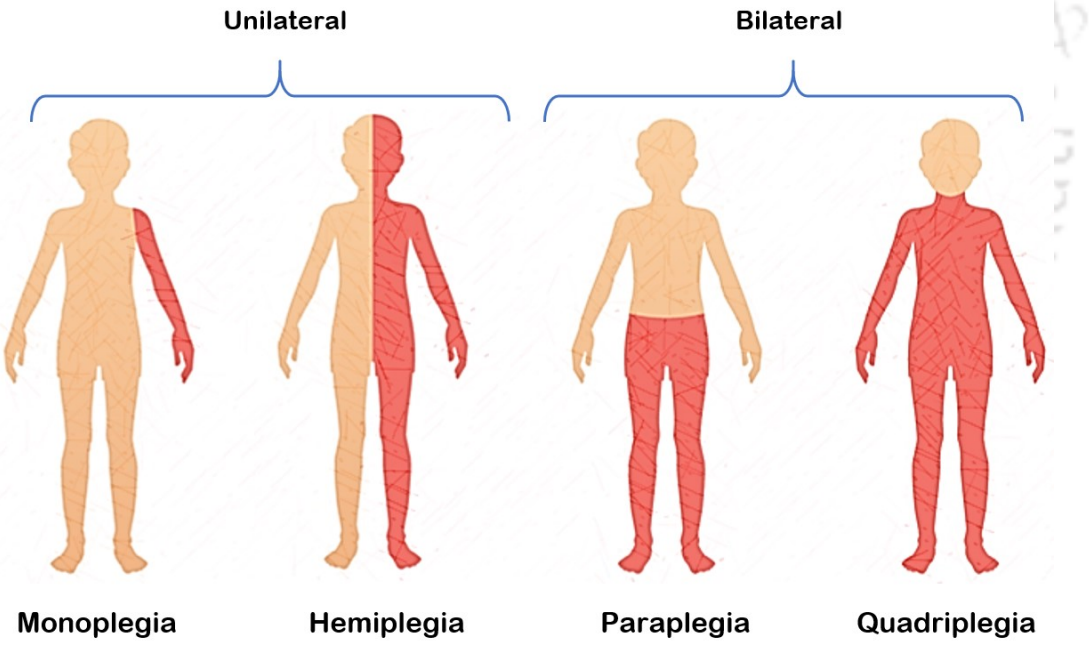

FIGURE 1.3: Types of CP based on topographical distribution

A benchmark and fairly reliable classification system are Gross Motor Function Classification System (GMFCS) where the CP subjects are divided into five levels depending on their gross motor capabilities [39]. It is defined as the investigation of self-procured movement with specific attention on sitting and walking activities. As shown in Figure 1.4, different levels can be classified as: Level I where subjects can walk without restriction while having some impairments in advanced gross

motor abilities; Level II where subjects can walk without mobility devices while having some restraints on walking in the open area; Level III individuals can walk with mobility devices while having some restraints on walking in the open community area; Level IV where subjects with mild restrictions are transported to the outdoors using self-assisted power mobility devices. Finally, individuals with Level V manifest severe mobility impairments and transport to the outdoors using assistant-driven mobility devices. The available literature on Robotic-assisted gait training (RAGT) in pediatric participants shows that gait therapy generally starts after age five [40].

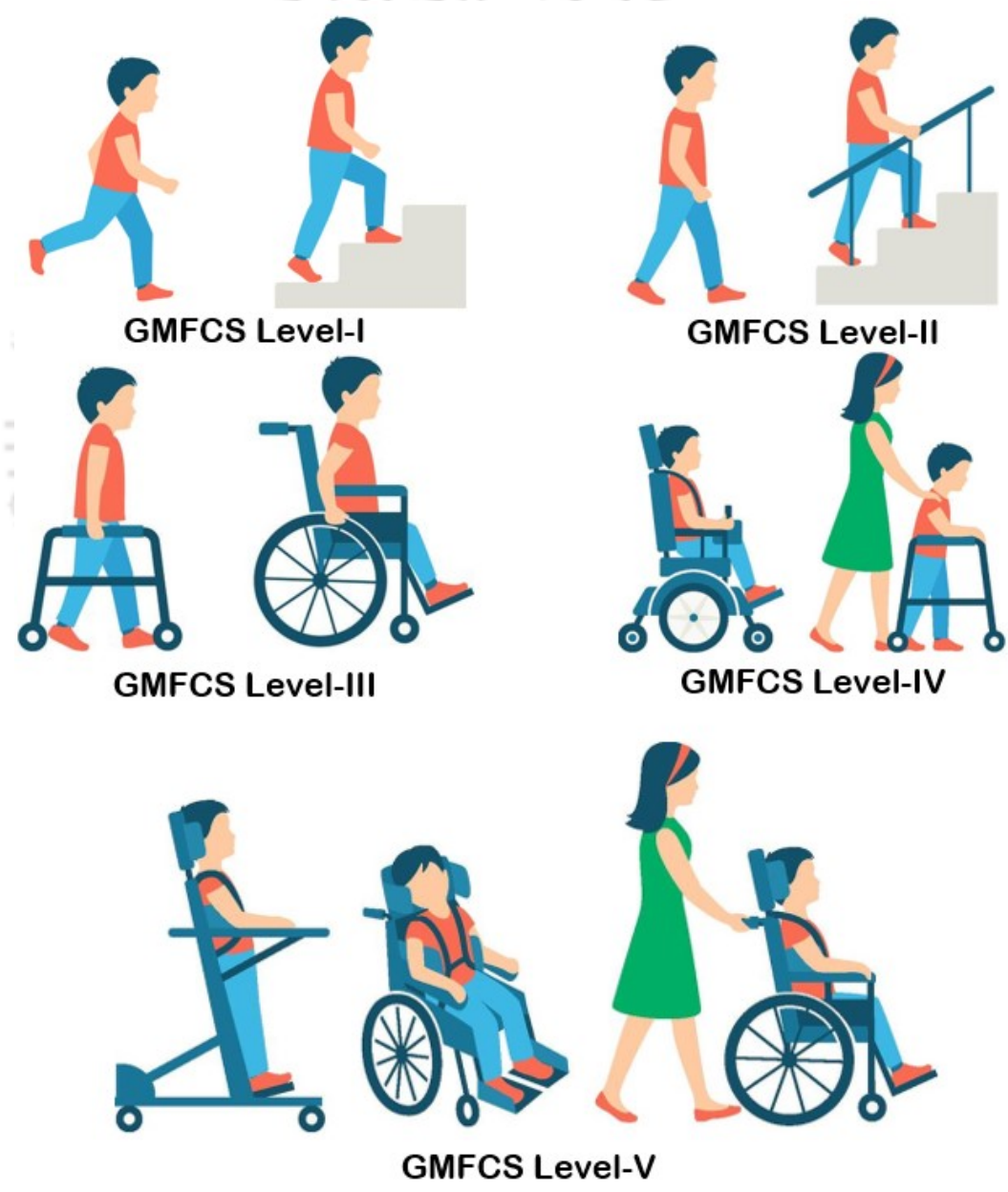

FIGURE 1.4: GMFCS levels

Typical gait patterns in CP can be divided into spastic hemiplegia and spastic diplegia [41, 42]. The spastic hemiplegia can be further divided into four groups based on the gait kinematics of the drop foot and equinus with different knee positions. On the other hand, spastic diplegia can be categorized into four main groups, i.e., true equinus, jump, apparent equinus, and crouch, depending upon the kinematics of pelvis, hip, knee, and ankle [41, 42].

Muscular Dystrophy

Muscular dystrophies (MD) represent a group of several genetic diseases marked by a progressive deficiency of the skeletal muscles that generate human movement. Some types of MD can be detected in childhood, while others can be delayed to middle age or later. The disorders vary according to the distribution of muscle weakness, rate of progression, and age of onset. The different types of muscular dystrophies are explained in [43].

1.3.2 Biomechanics of human gait

Exoskeleton systems can be considered wearable robotic devices that envelop the human body to provide mobility assistance. The interaction between the human body and the device should be cooperative to avoid discomfort to the user. The kinematic design of lower limb exoskeleton systems depends on the biomechanics of the human walking gait pattern. The gait cycle is defined as the time elapsed between two similar events performed by a leg during a normal walk. The five crucial events covered by each foot over a gait cycle are Initial heel strike (IHS), Heel rise (HR), Toe off (TO), Feet adjacent (FA) and End heel strike (EHS) . The foot position at the state of EHS is similar to the state of IHS with an interval of a gait cycle. The complete gait cycle is segmented into four phases, i.e., mid-stance, terminal stance, initial swing, and terminal swing [44]. The former two form a stance phase where some part of the foot is always shared with the ground and the latter two establish a swing phase where the foot remains in the air. The stance phase covers approximately 60% of the gait cycle. The model of human walking with relevant phases and events is shown in Figure 1.5. The other distinguishing attributes of human walking are cycle time, cadence, stride length, and walking speed. The distance covered between the initial heel strike (IHS) to the end heel strike (EHS) by the same leg over a gait cycle is called as stride length. The time duration involved in a gait cycle is known as cycle time, usually referred in seconds. The number of steps indulged per unit of time is expressed as the cadence, having

a unit of time in minutes. A measure of a half-gait cycle is, generally, termed cadence. The linear distance covered by the human body in a provided unit of time is defined as the walking speed, denoted in metres/seconds. The stride length and cycle time are measurable for every subject during the gait experiment.

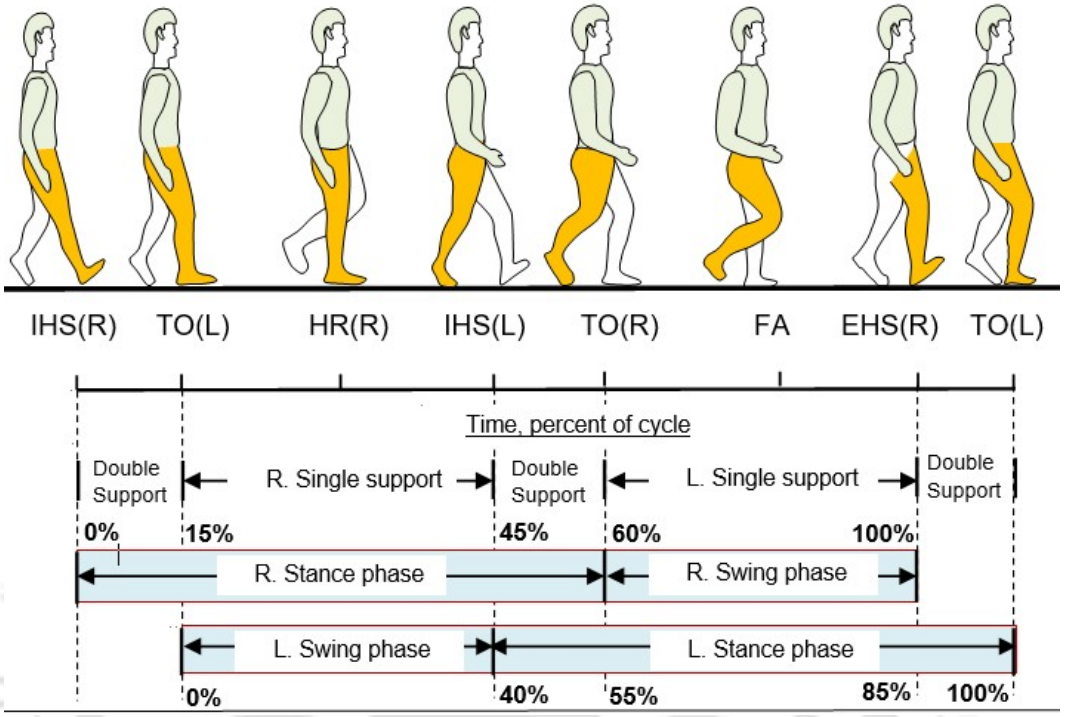

FIGURE 1.5: Gait pattern of normal human gait. (R- Right Leg, L- Left Leg

Additionally, the biomechanics aspect of the human lower limb should be precisely considered for the effective design of exoskeleton systems. In general, the human leg configuration consists of seven degrees of freedoms (DOFs) structure in each leg, i.e., three rotational DOFs at the hip, one at the knee and three at the ankle, as shown in Figure 1.6. The movements of the hip joint with three DOFs are abduction/adduction (a/a), flexion/extension (f/e) and hip intra/extra rotation (i/e), as shown in Figure 1.6(a). The movement of the knee joint with a single DOF is mentioned as flexion/extension (f/e) in Fig. Figure 1.6(b). The movements of the ankle joint with 3-DOFs are referred to as abduction/adduction (a/a), dorsi/planter flexion (d/p) and ankle inversion/eversion in Figure 1.6(c). These motions are stated repeatedly in the literature to describe the design of the mechanical structure of the available exoskeleton systems.

To perform gait analysis, model-dependent and model-independent approaches have been used in the literature [45]. Model-dependent approaches utilize the 'stick-figure' model to reconstruct the human gait over a gait cycle. These approaches extract kinematic and spatiotemporal parameters viz., gait sequence,

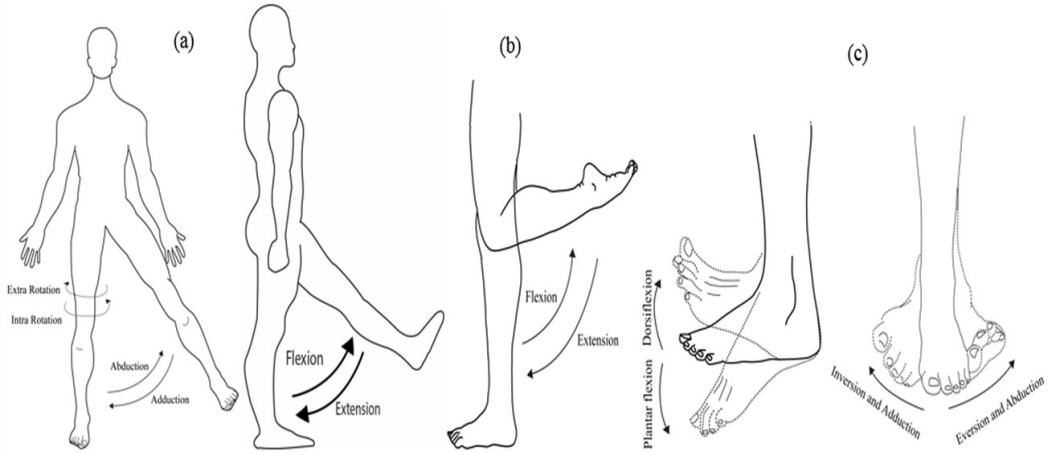

FIGURE 1.6: Joint movements of the lower limb (a) hip abduction/adduction (a/a), intra/extra rotation (i/e) and flexion/extension (f/e), (b) knee flexion/extension (f/e), (c) ankle dorsi/planter flexion (d/p), abduction/adduction (a/a), and ankle inversion/eversion (i/e)

single stance, double stance, stride length, cadence, length of body parts and joint angles of rigid body parts, based on predefined gait theory fundamentals. The characteristics feature of being view and scale-invariant makes these approaches suitable for real-life scenarios. However, these methods are quite cumbersome, computationally expensive and less efficient in practice than model-independent ones. Model-independent approaches rely on silhouette, a two-dimensional (2D) set of image attributes, extracted from a human body. They provide efficient results even for silhouettes having low-quality datasets. Therefore, they are considered to be computationally inexpensive approaches in comparison with model-dependent ones. However, the sensitiveness towards viewpoint and scale is a significant drawback of these approaches. All these approaches utilize the 2D dataset mostly as achieving the information for the third dimension is quite expensive. However, with the recent advancement of depth sensors like RGB-D, many efforts have been made to improvise the conventional model-independent approaches for gait identification in 3D.

Microsoft Kinect is an affordable device with an RGB camera and depth sensor, to track human joint movements using 3D skeletal image information [46]. Moreover, Haggag et al. [47] found that the Kinect along with the software development kit (SDK) is capable enough of establishing the joint centers, starting from hip joints and further extending to the head along with extremities, without any initial adjustments. Kinect has proven its worth for assessing posture control and standing balance, specifically in gross motor tasks [48]. Tanaka et al. [49] reported that hip

and knee joint angles evaluation using Kinect are found to be in strong correlation with the traditional marker-based setup during 20% - 60% of the gait cycle. In a recent study by Ma et al. [50] on the assessment of gait kinematic parameters for children with Cerebral Palsy, the Kinect v2 system is found to be reliable after a few calibrations as compared to traditional motion capture setup. They utilized the linear regression and long short-term memory (LSTM) neural network method to calibrate the Kinect-based joint angles for ten subjects. After calibration, the measurement inaccuracies of the range of motion (ROM) for every joint are improved. Few studies on gait recognition using Kinect are focused on treadmill walking rather than overground walking, leading to the disparity between visual pattern and actual movement pattern [51, 52].

Rodrigues et al. [53], in another recent study, proposed a low-cost 3D markerless motion capture (MOCAP) setup based on inertial sensors and Kinect cameras to assess the healthy human gait. They experimented with eight healthy subjects and found better results when compared with the VICON motion capture system. Roy et al. [54] presented the 3D gait analysis using a multi-camera system where optical-based passive markers are positioned to the different locations of the human lower limb. Moreover, force plates are used to estimate the kinetic parameters of the lower leg. Regazzoni et al. [55] investigated the effectiveness of the markerless MOCAP system towards clinical gait analysis after hip replacement. In a work by Chen et al. [56], using a MOCAP system having 17 inertial measurement units (IMUs), a preliminary test was carried out to estimate the reference trajectories of the hip and knee joints of healthy subjects in the sit-to-stand motion. Liu et al. [57] used LSTM techniques to map the gait features with gait trajectories validated by healthy participants to design a lower limb exoskeleton for knee joint rehabilitation. In a lower-limb exoskeleton design by Kim et al. [58], the flow parameters of the hydraulic actuator were decided using a gait analysis based on a MOCAP setup. Fournier et al. [59] exploited the CAREN Extended MOCAP system to estimate the gait analysis of healthy individuals at four slow speeds, which was further used as input parameters in the modeling of a lower extremity-powered exoskeleton. Sahoo et al. [60] carried out the real-time estimation of actual and early gait events during overground walking using a rule-based design where IMU sensors are used for detecting joint spatiotemporal parameters. In another work by Sahoo et al. [61], a neuro-fuzzy approach is used to estimate the step length for direct modulation of joint torques to walk comfortably.

1.3.3 Lower-limb exoskeleton: state-of-the-art

Generally, the exoskeleton systems have been developed by researchers to provide additional support to the different joints of the human lower limb. The main focus of these systems is to achieve freedom of movement for paraplegic people by aiding additional locomotion strength to the joints. In this subsection, lower-limb exoskeleton systems are categorized into single-joint and multijoint exoskeletons based on their actuated joints [11] as shwon in Figure 1.7. For each exoskeleton, available information regarding the mechanical design, actuator type, control strategy, and clinical developments has been delivered. Although this thesis presents some well-known gait exoskeleton robots for different age groups suffering with neurological disorders; the focus is kept on the available pediatric exoskeleton systems. Table 1.1 presents the details of the mechanical design of pediatric lower-limb exoskeleton systems.

1.3.3.1 Mechanical design and description

System configuration and parameters

Hip exoskeletons: Lower Extremity Powered Exoskeleton (LOPES) [25] and Active Leg Exoskeleton (ALEX II) [62–64] are the treadmill mounted robotic exoskeletons with the active hip joint. The other joints of the lower extremity are passive in nature. Although LOPES has been actuated for the hip f/e, a/a and knee f/e; however, only hip joint followed the protocol given by Ronsse et al. [65]. The location of both abduction axes relative to each other (pelvis width), and the location of the hip axis relative to the knee axis (thigh length) are adjustable to suit the anthropometric parameters of each patient. ALEX II is used as a hip f/e exoskeleton device and is majorly based on hip joint characteristics. Lewis and Ferris [66] designed an exoskeleton that comprises of a pelvic part and thigh cuffs attached to the hip joint for f/e motions. It is actuated by a pair of pneumatic muscles placed on the lateral side, which provides passive a/a. Active pelvis orthosis (APO) developed by d'Elia et al. [67] is another hip joint exoskeleton to assist the hip f/e movement with a minimum effect on the physiological human kinematics. Junius et al. [68] designed a hip exoskeleton that has six DOFs with hip f/e, a/a, and i/e rotation. The exoskeleton assembly includes a misalignment compensation mechanism with a parallel spring arrangement for two hip joints and torso and thigh braces. The design of the hip exoskeleton was based on the parallel axis theorem which ensures that any rotation around a biological axis is

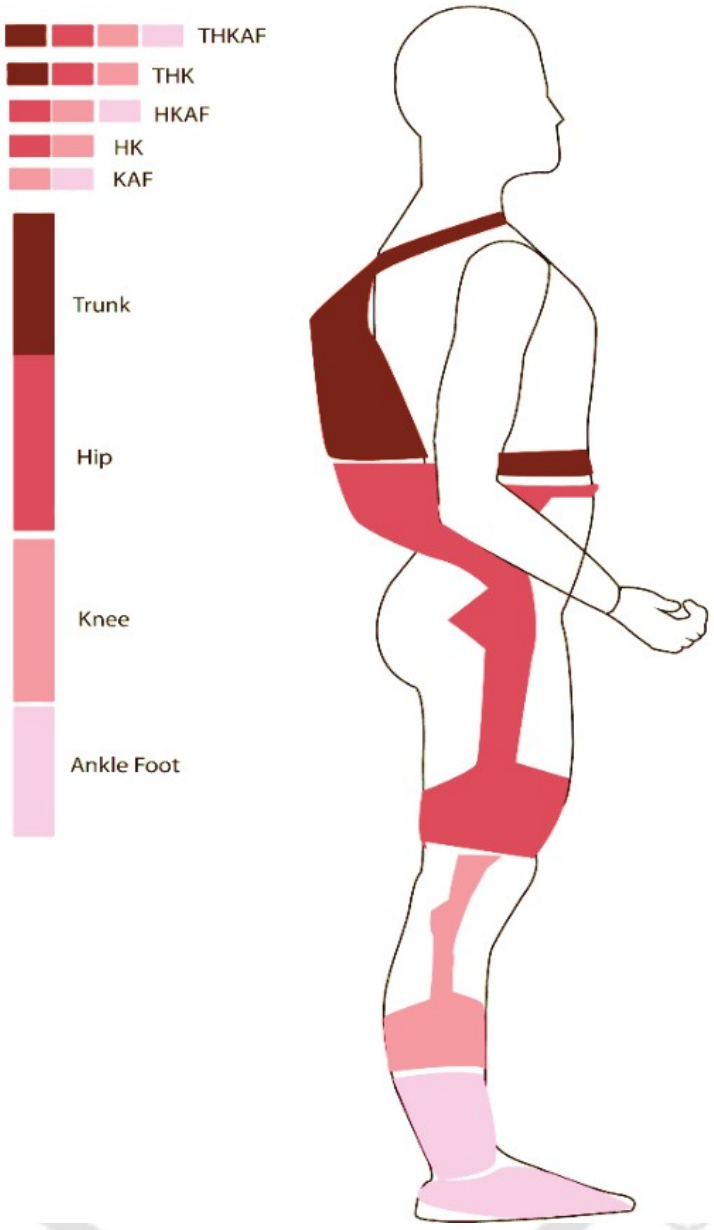

FIGURE 1.7: Classifications of joint-based lower-limb exoskeleton systems [11]

identical to a rotation around the corresponding exoskeleton axis if a translation of the exoskeleton axis in the plane perpendicular to it is allowed.

Knee exoskeletons: Fleischer and Hommel [69] developed a mono-lateral knee exoskeleton with knee f/e movement using a linear actuator. Ollinger et al. [70] designed a single DOFs knee joint to improve the leg-swing motion for elderly persons. A pneumatic actuated knee exoskeleton has been proposed by Kim et al. [71] with two pneumatic artificial muscle actuators (PAMs) which mimic the functions of rectus and biceps femoris muscles. In a recent work, Exoskeleton Intelligently Communicating and Sensitive to Intention (EICoSI) has been developed

as the active knee exoskeleton where the mechanical part and the actuator are kept onto one part of the device and the torque produced in the knee joint infers the motions from another part [72]. The shank parameters are estimated using the weighted least square optimization method. The mass and center of gravity of the shank are identified using Winter's work, provided the anthropometric parameters of the subject. The other parameters are considered after conducting the passive pendulum test. Khamar et al. [73] presented a knee exoskeleton based on the four-bar mechanism added with a curved segment. Considering shank angle, the precision points for the linkage bar are selected using an approximate synthesis method. Lerner et al. [74] and Yamada et al. [75] proposed two different knee exoskeletons in 2016 and 2018, respectively, to augment the knee extension for children affected with crouch gait. In 2018, Chen et al. [76] designed another knee exoskeleton (P-REX) to assist the CP-affected pediatric group outside of clinical settings. Washabaugh et al. [77] designed a lightweight and affordable wearable brace to provide resistive knee joint torque at different levels for stroke, SCI, and CP-affected individuals. In another work by Mohd Adib et al. [78], a low-cost device named exoskeleton robotic leg (ExRoLEG) is proposed to expedite the therapeutic training of CP individuals. The device mainly comprises metals, leading to a total weight of about 4 kg/leg.

Ankle-foot exoskeleton: Kao et al. [79] developed an ankle foot orthosis (AFO) for in-lab studies in the University of Michigan using two PAMs and analyzed the ankle d/p motion. Kim et al. [80] designed another AFO to provide ankle plantar flexion motion for elderly people, which comprises of a basic single DOF exoskeleton and an artificial pneumatic actuator. Malcolm et al. [81] developed an AFO with pneumatic muscles to study the effects of an active AFO for human movements. Chen et al. [82] proposed a 3-DOFs robotic device for ankle-foot rehabilitation. AssistOn-Ankle, designed by Erdogan et al. [83] is a reconfigurable Bowden cable-based series-elastic actuated exoskeleton for ankle movements to support both range of motion (ROM)/strengthening and balance/proprioception exercises. An underactuated 3UPS parallel mechanism was selected as the main kinematic configuration of the exoskeleton. Lerner at al. [84] designed a wireless reconfigurable ankle-foot exoskeleton in 2018 to lessen the metabolic expenditure of transfer during walking in CP-affected children and young adults.

Trunk-hip-knee-ankle-foot (THKAF) exoskeleton: The THKAF exoskeleton systems are mainly used for patients who require more stability of the trunk and hip in the lower extremity. Long et al. [93] designed an electrically actuated lower extremity exoskeleton device where the knee joint is active and the remaining

TABLE 1.1: Mechanical design of pediatric gait exoskeleton systems

Study	Device Name	Mechanical Design		
		Assist Joint	Active DOFs	Weight (kg)
Chen et al. [76]	P-REX	Knee	2	-
Lerner et al. [74]	-	Knee	2	3.2
Yamada et al. [75]	-	Knee	2	3.52
Washabaugh et al. [77]	-	Knee	2	1.6
Mohd Adib et al. [78]	ExoROLEG	Knee	2	8
Lerner et al. [84]	-	Ankle	2	1.8 (small), 2.2 (big)
Marsi-Bionics [27, 85]	ATLAS	THKAF	12	12 (ATLAS 2020), 14 (ATLAS 2030)
Bayon et al. [86]	CPWalker	HKAF	10	-
Eguren et al. [87]	P-LEGS	HKAF	6	8
Andrade et al. [28]	ExoRobo Walker	HKAF	6	6.57
Canela et al. [88]	-	HKAF	6	-
Laubscher et al. [89]	-	HK	4	5.1
Kawamoto et al. [90]	HAL	HK	4	-
Maggu et al. [91]	Trexo	HK	4	-
Patane et al. [92]	WAKE-Up	KAF	4	2.5

ones are actuated through the elastic elements. The lower extremity exoskeleton is dedicated to the subjects of height range 168 cm – 188 cm, where the thigh link can be altered from 430 mm to 470 mm and the shank link can be adapted from 470 mm to 510 mm. The length of the waist link can be varied from 340 mm to 360 mm. In other work by Chen et al. [94], the exoskeleton CUHK-EXO has been designed so that it can easily transfer the center of gravity to left and right during walking by adjusting the hip and ankle angle. Jin et al. [95] developed a THKAF lower extremity exoskeleton with two anthropomorphic legs, a spine and a pair of shoes. In each leg, the exoskeleton consists of seven DOFs i.e. three DOFs each at hip and ankle with one DOF at the knee. Mohan et al. [26] proposed a serial planar RRR passive exoskeleton ANKUR-LL II with a vertical planar 2PRP-2PPR parallel manipulator. This sitting or lying type of lower limb exoskeleton is mainly used for patient treatments in the sagittal plane. Later on, Vasanthkumar et al. [96] presented a hybrid serial-parallel 3-DOF lower limb rehabilitation device for the therapeutic treatment. In another study, a Biomimetic compliant lower limb exoskeleton robot (BioComEx) has been designed by considering active hip, knee and ankle joints. The ankle joint acts as a variable stiffness actuator and knee joint along with the hip joint acts as series elastic actuators (SEAs) [97]. The ATLAS exoskeleton is designed by Marsi-Bionics in different versions (ATLAS 2020 and ATLAS 2030) to advance the gait rehabilitation process and raise the life

expectancy of 3-14 years old pediatric subjects suffering from neuromuscular diseases such as Spinal Muscular Atrophy (SMA) and CP [85, 98]. The ATLAS 2020 comprised of ten active DOF and two passive DOF, and formed of two legs with a thoracic junction. The three joints at hip, knee, and ankle allow f/e movement in the sagittal plane, while hip a/d and ankle i/e movement offer movements in the frontal plane for the exoskeleton stability [98]. The ATLAS exoskeletons weigh about 12-14kg due to the lightweight materials such as aluminum and titanium.

Hip-knee-ankle-foot (HKAF) exoskeleton: The HKAF systems are bilateral and connected to a hip device through a pelvic band named lumbar sacral orthosis (LSO) or thoracic lumbar sacral orthosis (TLSO). These types of systems are designed for the f/e and a/a control with free or locking movement in the hip joint. Wearable Walking Helper (WWH) [24, 99] is another such type of gravity-compensating exoskeleton system where the torque supplied by the exoskeleton is proportional to the torques obtained from the human body movements and postures. He and Kiguchi [100] designed the lower-limb motion assist exoskeleton to provide locomotion assistance with one passive DOF for the ankle d/p, and two active DOFs for the hip and knee f/e joints. Another robotic device, H2 robotic exoskeleton, has been developed for the stroke rehabilitation of adults having a height from 1.50 m to 1.95 m with a maximum body weight of 100 kg. The exoskeleton actuates the three joints i.e. hip, knee and ankle of the human leg [101]. Wu et al. [102] designed a lower limb rehabilitation robot with 3-DOFs which has an adjustable yet simple structure with hip, knee and ankle joints for different heights of patients. CASWELL-II [103] is proposed with 5-DOFs, hip f/e (1 DOF), knee f/e (1 DOF), and ankle d/p (3 DOF), where the first hip and knee joints are driven by hybrid electro-hydraulic systems. Tu et al. [104] presented a design of a 3-DOF exoskeleton with active thigh f/e and shank f/e, and passive ankle d/p for subjects with diskinesia. An adaptable robotic platform for gait rehabilitation and assistance (AGoRA) developed by the Colombian School of Engineering Julio Garavito (CSEJV), has six active DOFs in hip, knee and ankle joints along the sagittal plane with one passive DOFs in hip a/a joint along the frontal plane [105]. In 2013, inspired by a former adult exoskeleton [106], Canela et al. introduced a 3-DOFs exoskeleton to assist the CP-affected pediatric individuals [88]. A robotic integrated platform, CPWalker, was developed in 2016 as the combination of a neuroprosthesis and a smart walker to mitigate the therapy period of the CP subjects after surgery [86]. The device has 10 active DOFs where six are for the exoskeleton and four are for the walker. In 2019, Eguren et al. [87] developed the 8kg pediatric lower-extremity gait system (P-LEGS) to rehabilitate

young subjects suffering from gait disorders. The system has six active DOFs in the sagittal plane and two passive DOF at the hip in the frontal plane for weight balance. Andrade et al. [28] proposed 6-DOFs ExoRoboWalker in 2019 to support the motion of the lower joints of both legs in CP-affected children and young adults. Chen et al. [107] designed the HKAF exoskeleton with active hip f/e, passive hip i/e, passive a/d, active knee f/e, and three passive ankle movements to assist the human gait in the swing phase.

Hip-knee (HK) exoskeleton: Belforte et al. [108] designed a pneumatic active HK exoskeleton with a commercially available passive lower-limb arrangement and a pneumatic actuation system to power hip and knee f/e movements. In another work, Exoskeleton for Patients and The Old by The Sogang University (EXPOS) has been designed by Kong and Jeon [109] with a smart caster walker which contains the heavy electrical components to make the device light in nature. The tendon-connecting motors and pulleys provide the additional power to the hip and knee joints depending on the user requirement. Hybrid Assistive Limb (HAL) was introduced by Sankai [23] and Kawamoto et al. [90] to support individuals with hemiplegia by using f/e and d/p movements on the sagittal plane. The hip and knee joints are active whereas the ankle joint is passive and connected through a spring. The HAL frame comprises steel and aluminum alloy materials to guarantee the lightness of the exoskeleton. Tagliamonte et al. [110] presented a treadmill-based lower limb exoskeleton for giving assistance to the flexion/extension movements for hip and knee joints. The whole weight of the exoskeleton is supported with an external system and the results are validated with the experiments. ABLE [111] is a powered lower-limb exoskeleton that allows the wearer to travel in a standing position, standing up from a chair and stair climbing. It mainly performs three functions viz. assistance by lower extremity exoskeleton, maintaining balance with the crutches and traveling around by standing still on the left and right moving platforms. Jin et al. [112] extended the design of ALEX II for cable-driven rehabilitation device i.e., C-ALEX to assist hip and knee joint of a single leg for motion assistance and gait rehabilitation. Long et al. [113] introduced an HK exoskeleton with two active joints of a single leg in the sagittal plane, which are knee joint and hip joint actuated by a hydraulic actuation system. Laubscher et al. [89] developed a 5.1kg HK exoskeleton in 2017 to assist CP-based gait disorders. A frame was initially designed with the exoskeleton; however, it is removed later for the pilot studies. Recently, in 2018, Maggu et al. [91] instituted the 4-DOFs Trexo Robotics (Mississauga, ON, Canada) as a safe walker-based assistive robot for children with with CP and SCI. Although the

device was launched in the market in 2021 after some successful clinical trials; the details about mechanical design, actuation, and control scheme are not provided in the literature.

Knee-ankle foot (KAF) exoskeleton: A KAF exoskeleton device is used to control the instabilities in the knee joint according to the rest of the lower limb by retaining a suitable arrangement and controlling the motion. Yeh et al. [114] developed a lower-limb pneumatic muscles exoskeleton system that has the knee f/e and keeps the ankle joints passive. Sawicki and Ferris [115] designed a KAF exoskeleton system by extending the AFO device of Kao et al. [79]. This device provides the motion for ankle joint d/p and knee joint f/e. In 2017, a Wearable Ankle Knee Exoskeleton (WAKE-up) was developed by Patane et al. [92] two actuated joint modules to rehabilitate pediatric subjects with neurological disorders. The device weighs about 2.5 kg which makes it the lightest multi-joint exoskeleton for CP children aged from 5 to 13 years old.

Static structural analysis

The static structural analysis ensures the strength of exoskeleton frames and components at different phases of the gait cycle. The literature on the methods of structural analysis are very limited for the lower-limb exoskeletons. In a work by Ding et al. [116], a finite element analysis (FEA) of the hip and ankle connection block was carried out in Solidworks to confirm the requirement of the intensity and rigidity. The material of the blocks was selected as aluminum alloy. As the maximum Von-Mises stress was within the yield limit of the selected material, the design parameters were optimized by 10%. In another study by Pan et al. [117], the effect of coupled subject-exoskeleton load on the hip joint was discussed using FEA for five instants over a gait cycle. The simulations were conducted in an ANSYS workbench. In a study by Huang et al. [118], FEA was carried out to investigate the translational and rotational deformation of the flexible structure of a compliant joint actuator in a lower limb exoskeleton. The material selected was aluminum alloy and simulations were carried out on ANSYS workbench. Wang et al. [119] presented the FEA for the hip connector and thigh link of a lower-limb exoskeleton which was made up of steel material. The simulation results have shown that the design was safe with 0.8 mm and 0.2 mm for hip connector and thigh link, respectively. In the case of the AGoRA exoskeleton, 3D FEA was performed to validate the loading capacity of the system with a maximum body weight of 90kg [105]. In work by Nithyaa et al. [120], FEA was performed for the thigh pan and shank link of a knee exoskeleton attached to the wheelchair. The materials

selected were aluminum and steel while simulations were carried out in an ANSYS workbench. Very recently, Varma et al. [121] conducted the feasibility study of the HKAF exoskeleton using FEA in ANSYS where the weight of the human subject and joint rotations are considered as input parameters to the model. Following the simulation results from the ANSYS, the design is further optimized to confirm the structural stability. As the works on FEA of exoskeleton components are either limited or not mentioned properly in the literature, there is an emergent necessity to discuss such aspects while designing the lower limb exoskeleton systems.

Dynamic analysis

The dynamic analysis is used to estimate the torque or voltage required to actuate the lower limb joint of the coupled subject-exoskeleton system. In literature, different mathematical (Newton-Euler, Euler-Lagrange) and software (OpenSim) models are used to express the dybamic behaviour of couple subject-exoskeleton system. Following a scaled version of the nominal hip torque dataset from Winter's study [122], an assistive torque was provided to user's hip joint in ALEX-II. From a literature survey on biomechanical joint torques, Ollinger et al. [70] have concluded that a 20 Nm continuous torque actuator produces significantly large assistive torques. Khamar et al. [73] have used the Euler-Lagrange approach to derive the dynamical formulations. Lerner et al. [123] utilized OpenSim [124] software to estimate kinematics and dynamics after scaling a 19 DOFs musculoskeletal model based on anthropometric parameters. Invoking inertial properties of the model, the Newton-Euler equations of motion determine the generalized forces necessary to simulate the gait trials. In the work by Washabaugh et al. [77], the net torque from the device is expressed using spring and pulley parameters. Chen et al. [82] described the dynamic model of the device using a 1-dimensional time-invariant model. Long et al. [93] applied Newton's second law of motion to determine the knee moment in the THKAF exoskeleton. Considering model error and uncertainties, Jin et al. [95] exploited the Euler-Lagrange principle to derive the dynamic model in the swing phase. In work by Mohan et al. [26], the Euler-Lagrange principle to derive the dynamic model of the parallel manipulator with friction effects in the sagittal plane and verified using multibody dynamics ADAMS software. Along with the friction and motor model, Wu et al. [102] derived the dynamic model of a 3-DOF single-leg exoskeleton using the Euler-Lagrange principle. To incorporate the human active participation, Tu et al. [104] used the Euler-Lagrange principle to present the coupled dynamic model of the 2-DOF leg exoskeleton. Inspired by the double pendulum approach, Andrade et al. [28] used the Euler-Lagrange principle to calculate the dynamic effects of the exoskeleton during the stance and swing

phases. Tagliamonte et al. [110] proposed a virtual stiffness model in joint space to estimate the required torque of SEAs. In the hydraulic HK exoskeleton by Long et al. [113], the physical human-robot interaction (pHRI) torque was processed via a Kalman smoother to avoid the lag between the movements of the human leg and exoskeleton. Laubscher et al. [89] calculated the actuator torques from motor current using the motor constant and transmission ratio. For the KAF exoskeleton by Patane et al. [92], the dynamic modeling was evaluated using Jacobian and load cell force. It could be clearly observed that most of the studies exploit the Lagrangian principle to formulate the dynamical equations. However, in the case of several lower limb exoskeletons, particularly pediatric ones, the dynamic analysis is not explicitly mentioned in the literature.

Furthermore, few rehabilitation devices have been developed based on the design concepts of bipedal robots [125]. Although the bipedal robots and lower-limb exoskeleton devices cannot be equated in view of applications; however, the stability and control aspects of bipedal robots can be exploited in the functional design of exoskeleton devices for mobility assistance. Invoking the concept of active dynamic walking bipedal robots, the well-known Berkeley lower extremity exoskeleton (BLEEX) has been developed according to the biological features of human beings. The exoskeleton was designed to adjust drive torques during walking with a different set of external loads on the back. Over the last few years, researchers have extensively explored the theory of passive dynamic walking for bipedal robots [126–129]. In the works by Added et al. [126], and Znegui et al. [129], the stabilization of compass model-based biped robots is carried out using analytical formulations of the Poincare map. Like passive dynamic walking, an unpowered robotic exoskeleton, Exobot, is designed by Collins et al. [130] to reduce the energy expenditure of human walking. The robotic system, developed with springs, utilizes carbon fiber and weighs about 700g.

1.3.3.2 Actuation Mode

The selection of actuators is a major part of the exoskeleton systems to regulate the various performance aspects like high power-to-weight ratio, ability to produce high power and force, compact size, high efficiency, high ability to be controlled, and ability to generate natural human-like motion. It is clear that for safety reasons, the actuator must also ensure active compliance with these robotic devices. In addition, some engineering requirements should also be fulfilled when designing

an actuator, e.g., lightweight, affordability, and modularity. There are a large number of types of actuators with different properties. The most common types of joint actuators used in the gait exoskeletons are electric (ANKUR-LL II [26], HKAF by Chen et al. [107], ATLAS 2020 and ATALS 2030 [85, 98], CUHK-EXO [94], ABLE [111]), pneumatic (Belforte et al. [108], Nitali et al. [131]), and hydraulic actuators (CASWELL-II [103], HK exoskeleton by Long et al. [113], Glowinski et al. [132]). Linear hydraulic and pneumatic actuators have high power density, but some works suggests that the use of electric motors provides a reduction in power consumption during gait [133]. Moreover, hydraulic and pneumatic actuators are usually bulky and cannot be easily controlled.

DC motors meet the criteria of necessary power with a compact and portable solution for wearable devices. Within the DC motors category, brushless motors offer several advantages for wearable devices, including higher efficiency, more torque density, increased reliability, reduced noise, longer lifetime, and reduction of electromagnetic interference. Moreover, DC motors can be coupled with a gearbox as the exoskeleton joints need more torque and less speed. To achieve a lightweight and small volume solution, strain wave gears, known as harmonic drive, were selected as a gearbox. In the ankle-foot rehabilitation device by Chen et al. [82], the motor suite consists of a permanent magnet DC-motor with a gearbox (reduction of 250:1) to improve the loading capacity up to 100 Nm. For two different sizes of the ankle-foot exoskeleton by Lerner et al. [84], two motors (24 V, 90 W and 24 V, 120 W) are used with 89:1 and 111:1 integrated planetary gearbox (EC-4pole, Maxon) which support up to 12 Nm, and 20 Nm, respectively. P-Rex exoskeleton [76] is customized with a bevel gear set (3:1 reduction ratio, planetary gearhead GP 32C (51:1 reduction ratio), and a Maxon motor to achieve the maximum continuous torque of 15.7 Nm. In HK exoskeleton by Laubscher et al. [89], a 70 W brushless DC motor is employed via a 3-stage belt transmission (40.6:1 reduction ratio) which offers a stall torque of 35.7 Nm, and a continuous torque of 5.4 Nm. P-Legs [87] included a 24 V Maxon motor with a 161:1 ratio gearbox to achieve the maximum momentary peak torque of 76 Nm and nominal torque of 13.5 Nm. ATLAS 2020 employs 70 W brushless DC motor with a 160:1 gearbox (rotation drive) to produce a maximum torque of 60 Nm in the sagittal plane and a similar 70 W brushless DC motor with a pre-stage reduction ratio 3:1 (linear drive) in the frontal plane [98].

To eliminate the drawbacks of the standard actuators, researchers have started to deploy some new kind of actuator like series elastic actuators (SEAs) (HK exoskeleton by Tagliamonte et al. [110], BioComEx [97], AssistOn-Ankle [83]) and

TABLE 1.2: Actuation details of pediatric gait exoskeleton systems

Study	Device Name	Actuated Joint	Actuator Type	Maximum Torque/Force
Chen et al. [76]	P-REX	Knee	Maxon BLDC	15.7 Nm
Lerner et al. [74]	-	Knee	Maxon BLDC	60 Nm
Yamada et al. [75]	-	Knee	Mikki Pulley EM Brake	7 Nm
Washabaugh et al. [77]	-	Knee	K&J EM Brake	56 Nm
Mohd Adib et al. [78]	ExoROLEG	Knee	Linear Actuator	500 N
Lerner et al. [84]	-	Ankle	Maxon BLDC	12 Nm, 20 Nm
Marsi-Bionics [27, 85]	ATLAS	THKAF	Maxon BLDC	60 Nm
Bayon et al. [86]	CPWalker	HKAF	Maxon BLDC (HD)	-
Eguren et al. [87]	P-LEGS	HKAF	Maxon BLDC	76 Nm
Andrade et al. [28]	ExoRobo Walker	HKAF	Maxon BLDC (HD)	-
Canela et al. [88]	-	HKAF	Maxon BLDC	34.3
Laubscher et al. [89]	-	HK	BLDC	35.7 Nm
Kawamoto et al. [90]	HAL	HK	DC	-
Maggu et al. [91]	Trexo	HK	-	-
Patane et al. [92]	WAKE-Up	KAF	Rotary SEA	-

pneumatic artificial muscle actuators (PAMs) (KAF by Yeh et al. [114], AFO by Kao et al. [79], AFO by Malcolm et al. [81]) to control the exoskeleton systems. A Rotary Series Elastic Actuator (RSEA) and a belt/pulley stage (reduction ratio 2:3) is used in the WAKE-up exoskeleton to improve the user's safety [92]. Recently, Kalita and Dwivedy [134, 135] conducted several studies to investigate the non-linear behaviour and instability regions of PAMs subject to direct and parametric excitations which can be straightforwardly extended for actuating the lower-limb exoskeleton. However, controlling PAM as an exoskeleton actuator is a computationally expensive process [136]. Depending on the application and user's requirements for the device, the actuators are selected for lower-limb exoskeletons. Moreover, the other accessories, like the sensors with the required power supply, are selected for the actuation of the exoskeleton. From Table 1.2, it can be noticed that all pediatric gait exoskeletons have used electric actuators as they produce a large amount of torque for precise movements. For developing an assistive device of a particular application, electric actuators are easily available with the required specification. However, the cost of high torque electric motor, particularly Maxon motors with harmonic drive, is very high and make the systems less affordable.

1.3.3.3 Control Scheme

In the last few decades, many researchers and designers have developed assistive devices for improving the support to the lower extremity with robotic-aided rehabilitation training. The main objective of these devices is to maintain a proper human-exoskeleton interaction between the device and the wearer. Therefore, it is very necessary to ensure a smooth control scheme to improve the effectiveness, accuracy, and comfort of the exoskeleton device based on the user's intentions. Yan et al. [11] categorized the control architecture of lower-limb exoskeletons into nine control schemes such as reference trajectory based gait control (ATLAS [27,137], HAL [90,138]), model based stability control (ABLE [111]), adaptive oscillator based control (Ronsse et al. [65], Tagliamonte et al. [110], LOPES [25], ALEX II [64]), predefined motion based control (Lewis and Ferris [66], Malcolm et al. [81]), sensitivity magnification control (BLEEX [20]), decision based fuzzy control (He and Kiguchi [100]), hybrid control (BLEEX [20], Yeh et al. [114]), muscle stiffness control (Kim et al. [71]), and myography based control (Kao et al. [79]). These control schemes could be achieved from the signals gathered from the human body as well as the exoskeleton along with the human body.

Another well-known classification for the lower-limb exoskeleton robots is the hierarchical level control scheme which classifies into the upper level control (ULC) and lower level control (LLC). Overall, ULC cares about the decision algorithms based on the human intent and resulting 'assist-as-needed' interactions with the exoskeleton robot during active-assist gait rehabilitation. On the other hand, LLC accounts for the servo control based on the position and torque tracking approaches. ULC is further classified into supervisory control (SC) and high-level control (HLC) schemes [139]. One such architecture of hierarchical level control is shown in Figure 1.8 where HLC represents the impedance controller and LLC inherits the torque controller.

In particular, SC schemes such as Finite State Machine (FSM) with force-sensitive resistors (FSR) (Lerner et al. [74], [84]), and inertial measurement units (IMU) (WAKE-up [92]) identifies gait phases as an additional input to the HLC with reference joint trajectory. Moreover, Electromyography (EMG) and Electroencephalographic (EEG) sensors at the supervisory level allow for the estimation and syncing of human intent with muscle activities which enables gait timing. In CP Walker, the human-robot interaction is carried out using a Multimodal Human-Robot Interface (MHRI) which includes an EEG unit, EMG system, IMU, and a

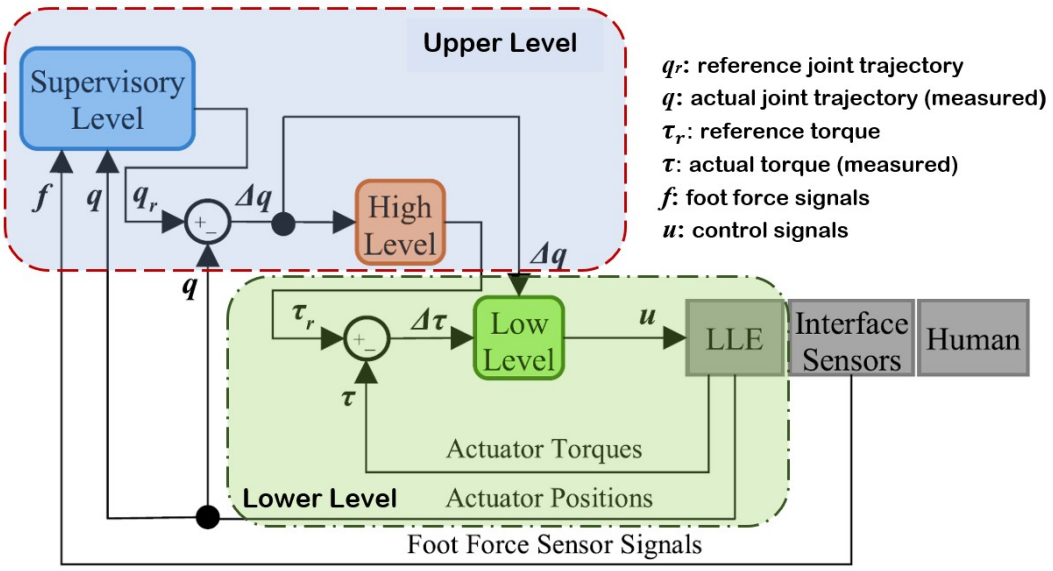

FIGURE 1.8: Hierarchical level control for lower-limb exoskeleton systems [14]

Laser Range Finder (LRF) to measure the gait cycle and control the device accordingly [86, 140]. However, abnormal gait patterns of children with CP make it difficult for the supervisory-level controller to detect or predict gait phases.

HLC schemes employ the admittance/impedance controller which allow the subjects to actively participate in the gait rehabilitation by taking the benefits of their residual muscle movement under the concept of "assist-as-needed" (ALEX-II [64], ATLAS [27, 85], P-LEGS [87]). Apart from the supervisory-level sensors, the coupled exoskeleton-human interaction forces can be measured using disturbance observers [141] and spring-mass-damper mathematical model [20, 104, 142]. In 2012, Ollinger et al. [70] proposed an active-impedance controller for the knee exoskeleton. In last five years, active research on the impedance/admittance controller for the gait exoskeletons have been started. For example, Luo et al. [143] used the central pattern generator (CPG) to regulate the impedance parameters and adapt as per the subject's involvement. Tu et al. [104] proposed an intent-based variable admittance control to regulate the participation level of the subject. Despite of above works, from Table 1.3, it may be noted that there are very limited research available on impedance control, particularly admittance control, for the pediatric gait exoskeleton systems.

On the other hand, LLC schemes focus on the torque or position control of the actuator in passive-assist rehabilitation mode where interaction from the subject is not considered [145]. The low-level torque control attempts to track a reference torque based on actuator's electric current as the input state [146]. This

TABLE 1.3: Control scheme in pediatric gait exoskeleton systems

Study	Device Name	Upper Level		Lower Level
		Supervisory-Level	High-Level	Servo-Level
Chen et al. [76, 144]	P-REX	FSM (FSR)	Impedance control (Adaptive control)	PID Torque control (Torque sensor)
Lerner et al. [74]	-	FSM (FSR)	-	PID Torque control (Torque sensor)
Yamada et al. [75]	-	(FSR)	-	-
Washabaugh et al. [77]	-	(EMG)	-	-
Mohd Adib et al. [78]	ExoROLEG	(EMG)	-	-
Lerner et al. [84]	-	FSM (FSR)	Sigmoid function (PJMC)	PID Torque control (Torque sensor)
Marsi-Bionics [27, 85]	ATLAS	(FSR, IMU)	Impedance control	PID Position control (Encoder)
Bayon et al. [86]	CPWalker	(FSR, EMG, EEG, IMU, LRF)	Impedance control	PID Position control (Potentiometer)
Eguren et al. [87]	P-LEGS	(FSR, IMU, Encoder)	Adaptive Impedance control	PD Position control (Encoder)
Andrade et al. [28]	ExoRobo Walker	FSM (FSR, Potentiometer)	Impedance control	PID Torque control (Strain Gauge)
Canela et al. [88]	-	-	-	-
Laubscher et al. [89]	-	(Angle sensor, Hall effect sensor)	-	PD Position control
Kawamoto et al. [90]	HAL	(EMG, Encoder)	-	-
Maggu et al. [91]	Trexo	-	-	-
Patane et al. [92]	WAKE-Up	FSM, (FSR, IMU, Encoder)	-	PID Position control

control approach exploits the difference between the reference torques and measured torques by sensors as shown in Figure 1.8. During initial stages of therapy, position control guarantees that the exoskeleton robot can track the desired gait trajectory where movement information is measured by potentiometers. The control architecture required for the exoskeleton systems poses extra complexity over the conventional robotic arm control due to the sophisticated mechanical configuration, complex motion trajectory, and human involvement. The researchers, in the literature, have regarded the predefined gait tracking control as the basis of every control scheme for exoskeleton systems, where the joint movements of the lower limb could be estimated using gait analysis experiments (PID control in EXPOS [109], fuzzy control in ABLE [111], PID control in CUHK-EXO [94]). Although the exoskeleton systems exploit the gait of healthy humans to replicate

the same using predefined trajectory control schemes, however, in practice, they are unable to attain the proper gait trajectory because of the parametric perturbations and external disturbances (PPED). Therefore, various robust control strategies have been designed to deal with the limitations of classical trajectory tracking control in lower limb exoskeleton systems (adaptive oscillators by d'Elia et al. [67], sliding mode control (SMC) by Long et al. [113], backstepping-SMC by Khamar et al. [73], proxy-based SMC by Chen et al. [82], active disturbance rejection with fast terminal SMC by Chen et al. [147]) has been carried out for the elderly gait exoskeletons in the literature.

In other work on robust position control, Yang et al. [148] presented a sliding mode control (SMC) scheme where a second-order command filter-aided backstepping is incorporated to avert the "explosion of complexity." Moreover, fuzzy logic is exploited to counter the chattering issues of the control scheme during the estimation of structured and unstructured uncertainties. In another work to address the model uncertainties and the unintended subject's response, Wu et al. [102] proposed an adaptive control scheme for a 3-DOF lower extremity rehabilitation device. Working on the decoupled control strategy, Sun et al. [149] designed a reduced-order adaptive fuzzy approach and implemented it on a two-link exoskeleton system for lower limb rehabilitation. Recently, several works on robust control schemes are being explored for different preliminary designs of the gait exoskeleton robots (model reference adaptive control [150], fractional order terminal SMC [151, 152], adaptive SMC [153], adaptive non-singular fast terminal SMC [154], time delay estimation-based model-free fractional-order nonsingular fast terminal SMC [155], and super-twisting SMC [156]). Moreover, in recent times, robust intelligent control schemes have gain popularity to address the adverse effects of PPEDs with effective approximation features [157–160]. Wang et al. [160] proposed an event-triggered SMC for HK exoskeleton where genetic algorithm-aided backpropagation NN is exploited to estimate the motion intent of the subject using EMG signals. Intelligent techniques such as neural network (NN) and neural-fuzzy (NF) have excellent approximation capabilities which benefit the classical PID control technique to form a robust control scheme. Zhang et al. [157] proposed a time-delay estimation-based model-free NN-PID controller for a virtual 5-DOFs lower-limb exoskeleton where online adaptation of radial basis function was carried out to address the PPEDs. However, in all such intelligent techniques, the initial selection of NN hyperparameters is an iterative and cumbersome task for effective model identification.

On the other hand, few researchers have explored the optimal control, especially

the linear quadratic regulator (LQR), to realize the natural gait [161–163]. The LQR scheme with full-state feedback yields control measures concerning the whole body compared to PD control for every independent joint [161]. In addition to that, the relative prominence of curtailing the tracking error and minimalizing the control torque can be regulated by computing optimal values of time-varying gain based on the design parameters of a single controller. Ajjanaromvat and Parnichkun [162] proposed an iterative online learning-based LQR control scheme for a treadmill-appended exoskeleton to investigate the robustness analysis. Moreover, the proposed control scheme is aided by an adaptive iterative learning control to address tracking errors. Castro et al. [163] proposed an integral-aided LQR (LQRi) and unknown input disturbance observer (UIO) to address external interferences of the lower limb exoskeleton system. The results of the proposed control are compared with proportional-derivative control and found to be more effective. Although the LQR is the most optimal control scheme and lacks to resolve uncertain exoskeleton dynamics.

Even for the elderly gait exoskeletons, most existing hierarchical control schemes exploit the non-robust position control in the inner loop to track the modified gait trajectory. In order to address uncertain dynamics and external disturbances, recently, sliding surface-based position control schemes are used to track the reference trajectory in the case of human-robot interaction [104, 147, 164]. However, the problem of fast convergence of error states has not been taken into account. Almaghout et al. [165] proposed a super-twisting nonsingular terminal SMC to perform the desired training tasks with finite-time convergence of the error states. However, the information on selecting the admittance parameters is not evident. In other work on robust inner loop position control, Mokhtari et al. [166] designed an adaptive high order super-twisting SMC for an lower limb exoskeleton robot. Although the authors obtained the optimal impedance parameters; however, they have not considered the varying impedance model as in the case of the real environment during active-assist gait rehabilitation. Furthermore, it is pertinent to mention that the conventional SMC generally suffers from the chattering phenomena, less robustness, and sensor drift. The high order sliding mode control can be used to reduce the chattering effect with the fact that the controller requires high gain values for the compensation of uncertainties and disturbances [167]. Such high gain values sometimes degrade the stability of the system.

In addition to the SMC, backstepping control (BC) is another well-known nonlinear control scheme that can guarantee trajectory tracking with global regulation [168]. The design of BC is a step-by-step recursive process that inherently

establishes the stability criteria using the appropriate Lyapunov candidate functions. The conventional BC can not ensure the system's robustness in the presence of parametric and non-parametric uncertainties. Therefore, in the literature, some adaptation laws have been used with BC, termed ABC, to deal with uncertain dynamics, and external disturbances [168, 169]. However, such control designs pose certain limitations such as overparameterization [170], the explosion of terms [171,172], larger magnitudes of control signals [173], and computationally expensive regression matrices [169,174]. Nowadays, researchers are working on the merger of SMC and ABC, i.e., the ABSMC (adaptive backstepping sliding mode control) to get their advantages altogether [175].

However, as observed from Table 1.3, most of the available pediatric gait exoskeletons utilize the proportional-integral-derivative (PID) control in the lower-level control scheme. For example, in the knee exoskeleton by Lerner et al. [176], a PID control scheme with a torque sensor is used as a LLC to estimate the desired torque output during each gait phase. In a knee exoskeleton by Chen et al. [144], a torque control based on a local PID controller and feedforward control scheme has been exploited to create an adequate control signal for the actuator. Eguren et al. [87] exploited the PD controller for each joint and tuned the gain parameters separately. ATLAS 2020 also exploits a PID controller in the LLC for the walking mode [27].

1.3.3.4 Development Stages

Most of the existing lower limb exoskeletons require autonomous power sources of high energy. Therefore, there is a need to develop some advanced arrangements that can accumulate and supply the energy for various phases of the gait pattern. Further, the gait pattern and the control strategies should be optimized so that the exoskeleton can store the energy for various applications. Moreover, the recent systems are very expensive and affordable to a less number of individuals [12]. Therefore, there is a need to think about the development of an affordable and reconfigurable exoskeleton device so that it can be utilized by different age groups. The price of the exoskeleton systems can be reduced by incorporating new technologies for the actuators, controllers, and sensors. Due to the above-discussed factors many exoskeleton systems were stopped in their tracks towards commercialization at the research stage itself [177].

However, some systems have already underwent clinical trials such as HAL [23], KAF exoskeleton by Kawamoto et al. [90], CUHK-EXO [94], knee exoskeleton by

Lerner et al. [74] and Bayon et al. [86]. As this thesis is focused on the pediatric gait exoskeleton systems, the brief clinical details of only well-developed pediatric gait systems are discussed here. Collectively, 184 participants are considered for clinical trials, of which 32.06% are for the ankle exoskeleton by Lerner et al. [84], 31.52% for HAL exoskeleton, and 29.35% for knee exoskeleton by Lerner et al. [74]. Ignoring 17 subjects with unclear GMFCS Level, 27% experiments are with GMFCS Level I, 39% with GMFCS Level II, 25% with GMFCS Level III, 8% with GMFCS Level IV, and 1% with GMFCS Level V. However, in all clinical trials for the pediatric exoskeletons, only one participant with CP had GMFCS Level (V) which shows that more researches on lower-limb exoskeletons are needed for CP subjects with severe mobility disorder.

1.4 Summary and Identification of the Research Gap

As observed from literature, most of the researches in lower-limb exoskeleton systems have been carried to address the mobility impairment and gait rehabilitation for the elderly group (> 50). There are very limited works in design and modeling of a multi-joint gait exoskeleton (09 devices) for the pediatric group suffering from CP and SCI. Moreover, in the design of multi-joint exoskeletons, especially with hip joint augmentation, there has always been a trade-off between the actuators' weight and cost involved. Although some alternative solutions have been proposed to bring lightweight and affordable actuators such as SEA and PAM; however, controlling such actuators becomes computationally expensive and requires several hardware manipulations. Few researchers have exploited the wheel-based walker system to place the heavy electric DC actuators and reduce the weight borne by the exoskeleton systems. Therefore, the wheeler stand-aided designs of the HKAF exoskeleton system could be explored further to offer more stability and safety to pediatric users in case of severe gait pathologies.

In a couple of studies, adjustable links have been considered in the design of pediatric gait exoskeletons to accommodate the different heights of pediatric subjects and to reach a wide range of end-users. Therefore, one could explore the adaptable or telescoping leg and waist links in view of the maturation growth of real pediatric subjects. The design parameters should be decided based on the anthropometric and biological parameters of the real healthy pediatric subjects. Moreover, the

reasoning behind the selection of structure material and actuators for the majority of lower limb exoskeletons are unclear and thereby, motivates to carry out the finite element analysis and dynamic analysis in different therapeutic modes.

In literature, a significant amount of work has been carried out to design and deploy robust gait-tracking control schemes for elderly exoskeletons. However, in the case of available pediatric exoskeleton systems, the conventional PID (position or torque) control schemes have only been applied in the servo-level for passive-assist training mode. In the case of pediatric rehabilitation, parametric perturbations and external disturbances become more significant due to substantial variations of dynamic parameters (system mass and length) and body reflexes (unintended subject response). Following the above fact, at first, there is an emergent need to design robust position control schemes for pediatric exoskeletons systems which can ensure effective gait tracking under parametric perturbations and external disturbances.

Even in the high-level hierarchical level control approach, only five pediatric exoskeletons have exploited the impedance control scheme. As impedance control requires real-time information on the reference torque using costly sensors, one can explore the admittance control scheme with a robust gait tracking control scheme to enable the human-in-the-loop cooperative control approach. Admittance control differs from impedance control in such a way that the former controls motion (position, velocity, acceleration) based on the mechanical admittance parameters at the expense of measured force, and the latter controls force based on the mechanical impedance parameters at the expense of measured deviation from a set position. Moreover, admittance control is relatively more accurate than impedance control when in contact with soft environments like a human leg. Admittance-based cooperative control approaches could benefit to the pediatric subjects while participating actively in gait rehabilitation process. In most of the studies, EMG, FSR, EEG based supervisory control schemes have been practiced to include the effects of physical human-robot interaction which requires an expensive hardware setup and skilled personnel. Therefore, if an effective high-low level-based cooperative control scheme can be explored, the need for supervisory level control can be ignored for time being to reduce the overall cost of exoskeleton systems.

One important aspect of the cooperative control scheme is to achieve the variable admittance parameters over a gait cycle to closely mimic the real-time changing admittance of biological leg and offers additional benefits of safety along with the flexibility to participate in the therapeutic training. Therefore, a variable

admittance model could be designed further in a cooperative control scheme. The benefits of applying such cooperative control in the presence of sudden interaction reflexes could be further investigated for the pediatric gait exoskeleton systems. Another challenge to obtain fast and finite-time convergence of gait tracking error during the human-in-the-loop cooperative control could also be inspected. The objectives of the present work are mentioned in the following section.

1.5 Objectives of the Present Work

The main objectives of the present work are to design and investigate the potential of robust control schemes for a pediatric lower-limb exoskeleton robot in passive- and active-assist rehabilitation mode. To achieve these objectives, following works are carried out:

- To design and develop a proof-of-concept exoskeleton device for lower-limb rehabilitation of pediatric subjects.
- To design and implement robust intelligent control schemes (LQR-based neural fuzzy and neuro-fuzzy compensated PID) for the exoskeleton device in passive-assist mode.
- To design and implement a robust adaptive backstepping control scheme for the exoskeleton device in passive-assist mode.
- To design and study the human-in-the-loop adaptive backstepping sliding mode cooperative control scheme for the exoskeleton device in active-assist mode.
- To design and study the human-in-the-loop adaptive backstepping integral-aided singularity-free fast terminal sliding mode cooperative control scheme for the exoskeleton device in active-assist mode.

1.6 Thesis Organization

The thesis is organized into seven chapters as follows:

In Chapter 1, an introduction, motivation, and existing state-of-the-art in literature are presented.

In Chapter 2, design and prototype development of the gait exoskeleton is presented in two versions (LLES$v1$ and LLES$v2$).

In Chapter 3, a robust LQR-based neural fuzzy (RLQR-NF) and neuro-fuzzy compensated PID (NF-CID) gait tracking control scheme are designed for the LLES$v1$ with PPED. The proposed control schemes is validated with the LLES$v1$ experimental setup and a human dummy.

In Chapter 4, a robust adaptive backstepping (RABS) gait tracking control scheme is introduced for the LLES$v2$ with PPED. The proposed control is tested with the LLES$v2$ experimental setup and pediatric subject.

In Chapter 5, a robust adaptive backstepping sliding mode subject-cooperative control (ABSM-SCC) is investigated for the exoskeleton system in active-assist mode. To mimic the real-time human-exoskeleton interaction, a neural-fuzzy based variable admittance model is proposed.

In Chapter 6, a robust adaptive backstepping integral singularity-free fast terminal sliding mode subject-cooperative control (ABISFFTSM-SCC) is presented for the exoskeleton device in active-assist mode, which ensures the fast and finite-time convergence of error states to the equilibrium on the sliding surface.

Finally, in Chapter 7, the overall conclusions from the present work are presented with the future scope.

Chapter 2

Design and Development of Pediatric Lower Limb Exoskeleton

2.1 Introduction

As discussed in the previous chapter, there are very limited pediatric exoskeletons available for motion assistance and gait rehabilitation. Moreover, there are few major concerns of existing pediatric exoskeletons such as less affordability, minimal adaptability, and less structural stability. Inspired from the work of Bayon et al. [86] and Andrade et al. [28] where the stability and balance of the subjects during overground gait training was augmented with a walker, the present work explores the designs of low-cost and adaptable stand-supported lower-limb exoskeletons for pediatric gait rehabilitation. In the present work, the criteria and requirements to design a lower-limb exoskeleton system is extensively described in Section 2.2. A NI-LabView-based motion capture experimental setup is prepared to estimate the gait analysis of the pediatric subjects in Section 2.3. A preliminary design and modeling of 6-DOFs gait exoskeleton system (LLES$v1$) based on kinematic and anthropometric data of five pediatric participants are presented in Section 2.4. Thereafter, modifying the structure and configuration of the preliminary design based on new set of 11 participants, the final design and modeling of the 6-DOFs exoskeleton system (LLES$v2$) are presented in Section 2.5. The dynamic analysis is derived for passive-assist and active-assist mode using Euler-Lagrange principle in Section 2.6. The results for prototyping of both designs are discussed along with

the actuator requirements Section 2.7. Finally, the outcomes from this chapter are summarized in Section 2.8

2.2 Design Criteria and Requirements

In the mechanical design of the exoskeleton, different design criteria should be considered. The fundamental outlook for designing a lower limb exoskeleton system is to decide the strength, stability, and safety considerations. The strength refers to the capability of links, frames, and joints of the system to transfer the required forces and torques for a paraplegic subject. However, the strength of the system increases the overall weight, which is not desirable for paraplegic users. Therefore, the mechanical and electric components in the complete design should be light as much as possible. Moreover, there should be some design criteria for the adaptability of different users. The next important aspect to consider is selecting actuators as they should be able to provide sufficient joint torques for a specified set of motions. Another critical factor is to choose degrees of freedom for each joint as when DOFs increases, the user feels more comfortable. However, providing all possible degrees of freedom to every joint can cause involuntary movements and start discomforting to the subject. The design criteria as outlined by researchers at the Selcuk University [178] includes ergonomic and anthropometric design, kinematic compatibility, high maneuverability, lightweight and strong structure, low-cost, adaptability to different users, and user safety.

Ergonomic and anthropometric design: In orthopedics, the continuous change in skeletal morphology of the human is observed which depends upon several reasons such as gender, shape, and skeletal deformities, especially, in childhood days. Moreover, the athropometric measurements vary significantly from country to country and from one region to another within a particular country [179]. In another work on cross-sectional multicentric study by Vispute et al. [180], it was observed that north Indian children were taller and children from the northeast were the shortest. For example, the leg length of children of age 9+ years boy from central India was found to be high (64.22cm) as compared to northeast India (61.2cm). This can create a challenge for the existing exoskeleton to fit the patient into the exoskeleton when having this change. On the other hand, attaching the subject limbs to the exoskeleton is a common ergonomic challenge as even a slight misalignment in between the exoskeleton joints and the corresponding patient joints produces unexpected and dangerous internal forces on the human limbs and

straps. *Therefore, to address such issues in this thesis work, authors have collected the anthropometric and ROM database for real pediatric subjects from Guwahati region of Northeast India. In this way, the ergonomic alignment of lower-limb joints has been taken care when defining the dimensions of the structures, joints' ROM, and interface materials for the exoskeleton system.*

Kinematic compatibility: The kinematic compatibility at the attachment interface is crucial to consider for effective and safe interaction between the lower-limbs of the subject and exoskeleton [181]. This offers a number of advantages such as workspace similarity, singularity avoidance, safe and compliant interaction, etc. However, the interference between the kinematic loops at the attachment interfaces is unavoidable in many cases due to impossibility to exactly match the human kinematics with the exoskeleton one. In practice, the rigidity between the limbs of subject and exoskeleton via physical interfaces is not desirable, especially, when subject is able to cooperate with his/her residual muscle strength. To address any such compatibility issues, keeping a passive or active degrees of freedom (DoF) at the connection interface to mimic the flexible behavior of muscles could be a potential solution. *In this thesis work, the physical attachment is modelled as a single-DOF spring-damper arrangement to allow flexible human-exoskeleton interaction.* Moreover, the limitation of the previous works is illustrated by the consideration of the open parallel chains (human, exoskeleton), where the ankle joints are not taken into account for their design. *The ankle joint of the exoskeleton is kept active in this research work to form a closed kinematic chain.*

Maneuverability: Ideally, the most maneuverable exoskeleton system should have ROM slightly less than the human's maximum ROM. However, it could not be possible in case of variable ROM of different subjects within a same exoskeleton system. As shown in Figure 1.6, the study of lower-limb biomechanics discloses the fact that the human leg contains 7 DOFs considering sagittal, frontal and transverse planes and enables humans to perform complex ADLs while maintaining stability. Although designing and developing a fully actuated lower-limb exoskeleton with all possible DOFs offers the subject to move without the aid of crutches or walkers; however such systems have several limitations such as additional cost due to system complexity, less adaptability, slower reflex to subject commands, and complicated control architecture. Moreover, the dominant plane for carry out the important ADLs is the sagittal plane [182]. *Thanks to the aid on walking such as, wheeler stands, the stability of the system can be achieved without actuating both transverse and frontal plane. In this thesis work, such wheeler stands are*

designed along with the exoskeleton system to provide the safety and stability to the subject.

Lightweight and durability: The selection of the structure material and arrangement of the components in the design are crucial factors which decide the strength and weight of the exoskeleton system. Majorly, there are two ways through which the weight of a lower-limb exoskeleton system can be significantly reduced. In first, the robot links can be designed as flexible structures or soft cable driven mechanisms [183]. However, such designs are prone to instability of the user during training purposes and require support arrangements to balance. On the other hand, in case of rigid links, the heavy duty actuators can be replaced with lightweight actuators (Maxon Motors with harmonic drive) [86,87]. However, such lightweight actuators are quite expensive for many developing countries which requires alternate solutions for reducing the weight borne by links. *Therefore, in thesis work, one such possible solution is incorporated by placing the heavy duty actuators on a stand such that the exoskeleton links have to bear their self-weight only.* Furthermore, the exoskeleton has to be made strong, in order to be able to handle the weight exerted by the exoskeleton and power supply itself, and also the payload that the user carries. In the literature, there are different materials used in the design of rigid-links of exoskeleton system such as carbon steel, aluminum, cast iron, carbon fibre and fiberglass [184, 185]. *In this thesis work, aluminum and cast iron is selected for two different design versions of the exoskeleton system. The selected material is verified with the static and dynamic calculations in structural analysis software. If the yield strength of the selected material is within the limits of the ultimate strength of the component, the design is considered to be safe.*

Affordability: The cost associated with the development of lower limb exoskeleton systems is another critical factor that needs to be considered. The price per unit of the lower limb rehabilitation devices for therapeutic training and motion assistance usually varies from 30000 USD to 130000 USD, which is beyond the affordability of many potential users [12]. One of the premier reason of such high cost is the sophisticated design of lightweight actuators and drives, viz., maxon motors along with harmonic drives. Compact actuators are costly and cheap ones are bulky and less energy efficient. Many developing countries export such actuators from the developed countries which increases the overall cost of device. Moreover, the works regrading exoskeleton technology are in preliminary stages and requires many aspects to be addressed before reaching to the end-users as 'fully-fledged affordable exoskeletons'. In a case study based on Exo-Legs project, 85.7% users

are found to be agreed that a price range of 2000–3000 Euros would be widely acceptable [12]. Another survey conducted recently in one of the Indian hospitals infers that 77% users are willing to pay upto 1,75,000 INR for lower-limb exoskeletons [186]. A potential approach to reduce the system's cost is to carry forward with existing designs and alleviate the non-essential factors such as a consumer exoskeleton with more than 40 sensors or actuation in all planes. *Therefore, this thesis work proposes an affordable exoskeleton technology using a simplified mechanical configuration with movement in sagittal plane, actuation modules from a local vendor, in-situ manufacture at the institute workshop, minimal set of position sensors, and a single microcontroller board.*

Adaptability: Human maturation can be interpreted as the major changes in different body segments and proportions. It is observed that the growth rate increases significantly from 5 years old to 12 years old and starts to decrease at 12 years old with a saturation by 19 years old. The variation of the pelvis shape is worth noted when age group varies from the childhood (6 years old) and the adulthood (25 years old) which demands the scalable exoskeleton design to adapt the subject [187, 188]. For instance, HAL exoskeleton takes two months for its optimal calibration in case of varying user's requirements. *In view of maturation, in this work, first version of exoskeleton is designed with adaptable links to accommodate different heights. However, in case of second and final version with the consideration of more pediatric subjects, the height of links is kept constant and waist width varies.*

User balance and safety: The user balance while using ambulatory unilateral or bilateral exoskeletons could be compromised due to the system's weight and its behaviour. In such cases, ambulatory exoskeletons are generally used with crutches to enhance subject's self-confidence, serve as a feedback tool, and minimize the risks of falls [189]. The non-ambulatory exoskeleton are usually aided with treadmill-based structures and safety harness [184]. *Therefore, in this work, the exoskeleton system is designed with a wheeler stand structure is to support the subject during walking and mitigate the risk of sudden falls.* Furthermore, non-compliant physical interaction between the subject and the exoskeleton leads to pain and discomfort [22], and ineffective transmission of forces [190]. The material used in attachments at the interface has to consider the inherent non-linear viscoelastic properties of human soft tissues, such as tendons, ligaments and skin. *Therefore, in this work, an elastic-based nylon cuffs are provisioned for the safety of the user's skin.*

2.3 Motion Capture Experiment Setup

This section presents the hardware-software integration, acquisition of skeleton data, and algorithm for computation of biomechanical joint angles using a Kinect-LabView motion capture (MOCAP) setup.

2.3.1 Hardware Specifications and Software Integration

Microsoft Kinect (MS), as shown in Figure 2.1(a) and Figure 2.1(b), was installed as a motion-sensing device in the laboratory to perform the experiment. This device was considered because of depth-sensing quality in low light environment and capability of resolving boundary ambiguities in any pose. The MS Kinect comprises an RGB camera, an infrared (IR) emitter, an infrared depth sensor, a tilt motor, an array of four microphones, and a 3-axis accelerometer. The RGB camera captures the color images at 30 frames/second (FPS) and stores the image data into 640×480 pixels. The IR emitter and IR depth sensor measure the distance between a human body and the sensor by modulating the reflected rays into depth data. The distance measured by the sensor is stored as depth information within a resolution of 640×480 pixels, having a precision of 4-30 mm. A tilt motor adjusts the orientation of the Kinect device at the specified position. An array of four microphones is used for audio recordings and locating the sound source along with the wave's direction. A 16-kHz frequency with 24-bit pulse code modulation is available in the device as an audio format. The audio input is characterized by four microphones with a 24-bit analog-digital conversion (ADC) channel, having echo and noise cancellation features. The 3-axis accelerometer, designed for 2G range having 10 accuracy, is used to specify the orientation of the device. The field of view is characterized by 430 and 570 view angles in the vertical and horizontal direction, respectively. The vertical tilt is specified by ± 270°. The hardware specifications used to deploy the Kinect-SDK for skeletal tracking are Core i5 processor, 8 GB DDR memory, and 64-bit Windows 10. The Microsoft SDK can track 20 joints; even the subject is in sitting position.

Thereafter, NI-Labview was installed to configure and analyze the hardware setup of MS Kinect using graphical programs [191]. Kinesthesia toolkit was further instated within NI-Labview to store and visualize the skeleton data of MS Kinect. The complete setup provides instant accessibility of information regarding depth camera and skeletal tracking. There are two window panels at the creation of the setup: a front display panel and a block diagram panel. The joints selection,

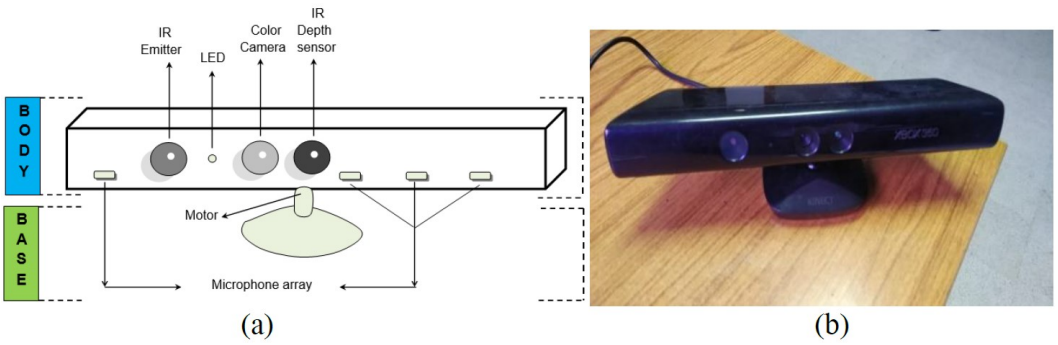

FIGURE 2.1: Illustration of (a) schematic diagram of MS Kinect and (b) MS Kinect camera used in the experiment

skeleton display and corresponding results are shown in the display panel. The block diagram panel is used to program the graphical algorithm for the analysis of joint movements. The algorithm starts with three fundamental operations for the Kinect device: first, initialization with the reference values; second, configuration using video feedback of 3D skeletal information; and third, display the skeleton information after reading and updating in a while loop. At last, a close command is used to stop the display of skeleton video. In this work, an angle evaluation block is connected with the third operation to access the lower limb's joint angles. The joint triples are attached to the angle evaluation block using three different lower limb joint blocks. The Euclidean distance between joints 1 and 2, and joint 2 and 3 are evaluated using joint vectors 1-2 and 2-3. Furthermore, the angle evaluation block calculates the joint angles using the resultant joint vector 1-3 and cosine formula, as mentioned in Equation 2.2. A detailed algorithm in the form of a flowchart is shown in Figure 2.2. The joint triples for the angle evaluation block can be changed in the front display plane according to the selected joint.

2.3.2 Computation of Biomechanical Joint Angles

The MS Kinect offers the skeleton image for 20 joints of human body, as shown in Figure 2.3, in three-dimensional space. Once the image information regarding the skeleton updates in the NI-LabView interface, the required joint angles can be calculated using corresponding joint triples (a, b, and c) and Euclidean distance for each pair in the triples (M, N, and O). The list for eleven triples, made up of human body upper limb and lower limb joint points, is shown in Table 2.1. The Euclidean distance is calculated using vector distance between each pair in a triple, as follows:

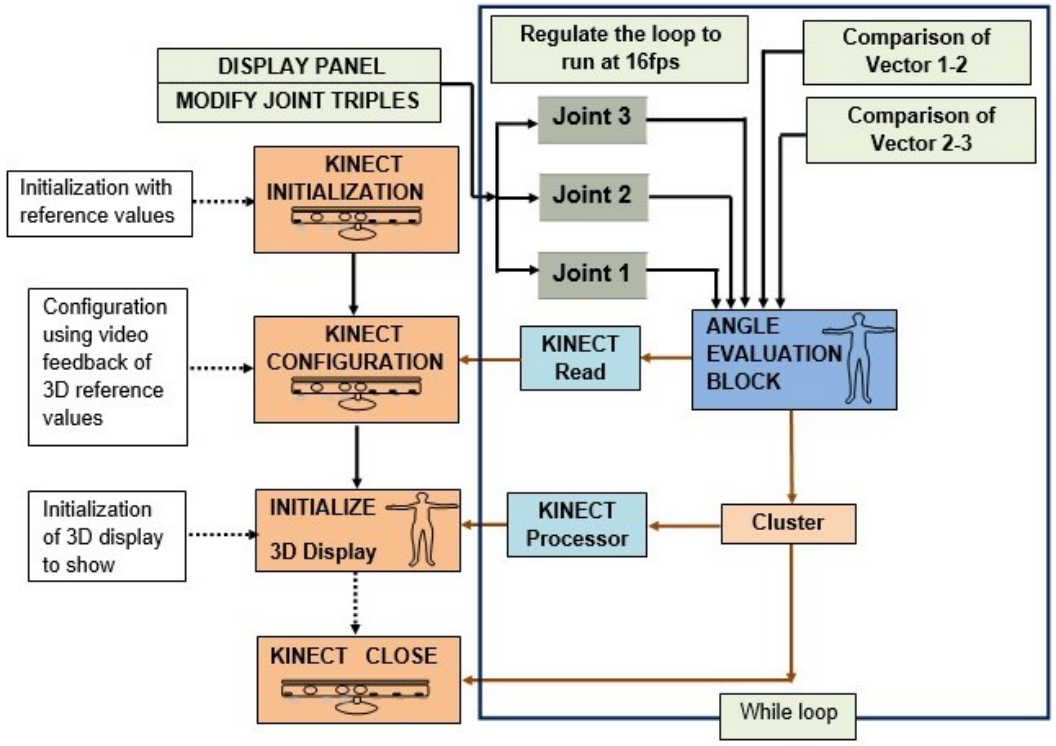

FIGURE 2.2: Flowchart algorithm for evaluation of joint angles

$$d_E(a,b) = \left[(x_a - x_b)^2 + (y_a - y_b)^2 + (z_a - z_b)^2\right]^{1/2} \tag{2.1}$$

The joint angle (q_j) can be further estimated between three body joints (a, b, and c) considering the middle joint (c) as a vertex. A simplified formulation for the same is as follows:

$$q_j = \cos^{-1}\left(\frac{N^2 - M^2 - O^2}{2MO}\right) \tag{2.2}$$

where,

$$M = \left[(x_a - x_b)^2 + (y_a - y_b)^2 + (z_a - z_b)^2\right]^{1/2}$$
$$N = \left[(x_a - x_c)^2 + (y_a - y_c)^2 + (z_a - z_c)^2\right]^{1/2}$$
$$O = \left[(x_b - x_c)^2 + (y_b - y_c)^2 + (z_b - z_c)^2\right]^{1/2}$$

To validate the accuracy of the skeleton information, the subjects' height is computed and compared with the actual height of the subjects. In the Equation 2.3, the length of both legs is averaged to subdue the measuring error of the sensor

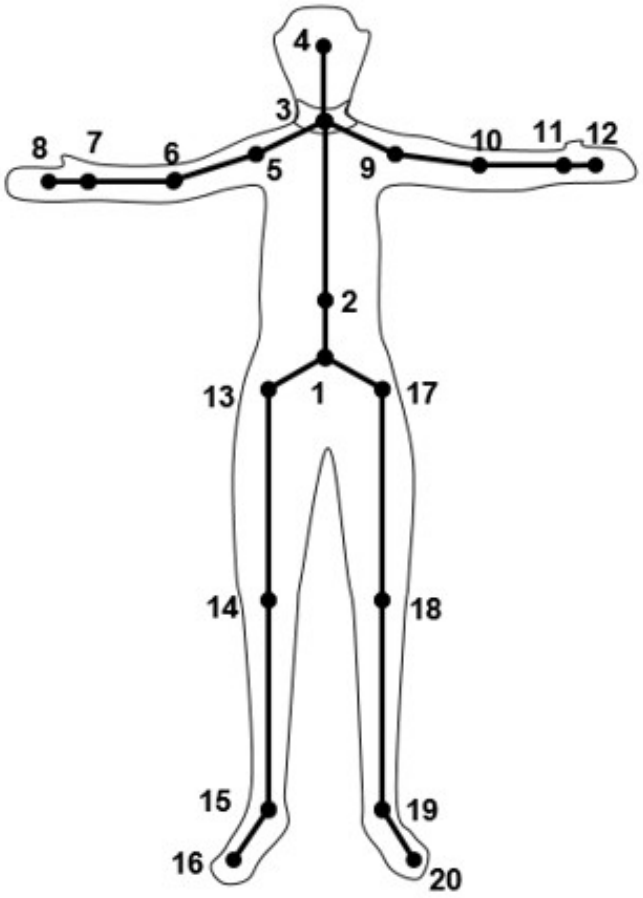

1. Hip Centre
2. Spine
3. Shoulder Centre
4. Head
5. Right Shoulder
6. Right Elbow
7. Right Wrist
8. Right Hand
9. Left Shoulder
10. Left Elbow
11. Left Wrist
12. Left Hand
13. Right Hip
14. Right Knee
15. Right Ankle
16. Right Foot
17. Left Hip
18. Left Knee
19. Left Ankle
20. Left Foot

FIGURE 2.3: Skeleton image with human body joints

TABLE 2.1: List of triples for human body joints using MS Kinect

First joint	**Second joint**	**Third joint**	**Joints order**
Hip Centre	Shoulder Centre	Head	$1-3-4$
Shoulder Centre	Right Shoulder	Right Elbow	$3-5-6$
Right Shoulder	Right Elbow	Right Wrist	$5-6-7$
Shoulder Centre	Left Shoulder	Left Elbow	$3-9-10$
Left Shoulder	Left Elbow	Left Wrist	$9-10-11$
Hip Centre	Right Hip	Right Knee	$1-13-14$
Right Hip	Right Knee	Right Ankle	$13-14-15$
Right Knee	Right Ankle	Right Foot	$14-15-16$
Hip Centre	Left Hip	Left Knee	$1-17-18$
Left Hip	Left Knee	Left Ankle	$17-18-19$

data for the farther leg.

$$\begin{aligned}\text{Height } &= [(1/2)\,(d_E(LA,LK)+d_E(LK,LH)+d_E(RA,RK)+d_E(RK,RH))\\ &\quad +d_E(HC,SP)+d_E(SP,SC)+d_E(SC,H)] \qquad (2.3)\end{aligned}$$

where, LA = Left Ankle, LK = Left Knee, LH = Left Hip, RA = Right Ankle, RK = Right Knee, RH = Right Hip, HC = Hip Centre, SP = Spine, SC = Shoulder Centre, H = Head

In this work, the right leg's hip, knee, and ankle joint angles are considered for the assessment of clinical gait analysis. The triples of the right leg and the corresponding selected joints (q_1, q_2, and q_3) are shown in Table 2.1. This method provides a relative form of biomechanical joint angles for the lower limb in the sagittal plane. To realize the effects of flexion and extension in a more meaningful way, as marked in Figure 2.4, the complementary set of hip, knee, and ankle joint angle ($q_{1,h}, q_{2,h}$, and $q_{3,h}$) of the right leg of healthy human is finally selected. As this work is focused on evaluating right leg joint angles, hereafter, right hip, right knee and right ankle joints are simply mentioned as hip, knee and ankle joint angles to avoid any confusion.

TABLE 2.2: List of triples for the right lower-limb and selected joint

First joint	**Second joint**	**Third joint**	**Selected Joint**
Hip Centre	Right Hip	Right Knee	Right Hip
Right Hip	Right Knee	Right Ankle	Right Knee
Right Knee	Right Ankle	Right Foot	Right Ankle

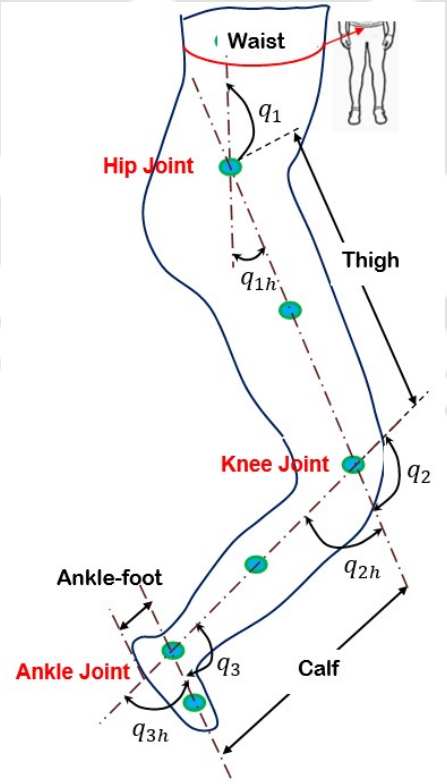

FIGURE 2.4: Biomechanical lower limb of a human

2.4 Preliminary Version of the Lower-Limb Exoskeleton System- LLES$v1$

In this section, the kinematic design and modeling of the preliminary version of the exoskeleton system are outlined. At first, the kinematic and anthropometric data of five healthy pediatric subjects are considered. Thereafter, the computer aided design (CAD) model of the exoskeleton system is designed in the SolidWorks software followed by the finite element analysis (FEA) to estimate the static structural strength.

2.4.1 Identification of System Parameters

The geometrical parameters of the exoskeleton device should be in close accordance with the anthropometric and spatiotemporal parameters of the targeted users. Particularly, one should care about the adaptability of the exoskeleton links in case of a range of different anthropometric parameters of the users. In this work, five pediatric participants (age 8-12 years, body height 115-125 cm, and body mass 25-40 kg) are considered from the nearby areas to the institute. The demographics of all subjects are recorded as given in Table 2.3.

Table 2.3: Demographics of pediatric participants in first phase

Participant Identification Number	Sex	Age	Grade	Languages Understand	Languages Spoken	Birth Place	Residence Area
C1	M	08	Fifth	B, H, E	B, H	Assam	Urban
C2	M	10	Fifth	A, B, H, E	A, B	West Bengal	Rural
C3	F	12	Sixth	A, B, E	A, B	Assam	Rural
C4	M	08	Fourth	A, H, E	A, H, E	Assam	Urban
C5	F	10	Fifth	A, B, H	A, B, H	Assam	Rural

M: Male, F: Female, B: Bengali, H: Hindi, E: English, A: Assamese

The participants' age, body height, body mass, waist width, thigh mass, calf mass, ankle-foot mass, thigh height, calf height, and ankle height are recorded as shown in Table 2.7. The anthropometric labels of lower-limb is shown in Figure 2.4. All participating subjects were considered healthy where being 'healthy' means no sign of trauma, neurological diseases, fractures, or surgery of lower limbs. Thereafter, the Kinect system is installed at a height of 0.8 m from the ground level. With due consent from the institute ethical committee and participant information sheet (PIS), the participants were asked to visit the Mechatronics and Robotics

TABLE 2.4: Anthropometric parameters of the participants in first phase

Participant	Age (yrs)	Body		Waist width, w_h (cm)	Thigh		Calf		Ankle-Foot	
		Height, l_h (cm)	Mass, m_h (kg)		Height, $l_{1,h}$ (cm)	Mass, $m_{1,h}$ (kg)	Height, $l_{2,h}$ (cm)	Mass, $m_{2,h}$ (kg)	Height, $l_{3,h}$ (cm)	Mass, $m_{3,h}$ (kg)
C1	08	122	28	32.9	24	3.5	28	2.2	5	0.54
C2	10	120	29	32.4	27	3.6	32	2.5	4	0.61
C3	12	124	40	33.1	26	4.1	30	2.9	5	0.65
C4	08	122	30	32.6	27	3.5	30	2.3	4	0.65
C5	10	115	25	32.5	22	3.1	27	2.1	4	0.48

Laboratory of the institute along with the parents. They were requested to follow an inclined path in front of the experimental setup. The horizontal and vertical distance between the device center and the subject's initial position was 0.7 m and 2.2 m, respectively. The subject started walking from the initial position and stopped at his exit from the device's field of view. The initial position and the line of the path were marked with black tape on the ground. The distances were selected after having recommended adjustments for better skeletal tracking. The setup configuration, as shown in Figure 2.5(a), recorded the skeletal information for at least one gait cycle with every subject. Figure 2.5(b) displays the participant along with his tracked body joints. Generally, the recordings lasted for 1.6 – 2.0 seconds with every subject following the specified path. The participants had light cloth wear because of the summer days. The whole experiment was conducted with artificial lighting at day time. Following the MOCAP experiment, ROM, stride length, and cycle time for each lower-limb joint is shown in Table 2.8.

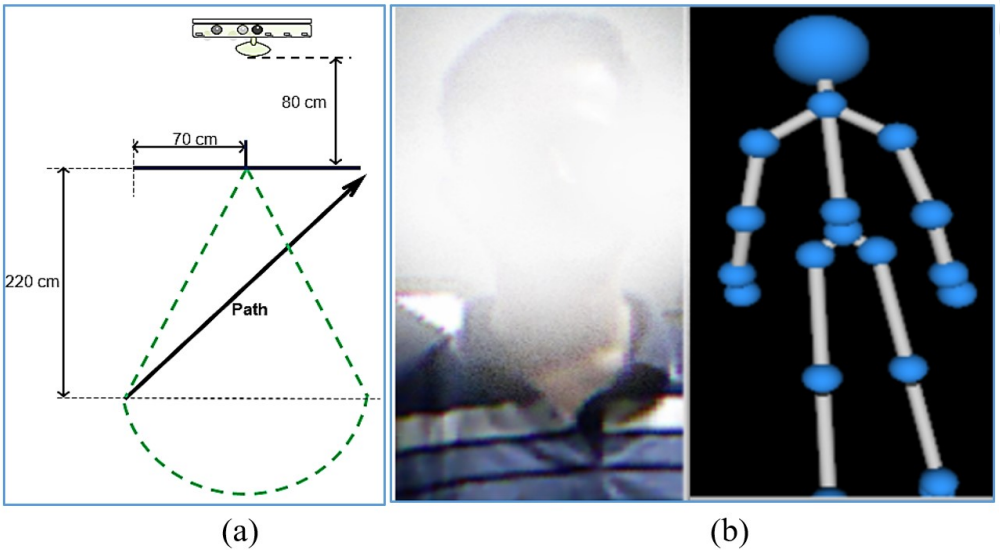

FIGURE 2.5: (a) Path configuration in experimental setup, (b) participant with tracked body joints

TABLE 2.5: ROM and spatiotemporal parameters of the participants in first phase

Participant	Age (yrs)	Hip		Knee		Ankle		Stride Length (cm)	Cycle Time (s)
		f (deg.)	e (deg.)	f (deg.)	e (deg.)	d (deg.)	p (deg.)		
C1	08	24.12	-8.31	53.21	-3.76	7.98	-12.98	81	0.88
C2	10	22.36	-9.38	58.16	1.11	5.32	-8.04	87	0.91
C3	12	27.82	-8.32	58.12	-4.21	9.72	-14.57	83	0.90
C4	08	22.16	-8.98	58.26	1.21	5.84	-7.94	82	1.09
C5	10	21.92	-7.53	55.42	1.32	5.27	-7.98	88	1.23

2.4.2 CAD of the LLES$v1$

Considering the above design requirements, a 6-DOFs lower limb exoskeleton system (LLES$v1$) is proposed in this section. As observed from Table 2.4, the variation in waist width is marginally variable, i.e., 32.7±0.26 cm. Therefore, in this design version, the waist width is kept constant at 32.7cm. From Table 2.4 the age range is selected as 08-12 years, body height as 115-125 cm, body mass as 25-40 kg, thigh height as 22-27 cm, thigh mass as 3.1-4.1 kg, calf height as 27-32 cm, calf mass as 2.1-2.9 kg, ankle-foot height as 4-5 cm, ankle-foot mass as 0.48-65 kg. LLES$v1$ consists of a pair of three links, thigh link, shank link, and foot link, along with the wheel support module. The hip joints perform f/e, knee joints perform f/e, and ankle joints perform d/p motions in the sagittal plane. The main objective of this exoskeleton is to offer rehabilitation training and provide motion assistance to the pediatric subjects. Furthermore, from Table 2.5, it can be inferred that the pediatric participant C3 (12 years) has maximum ROM for hip, knee, and ankle joint. Therefore, following the maximum ROM data and validating with the pediatric gait studies in the literature [192–194] for physiological comfort to the subjects, the ROM for the exoskeleton system is selected 30°/-12° (f/e), 60°/-10° (f/e) and 13°/-20° (d/p), respectively.

Each joint of the exoskeleton system is designed to drive with 1-DOF movement, i.e., flexion and extension. Two heavy-duty backdrivable DC stepper motors along with belt-pulley arrangement are used in the design to provide required torque and rotate the hip joints. Linear type leadscrew actuators appended via brackets are considered in the design to drive the knee joints. The stepper motor operating the lead screw is fixed to the thigh link of the mechanism, and the nut of the lead screw is fixed to the shank link of the leg mechanism. Rotation of the screw causes this nut to traverse up and down the screw, therefore providing motion at the knee of the mechanism. The dimensions of rectangular hollow bars used for making thigh links and calf links are 20cm and 30cm, respectively. The use of motorized lead

screws has allowed to bring down the cost factor associated with the mechanism. To ensure adaptability to different sizes to some extent, a telescopic link-joint connector is designed at the knee joint. The combination of holes in telescoping link-joint connectors allows for minimum 2cm variation in thigh and calf sizes within each setting. The ankle joint of the exoskeleton needs to be actuated to perform locomotion following the normal gait motion of a human body. To reduce the exoskeleton's cost, a less rated DC motor at the ankle joint, along with the cushion effect on the foot, is utilized to perform the required motion. For better stability and strength, a wheel support module is designed where a pair of two wheels with two vertical bars at the rear, a pair of wheels with a vertical bar at the mid of the chassis frame, and two wheels with two slant bars are used to support the exoskeleton system. Two vertical bars are connected with the chassis frame using horizontal bend links at one-third and two-third from the rear side. The other two vertical slant bars from the front side are connected by using angle shaped connectors. The wheels are 100 mm in diameter with a width of 26 mm. The shaft diameter is 10 mm. The wheels come with high quality silicon rubber grip which gives excellent traction. The overall weight of each wheel is 210 gm.

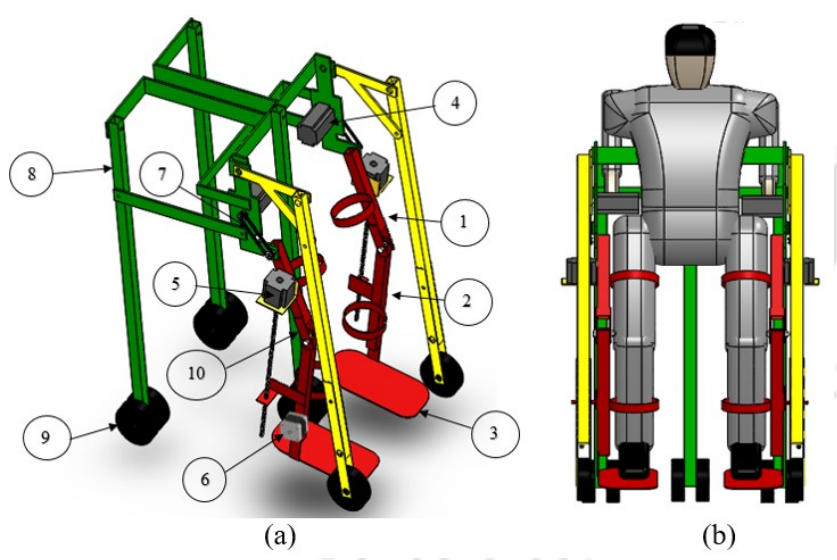

FIGURE 2.6: CAD model of (a) LLES (Labels: 1. Thigh link, 2. Shank link, 3. Foot link, 4. Hybrid stepper motor, 5. Lead screw actuator, 6. Stepper motor, 7. Timing belt 8. Support module, 9. Wheels, 10. Telescopic link-joint connector) (b) LEES with a human dummy

The CAD model of the LLES$v1$ is modeled in SolidWorks software, as shown in Figure 3.17(a) with the stand support structure and in Figure 3.17(b) with a human dummy. A limb of the exoskeleton system is shown in Figure 2.7(a). Figure 2.7(b) presents the exploded view of a single limb of the exoskeleton system. The density of the aluminum alloy material is 2700 kg/m3. The mass of the LLES$v1$ at

full actuator's capacity is 14.4 kg, respectively. The mass of thigh link ($m_{1,e}$), calf link ($m_{2,e}$), and ankle-foot link ($m_{3,e}$) is 2.75 kg, 1.6 kg, and 0.85 kg, respectively. The weight of thigh link holds the added effect of leadscrew actuator. However, the weight of hip joint actuator is not added to the link masses as the actuator is connected separately to the stand structure via the timing belt. The weight of calf link carries the effect of ankle-foot actuator attached at the distal end. The mass of the stand structure was 2.4 kg.

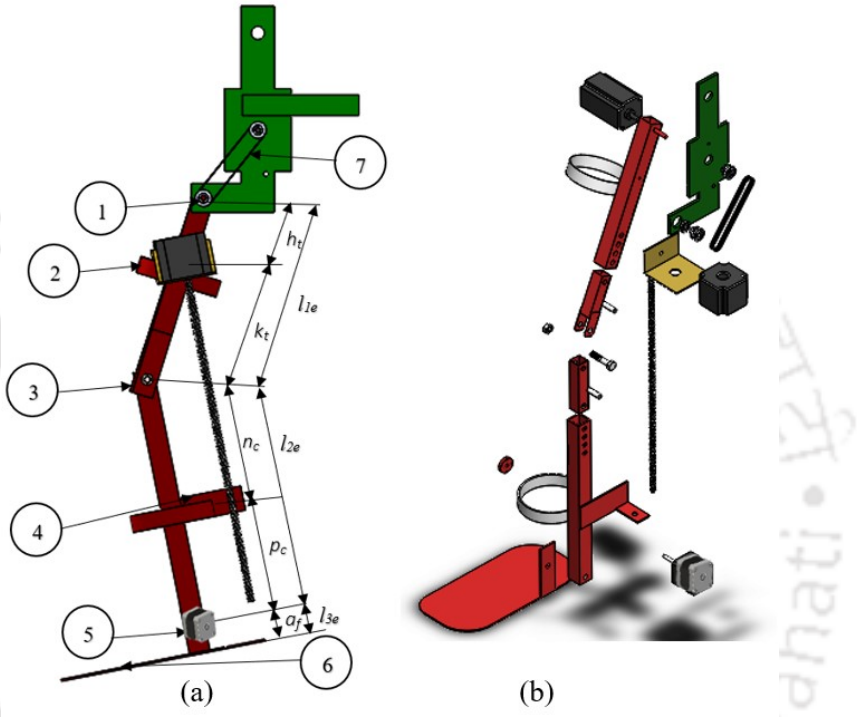

FIGURE 2.7: CAD model of one leg in LLES$v1$ (Labels: 1. Hip joint, 2. L-shaped bracket, 3. Knee joint, 4. Holding cuffs, 5. Ankle joint, 6. Foot, and 7. Timing belt); $h_t = 5$ cm, $k_t = 16 - 22$ cm, $n_c = 8 - 14$ cm, $p_c = 20$ cm, and $a_f = 5$ cm) and (b) Exploded view of one leg

2.4.3 Finite Element Analysis of LLES$v1$

Static structural analysis or finite element analysis (FEA) is utilized to confirm the strength of the designed model for different load conditions. In this work, finite element analysis of hip joint connector with wheeler stand are performed using the SolidWorks software. As the belt-pulley arrangement is used to transfer the actuator's rotation to the hip joint, the mass effect of heavy duty motors is not considered in FEA. The mass of the stand-aided exoskeleton system is 8 kg without taking the mass of hip joint actuators into account. It could be possible while applying forces at the hip joint, a small reaction force could be generated

in the upward direction at the location of hip actuators. However, that force is ignored in the present work due its small magnitude as compared to applied forces at the hip joint.

As per the studies by Bogert et al. [195] and Weinhandl et al. [196], the maximum load acts on the hip joint during a single support phase varies from 2.2 to 4.6 times of the total body weight. Assuming the four times of total body weight of the human-exoskeleton system, i.e., $1920N(4 \times (40 + 8)kg)$, the FEA of the hip joint connector attached with wheel support module is carried out in Figure 2.8. The hubs of all wheels are kept hinge-fixed while applying a downward force of 1920N at a vertical L-shaped hip joint connector, as shown in Figure 2.8(a). All other joint connections in the structure are kept contacted suing contact sets. The solid mesh (tetrahedral 3D) is formed with 31551 number of nodes and 15679 number of elements, having an element size of 22.64 mm. The maximum von Mises stress is found to be 252 MPa (at node 31343), and the maximum deformation is realized to be 7.22 mm (at node 18532) near the hip joint- thigh link connection, as shown in Figure 2.8(b) and 2.8(c). The maximum value of equivalent von Mises stress is within the yield limit of aluminum alloy (275 MPa).

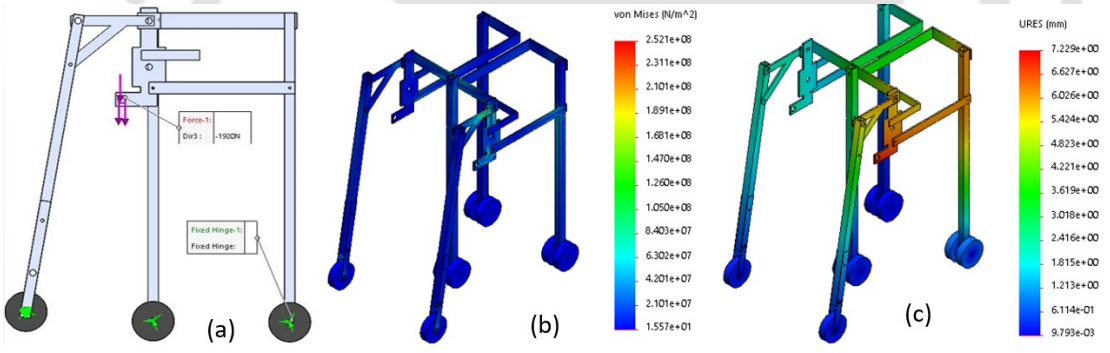

FIGURE 2.8: FEA of a hip joint with wheel support module during single support phase (maximum load) of a gait cycle (a) applied load (b) equivalent von Mises stress, (c) total deformation

Furthermore, as evident from the study by Pan et al. [117], the maximum load is distributed on both hip joints with a 65% load on the right hip and 35% on the left hip during the reaction period. Therefore, to confirm the strength of the hip joint during the reaction period (flat right foot and toe-tip left foot), FEA is performed by applying a downward force of 1248N and 672N on the right and left L-shaped hip joint connectors as shown in Figure 2.9(a). The hubs of all wheels are kept hinge-fixed, and all other joint connections in the structure are kept contacted in the form of contact sets. With 31551 nodes and 15679 elements, the mesh (tetrahedral 3D) is formed with an element size of 22.64 mm. At node

31321, the maximum von Mises stress is found to be 154 MPa, and at node 18532, the maximum deformation is obtained to be 5.08 mm near the hip joint- thigh link connection as shown in Figure 2.9(b) and 2.9(c). The maximum value of equivalent von Mises stress is again within the yield limit of aluminum alloy (275 MPa).

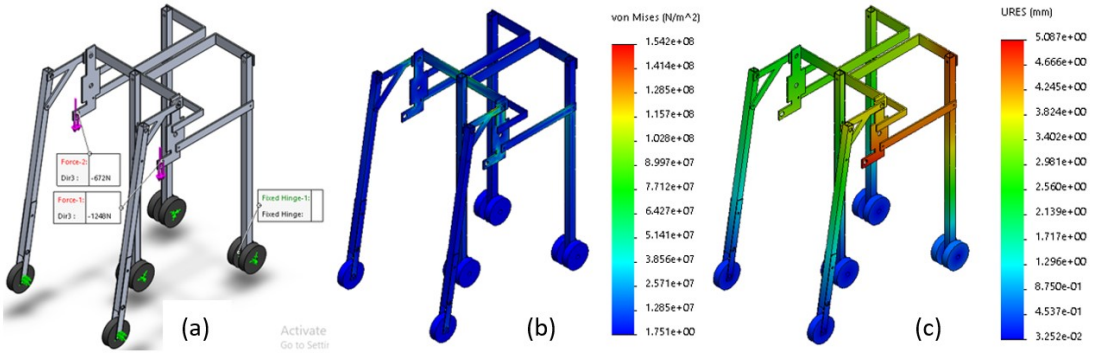

FIGURE 2.9: FEA of a hip joint with wheel support module during reaction phase of a gait cycle (a) applied load (b) equivalent von Mises stress, (c) total deformation

2.5 Final Version of the Lower-Limb Exoskeleton System- LLES*v*2

In this section, the kinematic design and modeling of the second, i.e., final version of the exoskeleton system are outlined. At first, the kinematic and anthropometric data of another 11 healthy pediatric subjects (three from previous experiment and eight fresh incomings) are considered. Based on the participants' anthropometric parameters, the CAD model of the exoskeleton system is re-designed in the SolidWorks software followed by FEA.

2.5.1 Identification of System Parameters

In this section, the anthropometric and spatiotemporal parameters of ten pediatric participants (age 8-12 years, body height 128-132 cm, and body mass 25-40kg) are considered, which reside from the nearby areas to the institute. The demographics of all subjects are recorded as given in Table 2.6. The participants' age, body height, body mass, waist width, thigh mass, calf mass, ankle-foot mass, thigh height, calf height, and ankle height are recorded as shown in Table 2.7. It is

pertinent to mention that, due to maturation, significant changes are observed in the body parameters and ROM of three subjects from previous experiment (i.e., C1, C3, and C4). Following the Kinect-LabView MOCAP experiment setup and guidelines, ROM, stride length, and cycle time for each lower-limb joint is shown in Table 2.8.

TABLE 2.6: Demographics of pediatric participants in second phase

Participant Identification Number	Sex	Age	Grade	Languages Understand	Languages Spoken	Birth Place	Residence Area
C1	M	09	Sixth	B, H, E	B, H	Assam	Urban
C2	M	11	Sixth	A, B, H, E	A, B	West Bengal	Rural
C4	M	09	Fifth	A, H, E	A, H, E	Assam	Urban
C6	M	08	Fifth	A, B, H	A, B	Assam	Rural
C7	F	10	Fifth	A, B, H, E	A, B	Assam	Urban
C8	M	10	Fifth	A, B, H, E	A, B	Assam	Rural
C9	F	10	Fifth	A, B, H, E	A, B	Assam	Rural
C10	M	09	Fourth	A, H, E	A, H, E	West Bengal	Rural
C11	F	11	Fifth	A, B, H, E	A, B, H, E	Assam	Urban
C12	M	12	Sixth	A, B, H, E	A, H, E	West Bengal	Rural
C13	F	10	Fifth	B, H, E	B, H	West Bengal	Urban

M: Male, F: Female, B: Bengali, H: Hindi, E: English, A: Assamese

TABLE 2.7: Anthropometric parameters of the participants in second phase

Participant	Age	Body		Waist	Thigh		Calf		Ankle-Foot	
	(yrs)	Height, l_h (cm)	Mass, m_h (kg)	width, w_h (cm)	Height, $l_{1,h}$ (cm)	Mass, $m_{1,h}$ (kg)	Height, $l_{2,h}$ (cm)	Mass, $m_{2,h}$ (kg)	Height, $l_{3,h}$ (cm)	Mass, $m_{3,h}$ (kg)
C1	09	128	30	33.1	27	3.7	28	2.5	6	0.54
C2	11	128	28	31.3	28	3.8	30	2.8	6	0.62
C4	09	130	35	35.7	28	4.1	30	3.1	6	0.67
C6	08	128	34	34.7	28	4.2	26	2.8	4	0.79
C7	10	131	29	31.1	27	3.8	27	2.7	5	0.49
C8	10	130	38	42.8	26	3.8	30	2.8	6	0.67
C9	10	128	34	43.4	27	4.1	29	3.1	5	0.65
C10	09	129	38	40.1	27	3.9	28	2.9	5	0.58
C11	11	130	33	45.8	27	4.2	30	3.2	6	0.57
C12	12	132	40	34.8	28	4.1	28	2.9	5	0.57
C13	10	129	37	43.1	28	3.8	29	3.1	6	0.61

2.5.2 CAD of the LLES$v2$

Invoking the above design parameters, the 6-DOFs LLES$v1$ is modified for better rigidity of stand support, decreased link masses, the simplified arrangement of the hip motors, variable waist size, and free movements of the stand wheels in this section. As observed from Table 2.7, the variation in waist width is significant, i.e., from 31.1 cm to 45.8 cm which motivates to vary the back link in the exoskeleton

TABLE 2.8: ROM and spatiotemporal parameters of the participants in second phase

Participant	Age (yrs)	Hip		Knee		Ankle		Stride Length (cm)	Cycle Time (s)
		f (deg.)	e (deg.)	f (deg.)	e (deg.)	d (deg.)	p (deg.)		
C1	09	19.12	-7.31	53.21	-3.76	7.98	-10.87	81	0.88
C2	11	22.72	-8.17	57.76	2.23	5.32	-7.20	87	0.91
C4	09	21.42	-8.48	58.66	-1.91	5.55	-9.09	82	1.09
C6	08	22.30	-9.35	58.30	1.12	5.30	-8.11	88	1.11
C7	10	22.77	-7.78	57.45	0.21	8.76	-7.89	76	1.23
C8	10	23.64	-9.12	58.91	-1.08	9.67	-6.98	87	1.45
C9	10	25.78	-11.83	58.43	-1.86	10.34	-6.78	76	0.89
C10	09	26.87	-10.23	55.23	-5.78	11.12	-5.67	75	0.78
C11	11	28.32	-6.34	56.79	-3.78	11.34	-12.57	88	1.18
C12	12	22.23	-8.93	58.21	1.15	5.81	-7.96	91	0.92
C13	10	22.21	-9.23	58.37	-4.98	6.98	-5.34	72	1.03

design. From Table 2.7 the age range is selected as 08-12 years, body height as 128-132cm, body mass as 25-40 kg, thigh mass as 3.7-4.2 kg, thigh mass as 2.1-2.9 kg, and thigh mass as 0.48-65 kg. However, this time, there is a marginal variation in case of thigh height as 26±2 cm, calf height as 28.99±0.995 cm, and ankle-foot height as 5.5±0.5 cm. Similar to LLEs $v1$, a 1-DOF movement (hip f/e, knee f/e, and ankle d/p) is provided to each joint in the LLES $v2$. From Table 2.8, it can be inferred that the pediatric participant C9 (10 years) has maximum ROM for hip joint, C13 (10 years) has maximum ROM for knee joint, and C11 (11 years) has maximum ROM for ankle joint. Therefore, following the maximum ROM data and the pediatric gait studies in the literature [192–194], the ROM for the upgraded exoskeleton system is kept same as LLES$v1$, i.e., 30°/-12° (f/e), 60°/-10° (f/e) and 13°/-20° (d/p), respectively.

However, unlike the normal DC motors in the first version, two heavy duty back-drivable planetary geared DC stepper motors are used in LLES v2 to provide necessary torque for the rotation of the hip joints. Moreover, these motors are mounted on the plate welded over the stand structure unlike the cantilever mounting in first version. To rotate the knee joint, linear leadscrew actuator is mounted on the L-shaped clamps, attached at the thigh and shank link. A less torque rated DC stepper motor is used to actuate the ankle joint. A foot pad is attached to the ankle joint with the help of a coupler where the subject boards initially. To facilitate the actuators placement in LLES $v2$, the preliminary dimensions are modified accordingly. In upgraded design, the stand is extended at the front and exoskeleton is located at the back as compared to previous version. This modification is done to increase the stability of the user, as now the user can take support of the

stand assembly. Furthermore, a castor wheel is used at the end of the stand to offer multi-directional walking flexibility to the coupled subject-exoskeleton system. The CAD model of the LLES$v2$ is shown in Figure 2.10. Figure 2.10(a), 2.10(b), and 2.10(c) illustrates the exoskeleton system, the exoskeleton system with wheel supported stand, and the full exoskeleton system with a human dummy, respectively. The major changes in the LLES$v2$ as compared to the previous version LLES$v1$ are highlighted in the Figure 2.11.

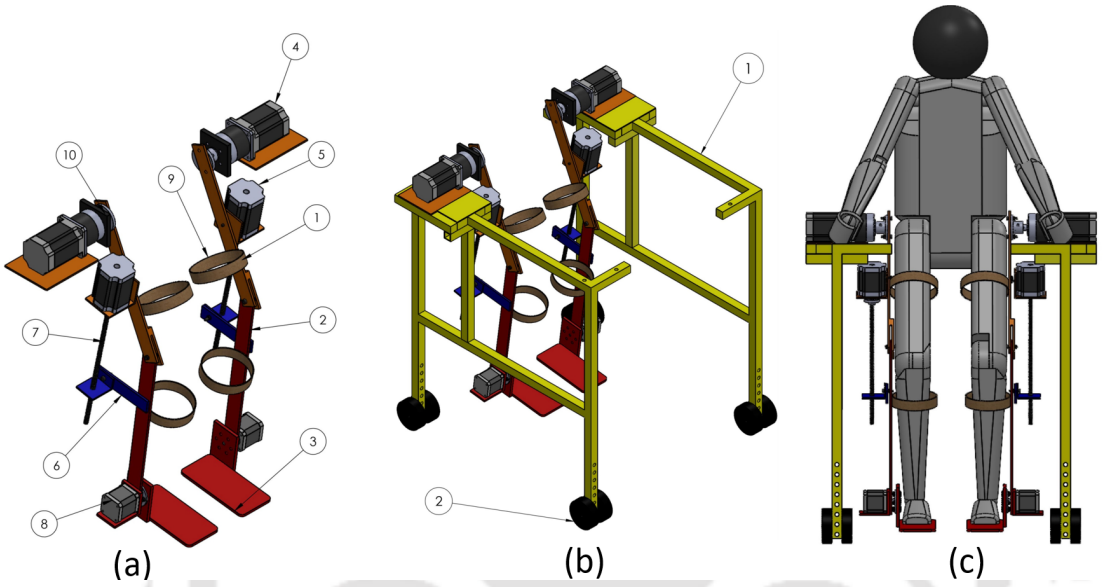

FIGURE 2.10: CAD model of: (a) LLES$v2$ (Labels: 1. Thigh link, 2. Shank link, 3. Foot link, 4. Hybrid stepper motor, 5. Lead screw actuator, 6.Extended shank link, 7. Lead screw, 8. Stepper motor, 9. Holding splints, 10. Coupler), (b) Exoskeleton assembly (Labels: 1. Stand assembly, 2. Wheel support), and (c) Exoskeleton with human dummy

The exoskeleton leg is represented in Figure 2.12(a). The exploded view of one of the legs of the exoskeleton is shown in Figure 2.12(b). The design dimensions for the stand structure in side and front view is shown in Figure 2.13(a) and 2.13(b). The back support in stand structure is kept variable using three adjustable links to accommodate different waist sizes (31-46 cm). The combination of holes in adjustable links allows for minimum 3cm variation in waist sizes in each setting. The material selected for the stand assembly and LLES$v2$'s legs is the mild steel. The mass of the upgraded exoskeleton limbs at full actuators' capacity is 14 kg. The mass of thigh link ($m_{1,e}$), calf link ($m_{2,e}$), and ankle-foot link ($m_{3,e}$) is 4.55 kg, 1.75 kg, and 0.70 kg, respectively. Again, similar to LLES$v1$, the masses of links are computed without the effect of hip joint actuator as the actuator is placed separately over the stand structure. The stand assembly's mass is about 7.44 kg.

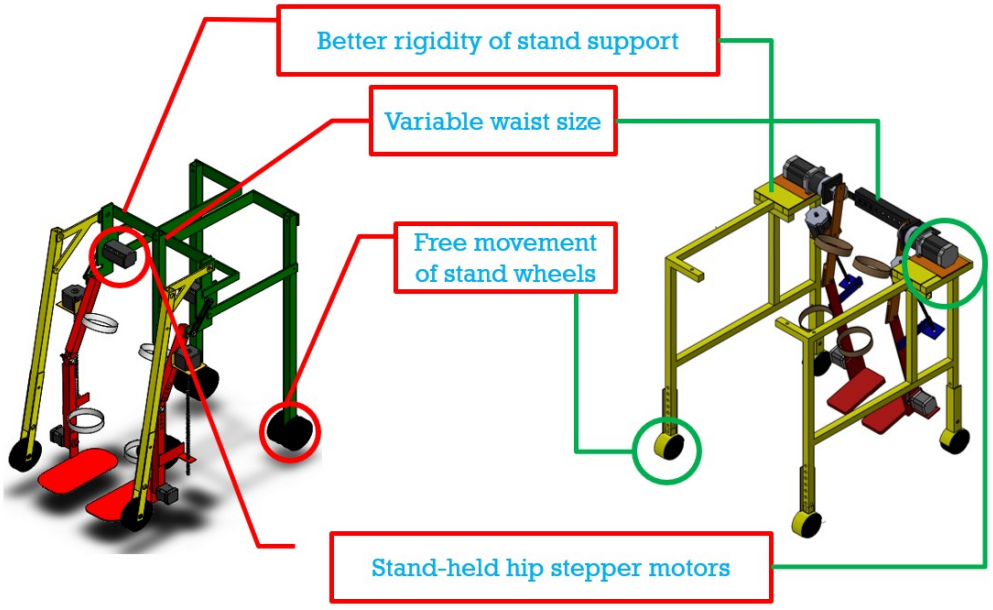

FIGURE 2.11: Major design changes from LLES$v1$ to LLES$v2$

In forthcoming sections, the selection of ASTM A36 steel for stand assembly and AISI 4340 for foot pad is justified by carrying the FEA of the respective structure.

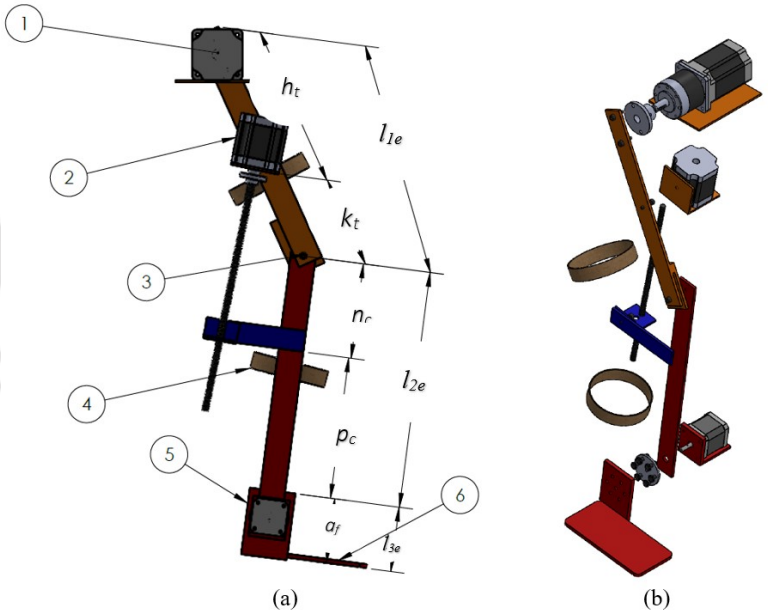

FIGURE 2.12: CAD model of (a) Leg of exoskeleton device (Labels: 1. Hip joint, 2. L clamp, 3. Knee joint, 4. Holding cuffs, 5. Ankle joint, 6. Foot pad); $h_t = 15\text{cm}, k_t = 13\text{cm}, n_c = 13\text{cm}, p_c = 16\text{cm}$, and $a_f = 6\text{cm}$) and (b) Exploded view of one leg

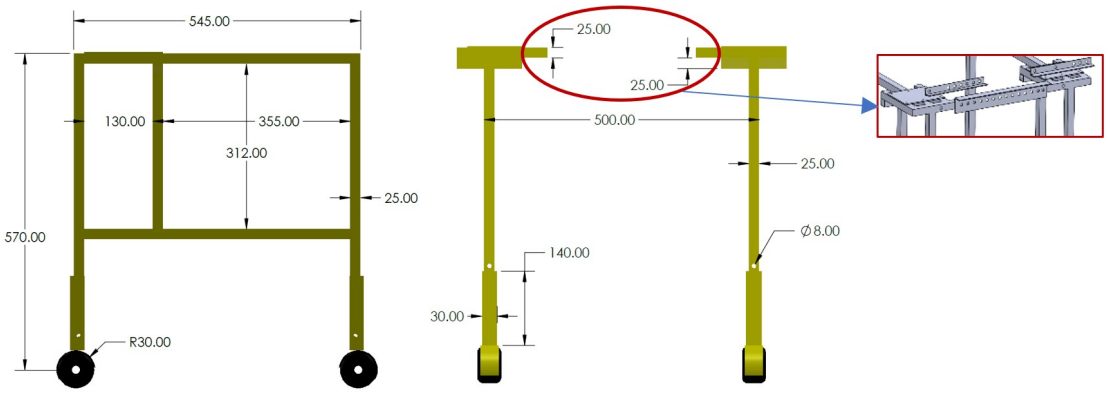

FIGURE 2.13: Dimensions of the stand structure in (a) side view, and (b) front view with adjustable back frame

2.5.3 Finite Element Analysis of LLES*v*2

Finite element analysis is performed to find the strength of hip joint with wheeler stand structure and foot pad working in the full capacity coupled subject-exoskeleton system. Similar to the LLES*v*1, FEA is carried out in the SolidWorks software for two gait events, i.e., the reaction period (toe tip left foot and flat right foot) where the maximum load gets distributed, and the single support phase where maximum load is applied on one leg.

Unlike the FEA of LLES*v*1, a total weight of 14kg is considered for the FEA of LLES*v*2 without reducing the weight of the hip actuator as the joint shaft is directly connected to the thigh link. Assuming four times the entire weight of the human and exoskeleton, the acting force will be (4× (40+14) kg) i.e. 2160 N, a total force of 2160 N is applied on the right side of the exoskeleton device during single support phase. Figure 2.14(a) shows the true location and direction of external fixed loads and fixed hinge support applied for single support phase. The solid mesh (Tetrahedral 3D) is formed for the ASTM steel material with 46,561 and 22,488 as number of nodes and elements respectively, and having element size of 23.7 mm. Figure 2.14(b) and 2.14(c) illustrates the variation of the von-Mises stress and related displacement for ASTM A36 Steel under the boundary conditions of single support phase. The maximum equivalent von Mises stress is found to be 109.50 MPa at node 28,273, at the right front end of the plate. This stress value is within the yield strength limit of ASTM A36 (250 MPa). The maximum deformation is found to be 4.223 mm (at node 11,743). Therefore, the design of stand assembly with ASTM A36 Steel is observed to be safe with the FOS of 2.28.

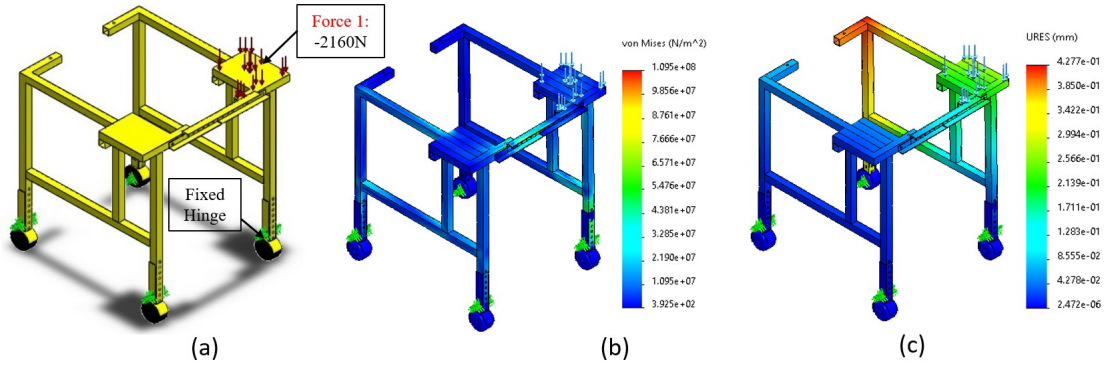

FIGURE 2.14: FEA of a wheel stand assembly during single support phase (maximum load) of a gait cycle (a) applied load (b) equivalent von Mises stress, and (c) total deformation

Considering the reaction phase of the gait cycle, a force of 1404 N and 756 N is applied on the right and left hip joint connection. Figure 2.15(a) shows the true location and direction of external fixed loads and fixed hinge support applied during reaction phase. The solid mesh (Tetrahedral 3D) is formed for the ASTM steel material with 46,561 and 22,488 as number of nodes and elements respectively, and having element size of 23.7 mm. In case of ASTM A36 steel, Figure 2.15(b) and 2.15(c) presents the respective variation of von-Mises stress and deformation for the boundary conditions of reaction period. The maximum equivalent von Mises stress is found to be 37 MPa at node 28,273, which is within the yield strength limit of ASTM A36 (250 MPa). The maximum deformation is found to be 1.653 mm (at node 11,503) is found near the front end of the plate. Therefore, the structural design with ASTM A36 steel is considered to be safe with FOS of 6.75.

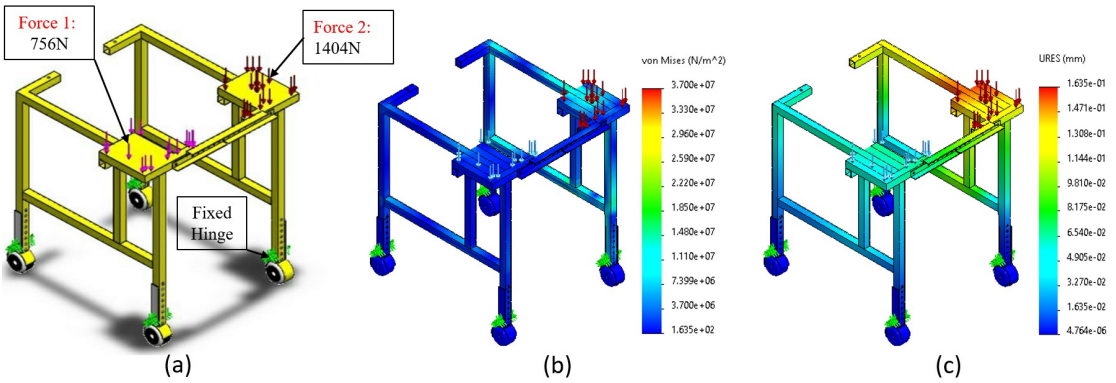

FIGURE 2.15: FEA of a wheel stand assembly during reaction phase of a gait cycle (a) applied load (b) equivalent von Mises stress, and (c) total deformation

2.6 Dynamic Analysis

Rehabilitation training with exoskeleton robots can be majorly classified into two modes depending upon the indulgent of subject, i.e., passive-assist (PA) and active-assist (AA) mode. In PA mode, subject's limbs are completely supervised by the exoskeleton with least possible interaction between subject and human. This mode is helpful to avoid the muscular atrophy post-neurological diseases. On the other hand, in AA mode, the subject exerts his/her own muscle energy in association with the exoskeleton power. The subject-robot collaboration leads to the joint's misalignment and induces interaction forces. These interaction forces can be measured in different ways, i.e., using force/torque sensors [104], spring-damper models [142], disturbance observers [141], etc. The AA mode is useful for those patients who have a considerable amount of muscle energy in their lower limbs. Exploiting the exoskeleton in different rehabilitation settings greatly depends on the applied dynamic analysis and control scheme, i.e., position/trajectory control for PA mode and impedance/admittance control for AA mode. In the coupled subject-exoskeleton model, sufficient torques are needed to drive the joint actuators during gait training which allows the subject to move further at significant speed. Therefore, the dynamic analysis of the lower extremity exoskeleton system is required to obtain the information of joint torques depending upon the geometrical parameters of exoskeleton links and anthropometric parameters of human leg. In this section, dynamic analysis for the coupled human-exoskeleton in passive-assist and active-assist mode is presented using the Euler-Lagrange principle. In this work, it is assumed that even with the post-stroke muscle impairments, the subject can experience the considerable ground reaction forces (GRFs) without any kind of assistance [197]. Therefore, the effect of ground reaction force is excluded from the dynamic analysis while calculating the joint torques. Now, applying Euler-Lagrange principle, the dynamics of the coupled system can be expressed as below.

$$\tau_{j(h,e)} = \frac{d}{dt}\left(\frac{\partial L_{(h,e)}}{\partial \dot{q}_{j(h,e)}}\right) - \frac{\partial L_{(h,e)}}{\partial q_{j(h,e)}} \tag{2.4}$$

$$L_{(h,e)} = K_{(h,e)} - P_{(h,e)} \tag{2.5}$$

where,

$$K_{(h,e)} = \sum_{i,j=1}^{i,j=3}\left[\frac{1}{2}m_{i(h,e)}\left(\dot{x}^2_{i(h,e)} + \dot{y}^2_{i(h,e)}\right) + \frac{1}{2}I_{i(h,e)}\dot{q}^2_{j(h,e)}\right] \tag{2.6}$$

$$P_{(h,e)} = \sum_{i=1}^{i=3} \left[m_{i(h,e)} g y_{i(h,e)} \right] \tag{2.7}$$

where h and e abbreviates the term human and exoskeleton robot; i $(= 1, 2, 3)$ represents the thigh, shank, and foot link, respectively; j $(= 1, 2, 3)$ represents the hip, knee, and ankle joint, respectively; $\tau_{j(h,e)}$ denotes the joint torque vector; $q_{j(h,e)}$ and $\dot{q}_{j(h,e)}$ signify the angular position and angular speed for the ith link; $L_{(h,e)}$ is the Lagrangian; $P_{(h,e)}$ and $K_{(h,e)}$ designates the potential and kinetic energy of the human-exoskeleton system; $m_{i(h,e)}$ and $I_{i(h,e)}$ are the mass and rotational moment of inertia of the coupled i-link; $(x_{i(h,e)}, y_{i(h,e)})$ infers the centroid position of the coupled ith link about origin (0, 0) at hip joint, and g is the acceleration due to gravity.

Solving the kinetic energy (Equation 2.6) and potential energy (Equation 2.7) for each segment for human and exoskeleton system separately and substituting in Lagrange Equation 2.5 to get,

$$\tau_{j,h} + \tau_{eth} = \mathcal{M}_h(q_{j,h})\ddot{q}_{j,h} + \mathcal{C}_h(q_{j,h}, \dot{q}_{j,h})\dot{q}_{j,h} + G_h(q_{j,h}) \tag{2.8}$$

$$\tau_{j,e} + \tau_{hte} = M_e(q_{j,e})\ddot{q}_{j,e} + C_e(q_{j,e}, \dot{q}_{j,e})\dot{q}_{j,e} + G_e(q_{j,e}) \tag{2.9}$$

where $\mathcal{M}_h(q_{j,h}) \in \mathbb{R}^{3\times3}$ and $M_e(q_{j,e}) \in \mathbb{R}^{3\times3}$ are the positive definite inertial matrix; $\mathcal{C}_h(q_{j,h}) \in \mathbb{R}^{3\times3}$ and $C_e(q_{j,e}) \in \mathbb{R}^{3\times3}$ carries Coriolis/centrifugal effect in matrix form; $G_h(q_{j,h}) \in \mathbb{R}^3$ and $G_e(q_{j,e}) \in \mathbb{R}^3$ refers the gravitational vector; $\tau_{j,h} \in \mathbb{R}^3$ and $\tau_{j,e} \in \mathbb{R}^3$ are the joint torque vectors (*j=1,2,3*); τ_{eth} and τ_{hte} denote the interaction torque from the exoskeleton to human and otherwise.

An interaction force develops due to the soft coupling between the lower limb of the human and the exoskeleton robot. The resulting reaction torque acts as a supplement for the subjects with residual muscle energy while behaving as a renitence for the exoskeleton robot. The interaction mechanics for the coupled human-exoskeleton system is shown in Figure 2.16(a) and 2.16(b).

Passive Assist Mode

In PA mode, interaction torques are considered negligible by assuming the structure rigid with insignificant disparities of human-exoskeleton joint movements. Mathematically, following relation can be realized:

$$\tau_{eth} = -\tau_{hte} = 0; \quad \ddot{q}_{j,e} = \ddot{q}_{j,h}, \dot{q}_{j,e} = \dot{q}_{j,h}, q_{j,e} = q_{j,h}; \quad \tau_{j,h} \approx 0 \tag{2.10}$$

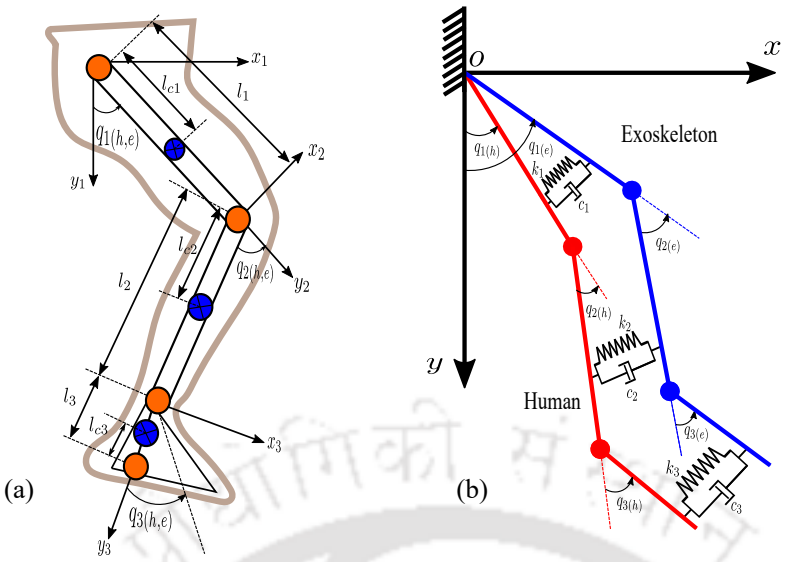

FIGURE 2.16: Coupled human-exoskeleton model (a) a simplified-linkage structure ($l_1 : l_{1(h,e)} : l_{1(e)}, l_{1(h)}$; $l_2 : l_{2(h,e)} : l_{2(e)}, l_{2(h)}$; $l_3 : l_{3(h,e)} : l_{3(e)}, l_{3(h)}$ denote the thigh, calf, and foot length of the exoskeleton and human. l_{c1}, l_{c2}, and l_{c3} signify the centre of mass distance for the respective lengths) (b) interaction dynamics ($c : c_1, c_2, c_3$ and $k : k_1, k_2, k_3$ represent the damping and spring coefficient of thigh, calf and foot bracing straps

Therefore, the dynamic formulation in Equation 2.8 and 2.9 is modified for the coupled system as follows:

$$\tau_{j,e} = \mathcal{M}_{h,e}(q_{j,e})\ddot{q}_{j,e} + \mathcal{C}_{h,e}(q_{j,e}, \dot{q}_{j,e})\dot{q}_{j,e} + \mathcal{G}_{h,e}(q_{j,e}) \tag{2.11}$$

where,

$$\begin{cases} \mathcal{M}_{h,e}(q_{j,e}) & = M_e(q_{j,e}) + \mathcal{M}_h(q_{j,e}) \\ \mathcal{C}_{h,e}(q_{j,e}, \dot{q}_{j,e}) & = C_e(q_{j,e}, \dot{q}_{j,e}) + \mathcal{C}_h(q_{j,e}, \dot{q}_{j,e}) \\ \mathcal{G}_{h,e}(q_{j,e}) & = G_e(q_{j,e}) + G_h(q_{j,e}) \end{cases} \tag{2.12}$$

The element-wise expression for coupled inertia matrix ($\mathcal{M}_{h,e}$), Coriolis/Centrifugal matrix ($\mathcal{C}_{h,e}$), and gravity matrix ($\mathcal{G}_{h,e}$) is provided in Appendix A.

Active-Assist Mode

On the contrary, the AA mode allows the deviations between the human limb and exoskeleton structure which can be used to model the flexible behaviour in coupled

system. Mathematically,

$$\tau_{eth} = -\tau_{hte} = \tau_{j,int} \neq 0; \quad \ddot{q}_{j,e} \neq \ddot{q}_{j,h}, \dot{q}_{j,e} \neq \dot{q}_{j,h}, q_{j,e} \neq q_{j,h}; \quad \tau_{j,h} \neq 0 \tag{2.13}$$

where $(\tau_{j,int})$ denotes the interaction torque vector with the effect of human-exoskeleton collaboration.

Now, the dynamics of the coupled system from Equation 2.8 and 2.9 can be modified as follows,

$$\tau_{j,h} + \tau_{j,int} = \mathcal{M}_h(q_{j,h})\ddot{q}_{j,h} + \mathcal{C}_h(q_{j,h}, \dot{q}_{j,h})\dot{q}_{j,h} + G_h(q_{j,h}) \tag{2.14}$$

$$\tau_{j,e} - \tau_{j,int} = M_e(q_{j,e})\ddot{q}_{j,e} + C_e(q_{j,e}, \dot{q}_{j,e})\dot{q}_{j,e} + G_e(q_{j,e}) \tag{2.15}$$

In practical scenarios, the interaction forces/torques are directly measured by sensor devices. However, researchers have investigated a spring-damper model of the coupling material which can avoid the cost of expensive sensors [104] [142]. Following Figure 2.16, the interaction torque can be modeled as

$$\begin{aligned} \tau_{j,int} = J^T f_{j,int} &= J^T\big(c(\dot{x}_{i,e} - \dot{x}_{i,h}) + k(x_{i,e} - x_{i,h})\big) \\ &= c(\dot{q}_{j,e} - \dot{q}_{j,h}) + k(q_{j,e} - q_{j,h}) \end{aligned} \tag{2.16}$$

where $f_{j,int}$ represents the vector of interaction forces; J^T is the transpose of Jacobian matrix based on the locations of bracing straps; $(\dot{x}_{i,e} - \dot{x}_{i,h})$ and $(x_{i,e} - x_{i,h})$ signifies the velocity and positional difference for the ith link at the contact points, respectively; $(\dot{q}_{j,e} - \dot{q}_{j,h})$ and $(q_{j,e} - q_{j,h})$ denotes the disparity in angular velocity and position for the respective jth joint; c and k is the damping and spring coefficient of the bracing straps, respectively.

Furthermore, it is worth mentioning that the hip and ankle joint torques obtained from Euler-Lagrange principle $(\tau_{1(h,e)}, (\tau_{3(h,e)}))$ are equivalent to the respective actuator torques $(\tau_{1a(h,e)}, (\tau_{3a(h,e)}))$ due to the rotary joint and can be presented as below.

$$\tau_{1(h,e)} = \tau_{1a(h,e)} \tag{2.17}$$

$$\tau_{3(h,e)} = \tau_{3a(h,e)} \tag{2.18}$$

However, in case of knee joint, the rotary joint torque from the Euler-Lagrange principle $(\tau_{2(h,e)})$ shares an empirical relation with leadscrew actuator torque $(\tau_{2a(h,e)})$

using a numerical parameter l_s as follows.

$$\tau_{2(h,e)} \approx l_s \times \tau_{2a(h,e)} \approx l_s \times F_t \times p_r \tag{2.19}$$

where F_t denotes the thrust force required by the leadscrew actuator to lift the lower leg coupled system (calf and ankle-foot) and p_r refers to the pitch of the leadscrew per revolution. The reading of thrust force can be estimated from CAD model of the exoskeleton system at different instants of the gait cycle.

2.7 Results and Discussions

In this section, the estimation of actuator torques for both exoskeleton systems is carried out using the passive-assist coupled dynamic model and empirical relation which further helps to select the other specifications from the local vendor. Although the gait cycle at the self-selected is observed between 0.82 s and 1.22 s; however, keeping the computational complexity of coupled subject-exoskeleton hardware model and control scheme in both passive and active-assist mode, the gait cycle of 2s is considered throughout the thesis. Several researchers have conducted their coupled subject-exoskeleton experiment with different gait cycles such as 1 s [198], 2 s [199–201], 4 s [202] for motion assistance and gait rehabilitation.

In case of LLESv1, the mean values of anthropometric parameters and natural joint movement of all five participants are considered from Table 2.4 as input parameters to the coupled dynamic model. The mean values are: $\bar{l}_{1,h} = 25.2$ cm, $\bar{m}_{1,h} = 3.56$ kg, $\bar{l}_{2,h} = 29.4$ cm, $\bar{m}_{2,h} = 2.4$ kg, $\bar{l}_{3,h} = 4.4$ cm, $\bar{m}_{3,h} = 0.58$ kg, $\overline{ROM}_{\text{hip}} = 23.67°/-8.5°$, $\overline{ROM}_{\text{knee}} = 56.63°/-0.866°$, $\overline{ROM}_{\text{ankle}} = 6.83°/-10.3°$. The lower limb parameters of the exoskeleton are $m_{1,e} = 2.75$ kg, $m_{2,e} = 1.6$ kg, and $m_{3,e} = 0.85$ kg. The numerical parameter l_s is found to be 8.15 from the CAD simulations. The respective joint movements and joint actuator torques are shown in Figure 2.17(a) and Figure 2.17(b). The highest peak value for joint torques is found between 7% and 14% of the gait cycle. From Figure 2.17(b), it is realized that the absolute magnitude of the maximum hip joint torque is 12.92 Nm. The absolute magnitude of maximum knee joint torque is 2.24 Nm. The absolute magnitude of maximum ankle joint torque is 0.28 Nm.

Similarly, for LLESv2, average values of anthropometric parameters and joint trajectory of all 11 participants are considered from Table 2.7 to input into the dynamic model. The mean values are: $\bar{l}_{1,h} = 27.37$ cm, $\bar{m}_{1,h} = 3.61$ kg, $\bar{l}_{2,h} =$

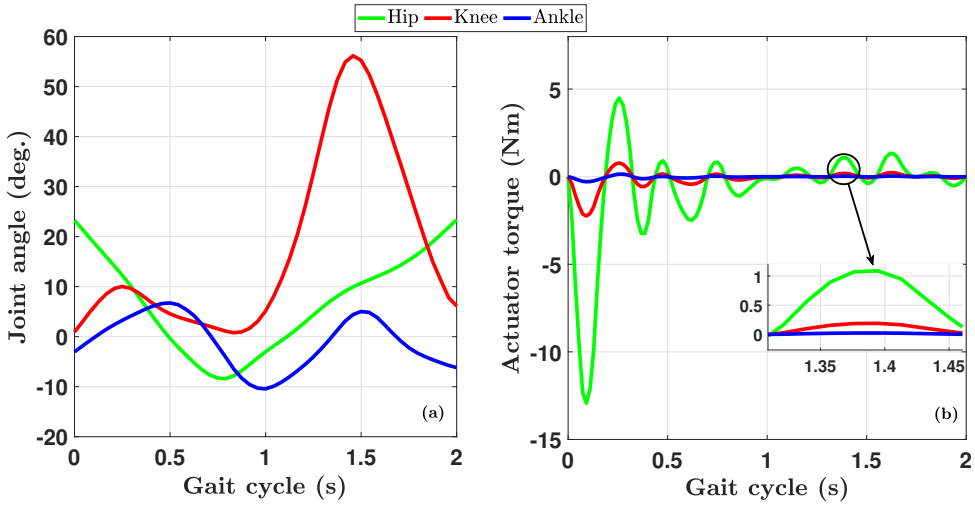

FIGURE 2.17: Desired (a) trajectory and (b) actuator torque for hip, knee, and ankle joint of LLES$v1$

28.64 cm, $\bar{m}_{2,h} = 2.9$ kg, $\bar{l}_{3,h} = 5.45$ cm, $\bar{m}_{3,h} = 0.61$ kg, $\overline{ROM}_{\text{hip}} = 23.4°/-8.8°$, $\overline{ROM}_{\text{knee}} = 57.39°/-1.68°$, $\overline{ROM}_{\text{ankle}} = 8.02°/-8.04°$. The lower limb parameters of the exoskeleton are $m_{1,e} = 4.55$ kg, $m_{2,e} = 1.75$ kg, and $m_{3,e} = 0.70$ kg. The numerical parameter l_s is found to be 8.65 from the CAD simulations. The mean joint movements and resulting joint actuator torques are shown in Figure 2.18(a) and Figure 2.18(b). The highest peak value for joint torques is found between 7% and 14% of the gait cycle. From Figure Figure 2.18(b), it is realized that the absolute magnitude of the maximum hip joint torque is 27.02 Nm. The absolute magnitude of maximum knee joint torque is 2.35 Nm. The absolute magnitude of maximum ankle joint torque is 0.36 Nm.

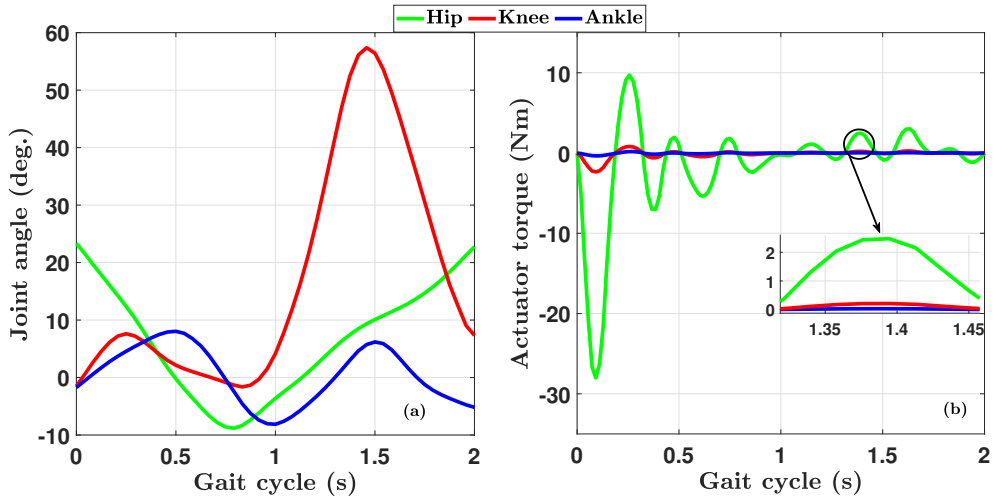

FIGURE 2.18: Desired (a) trajectory and (b) actuator torque for hip, knee, and ankle joint of LLES$v2$

The change from positive to negative torque values represent the effort applied by the actuator shaft to accelerate and decelerate from the previous speed, which is prominent in mid stance phase. Based on the above results for a given ROM of each joint, the required actuators are considered from the market with specifications given in Table 2.9. In case of LLES$v1$, a holding torque of 17.55 Nm (195 USD and 5.1 kg) was sufficient to produce the required control signals for preliminary experimental runs and the same could be observed in control results (Figure 3.21) of this thesis. However, to reduce the weight of hip joint actuators and maintain a trade-off between increased load carrying capacity and cost involved, the hip joint actuator with holding torque of 30 Nm (205 USD and 2.28 kg) was finally selected for LLES$v2$ to ensure effective working of the exoskeleton for different subjects. Moreover, the generated control signals for any actuators depend on many factors such as actuator specifications, actuator placements, subjects' anthropometric parameters, level of pathological conditions (if any), subjects' musculoskeletal parameters, and rehabilitation mode.

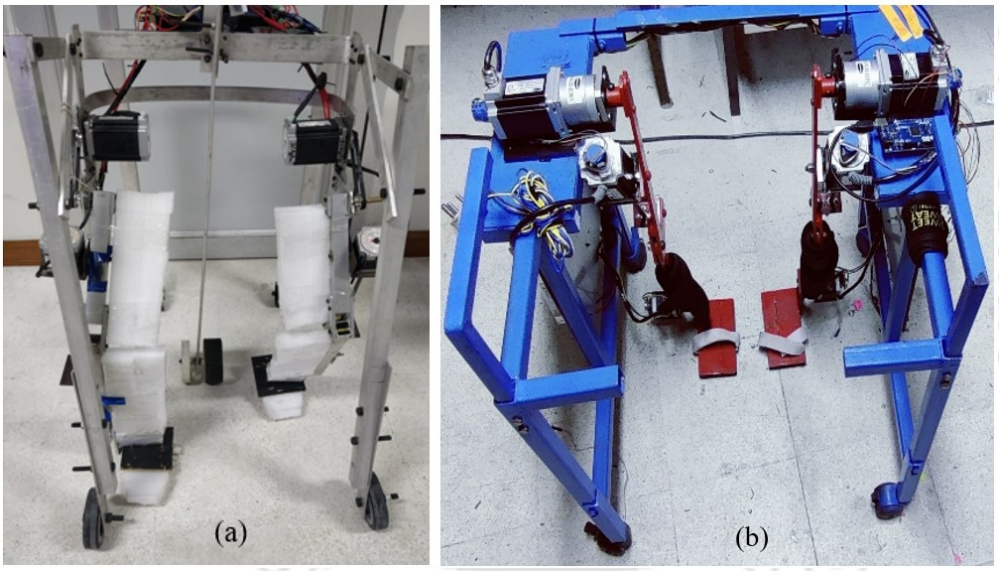

FIGURE 2.19: Prototype of (a) LLES$v1$ and (b) LLES$v2$

The final prototype of the LLES$v1$ and LLES$v2$ is shown in Figure 2.19(a) and 2.19(b), respectively. The major components of both exoskeleton systems are shown in Figure 2.21 and Figure 2.20, respectively. The working of both the exoskeleton system are similar irrespective the component specifications. The actuation for hip joint is formed with a pair of DC motors (stepper motor for LLES$v1$ and planetary-geared stepper motor for LLES$v2$). The knee joint actuation is made up of a pair of linear actuator (leadscrew length 250 mm for LLES$v1$ and 300 mm for LLES$v2$) and ankle joint is powered with a pair of light duty stepper

TABLE 2.9: Actuator specifications for LLES$v1$ and LLES$v2$

System	Joint and actuator model	Armature resistance, $R_m(\Omega)$	Holding Torque, τ_o (Nm)	Current, $I_m(A)$	Armature inductance, L_m(mH)	Operating Voltage, V_0(Volt)	Step angle, A (deg.)	Linear step size, L_s (micron)
LLES$v1$	Hip (BH86SH156-6204AKS- IP 65)	0.85	17.55	6.2	9.4	24 – 140	1.8	–
	Knee (BH57SH100-3004 LA-TR8)	1.55	2.5(250mm leadscrew length)	3.1	6.75	24 – 48	1.8	40
	Ankle (BH42SH47-1504AF)	2.88	0.55	1.5	5.7	12 – 24	1.8	-
LLES$v2$	Hip (BH60SH86-4004PL-13)	0.69	30 (Gear ratio: 13:1)	4.0	2.65	24-48	1.8	-
	Knee (BH57SH100-3004 LA-TR8)	1.55	2.5 (300mm leadscrew length)	3.1	6.75	24-48	1.8	40
	Ankle (BH42 SH 47-1704 AF)	1.7	0.44	1.7	2.5	12-24	1.8	-

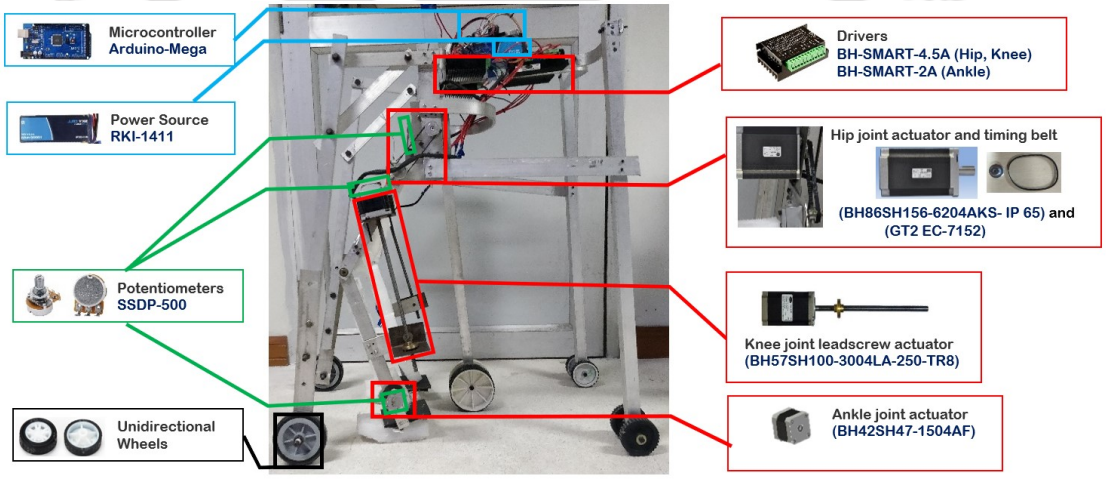

FIGURE 2.20: Prototype of LLES$v1$ with various components

motors. The potentiometer at hip and knee joint (single turn for LLES$v1$ and 10-turns for LLES$v2$), and single-turn potentiometer at ankle joint (both systems) is kept fixed in contact with the shaft of the actuators to process the feedback signals. In case of knee joint of both systems, as the feedback sensor (potentiometer) is fixed at the leadscrew actuator shaft, there is a need to derive some geometrical relations to transform the knee joint rotary movement (q_{2e}) to the actuator's rotary movement (q_{22e}). Referring Figure 2.22, following relation can be established between knee joint rotation (q_{2e}) and leadscrew translation (l_{12e}),

$$cos(180 - q_{2e}) = \frac{-{l_{12e}}^2 - {o_{12}}^2 + 2l_{12e}o_{12}cos(q_s) + {k_t}^2 - {n_c}^2}{2k_t n_c} \tag{2.20}$$

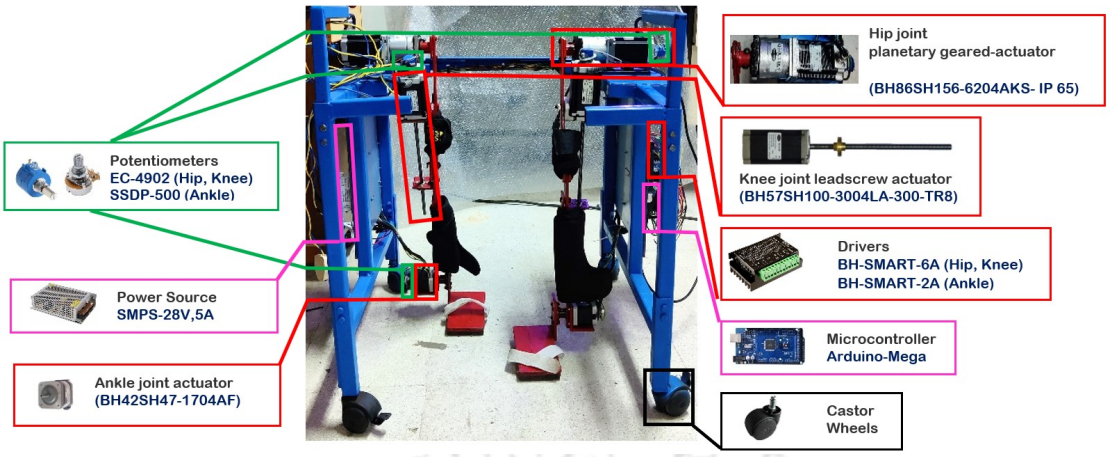

FIGURE 2.21: Prototype of LLES$v2$ with various components

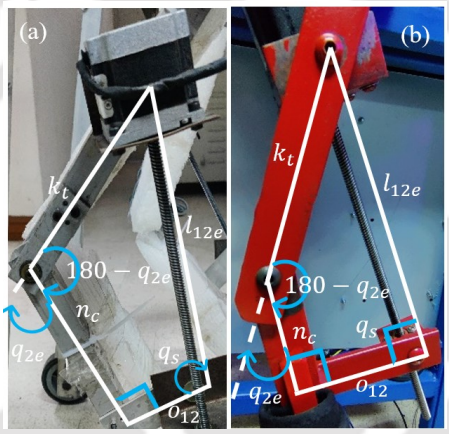

FIGURE 2.22: Geometrical arrangement between knee joint angle and leadscrew translational traverse for (a) LLES$v1$ and (b) LLES$v2$

where k_t and n_c are fixed design parameters for a particular subject; o_{12} and q_s are always kept as constant geometrical parameters. Thereafter, another relation between leadscrew translation (l_{12e}) and actuator's rotary movement (q_{22e})

$$l_{12e} = \frac{q_{22e} \times p_r}{360} \tag{2.21}$$

where, q_{22e} and p_r denotes the leadscrew actuator rotary movement and pitch of the leadscrew per revolution. It is pertinent to mention that the above resulting formulations are only required if the feedback sensor is connected to the shaft of leadscrew actuator.

As per the characteristics of the DC stepper motors, drivers (bipolar 4.5 A for hip and knee actuator, and bipolar 2 A for ankle in LLES$v1$; bipolar 6 A for hip and knee, bipolar 2 A for ankle in LLES$v2$) are exploited to provide the control signals by regulating the duty of pulse width modulation (PWM). Although the

control signals are directly generated based on the proposed control actions during the experiment; however, one can realize the relation between actuator torque and control signals using well known torque-voltage equations, depending upon actuator specifications [102]. The control system includes a microcontroller board (Arduino Mega 2560) connected to the computer software (MATLAB/Simulink, 2020b) through which the proposed control algorithm is inputted. Based on subject's height and waist width, the mechanical links are first adjusted and desired gait is computed using a motion capture setup. Thereafter, the required control algorithm with desired gait trajectory is build in the computer system. Combining all the above steps, an coupled subject-exoskeleton starts working with real-time control architecture.

2.8 Summary

This chapter presents the design, modeling, and proof-of-the-concept prototype of the 6-DOFs stand-aided lower-limb exoskeleton system for pediatric gait rehabilitation and motion assistance. The CAD and FE modeling of the exoskeleton system are presented in two phases based on the anthropometric and kinematic parameters of the pediatric participants. The first design, LLES$v1$ is dedicated to subjects of 08-12 years, body height as 115-125cm, body mass as 25-40 kg. However, in second phase, the prelimnary design is modified for better balance to the subject during gait training, improved structural strength, multi-directional movement of the stand, adaptable back frame to accommodate different waist width, and better placement of hip motors to reduce the weight borne by the links. The final design, i.e., LLES$v2$ ensures the effective gait rehabilitation for subjects 08-12 years, body height as 128-132 cm, body mass as 25-40 kg. The dynamic analysis of the coupled human-exoskeleton system is carried out using Euler-Lagrange principle. The actuators specifications for maximum requirements are decided in passive-assist mode. As the development of the exoskeleton system is completed, intelligent controllers are designed in the next chapter for precise gait tracking in passive-assist mode.

Chapter 3

Robust Intelligent Control Schemes for Passive-Assist Gait Tracking of the Pediatric Exoskeleton

3.1 Introduction

The developed prototypes in the previous chapter require appropriate control schemes to track the desired healthy gait trajectory of the pediatric subject in passive-assist mode. As the coupled pediatric exoskeleton system inherits the parametric uncertainty and external disturbances, two robust intelligent control schemes are presented for the LLES$v1$ in this chapter. The intelligent techniques such as neural network (NN) and neural-fuzzy (NF) has excellent approximation capabilities which benefits the classical optimal and PID control technique to form a robust control scheme. At first, a robust LQR-based neural fuzzy (RLQR-NF) gait tracking control scheme is designed for the exoskeleton device with parametric perturbations (PP) in Section 3.2. Thereafter, in Section 3.3, another robust neuro-fuzzy compensated PID (NF-CID) gait tracking control is proposed for the exoskeleton device with parametric perturbations and external disturbances (PPED), where asymptotic stability is ensured using a Lyapunov candidate function. The simulation results for RLQR-NF are compared with another robust

ERL-SM control scheme in Section 3.4. In same section, the simulation and experimental results of the NF-CPID control is implemented on the LLES$v1$ experimental setup coupled with a human dummy. Finally, the outcomes from this chapter are summarized in Section 3.5

3.2 RLQR-NF Gait Tracking Control with Parametric Uncertainties

In this section, the dynamic modeling is presented by transforming nonlinear model of coupled subject-exoskeleton system into linear one using input-output linearization method. Thereafter, the brief details of ANFIS architecture is presented. Finally, the robust dataset based on the LQR gain, error states and control input is prepared to train in an offline neural-fuzzy architecture.

3.2.1 Input-Output Linearization

The input-output feedback linearization approach is exploited to linearize the nonlinear behavior of the dynamical system [203]. The transformed linear state-space relation is established for the dynamics of the coupled human-exoskeleton system in passive-assist mode. The main objective of the feedback linearization is to correctly linearize the non-linear dynamics with suitable modifications in state-space coordinates using an inner loop control [204]. Thereafter, an outer loop control with a new set of coordinates can be formed to establish a linear relationship between the output vector and input vector and validate the cost-functions of control design. The non-linear multi-input multi-output (MIMO) dynamical relation with n as order and p as the total number of inputs as well as outputs, can be defined in the affine state as below.

$$\begin{cases} \dot{x}(t) = \Psi(x(t)) + \sum_{i=1}^{p} \Gamma_i(x(t))v_i(t) \\ y_i(t) = \Lambda_i(x(t)) \end{cases} \tag{3.1}$$

Here, $x = [x_1, x_2...x_n]^T \in \mathbb{R}^n$ denotes the state vector, $v = [v_1, v_2...v_p]^T \in \mathbb{R}^p$ signifies the control input vector and $y = [y_1, y_2...y_p]^T \in \mathbb{R}^p$ indicates the output vector.

Considering the 3-DOFs subject-exoskeleton system in passive-assist mode, the state vectors (x), control input vector (v), smooth vector fields $(\Psi(x), \Gamma_i(x))$, and output vector (y) in the above affine form can be represented as

$$x_1 = q_{1,e} \quad x_2 = q_{2,e} \quad x_3 = q_{3,e} \quad x_4 = \dot{q}_{1,e} \quad x_5 = \dot{q}_{2,e} \quad x_6 = \dot{q}_{3,e} \tag{3.2}$$

$$\Psi(x) = \begin{bmatrix} x_4 \\ -\mathcal{M}_{h,e}(x_1)^{-1}\left[\mathcal{C}_{h,e}(x_1, x_4)\, x_4 + \mathcal{G}_{h,e}(x_1)\right] \\ x_5 \\ -\mathcal{M}_{h,e}(x_2)^{-1}\left[\mathcal{C}_{h,e}(x_2, x_5)\, x_5 + \mathcal{G}_{h,e}(x_2)\right] \\ x_6 \\ -\mathcal{M}_{h,e}(x_3)^{-1}\left[\mathcal{C}_{h,e}(x_3, x_6)\, x_6 + \mathcal{G}_{h,e}(x_3)\right] \end{bmatrix} \tag{3.3}$$

$$\Gamma_1(x) = \begin{bmatrix} 0 \\ \mathcal{M}_{h,e}(x_1)^{-1} \\ 0 \\ 0 \\ 0 \\ 0 \end{bmatrix}; \Gamma_2(x) = \begin{bmatrix} 0 \\ 0 \\ 0 \\ \mathcal{M}_{h,e}(x_2)^{-1} \\ 0 \\ 0 \end{bmatrix}; \Gamma_3(x) = \begin{bmatrix} 0 \\ 0 \\ 0 \\ 0 \\ 0 \\ \mathcal{M}_{h,e}(x_3)^{-1} \end{bmatrix} \tag{3.4}$$

$$v_1 = \tau_{1,e} \quad v_2 = \tau_{2,e} \quad v_3 = \tau_{2,e} \tag{3.5}$$

$$\begin{aligned} y_1 &= \Lambda_1(x) = x_1 = q_{1,e} \\ y_2 &= \Lambda_2(x) = x_2 = q_{2,e} \\ y_3 &= \Lambda_3(x) = x_3 = q_{3,e} \end{aligned} \tag{3.6}$$

Now, a linear relationship between the inputs and outputs is to be established by performing the differentiation of the outputs (y_i) till the input terms appear in the formulation. Considering d_p is the smallest integer, $(y_j{}^{(d_p)})$ can be evaluated with a complete term of inputs as follows:

$$y_j^{(d_p)} = L_\Psi^{d_p} \Lambda_j(x) + \sum_{i=1}^{p} L_{\Gamma_i}\left(L_\Psi^{d_j - 1} \Lambda_j(x)\right) v_i \quad i, j = 1, 2, ..., p \tag{3.7}$$

where, $L_\Psi^i \Lambda_j$ and $L_\Gamma^i \Lambda_j$ signifies the i^{th} Lie derivatives of $\Lambda_j(x)$ in the direction of Ψ and Γ, respectively [203,205]. In Equation 3.7, d_p denotes relative degree for the output y_j which provides information about the number of derivatives required to carry out at least one of the inputs in the formulation [203] [206]. The sum of every relative degree from Equation 3.7 constitutes the total relative degree (d)

which needs to be less than or equal to the system's order.

$$d = \sum_{j=1}^{n} d_p \leq n \tag{3.8}$$

Furthermore, rewriting the Equation 3.7 and expressing the non-linear control law v to form the linear relationship between the input and the output as follows, one can get

$$\begin{bmatrix} y_1^{d_1} & \dots & y_p^{d_p} \end{bmatrix}^T = \delta(x) + \sigma(x) \cdot v \tag{3.9}$$

$$u = \begin{bmatrix} u_1, u_2 \dots & u_p \end{bmatrix}^T = \begin{bmatrix} y_1^{d_1} & \dots & y_p^{d_p} \end{bmatrix}^T \tag{3.10}$$

where,

$$\begin{cases} \delta(x) = \begin{bmatrix} L_\Psi^{d_1}\Lambda_1(x) \\ \vdots \\ \vdots \\ L_\Psi^{d_p}\Lambda_p(x) \end{bmatrix} \\ \sigma(x) = \begin{bmatrix} L_{\Gamma_1}\left(L_\Psi^{(d_1-1)}\Lambda_1(x)\right) & L_{\Gamma_2}\left(L_\Psi^{(d_1-1)}\Lambda_1(x)\right) & \dots & L_{\Gamma_p}\left(L_\Psi^{(d_1-1)}\Lambda_1(x)\right) \\ L_{\Gamma_1}\left(L_\Psi^{(d_2-1)}\Lambda_2(x)\right) & L_{\Gamma_2}\left(L_\Psi^{(d_2-1)}\Lambda_2(x)\right) & \dots & L_{\Gamma_p}\left(L_\Psi^{(d_2-1)}\Lambda_2(x)\right) \\ \vdots & \vdots & & \vdots \\ L_{\Gamma_1}\left(L_\Psi^{(d_p-1)}\Lambda_p(x)\right) & L_{\Gamma_2}\left(L_\Psi^{(d_{p-1})}\Lambda_p(x)\right) & \dots & L_{\Gamma_p}\left(L_\Psi^{(d_p-1)}\Lambda_p(x)\right) \end{bmatrix} \end{cases} \tag{3.11}$$

Assuming $\sigma(x)$ is not singular, the input transferred form, i.e., the non-linear control law, can be possibly defined as

$$v = \sigma(x)^{-1}(-\delta(x) + u) \tag{3.12}$$

where, $u = [u_1, u_2, .., u_p]^T, v = [v_1, v_2, ..., v_p]^T$

In the Equation 3.12, u denotes the new input vector, v refers to decoupling control law, $\sigma(x)$ signifies an invertible matrix of order p×p, and $\delta(x)$ represents a decoupling matrix of the system.

Finally, solving for above non-linear control law and using the concept of diffeomorphism [203, 205], Equations 3.2-3.6 can be transformed into a linear form as follows:

$$\begin{cases} \dot{z} = \mathcal{A}z + \mathcal{B}u \\ y = \mathcal{C}z \end{cases} \tag{3.13}$$

where $\mathcal{A}, \mathcal{B}$, and $\mathcal{C}$ are the state-weight factor matrices; z and y denotes the state vector and output vector, respectively.

In the present work, the state vector and output vector related of the coupled dynamical system is considered as $z = \begin{bmatrix} q_{1,e} & q_{2,e} & q_{3,e} & \dot{q}_{1,e} & \dot{q}_{2,e} & \dot{q}_{3,e} \end{bmatrix}^T$ and $y = \begin{bmatrix} q_{1,e} & q_{2,e} & q_{3,e} \end{bmatrix}^T$, respectively. The input vector for system parameters is defined as $u = \begin{bmatrix} u_{1,e} & u_{2,e} & u_{3,e} \end{bmatrix}^T$. Moreover, the respective state-weight factor matrices $\left(\mathcal{A} \in \mathbb{R}^{6\times6}, \mathcal{B} \in \mathbb{R}^{6\times3}, \text{and } \mathcal{C} \in \mathbb{R}^{3\times6}\right)$ can be formulated as below. The entries of these matrices are extensively presented in the Appendix B.

$$\begin{cases} \mathcal{A} = \begin{pmatrix} [0]_{3\times3} & I_3 \\ \begin{matrix} \frac{\alpha_{41}}{\tilde{\alpha}_{41}} & \frac{\alpha_{42}}{\tilde{\alpha}_{42}} & \frac{\alpha_{43}}{\tilde{\alpha}_{43}} \\ \frac{\alpha_{51}}{\tilde{\alpha}_{51}} - \frac{\alpha_{51'}}{\tilde{\alpha}_{51'}} + \frac{\alpha_{51''}}{\tilde{\alpha}_{51''}} & \frac{\alpha_{52}}{\tilde{\alpha}_{52}} - \frac{\alpha_{52'}}{\tilde{\alpha}_{52'}} + \frac{\alpha_{52''}}{\tilde{\alpha}_{52''}} & \frac{\alpha_{53}}{\tilde{\alpha}_{53}} + \frac{\alpha_{53'}}{\tilde{\alpha}_{53'}} - \frac{\alpha_{53''}}{\tilde{\alpha}_{53''}} \\ \frac{\alpha_{61}}{\tilde{\alpha}_{61}} - \frac{\alpha_{61'}}{\tilde{\alpha}_{61'}} - \frac{\alpha_{61''}}{\tilde{\alpha}_{61''}} & \frac{\alpha_{62}}{\tilde{\alpha}_{62}} - \frac{\alpha_{62'}}{\tilde{\alpha}_{62'}} - \frac{\alpha_{62''}}{\tilde{\alpha}_{62''}} & \frac{\alpha_{63}}{\tilde{\alpha}_{63}} - \frac{\alpha_{63'}}{\tilde{\alpha}_{63'}} - \frac{\alpha_{63''}}{\tilde{\alpha}_{63''}} \end{matrix} & [0]_{3\times3} \end{pmatrix}, \\ \mathcal{B} = \begin{pmatrix} [0]_{3\times3} \\ \begin{matrix} \frac{\beta_{41}}{\tilde{\beta}_{41}} & \frac{\beta_{42}}{\tilde{\beta}_{42}} & \frac{\beta_{43}}{\tilde{\beta}_{43}} \\ \frac{\beta_{51}}{\tilde{\beta}_{51}} & \frac{\beta_{52}}{\tilde{\beta}_{52}} & \frac{\beta_{53}}{\tilde{\beta}_{53}} \\ \frac{\beta_{61}}{\tilde{\beta}_{61}} & \frac{\beta_{62}}{\tilde{\beta}_{62}} & \frac{\beta_{63}}{\tilde{\beta}_{63}} \end{matrix} \end{pmatrix} \\ \mathcal{C} = \begin{pmatrix} 1 & 0 & 0 & 0 & 0 & 0 \\ 0 & 1 & 0 & 0 & 0 & 0 \\ 0 & 0 & 1 & 0 & 0 & 0 \end{pmatrix} \end{cases} \tag{3.14}$$

3.2.2 Adaptive Neural-Fuzzy Inference System

Adaptive Neural-Fuzzy Inference System (ANFIS), colloquially known as Neural-Fuzzy or Neuro-Fuzzy (NF) system, was proposed by Jang and Sun [207] by augmenting the benefits of adaptive neural networks and fuzzy reasoning. In the NF system, IF-THEN-based fuzzy logic inferences are constructed to form the learning rules with a defined input-output dataset and reproduce the output vector with zero error tolerance. A neural-fuzzy system exploits the fuzzy input variables and input dependent non-fuzzy output variable, given by Takagi and Sugeno [208]. For

instance,

$$\begin{aligned} &\textit{If acceleration of robot's end-effector is high, then} \\ &f(t) = c \times (\textit{acceleration of robot's end-effector})^2 \end{aligned} \tag{3.15}$$

In Equation 3.25, *high* signifies a fuzzy label with the membership function (MF), representing the *acceleration of robot's end-effector* in the proposition of rule. The rule subsequent with non-fuzzy behavior is formulated according to the input variable of premise step, *acceleration of robot's end-effector*.

A neural-fuzzy system inherently exploits the five layers, i.e., node layer (NL), membership layer (ML), rule layer (RL), defuzzification layer (DL), and output layer (OL). The primary network architecture with two input vectors (x,y) and one output vector (z) is considered to show the generalized process of ANFIS. As shown in Figure 3.1, two kinds of nodes are employed in the architecture; first, a square node for adaptation of the parameters, and second, a circular node behaves as a fixed node with no parameter. The layer-by-layer development of the ANFIS structure is given below [207, 209, 210].

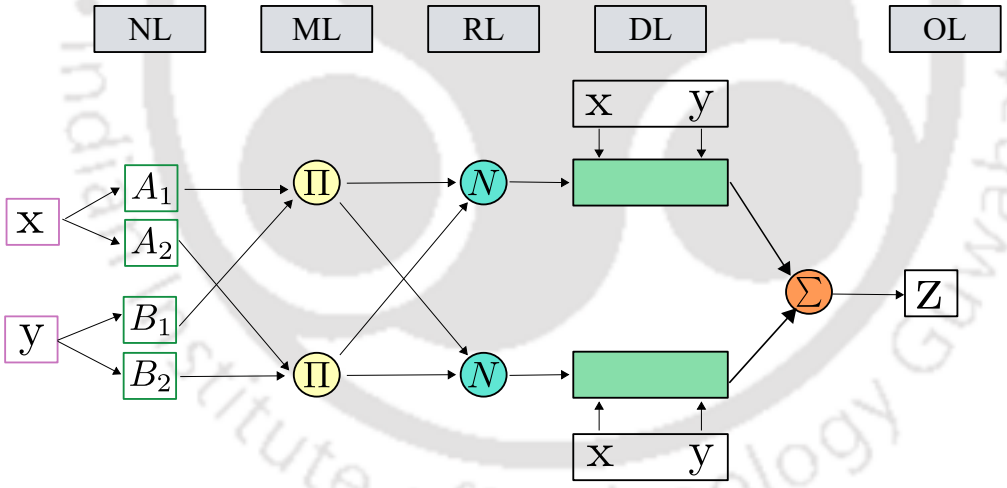

FIGURE 3.1: ANFIS Architecture

Layer 1: This layer acts as a conversion function for the crisp value of the input vector into an appropriate MF based fuzzy language, depicted as follows:

$$\mathcal{O}_j^1 = \omega_{A_j}(\mathrm{x}), \mathcal{O}_j^1 = \omega_{B_j}(\mathrm{y}) \tag{3.16}$$

where, $\mathcal{O}_j^1$ represents the jth node output for the first layer. $\omega_{A_j}(\mathrm{x})$ and $\omega_{B_j}(\mathrm{y})$ denote the membership weightage of respective input variables, defined for A_j and B_j type MF. In this work, the generalized bell membership function is chosen to

replicate a proper probability distribution behavior and expressed as follows.

$$\text{bell}\,(\text{z} : a_j, b_j, c_j) = \omega_{A_j}(\text{x}) = \omega_{B_j}(\text{y}) = \frac{1}{1 + \left[\left(\frac{z-c_j}{a_j}\right)^2\right]^{b_j}} \tag{3.17}$$

In Equation (28), a_j and b_j signify the width and shape parameter of the membership function. The value of b_j is generally positive; however, it can be considered negative in case of inverted shape. c_j indicates the center position of the membership function. Having an extra parameter compared to Gaussian MF, the generalized bell has the added advantage of tuning the steepness at crossover positions.

Layer 2: This layer evaluates the firing strength for every rule using a product of incoming signals from each circular node. It is designated by notation Π in the ANFIS architecture. The following expression is used to estimate the firing strength (m_j) as follows

$$\mathcal{O}_j^2 = m_j = \omega_{A_j}(\text{x}) \times \omega_{B_j}(\text{y}), \quad j = 1, 2, 3 \tag{3.18}$$

Layer 3: In this layer, the normalization of the node's firing strength is carried out by dividing the j-th rule firing strength to all rules' total firing strength. This layer is designated by notation N in the ANFIS architecture. The firing strength is normalized as follows.

$$\mathcal{O}_j^3 = \bar{m}_j = \frac{m_j}{m_1 + m_2}, \quad j = 1, 2, 3 \tag{3.19}$$

Layer 4: This layer, having the square nodes, is used to estimate the rule's involvement by defuzzification of input variables and produce the respective output as follows.

$$\mathcal{O}_j^4 = \bar{m}_j \angle_j = \bar{m}_j \left(p_j \text{x} + q_j \text{y} + r_j\right) \tag{3.20}$$

where $\bar{m}_j$ indicates the normalized firing strength and p_j, q_j and r_j signifies subsequent limits.

Layer 5: This layer, having circular shape nodes with the designation $\sum$, processes the final output using the summation of all incomings from the preceding layer.

Mathematically, it can be expressed as follows.

$$\mathcal{O}_j^5 = \sum_j \bar{m}_j \angle_j = \frac{\sum_j m_j \angle_j}{\sum_j m_j} \tag{3.21}$$

3.2.3 Robust Design of LQR based Neural-Fuzzy Control

The design procedure of RLQR-NF control is organized into two stages: first, the formulation of a robust training dataset, and second, the stepwise layout of the proposed control strategy for the exoskeleton device. The details of ANFIS training parameters are discussed in the second stage of the design process. As shown in Figure 3.2, both the stages are explained extensively in this section.

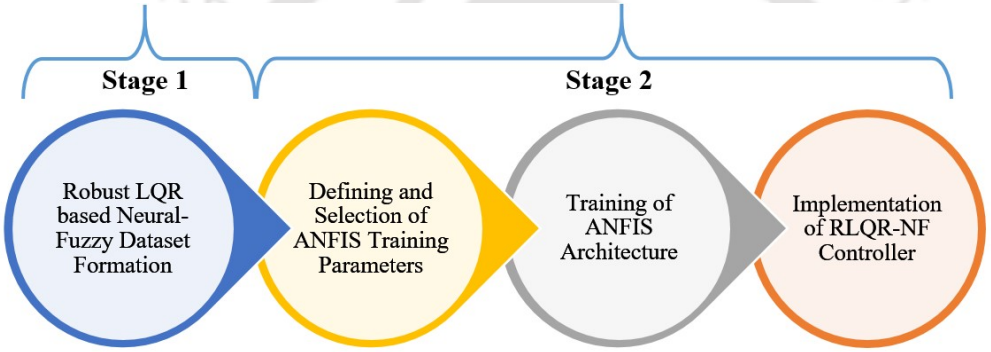

FIGURE 3.2: Flowchart representation of the stage-wise design procedure

3.2.3.1 Formulation of Robust Neural-Fuzzy Training Dataset

The training dataset, having multiple-input and multiple-output (MIMO), is formed by employing the concepts of the LQR control strategy as shown in Equation 3.22. The LQR cost function is considered a minimization problem while applying the optimality conditions and is expressed as follows [211, 212].

$$\mathcal{J} = \frac{1}{2} \int_0^\infty \left(z^T \mathcal{Q} z + u^T \mathcal{R} u \right) dt \tag{3.22}$$

where $\mathcal{Q}$ and $\mathcal{R}$ denote the user-defined state-weighing matrix and control cost matrix, respectively. An appropriate selection of both the matrices directly influences the performance characteristics of the controller.

The generalized input (u) to the control system is articulated by regulating the error vector (E) as follows:

$$u = \mathcal{K}E = \mathcal{G}\left(z_{\text{des}} - z\right) \tag{3.23}$$

where z_{des}, z represent the desired and actual state vectors, respectively. The optimal state gain matrix $(\mathcal{K})$ can be expressed in terms of control cost matrix $(\mathcal{R})$ and a state weight factor matrix $(\mathcal{B})$, as follows:

$$\mathcal{K} = \mathcal{R}^{-1}\mathcal{B}^{T}\mathcal{P} \tag{3.24}$$

where, $\mathcal{P}$ is the answer for the algebraic form of the Riccati equation expressed in the form of state-weight factor matrices $(\mathcal{A}, \mathcal{B})$, state-weighing matrix $(\mathcal{Q})$, and control cost matrix (R) as given below.

$$\mathcal{P}\mathcal{A} + \mathcal{A}^{\mathrm{T}}\mathcal{P} - \mathcal{P}\mathcal{B}\mathcal{R}^{-1}\mathcal{B}^{T}\mathcal{P} + \mathcal{Q} = 0 \tag{3.25}$$

It is truly evident from Equation (34) that state gain matrix $(\mathcal{K})$ is regulated by $\mathcal{A}, \mathcal{B}, \mathcal{Q}$ and $\mathcal{R}$ matrix where $\mathcal{A}$ and $\mathcal{B}$ are reliant on the mechanical arrangement and dynamical parameters of the requisite system.

Exploiting the controller's gain $(\mathcal{K})$, a generalized dataset (S_d) with error vector (E) and respective input (u) to the control system can be created in the following form.

$$S_d = \begin{bmatrix} E^T & u \end{bmatrix} \tag{3.26}$$

In this work, the dataset (S_d) is expanded into a robust form by evaluating the controller's gain $\left(\mathcal{K}_{m_{1(h,e)}, m_{2(h,e)}, m_{3(h,e)}}\right)$ for a bounded variation of the coupled thigh $\left(m_{1(h,e)}\right)$, calf $\left(m_{2(h,e)}\right)$, and heel-foot $\left(m_{3(h,e)}\right)$ masses of the human-exoskeleton system. Thereafter, the controller input (u) for hip, knee, and ankle joint is formulated as follows:

$$u = \mathcal{K}_{m_{1(h,e)}, m_{2(h,e)}, m_{3(h,e)}} E \tag{3.27}$$

where,

$$u = \begin{bmatrix} u_{1,e} & u_{2,e} & u_{3,e} \end{bmatrix}^{T} \tag{3.28}$$

$$E = \begin{bmatrix} \xi_{1q_1} & \xi_{1q_2} & \xi_{1q_3} & \xi_{1\dot{q}_1} & \xi_{1\dot{q}_2} & \xi_{1\dot{q}_3} \end{bmatrix}^{T} \tag{3.29}$$

In Equation 3.28, $u_{1,e}, u_{2,e}, u_{3,e}$ denote the controller output for the hip knee and ankle joint of the exoskeleton device, respectively. In Equation 3.29 $\xi_{1q_1}, \xi_{1q_2}, \xi_{1q_3}$

signifies the hip, knee, and ankle joint angular error, respectively. $\xi_{1\dot{q}_1}, \xi_{1\dot{q}_2}, \xi_{1\dot{q}_3}$ represents the respective error of hip, knee, and ankle joint angular velocity. The expanded structure of the robust dataset (S_{rd}) is finally depicted as below.

$$S_{rd} = \begin{bmatrix} E^T & u \end{bmatrix} \tag{3.30}$$

where,

$$S_{rd} = \begin{bmatrix} S(1)_{rd} & S(2)_{rd} & S(3)_{rd} \end{bmatrix}^T \tag{3.31}$$

3.2.3.2 Stepwise Layout of RLQR-NF Control Strategy

Step 1: The state gain matrix $\mathcal{K}_{m_{1(h,e)},m_{2(h,e)},m_{3(h,e)}}$ is evaluated by solving Equation (34) and (35) for a different set of coupled thigh ($m_{1(h,e)}$), calf ($m_{2(h,e)}$), and heel-foot ($m_{3(h,e)}$) masses, as shown in Table 3.1. The parametric variation is incorporated by increasing the nominal mass values upto 20%, with an increment of 0.3, 0.15, and 0.06 kg for thigh, calf, and heel-foot. After performing several numerical experiments, the state-weighing matrix and control cost matrix are selected as $\mathcal{Q} = diag(500000, 5000, 10000, 1000, 10000, 1000)$ and $\mathcal{R} = eye(3, 3)$

TABLE 3.1: Variation in lower limb mass parameters of the coupled human-exoskeleton system

Thigh, $m_{1(h,e)}$(kg)	Calf, $m_{2(h,e)}$(kg)	Heel-Foot, $m_{3(h,e)}$(kg)
8.25	3.85	1.50
8.58	4.00	1.56
8.91	4.16	1.62
9.24	4.31	1.68
9.57	4.47	1.74
9.90	4.62	1.80

Step 2: Applying Equation (37) to compute the controller input (u) for operating range of state variables in error vector as shown in Table 3.2. The structure of three robust datasets is formed by exploiting Equations (40) and (41).

Step 3: The training of robust datasets is carried out using the ANFIS approach. The first six columns of every dataset are inherently considered the input set. The last column of every dataset is regarded as the output set. The input set comprises of error vector (E), and the output set contains the controller input vector (u). The three ANFIS architectures are formed, trained, and saved as *anfis1.fis*, *anfis2.fis*, and *anfis3.fis* for three controller inputs. Several simulation runs are performed by varying the number of MFs from 1 to 50 and epochs from 1 to 30. Thereafter,

TABLE 3.2: Operating range of error in state variables

Variables in error vector	Minimum value	Maximum value	Units
ξ_{1q_1}	-60	60	degree
ξ_{1q_2}	-60	60	degree
ξ_{1q_3}	-30	30	degree
$\xi_{1\dot{q}_1}$	-90	90	degree/sec
$\xi_{1\dot{q}_2}$	-90	90	degree/sec
$\xi_{1\dot{q}_3}$	-60	60	degree/sec

the training parameters are selected based on the zero tolerance of error between desired and predicted output vectors. In general, ANFIS utilizes two optimization methods: backpropagation, and hybrid, to establish the learning between input and output vectors. A gradient descent model is employed to evaluate the node error in the backpropagation method. In contrast, a least square algorithm along with the gradient descent model is exploited to regulate the errors in the hybrid method. In this work, the hybrid method is used with all three datasets for training the neural-fuzzy networks. The complete details of training parameters are given in Table 3.3.

TABLE 3.3: Operating range of error in state variables

Training Parameters	anfisl. fis	anfis2.fis	anfis3.fis
MF Type	Bell	Bell	Bell
MF Number	5	12	3
Error Tolerance	0.00001	0.0001	0.001
Epochs	10	15	5
Learning Model	Hybrid	Hybrid	Hybrid

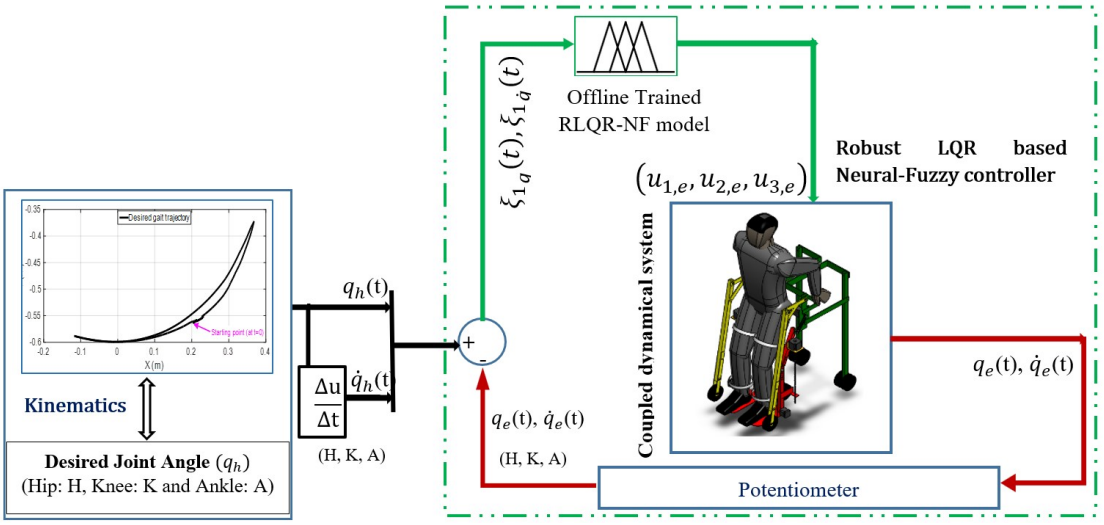

FIGURE 3.3: RLQR-NF Control Architecture

After forming the offline trained ANFIS architectures, the closed-loop architecture for RLQR-NF control scheme can be designed as given in Figure 3.3. To address the external disturbances along with the parametric perturbations, another intelligent controller termed as neural-fuzzy compensated PID control is proposed in further section.

3.3 NF-CPID Gait Tracking Control with Parametric Uncertainties and External Disturbances

In this section, at first, a conventional PID control is presented. Based on the control output, an offline neural-fuzzy dataset is built for inverse model identification. Thereafter, the same neural-fuzzy architecture is used along with the conventional PID control and adaptive law of weights are exploited to compensate the PPED in an online mode. Finally, the stability of the coupled system with proposed NF-CPID control is ensured using Lyapunov candidate function.

3.3.1 Conventional PID Controller

A classical PID control strategy is considered for tracking of desired gait trajectory with three well-known attributes: the first one where stable response action is monitored by the proportional control with converging steady-state error, the second one where the steady-state error is kept minimum using the integral control, and the third one where the settling time is improved using the derivative control after estimation of the errors' in future [204]. As shown in Figure 3.4, the mathematical form of PID controller, utilized in a continuous-time domain, is as follows:

$$\tau_{PID} = K_p\xi_1 + K_i \int \xi_1 + K_d\dot{\xi}_1 \tag{3.32}$$

where τ_{PID} denotes the PID controller output, ξ_1 signifies angular error due to the difference between the desired $q_{j,h}$ and actual joint position $q_{j,e}$, and K_p, K_i, K_d denotes the proportional, integral and derivative controller gains, respectively.

Several heuristic based numerical iterations are performed to select the tuned values of K_p, K_i, and K_d. The value of proportional gain is first altered while keeping

the integral and derivative gain constant for converging steady state error. Thereafter, integral gain is increased to remove the residual error and derivative gain is kept constant. Finally, after fixing the proportional and integral gain, the derivative one is tuned to achieve the minimal overshoot in the actual gait trajectory. However, when the unknown dynamic uncertainties are significant, integral gain (K_i) needs to be magnified to ensure asymptotic stability. With large values of (K_i), the system may realize high overshoot and bad stability. Therefore, an offline-online neuro-fuzzy compensator is proposed in the forthcoming sections to maintain an effective balance between minimal overshoot and maximum stability under parametric perturbations and external disturbances.

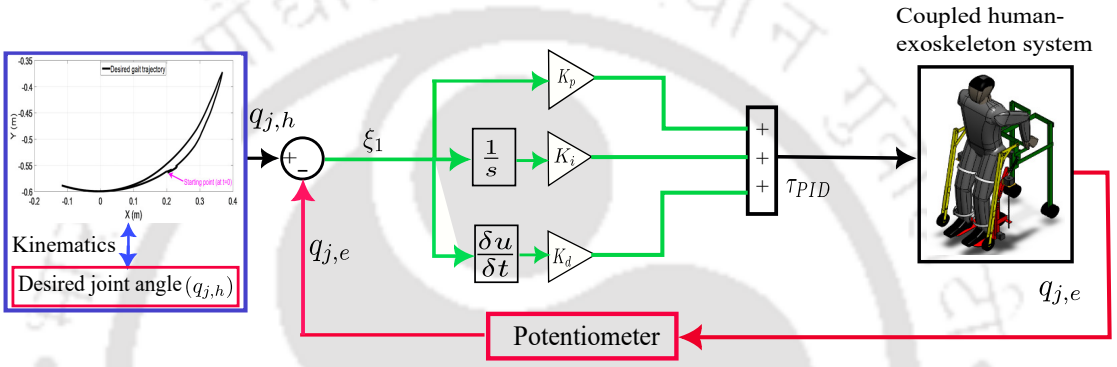

FIGURE 3.4: Conventional PID control architecture

3.3.2 Offline Trained Neuro-Fuzzy Approach for Inverse Model Identification

In the offline neuro-fuzzy training, the input dataset comprises of integral angular error, angular error and the derivative angular error from the coupled dynamic model without any control scheme. The output dataset consists of a linear distribution of PID controller torques/signals associated with each lower limb joint. The maximum and minimum bound of every linear distribution are defined according to the maximum and minimum output values of the conventional PID controller designed in previous section. The complete workflow is shown in Figure 3.5. The numerical runs for neuro-fuzzy training are performed with a different number of MFs and epochs varying from 1–50 to 1–30. However, it has been noticed that the better results of gait trajectory tracking are found with 11 MFs and 10 epochs for each input. A total of 99 rules is generated for each training dataset, leading to overall 297 rules for three training dataset. A hybrid optimization method, comprises of gradient descent and least square algorithm, is used in this work to adjust the errors. The training phase stops as tolerance error approaches to zero.

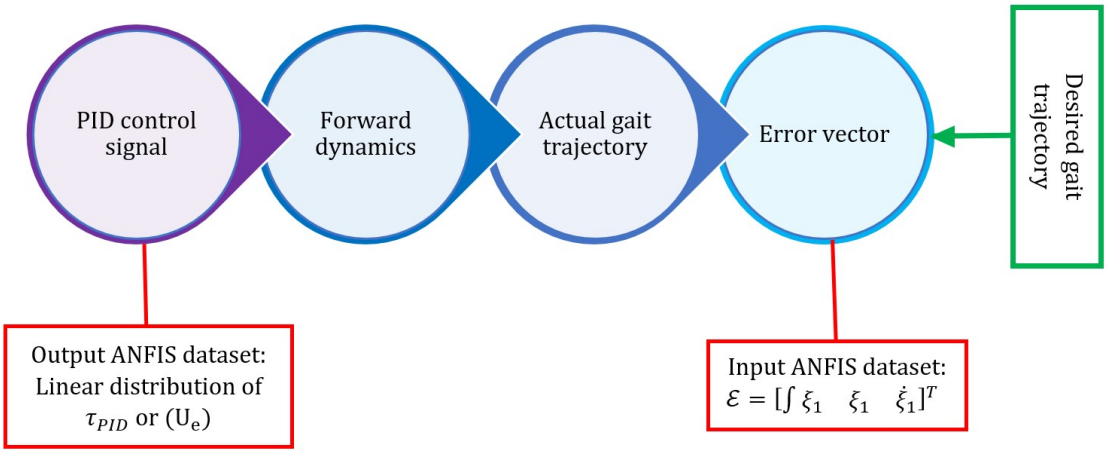

FIGURE 3.5: Formation of offline ANFIS training dataset

3.3.3 ANFIS compensated PID Control with Online Weight Adjustment

After obtaining the inverse human-exoskeleton model using offline neuro-fuzzy architecture, the same network architecture is connected in parallel with a conventional PD controller and makes system more accurate. This refers that two control actions are carried out to generate the controller output. First, the difference between the desired and actual joint angles, as an error, is fed to the PID controller; and second, the desired joint angles along with the derivatives are provided into already trained ANFIS structure. The former controller action ensures minimal tracking error during gait rehabilitation while the latter one deals with parametric uncertainties and unstructured disturbances by compensating the response of the former one using online adaptation of weights. The complete architecture of neuro-fuzzy compensated PID controller is shown in Figure 3.6 The combined effect of both control actions is summarized as

$$\tau_{NCP} = \tau_{NF} + \tau_{PID} \tag{3.33}$$

where, τ_{NCP} is the output neuro-fuzzy compensated PID controller, τ_{NF} is the output torque of neuro-fuzzy controller and τ_{PID} is the torque produced by the PID controller.

Introducing the dynamic uncertainties and external disturbances in Equation 2.11, the modified dynamic formulation is as follows:

$$\tau_{NCP} = \tau_{j,e} = \mathcal{M}_{oe}(q_{j,e})\ddot{q}_{j,e} + \mathcal{C}_{oe}(q_{j,e}, \dot{q}_{j,e})\dot{q}_{j,e} + \mathcal{G}_{oe}(q_{j,e}) - \rho \tag{3.34}$$

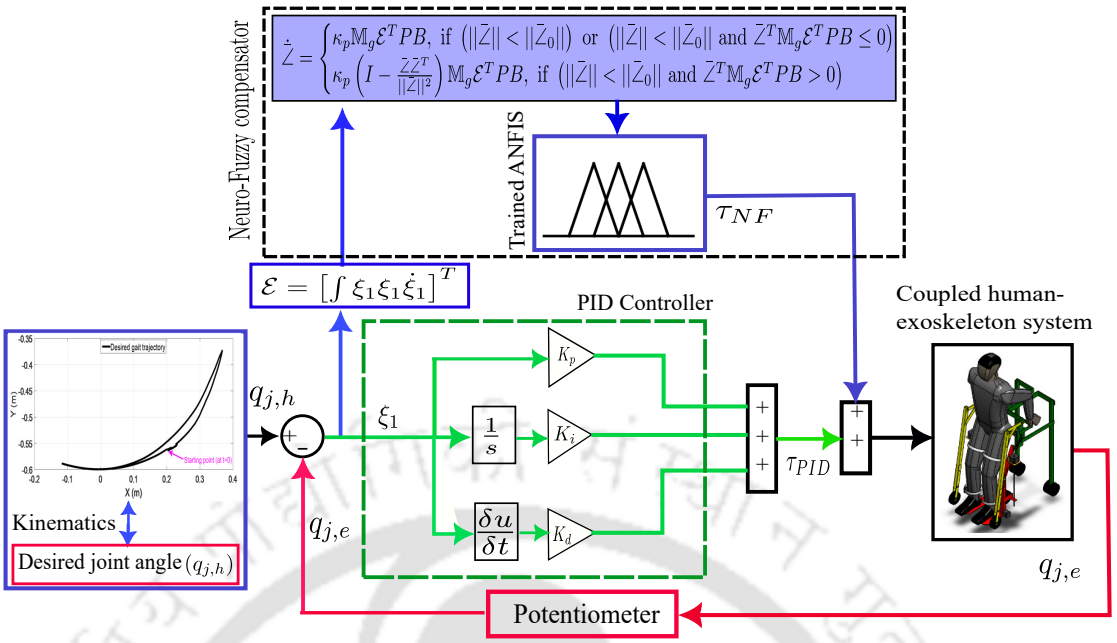

FIGURE 3.6: NF-CPID Control architecture

with

$$\rho = \tau_d - \mathcal{F}(\dot{q}_{j,e}) - \delta_s\big(\mathcal{M}_{h,e}(q_{j,e})\ddot{q}_{j,e} + \mathcal{C}_{h,e}(q_{j,e}, \dot{q}_{j,e}) + \mathcal{G}_{h,e}(q_{j,e})\big) \tag{3.35}$$

where ρ denotes the lumped form of parametric uncertainties and external disturbances; $\tau_d \in \mathbb{R}^3$ is the disturbance vector; $\mathcal{M}_{oe} \in \mathbb{R}^{3\times3}$, $\mathcal{C}_{oe} \in \mathbb{R}^{3\times3}$, and $\mathcal{G}_{oe} \in \mathbb{R}^3$ is the nominal value of inertia, Coriolis, gravity matrix, respectively; 'δ_s' indicates the uncertain scaling factor; and $\mathcal{F}(\dot{q}_{j,e}) \in \mathbb{R}^3$ denotes the friction model comprised of the Coulomb friction $C_f \in \mathbb{R}^3$ and viscous friction $\mathcal{V}_f \in \mathbb{R}^3$. The friction model is formulated as

$$\mathcal{F}(\dot{q}_{j,e}) = C_f sgn(\dot{q}_{j,e}) + \mathcal{V}_f = C_f sgn(\dot{q}_{j,e}) + \sigma_v \dot{q}_{j,e} \tag{3.36}$$

where σ_v denotes the velocity factor in $\mathrm{Nm/rad}^{-1}$, and *sgn* represents the signum function.

Employing the Equations 3.33-3.34 and Equation 3.32, the exoskeleton error vector $\mathcal{E} = [\int \xi_1 \quad \xi_1 \quad \dot{\xi}_1]^T$ can be obtained as

$$\dot{\mathcal{E}} = A\mathcal{E} + B[\tau^*_{NF} - \tau_{NF}] \tag{3.37}$$

$$= A\mathcal{E} + B[(\bar{Z}^* - \bar{Z})^T \mathbb{M}_g] \tag{3.38}$$

where, $A = -\begin{bmatrix} 0 & -I & 0 \\ 0 & 0 & -I \\ {\mathcal{M}_{oe}}^{-1}K_i & {\mathcal{M}_{oe}}^{-1}K_p & {\mathcal{M}_{oe}}^{-1}K_d \end{bmatrix}$; $B = \begin{bmatrix} 0 \\ 0 \\ \mathcal{M}_{oe}(q_{j,e})^{-1} \end{bmatrix}$;
$\mathbb{M}_g$ denotes the matrix form of normalized firing strength formed with Gaussian activation functions; $\bar{\mathcal{Z}}^*$ and $\bar{\mathcal{Z}}$ represent the optimal and actual weight matrices of the ANFIS architecture shown in Figure 3.1.

Assuming the input-output vector (z : x, y) shown in subsection 3.2.2, the Gaussian activation function can be represented as:

$$\text{Gaussian}(\text{z}; c_j, \sigma_{wj}) = \exp\left[\frac{-(\text{z}-c_j)^2}{\sigma_{wj}^2}\right], \quad j = 1, 2 \tag{3.39}$$

where, c_j and σ_{wj} denotes the centre distance from the origin and curve width, respectively.

During online training, $\bar{\mathcal{Z}}$ need to be further adjusted to minimize the tracking error. The adaptation of $\bar{\mathcal{Z}}$ is selected as [213]

$$\dot{\bar{\mathcal{Z}}} = \begin{cases} \kappa_p \mathbb{M}_g \mathcal{E}^T P B, \text{ if } \left(||\bar{\mathcal{Z}}|| < ||\bar{\mathcal{Z}}_0||\right) \text{ or } \left(||\bar{\mathcal{Z}}|| < ||\bar{\mathcal{Z}}_0|| \text{ and } \bar{\mathcal{Z}}^T \mathbb{M}_g \mathcal{E}^T P B \leq 0\right) \\ \kappa_p \left(I - \frac{\bar{\mathcal{Z}}\bar{\mathcal{Z}}^T}{||\bar{\mathcal{Z}}||^2}\right) \mathbb{M}_g \mathcal{E}^T P B, \text{ if } \left(||\bar{\mathcal{Z}}|| < ||\bar{\mathcal{Z}}_0|| \text{ and } \bar{\mathcal{Z}}^T \mathbb{M}_g \mathcal{E}^T P B > 0\right) \end{cases} \tag{3.40}$$

where, where $\bar{\mathcal{Z}} = \begin{bmatrix} \bar{\mathcal{Z}}_1 & \bar{\mathcal{Z}}_2 \ldots \bar{\mathcal{Z}}_p \end{bmatrix}, B = \begin{bmatrix} B_1 & B_2 \ldots B_p \end{bmatrix}$, κ_p is a positive constant, p is the number of robot joints or number of output variables of the ANFIS, i.e., each $\bar{\mathcal{Z}}_i$ is a column vector associated with each output variable, and P is a symmetric positive-definite matrix that satisfies the following relationship:

$$PA + A^T P = -Q \tag{3.41}$$

where Q is a symmetric positive definite matrix and is selected by the user.

To ensure the stability of the coupled system, the neuro-fuzzy control should converge which is possible in case of weights $\bar{\mathcal{Z}}$ bounded by the constraint set $\mathcal{W}$ as follows [213]:

$$\mathcal{W} = \left\{\left\|\bar{\mathcal{Z}}_i\right\| \leq \left\|\bar{\mathcal{Z}}_0\right\|\right\}, \quad i = 1, 2, \ldots p \tag{3.42}$$

where ||.|| represents two-norm of a vector and $\bar{\mathcal{Z}}_0$ denotes the initial weights at $t = 0$.

Assuming the Lyapunov candidate function based on Equation 3.38 as follows:

$$V = \frac{1}{2}\mathcal{E}^T P\mathcal{E} + \frac{1}{2}\kappa_p^{-1}\,\mathrm{tr}\left[\left(\bar{\mathcal{Z}}^* - \bar{\mathcal{Z}}\right)^T\left(\bar{\mathcal{Z}}^* - \bar{\mathcal{Z}}\right)\right] \tag{3.43}$$

Evaluating the derivative of Lyapunov function as:

$$\dot{V} = \frac{1}{2}\dot{\mathcal{E}}^T P\mathcal{E} + \frac{1}{2}\mathcal{E}^T P\dot{\mathcal{E}} - \kappa_p^{-1} tr\left[\left(\bar{\mathcal{Z}}^* - \bar{\mathcal{Z}}\right)^T\dot{\bar{\mathcal{Z}}}\right] \tag{3.44}$$

Substituting Equations 3.41 and 3.38 in Equation 3.44,

$$\dot{V} = -\frac{1}{2}\mathcal{E}^T Q\mathcal{E} + \mathcal{E}^T PB\left(\bar{\mathcal{Z}}^* - \bar{\mathcal{Z}}\right)^T\mathbb{M}_g - \kappa_p^{-1}\,\mathrm{tr}\left[\left(\bar{\mathcal{Z}}^* - \bar{\mathcal{Z}}\right)^T\dot{\bar{\mathcal{Z}}}\right]. \tag{3.45}$$

Following first condition of adaptation law from Equation 3.40, Equation 3.45 can be modified as

$$\begin{aligned}\dot{V} =& -\frac{1}{2}\mathcal{E}^T Q\mathcal{E} + \mathcal{E}^T PB\left(\bar{\mathcal{Z}}^* - \bar{\mathcal{Z}}\right)^T\mathbb{M}_g - tr\left[\left(\bar{\mathcal{Z}}^* - \bar{\mathcal{Z}}\right)^T\mathbb{M}_g\mathcal{E}^T PB\right]\\ =& -\frac{1}{2}\mathcal{E}^T Q\mathcal{E} + \mathcal{E}^T PB\left(\bar{\mathcal{Z}}^* - \bar{\mathcal{Z}}\right)^T\mathbb{M}_g - tr\left[\mathcal{E}^T PB\left(\bar{\mathcal{Z}}^* - \bar{\mathcal{Z}}\right)^T\mathbb{M}_g\right]\\ =& -\frac{1}{2}\mathcal{E}^T Q\mathcal{E} \leq 0\end{aligned} \tag{3.46}$$

Similarly, following second condition of adaptation law from Equation 3.40, Equation 3.45 can be modified as

$$\begin{aligned}\dot{V} =& -\frac{1}{2}\mathcal{E}^T Q\mathcal{E} + \mathcal{E}^T PB\left(\bar{\mathcal{Z}}^* - \bar{\mathcal{Z}}\right)^T\mathbb{M}_g -\\ & \kappa_p^{-1}\sum_{i=1}^{n}\left[\left(\bar{\mathcal{Z}}_i^* - \bar{\mathcal{Z}}_i\right)^T\kappa_p\left(I - \frac{\bar{\mathcal{Z}}_i\bar{\mathcal{Z}}_i^T}{\left\|\bar{\mathcal{Z}}_i\right\|^2}\right)\mathbb{M}_g\mathcal{E}^T PB_i\right]\\ =& -\frac{1}{2}\mathcal{E}^T Q\mathcal{E} - \sum_{i=1}^{n}\left[\left(1 - \frac{\left(\bar{\mathcal{Z}}_i^*\right)^T\bar{\mathcal{Z}}_i}{\left\|\bar{\mathcal{Z}}_i\right\|^2}\right)\bar{\mathcal{Z}}_i^T\mathbb{M}_g\mathcal{E}^T PB_i\right]\end{aligned} \tag{3.47}$$

Since $\bar{\mathcal{Z}}_i^* \in \mathcal{W}$ and $1 - \left(\bar{\mathcal{Z}}_i^*\right)^T\bar{\mathcal{Z}}_i/\left\|\bar{\mathcal{Z}}_i\right\|^2 \geq 0$, Equation 3.47 can be further modified as

$$\dot{V} \leq -\frac{1}{2}\mathcal{E}^T Q\mathcal{E} \leq 0 \tag{3.48}$$

From Equations 3.43, 3.46 and 3.48, it can be easily observed that $V \geq 0$ and $\dot{V} \leq 0$. Moreover, Equation 3.46 shows that $V = 0$ if and only if $\mathcal{E} = 0$ and Equation (21) infers that $\dot{V} = 0$ if and only if $V = 0$. In this manner, the global stability of the neuro-fuzzy compensated PID controller is ensured. Exploiting

Barbalat's lemma [214], it can be also shown that $V \to 0$ as $t \to \infty$ which ensures the proposed control scheme asymptotically stable.

3.4 Results and Discussions

In this section, the simulation results and experimental findings of the RLQR-NF and NF-CPID control strategy are presented for the LLES$v1$ during passive-assist rehabilitation measures. The pediatric subject of age 08 years, body mass 30 kg, body height 122 cm (C4 from Table 2.6) is considered. The desired joint angles with the Cartesian gait trajectory for the pediatric subject are estimated using a wireless Kinect-based NI-LabVIEW experimental model, described in Section 2.3 of Chapter 2. The effectiveness of the RLQR-NF control scheme is validated by comparing with the exponential reaching law based sliding mode (ERL-SM) control [215]. The simulation and experimental runs for all control schemes in this chapter are carried out in MATLAB/Simulink R2020b (ode45 solver with variable step and non-adaptive zero crossing algorithm). On the other hand, effectiveness of the NF-CPID control strategy is compared with the RLQR-NF control scheme. The performance index (PI), based on the root mean square error (RMSE), is calculated to analyze the improvement of the proposed control scheme over the contrast control scheme.

$$RMSE = \sqrt{\frac{1}{N}\sum^{N} \|\xi_1\|^2} \tag{3.49}$$

$$PI = \frac{RMSE_{Contrast} - RMSE_{Proposed}}{RMSE_{Contrast}} \times 100 \tag{3.50}$$

where ξ_1 represents the error between desired and actual joint angles, and N is the size of the error vector. $RMSE_{Contrast}$ and $RMSE_{Proposed}$ signify the root mean square error related to contrast control and proposed control strategy.

3.4.1 Simulation results of RLQR-NF Control with parametric perturbations

The results are contemplated to demonstrate the controller's robustness while increasing the nominal mass values in two different cases. Begin with Case-I, the system masses are perturbed by 20% ($m_{1(h,e)} = 9.90,\ m_{2(h,e)} = 4.62,\ m_{3(h,e)} = 1.80$).

As shown in Figure 3.7, the healthy gait trajectory is tracked by incorporating the kinematic and dynamic parameters into the proposed control (RLQR-NF) and ERL-SM control strategy. The starting Cartesian position $(X, Y : 0.25m, -0.60m)$ of the desired gait trajectory is illustrated in black color. The actual trajectories in the Cartesian coordinate frame are presented by the dashed blue line (RLQR-NF) and the green line (ERL-SM). Figure 3.8(a) and 3.8(b) depicts the tracking error in both the directions, i.e., $X-$ and $Y-$direction (ξ_X and ξ_Y). The maximum absolute deviation in X-direction ($|\xi_X|_{max}$) for ERL-SM and RLQR-NF control scheme is 0.013 m and 0.008 m, respectively. In the Y-direction, the respective deviation ($|\xi_Y|_{max}$) is observed to be 0.009 m and 0.006 m for ERL-SM and RLQR-NF control strategy.

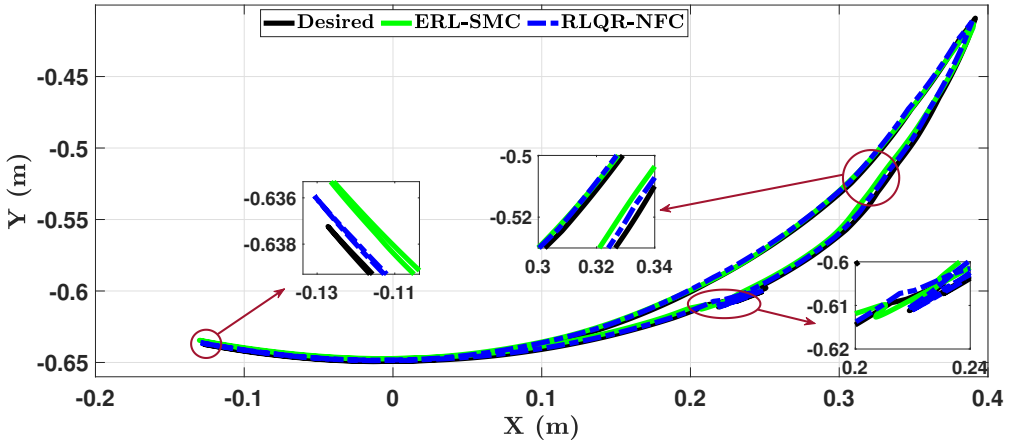

FIGURE 3.7: Cartesian gait tracking for 20% perturbed mass values with ERL-SM and RLQR-NF control

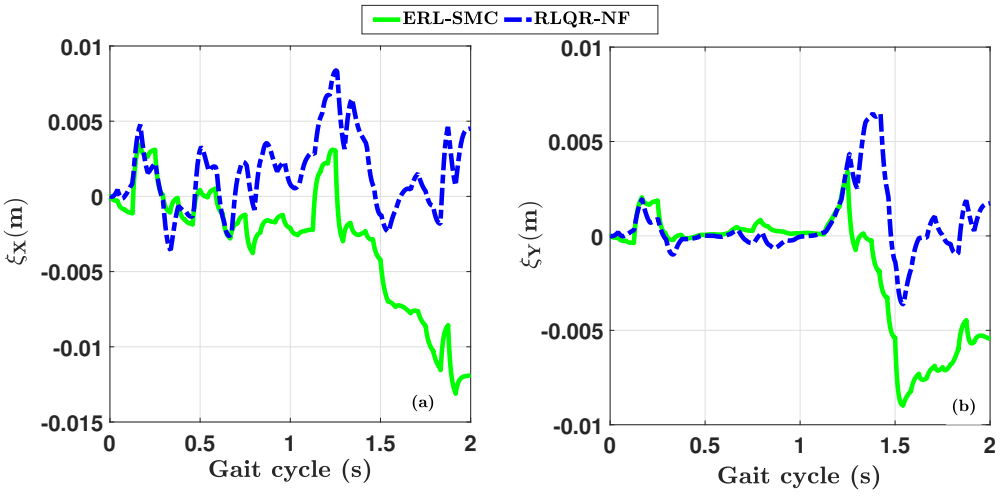

FIGURE 3.8: Gait tracking error in (a) X-direction and (b) Y-direction for 20% perturbed mass values with ERL-SM and RLQR-NF control

The tracking of desired joint angles with applied control strategies are illustrated in Figure 3.9(a), 3.9(b), and 3.9(c). The hip, knee, and ankle angular deviations (ξ_1) from desired joint trajectories are shown in Figure 3.10(a), 3.10(b), and 3.10(c), respectively. Considering hip joint, it is observed that the RMSE for respective controllers is 0.711° (ERL-SM) and 0.213° (RLQR-NF). In case of the knee joint, the RMSE is found to be 2.221° and 1.201° for the system with ERL-SM and RLQR-NF control strategy, respectively. For ankle joint, the respective RMSE are estimated as 0.709° (ERL-SM) and 0.521° (RLQR-NF).

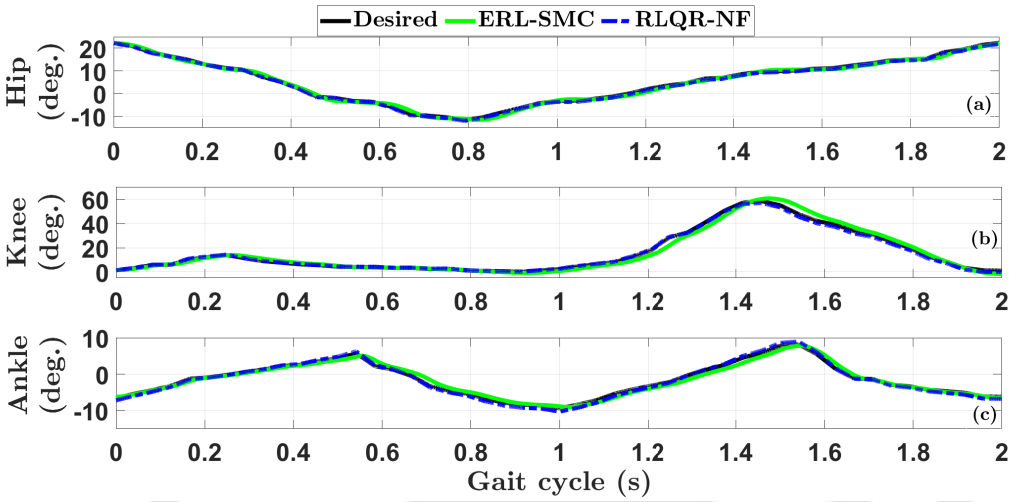

FIGURE 3.9: (a) Hip, (b) knee, and (c) ankle joint tracking for 20% perturbed mass values with ERL-SM and RLQR-NF control

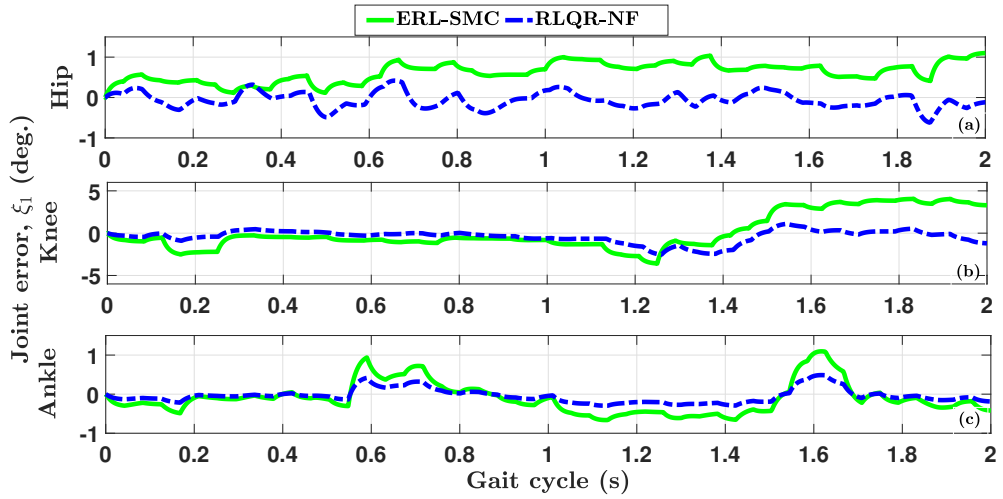

FIGURE 3.10: (a) Hip, (b) knee, and (c) ankle joint tracking error for 20% perturbed mass values with ERL-SM and RLQR-NF control

Figure 3.11(a), 3.11(b), and 3.11(c) demonstrate the generated control input ($u_{1,e}$, $u_{2,e}$, and $u_{3,e}$) following the desired trajectory through repetitive gait rehabilitation exercises. With the ERL-SM control scheme, the peak values of hip, knee, and ankle

signal are estimated as 51.25 Nm, 28.68 Nm, and 2.15 Nm. On the other hand, with the RLQR-NF control scheme, the respective values of control signals are found to be 35.57 Nm, 18.81 Nm, and 1.37 Nm. Although it is evident from the results that the proposed control strategy (RLQR-NF) outperforms the contrast control strategy (ERL-SM) to track the desired gait trajectory, however, with a marginal difference. Therefore, to demonstrate the effectiveness of the proposed control, more variations in mass parameters are considered further.

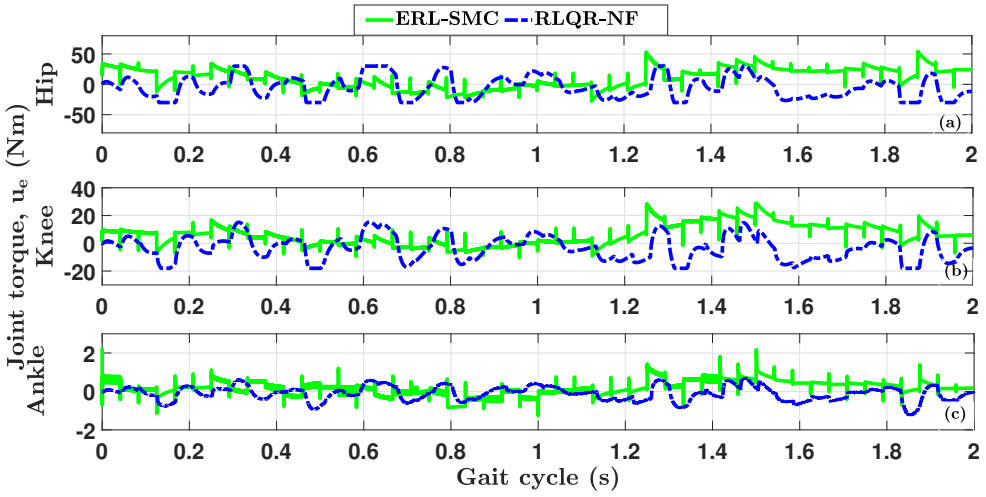

FIGURE 3.11: (a) Hip, (b) knee, and (c) ankle joint torque for 20% perturbed mass values with ERL-SM and RLQR-NF control

Furthermore, in Case-II with 30% perturbed system masses ($m_{1(h,e)} = 10.73$, $m_{2(h,e)} = 5.00$, $m_{3(h,e)} = 1.95$), the angular deviations (ξ_1) from desired joint trajectories are shown in Figure 3.12(a), 3.12(b), and 3.12(c). Considering hip joint, it is observed that the RMSE for respective controllers is 0.719° (ERL-SM) and 0.248° (RLQR-NF). In case of the knee joint, the RMSE is found to be 2.234° and 1.239° for the system with ERL-SM and RLQR-NF control strategy, respectively. For ankle joint, the respective RMSE are estimated as 0.714° (ERL-SM) and 0.546° (RLQR-NF).

Table 3.4 presents the performance index (PI) of the proposed control over the contrast control. The proposed control is promising in desired gait tracking compared to the contrast control, subjected to parametric variations. Moreover, as observed from Table 3.4, the performance index (PI) is degraded by 4.6%, 1.4%, and 3% when perturbing the system masses from 20% to 30%. As the robust dataset (S_{rd}) is formed and trained with a parametric perturbation of 20%, the tracking results start degrading beyond the training workspace which is observed in case of 30%

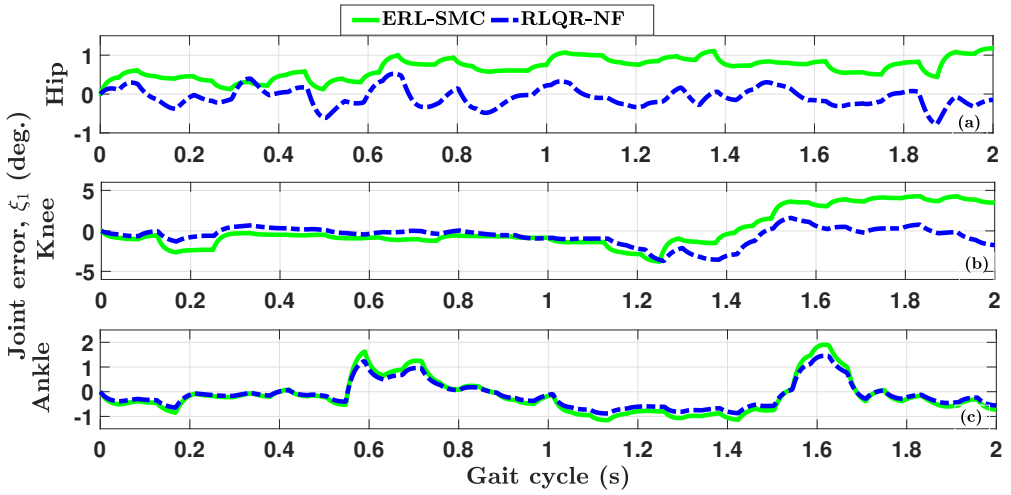

FIGURE 3.12: (a) Hip, (b) knee, and (c) ankle joint tracking error for 30% perturbed mass values with ERL-SM and RLQR-NF control

TABLE 3.4: Comparative performance analysis of proposed control

Case-I: With 20% increment in mass parameters $(m_{1(h,e)} = 9.90, m_{2(h,e)} = 4.62, m_{3(h,e)} = 1.80)$			
Joint	RMSE (ERL-SMC)	RMSE (RLQR-NF)	PI (%)
Hip	0.711	0.213	70.1
Knee	2.221	1.201	45.9
Ankle	0.709	0.521	26.5
Case-II: With 30% increment in mass parameters $(m_{1(h,e)} = 10.73, m_{2(h,e)} = 5.00, m_{3(h,e)} = 1.95)$			
Joint	RMSE (ERL-SMC)	RMSE (RLQR-NF)	PI (%)
Hip	0.719	0.248	65.5
Knee	2.234	1.239	44.5
Ankle	0.714	0.546	23.5

parametric perturbation. During rehabilitation exercises, this performance investigation allows the lower-limb exoskeleton system to carry out repetitive movements with greater accuracy under the predefined limit of parametric variations.

TABLE 3.5: Settling time of ERL-SM and RLQR-NF control for convergence analysis

Control scheme	Joint	Settling time (sec)	
		Case-I	Case-II
ERL-SM	Hip	1.986	1.993
	Knee	1.974	1.988
	Ankle	1.943	1.969
RLQR-NF	Hip	1.967	1.991
	Knee	1.959	1.987
	Ankle	1.933	1.958

The convergence of both control schemes is investigated by evaluating the settling time, i.e., the time lapsed for the error to drop within 2% of the final value. The settling time for the error in the hip, knee, and ankle joint for every set of mass values is presented in Table 3.5. The low values of settling time indicate the faster convergence of for proposed controller (RLQR-NF) over the contrast controller (ERL-SM) before achieving the full stable state.

3.4.2 Simulation Results of NF-CPID control with Parametric Perturbations and External Disturbances

To validate the effectiveness of proposed controller with respect to the contrast controllers, two cases are considered. In first case (Case-I), as a model parametric uncertainty, a variation in system masses is realized by increasing 30% of thigh, calf and foot masses of coupled system, i.e, $\delta_s = 0.3$. In second case (Case-II), along with the uncertainty, input disturbances in the form sinusoidal function $\tau_{d_1} = 6sin(4\pi t), \tau_{d_2} = 5sin(3\pi t)$, $\tau_{d_3} = 3sin(2\pi t)$ are inputted into the system externally. In this work, a periodic (sinusoidal) form of external disturbances is added to mimic the effect of sudden reflexes induced at the joints throughout a gait cycle. These reflexes are caused due to the pathological gait (altered one) in the case of post-stroke subjects. The Coulomb friction, and viscous velocity factor are selected as $C_f = [0.8, 0.8, 0.8]^T, \sigma_v = [1.2, 1.2, 1.2]^T$. In the offline training and online adaptation of weights, the proportional, integral, and derivative gain values are $K_p = 250, K_i = 4, K_d = 40$ for hip joint, $K_p = 220, K_i = 5, K_d = 40$ for knee joint and $K_p = 212, K_i = 2, K_d = 30$ for ankle joint.

Furthermore, as observed from the offline trained neuro-fuzzy architecture, a total of eleven Gaussian activation functions are considered in the online NF-CPID control architecture. The centre distance parameter matrix is selected as $c_j = (-5, -4, -3, -2, -1, 0, 1, 2, 3, 4, 5)_{9\times 11}$ and curve width for the Gaussian function is taken as $\sigma_{wj} = 4$. The positive constant in adaptive law (Equation 3.40) is selected as $\kappa_p = 20$ after performing several numerical iterations.

Begin with the Case-I, the Cartesian tracking error in $X-$ and $Y-$direction (ξ_X and ξ_Y) is shown in Figure 3.13(a) and 3.13(b). A marginal performance loss is observed in X-direction for proposed NF-CPID control ($|\xi_X|_{max} = 0.028$ m) as compared to RLQR-NF control ($|\xi_X|_{max} = 0.025$ m). The maximum absolute deviation in Y-direction ($|\xi_Y|_{max}$) is observed to be 0.015 m and 0.013 m for RLQR-NF and NF-CPID control strategy. The hip, knee, and ankle joint angular

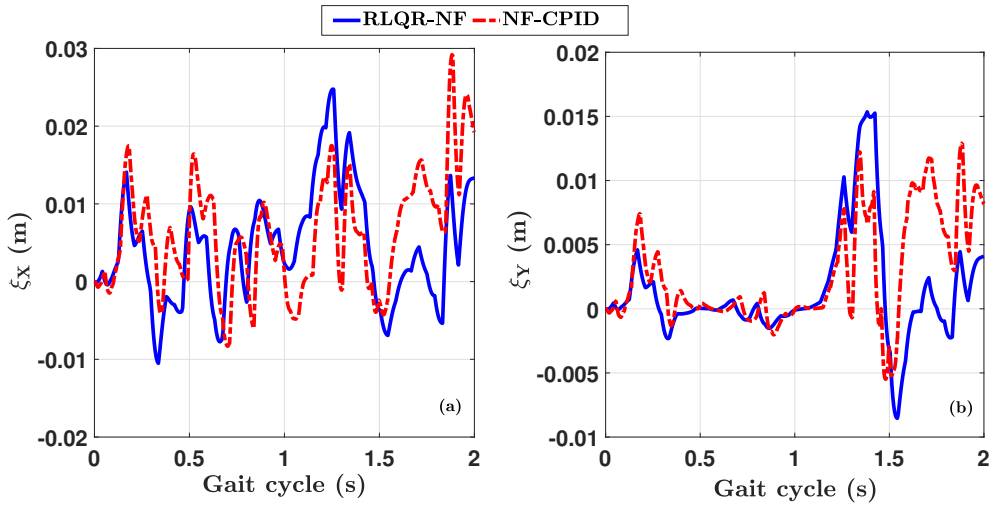

FIGURE 3.13: Gait tracking error in (a) X-direction and (b) Y-direction for 30% perturbed mass values with RLQR-NF and NF-CPID control

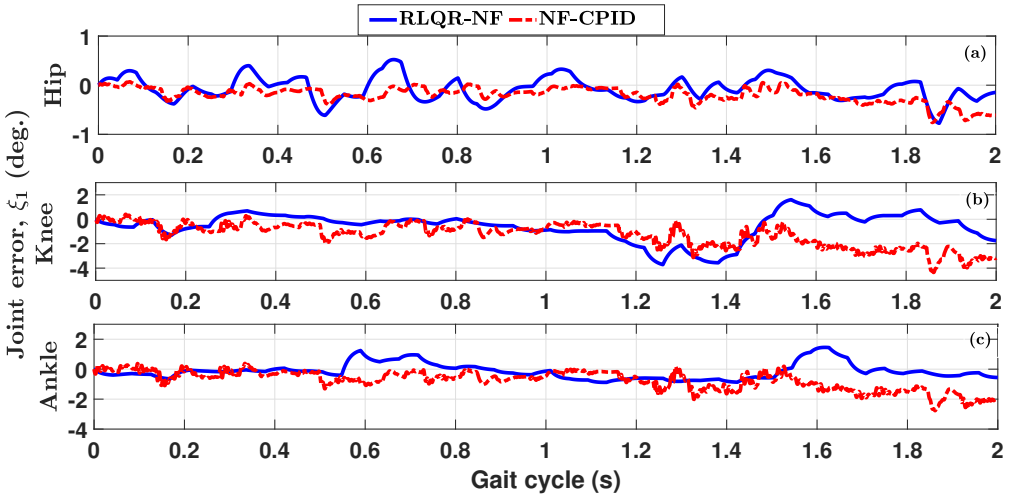

FIGURE 3.14: (a) Hip, (b) knee, and (c) ankle joint error for 30% perturbed mass values with RLQR-NF and NF-CPID control

error (ξ_1) are shown in Figure 3.14(a), 3.14(b), and 3.14(c), respectively. The performance of the proposed NF-CPID control is decreased by 1.2%, 29.1%, and 78.9% for hip, knee and ankle joint, respectively, as shown in 3.6.

On the other hand, referring Figure 3.15(a) and 3.15(b), the gait tracking error in Case-II is found to be more effective for proposed NF-CPID control ($|\xi_X|_{max}$ = 0.027 m, $|\xi_Y|_{max}$ = 0.012m) as compared to the RLQR-NF control ($|\xi_X|_{max}$ = 0.058 m, $|\xi_Y|_{max}$ = 0.030 m). The angular error (ξ_1) for hip, knee, and ankle joint are shown in Figure 3.16(a), 3.16(b), and 3.16(c), respectively. The performance of the proposed NF-CPID control is improved by 43.03%, 33.37%, and 12.28% for hip, knee and ankle joint, respectively, as shown in 3.6.

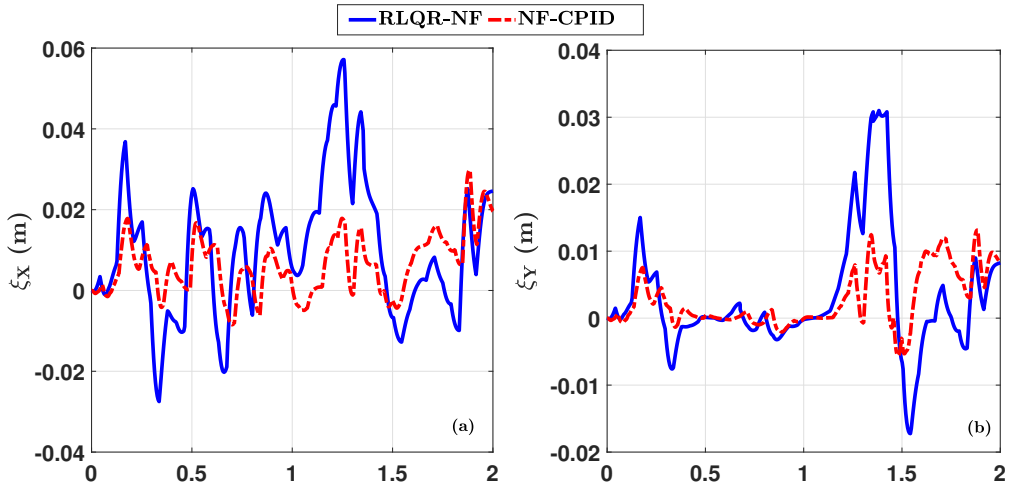

FIGURE 3.15: Gait tracking error in (a) X-direction and (b) Y-direction for 30% perturbed mass values and periodic disturbances with RLQR-NF and NF-CPID control

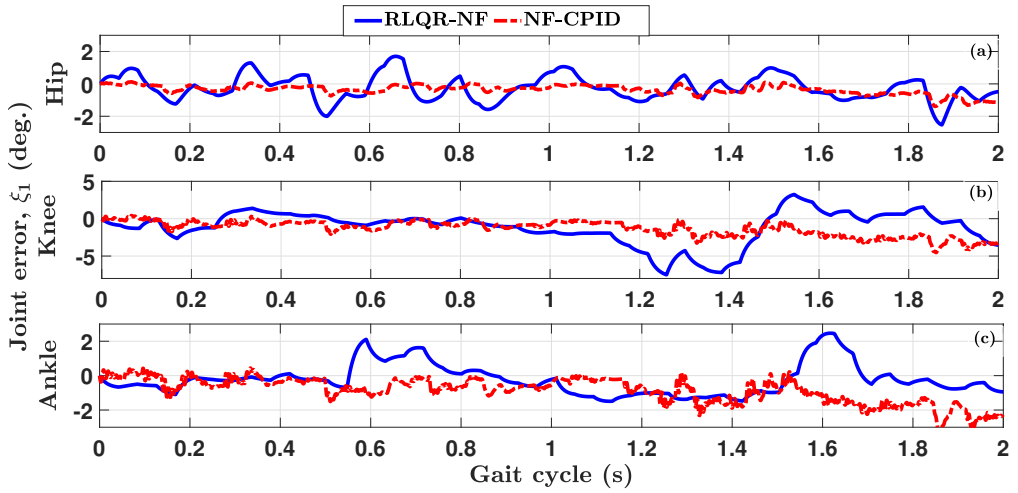

FIGURE 3.16: (a) Hip, (b) knee, and (c) ankle joint error for 30% perturbed mass values and periodic disturbances with RLQR-NF and NF-CPID control

Referring the Table 3.6, it can be clearly noticed that the effective performance of the proposed control is increased by 44.23%, 62.47%, and 91.18% while moving from Case-I to Case-II. Therefore, it can be finally concluded that the proposed NF-CPID control is far more robust to external disturbances rather than parametric perturbations. Moreover, the tuning of neuro-fuzzy hyperparameters such as number of hidden nodes, width of membership function, and number of epochs in the offline training make the control approach computationally expensive. With the knowledge base of simulation results, in the following section, the proposed NF-CPID control is implemented on the experimental setup of LLES$v1$ for a child dummy.

TABLE 3.6: Comparative performance analysis of proposed control

Case-I: With 30% increment in mass parameters $(m_{1(h,e)} = 10.73, m_{2(h,e)} = 5.00, m_{3(h,e)} = 1.95)$			
Joint	RMSE (RLQR-NF)	RMSE (NF-CPID)	PI (%)
Hip	0.248	0.251	-1.2
Knee	1.239	1.600	-29.1
Ankle	0.546	0.977	-78.9
Case-II: With 30% increment in mass parameters and external disturbances $(m_{1(h,e)} = 10.73, m_{2(h,e)} = 5.00, m_{3(h,e)} = 1.95)$ $(\tau_{d_1} = 6sin(4\pi t), \tau_{d_2} = 5sin(3\pi t), \tau_{d_3} = 3sin(2\pi t))$			
Joint	RMSE (RLQR-NF)	RMSE (NF-CPID)	PI (%)
Hip	0.811	0.462	43.03
Knee	2.502	1.667	33.37
Ankle	1.124	0.926	12.28

3.4.3 Experimental Results of NF-CPID Control on Coupled Dummy-Exoskeleton System

The experimental setup of LLES$v1$ is considered with a child dummy whose specifications are kept similar to the pediatric subject of age 08 years, body mass 30 kg, body height 122 cm. The lower-limb of the dummy's subject is attached with the exoskeleton at thigh, calf, and ankle joint using nylon cuffs. The real-time control architecture for the coupled dummy-exoskeleton system is shown in Figure 3.17. The actuators are controlled by electronic drivers which receives input PWM via the microcontroller board. Then, the relevant control voltage will be realized on DC motor. Meanwhile, the angular positions and velocities of the actuators are measured using feedback units and reverted back to in the control scheme via the microcontroller board. This way, the PWM signal is adjusted based on the desired and actual (feedback) gait data for each step size and closed loop system is completed. The specifications for each component are provided in section 2.4 of the Chapter 2. An emergency stop button is provisioned in the software and hardware interface to terminate the complete training process in case of discomfort. The complete control architecture is created in the MATLAB/Simulink interface. The root mean square vlaue of voltage signals (RMSV) is used to identify the overall control evolution (U_e) more effectively.

$$RMSV = \sqrt{\frac{1}{N}\sum_{v=1}^{N} V^2} \tag{3.51}$$

where V denotes the control voltage for respective joint and N represents the total number of data points.

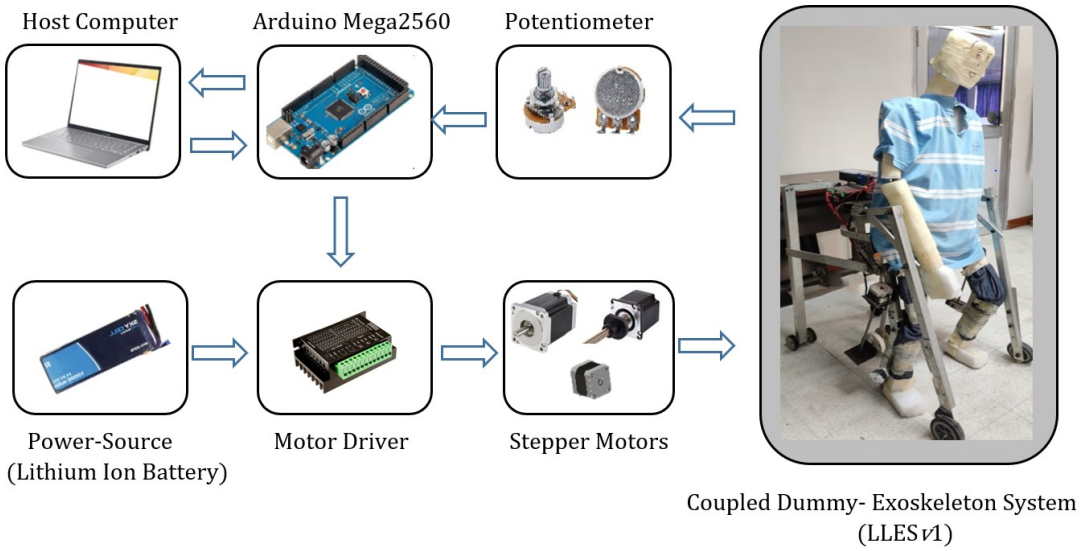

FIGURE 3.17: Real-time control architecture of LLES$v1$ with a pediatric dummy

The proportional, integral, and derivative gain values during the offline and online training are used as $K_p = 0.5, K_i = 0.001, K_d = 0.04$ for hip joint, $K_p = 0.4, K_i = 0.004, K_d = 0.009$ for knee joint and $K_p = 0.09, K_i = 0.001, K_d = 0.01$ for ankle joint. Similar to the simulation, a total of eleven Gaussian activation functions are again considered in the online NF-CPID control architecture. The centre distance parameter matrix and curve width for the Gaussian function is selected as $c_j = (-5, -4, -3, -2, -1, 0, 1, 2, 3, 4, 5)_{9\times 11}$ and $\sigma_{wj} = 4$, respectively. Investigating the gait tracking results for several experimental runs, $\kappa_p = 2$ is selected as the positive parameter in adaptive law (Equation 3.40).

The tracking of healthy gait trajectory using proposed NF-CPID and contrast RLQR-NF control is carried out by coupled dummy-exoskeleton system as shown in Figure 3.18. The starting point of the Cartesian desired gait trajectory, marked in blue color, is $(X, Y : 0.25m, \ -0.60m)$. The actual Cartesian trajectory are presented by the dashed blue line (RLQR-NF) and the red line (ERL-SM). The following tracking error of heel-foot point in $X-$ and $Y-$ direction (ξ_X and ξ_Y) is shown in Figure 3.21(a) and 3.21(b). The maximum absolute error in X-direction ($|\xi_X|_{max}$) is recorded as 0.067 m for RLQR-NF and 0.055 m for NF-CPID control scheme. In the Y-direction, The respective error in Y-direction ($|\xi_Y|_{max}$) is 0.048 m for RLQR-NF and for 0.036 m NF-CPID control strategy. The noisy response is predominantly observed in the X-direction as compared to Y-direction, especially during the stance phase of the gait cycle.

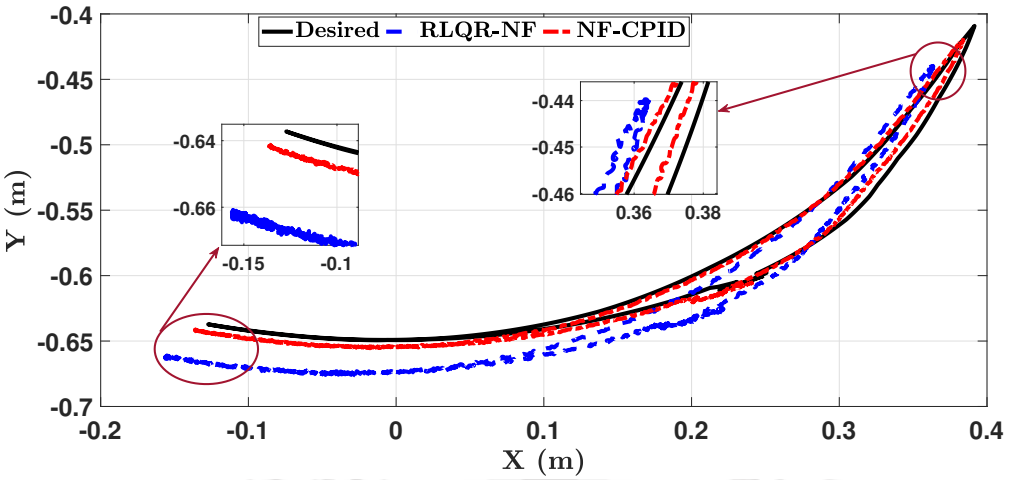

FIGURE 3.18: Cartesian gait tracking for coupled dummy-LLES$v1$ system with RLQR-NF and NF-CPID control

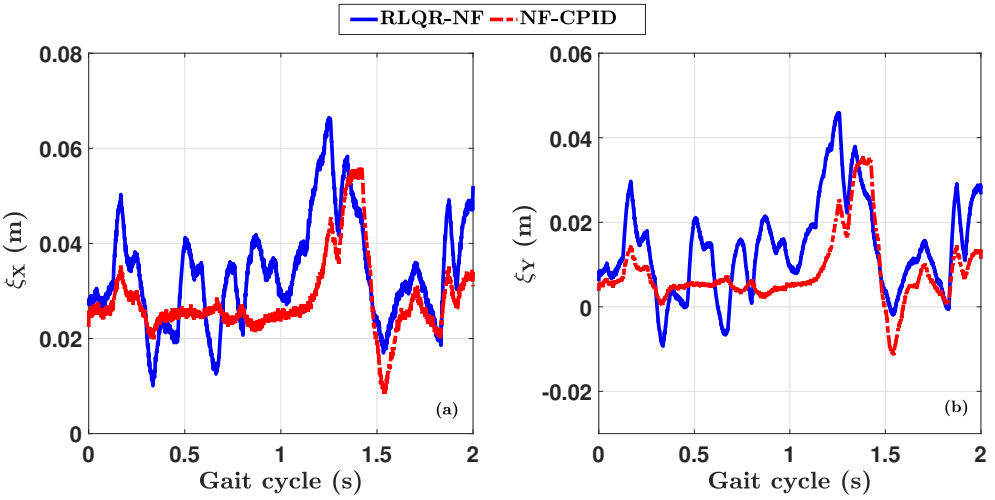

FIGURE 3.19: Gait tracking error in (a) X-direction and (b) Y-direction for coupled dummy-LLES$v1$ system with RLQR-NF and NF-CPID control

Figure 3.20(a), 3.20(b), and 3.20(c) demonstrates the tracking of hip, knee, and ankle joint by coupled experimental system using proposed and contrast control schemes. The hip, knee, and ankle angular deviations (ξ_1) are shown in Figure 3.21(a), 3.21(b), and 3.21(c), respectively. For better readability, a zoom-in view is shown for the tracking results of each joint. The proposed NF-CPID control effectively allows the system to track the hip, knee, and ankle joint by 71.8% ($\text{RMSE}_{RLQR-NF}$: 3.266°, $\text{RMSE}_{NF-CPID}$: 0.921°), 59.5% ($\text{RMSE}_{RLQR-NF}$: 2.366°, $\text{RMSE}_{NF-CPID}$: 0.968°), and 32.15% ($\text{RMSE}_{RLQR-NF}$: 0.706°, $\text{RMSE}_{NF-CPID}$: 0.479°),respectively. From zoom-in views, a significant amount of noise is clearly observed in the joint error response, especially for hip and knee joint.

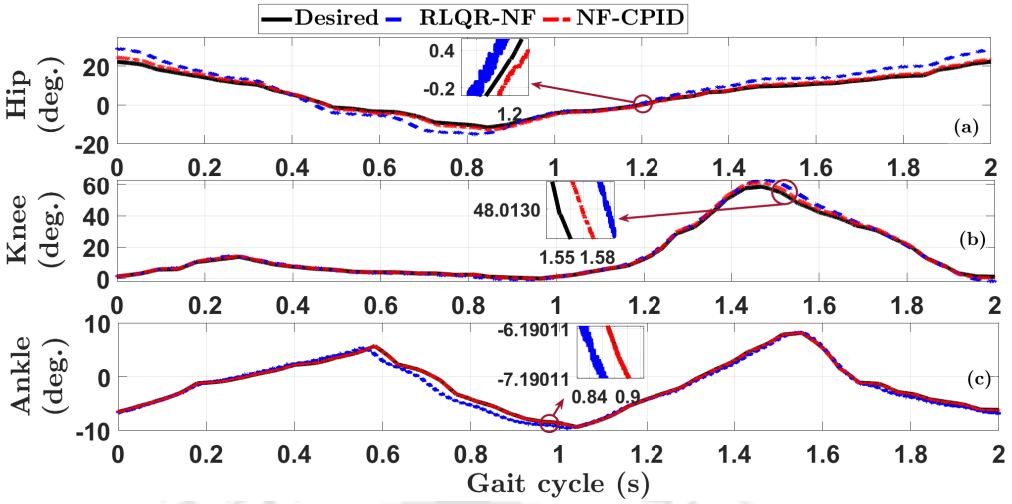

FIGURE 3.20: (a) Hip, (b) knee, and (c) ankle joint tracking for coupled dummy-LLES$v1$ system with RLQR-NF and NF-CPID control

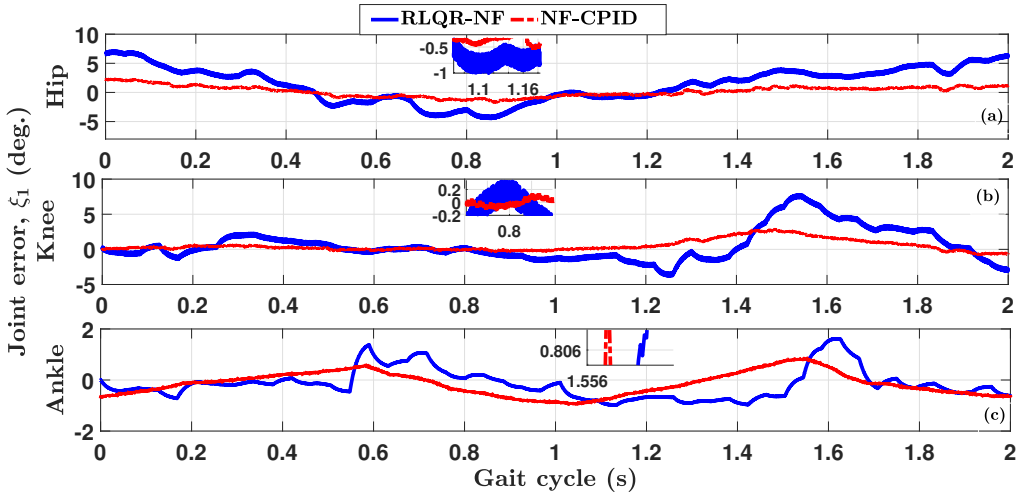

FIGURE 3.21: (a) Hip, (b) knee, and (c) ankle joint tracking error for for coupled dummy-LLES$v1$ system with RLQR-NF and NF-CPID control

The control evolution (U_e) for hip, knee, ankle joint actuator during desired gait tracking exercise is shown in Figure 3.22(a), 3.22(b), and 3.22(c). The RMSV for RLQR-NF control scheme are estimated as 15.31 V (hip), 1.11 V (knee), and 0.09 V (ankle). On the other hand, the respective values of control signals for NF-CPID scheme are found to be 4.54 V, 0.55 V, and 0.05 V. Although it is evident from the results that the proposed control strategy (NF-CPID) outperforms the contrast control strategy (RLQR-NF) to track the desired gait trajectory; however, both the control schemes show significant chattering. Therefore, a chattering index $\left(CI = \frac{1}{\sqrt{T}}\left[\sum_{i=1}^{i=T}(\dot{U}_e)^2\right]^{1/2}, \quad T = \text{gait cycle/sampling time}\right)$ is used further to quantify the chattering behavior in the control signals. The chattering is found to be less for proposed NF-CPID control (CI_{hip} : 2.35×10^3, CI_{knee} : 592.64,

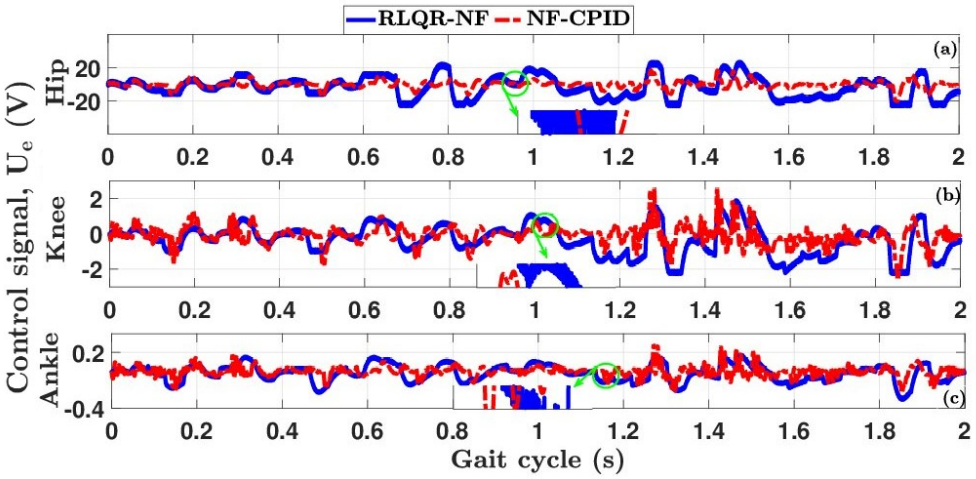

FIGURE 3.22: (a) Hip, (b) knee, and (c) ankle joint control evolution for coupled dummy-LLES$v1$ system with RLQR-NF and NF-CPID control

and CI_{ankle} : 75.25) compared to the contrast LQR-NF control scheme (CI_{hip} : 2.88×10^4, CI_{knee} : 1.08×10^3, and CI_{ankle} : 101.51). Moreover, due to heuristic tuning of neuro-fuzzy hyperparameters, the computational complexity to execute and build the code in MATLAB/Simulink-Arduino interface increases.

3.5 Summary

This chapter proposes two intelligent gait tracking controllers in passive-assist mode, i.e., RLQR-NF to dealt the parametric perturbations and NF-CPID for the parametric perturbations and external disturbances (PPED). In case of RLQR-NF control, an input-output linearization approach has been employed to transform the non-linear model to linear one before applying LQR control. A robust NF dataset is formed by varying the coupled system's masses by 20% and 30% in two different cases. The performance of the proposed control is found better by 70.1%, 45.9%, and 26.5% while perturbing the system's masses by 20% and compared to the ERL-SMC contrast control. The performance is degraded by 4.6%, 1.4%, and 3% when perturbing the system masses from 20% to 30%. On the other hand, in case of NF-CPID control, an offline-online training approach is used to dealt external disturbances along with the parametric perturbations. The initialization of NF weights and hyperparameters are decided using the offline identification of inverse model based on PID control signals. Thereafter, the adaptive law of neural-fuzzy weights are exploited to compensate the effect of lumped PPED in NF-CPID model. It is observed from simulation runs that NF-CPID control performs less

effectively in case of PP only as compared to contrast control (RLQR-NF), especially in swing phase of the gait cycle. However, in case of PPED, a significant improvement is noted for the NF-CPID control. Based on the experiment carried out with a child dummy and LLES$v1$, the proposed NF-CPID is found effective by 71.8%, 59.5%, and 32.15% for the gait tracking in passive-assist mode. Although less than the contrast control, a considerable noise has been observed in the experimental results with NF-CPID control. Moreover, the computational complexity arises due to the iterative tuning and selection of neural-fuzzy hyperparameters. Therefore, in next chapter, a robust gait tracking control based on backstepping approach is presented to deal uncertain scenarios with lesser complexities.

Chapter 4

Robust Adaptive Backstepping Control for Passive-Assist Gait Tracking of the Pediatric Exoskeleton

4.1 Introduction

Due to the challenge of selecting neural-fuzzy hyperparameters, a robust adaptive backstepping control scheme is proposed in this chapter to address the PPED. In general, most control designs suffer from the difficulty of selecting an appropriate Lyapunov function, which is fundamentally based on heuristic methods. Furthermore, in the case of pediatric rehabilitation, PPED become more significant due to substantial variation of dynamic parameters (system mass and length) and body reflexes (unintended subject response). Therefore, to address these benchmark problems, a robust adaptive backstepping control is proposed in this chapter which involves a systematic design approach to construct the Lyapunov candidate function for nonlinear parametric strict-feedback form of coupled subject-exoskeleton system. At first, the dynamic modeling is introduced with frictional and external disturbances in Section 4.2. The complete design process and stability analysis of RABS control, presented in Section 4.3, does not require linear input-output dynamics compared to most other control approaches. To the author best knowledge, the proposed control has hardly been designed and implemented for the gait exoskeleton systems to date. The proposed RABS control is implemented on

the LLES$v2$ coupled with a pediatric subject of GMFCS-Level III and results are discussed in Section 4.4. Finally, Section 4.5 summarizes the concluding remarks.

4.2 Dynamic Modeling

Introducing the frictional interference and external disturbances, the relation of the subject-exoskeleton robot in Equation 2.11 can be represented as follows.

$$\tau_{j,e} + \tau_d = \mathcal{M}_{h,e}(q_{j,e})\ddot{q}_{j,e} + \mathcal{C}_{h,e}(q_{j,e}, \dot{q}_{j,e})\dot{q}_{j,e} + \mathcal{G}_{h,e}(q_{j,e}) + \mathcal{F}(\dot{q}_{j,e}) \tag{4.1}$$

Here, $\tau_d \in \mathbb{R}^3$ is the disturbance vector and $\mathcal{F}(\dot{q}_{j,e}) \in \mathbb{R}^3$ denotes the friction model as presented in Equation 3.36. The dynamic model, presented in Equation 4.1, holds the following two properties (P1 and P2) and an assumption (A) [204].

(P1) $\mathcal{M}_{h,e}(q_{j,e})$ poses symmetric as well as positive definite behavior in the matrix form and holds the following relation

$$\tilde{a}_1\|\varsigma\|^2 \leq \varsigma^T\mathcal{M}_{h,e}(q_{j,e})\varsigma \leq \tilde{a}_2\|\varsigma\|^2 \quad \forall\varsigma \in \mathbb{R}^3 \tag{4.2}$$

where, $\tilde{a}_1$ and $\tilde{a}_2$ are positive constants.

(P2) $\dot{\mathcal{M}}_{h,e}(q_{j,e}) - 2\mathcal{C}_{h,e}(q_{j,e}, \dot{q}_{j,e})$ holds a behavior of skew-symmetric matrix when $\forall\varrho \in \mathbb{R}^3$

$$\varrho^T(\dot{\mathcal{M}}_{h,e_{h,e}}(q_{j,e}) - 2\mathcal{C}_{h,e}(q_{j,e}, \dot{q}_{j,e}))\varrho = 0 \tag{4.3}$$

(A) The external disturbances are bounded in such a way to confirm the following condition:

$$||\tau_d|| \leq \bar{\tau}_d \tag{4.4}$$

where, $\bar{\tau}_d$ denotes a positive constant.

4.3 Adaptive Backstepping Control Design

In this section, the concept of adaptive backstepping [168] is exploited to design the robust structure of trajectory tracking control for the lower limb exoskeleton system during passive-assist rehabilitation. The proposed design is dedicated to

controlling the human gait using the exoskeleton system, with dynamic uncertainties and subject response-based external disturbances. The dynamic model of a simplified 3-joint lower limb robotic exoskeleton in parametric-based strict-feedback representation can be expressed below.

$$r_1 = q_{j,e}, r_2 = \dot{q}_{j,e}, r = [r_1, r_2]^T \tag{4.5}$$

$$\begin{cases} \dot{r}_1 & = r_2 \\ \dot{r}_2 & = \mathcal{M}_{h,e}^{-1}(q_{j,e})\big(\tau_{j,e} + \tau_d - \mathcal{C}_{h,e}(q_{j,e}, \dot{q}_{j,e})\dot{q}_{j,e} - \mathcal{G}_{h,e}(q_{j,e}) - \mathcal{F}(\dot{q}_{j,e})\big) \end{cases} \tag{4.6}$$

where $r_1 \in \mathbb{R}^3, r_2 \in \mathbb{R}^3$ are the state vectors of the exoskeleton robot.

The gait tracking error variables can be selected as

$$\xi_1 = q_{j,e} - q_{j,h} \tag{4.7}$$

$$\xi_2 = \dot{\xi}_1 - \zeta = r_2 - \dot{q}_{j,h} - \zeta \tag{4.8}$$

where, ζ denotes the virtual control law to be selected in backstepping approach for stabilizing the dynamical system.

The objective is to guarantee the tracking of the desired angular trajectory $q_{j,h}$ by the actual angular vector $q_{j,e}$ in the presence of unknown dynamics and external disturbances. Therefore, the following stepwise process can be employed for the design of RABS control.

Step 1:

The derivative of the first error variable ξ_1 could be explained in terms of the second error ξ_2 and virtual control parameter ζ, as follows:

$$\dot{\xi}_1 = \dot{r}_1 - \dot{q}_{j,h} = r_2 - \dot{q}_{j,h} = \xi_2 + \zeta \tag{4.9}$$

The virtual control law ζ is supposed to be chosen to stabilize the first error of the subsystem in Equation 4.9. Consequently, the Lyapunov function candidate can be selected as:

$$V_1 = \frac{1}{2}({\xi_1}^T \xi_2) \tag{4.10}$$

Substituting the Equation 4.9 after differentiation of the Equation 4.10, the derivative of the Lyapunov function can be obtained as:

$$\dot{V}_1 = \xi_1^T \dot{\xi}_1 = \xi_1^T \xi_2 + \xi_1^T \zeta \tag{4.11}$$

The virtual control law ξ can be defined as:

$$\zeta = -\epsilon_1 \xi_1 = -\epsilon_1 r_1 + \epsilon_1 q_{j,h} \tag{4.12}$$

where, ϵ_1 is characterized by a diagonal matrix of positive value.

Now, from Equations 4.11 and 4.12,

$$\dot{V}_1 = -\xi_1^T \epsilon_1 \xi_1 + \xi_1^T \xi_2 \tag{4.13}$$

From 4.13, it is evident that $\dot{V}_1$ is negative definite for $\xi_2 = 0$ and therefore, the first error variable ξ_1 is ensured to be converging.

Step 2:

The derivative of the second error variable $\dot{\xi}_2$ can be described as follows:

$$\dot{\xi}_2 = \dot{r}_2 - \dot{\zeta} - \ddot{q}_{j,h} = \mathcal{M}_{h,e}^{-1}(q_{j,e})\big(\tau_{j,e} + \tau_d - \mathcal{C}_{h,e}(q_{j,e}, \dot{q}_{j,e})\dot{q}_{j,e} - \mathcal{G}_{h,e}(q_{j,e}) - \mathcal{F}(\dot{q}_{j,e})\big) - \dot{\zeta} - \ddot{q}_{j,h} \tag{4.14}$$

where

$$\dot{\zeta} = -\epsilon_1 \dot{r}_1 + \epsilon_1 \dot{q}_{j,h} = -\epsilon_1 r_2 + \epsilon_1 \dot{q}_{j,h} \tag{4.15}$$

The appropriate Lyapunov function candidate, constructed on the property (P1) from 4.2, can be selected as:

$$\bar{V}_2 = V_1 + V_2 = V_1 + \frac{1}{2}\left(\xi_2^T \mathcal{M}_{h,e}(q_{j,e})\xi_2\right) \tag{4.16}$$

The derivative of the Lyapunov function defined in 4.16 can be evaluated as:

$$\dot{\bar{V}}_2 = \dot{V}_1 + \xi_2^T \mathcal{M}_{h,e}(q_{j,e})\dot{\xi}_2 + \frac{1}{2}\xi_2^T \dot{\mathcal{M}}_{h,e}(q_{j,e})\xi_2 \tag{4.17}$$

Furthermore, exploiting the property (P2) from Equation 4.3, the second Lyapunov function holds the derivative form as below:

$$\dot{\bar{V}}_2 = \dot{V}_1 + \xi_2^T \left(\mathcal{M}_{h,e}(q_{j,e})\dot{\xi}_2 + \mathcal{C}_{h,e}(q_{j,e}, \dot{q_{j,e}})\xi_2\right) \tag{4.18}$$

Based on 5.13 and 4.14, the expression $\mathcal{M}_{h,e}(q_{j,e})\dot{\xi}_2 + \mathcal{C}_{h,e}(q_{j,e}, \dot{q_{j,e}})\xi_2$ in above equation can be represented as:

$$\begin{aligned}\mathcal{M}_{h,e}(q_{j,e})\dot{\xi}_2 + \mathcal{C}_{h,e}(q_{j,e}, \dot{q}_{j,e})\xi_2 =& \mathcal{M}_{h,e}(q_{j,e})\left(\dot{r}_2 - \dot{\zeta} - \ddot{q}_{j,h}\right) \\ &+ \mathcal{C}_{h,e}(q_{j,e}, \dot{q}_{j,e})\left(r_2 - \zeta - \dot{q}_{j,h}\right) \\ =& \mathcal{M}_{h,e}(q_{j,e})\left(-\dot{\zeta} - \ddot{q}_{j,h}\right) \\ &+ \mathcal{C}_{h,e}(q_{j,e}, \dot{q}_{j,e})\left(-\zeta - \dot{q}_{j,h}\right) + \tau_{j,e} + \tau_d \\ &- \mathcal{G}_{h,e}(q_{j,e}) - \mathcal{F}(\dot{q}_{j,e})\end{aligned} \tag{4.19}$$

However, the dynamic parameters in the realistic model of the lower limb exoskeleton system are not precisely known, and the matrices in Equation 4.19 cannot be applied in the design of the control strategy. Therefore, the direct adaptation law is practiced to estimate the unknown dynamic parameters. The right-hand side of the Equation 4.19, representing the unknown model parameters, can be rearranged as follows:

$$\begin{aligned}\mathcal{M}_{h,e}(q_{j,e})\left(-\dot{\zeta} - \ddot{q}_{j,h}\right) + \mathcal{C}_{h,e}(q_{j,e}, \dot{q}_{j,e})\left(-\zeta - \dot{q}_{j,h}\right) + \tau_{j,e} + \tau_d - \mathcal{G}_{h,e}(q_{j,e}) - \mathcal{F}(\dot{q}_{j,e}) \\ = \Phi\Omega + \tau_{j,e} + \tau_d - \mathcal{F}(\dot{q}_{j,e})\end{aligned} \tag{4.20}$$

Thereafter, Equation 4.18 can be rewritten as:

$$\dot{\bar{V}}_2 = \dot{V}_1 + \xi_2^T\left(\Phi\Omega + \tau_{j,e} + \tau_d - \mathcal{F}(\dot{q}_{j,e})\right) \tag{4.21}$$

where $\Phi \in \mathbb{R}^{3\times 16}$ refers to a regression matrix derived from the sensor-based feedback and $\Omega \in \mathbb{R}^{16\times 1}$ denotes unknown nonlinear parameters. The element wise regression matrix and vector of unknown nonlinear parameters are presented in Appendix C. As per the earlier discussion, the Lyapunov function from Equation 4.16 can be revised as given below:

$$V = \bar{V}_2 + \frac{1}{2}\widetilde{\Omega}\sqcap^{-1}\widetilde{\Omega}; \quad \widetilde{\Omega} = \Omega - \hat{\Omega} \tag{4.22}$$

where estimation of the unknown parameters in matrix form is indicated by $\widetilde{\Omega}$ and $\sqcap$ denotes an arbitrary selected positive definite matrix. Now, one may get the following expression after differentiating Equation 4.22,

$$\dot{V} = \dot{\bar{V}}_2 - \widetilde{\Omega}^T\sqcap^{-1}\dot{\hat{\Omega}} = \dot{V}_1 + \xi_2^T\left(\Phi\Omega + \tau_{j,e} + \tau_d - \mathcal{F}(\dot{q}_{j,e})\right) - \widetilde{\Omega}^T\sqcap^{-1}\dot{\hat{\Omega}} \tag{4.23}$$

By performing addition and subtraction of the term $\xi_2^T \Phi\hat{\Omega}$ to the right-hand side of Equation 4.23,

$$\dot{V} = \dot{V}_1 + \xi_2^T \Phi\hat{\Omega} + \xi_2^T \Phi\tilde{\Omega} + \xi_2^T \left(\tau_{j,e} + \tau_d - \mathcal{F}(\dot{q}_{j,e})\right) - \widetilde{\Omega}^T \sqcap^{-1} \dot{\hat{\Omega}} \tag{4.24}$$

With the transpose of $\xi_2^T \Phi\tilde{\Omega}$, Equation 4.24 can be rewritten as:

$$\dot{V} = \dot{V}_1 + \xi_2^T \Phi\hat{\Omega} + \xi_2^T \left(\tau_{j,e} + \tau_d - \mathcal{F}(\dot{q}_{j,e})\right) + \widetilde{\Omega}^T \left(\Phi^T \xi_2 - \sqcap^{-1}\dot{\hat{\Omega}}\right) \tag{4.25}$$

Now by selecting $\dot{\hat{\Omega}}$ as

$$\dot{\hat{\Omega}} = \sqcap \Phi^T \xi_2 \tag{4.26}$$

After incorporating Equation 4.26 and Equation 4.13 into Equation 4.25, the derivative of the Lyapunov function can be modified as:

$$\begin{aligned} \dot{V} &= \dot{V}_1 + {\xi_2}^T \Phi\hat{\Omega} + {\xi_2}^T \left(\tau_{j,e} + \tau_d - \mathcal{F}(\dot{q}_{j,e})\right) \\ &= -\xi_1^T \epsilon_1 \xi_1 + \xi_1^T \xi_2 + \xi_2^T \Phi\hat{\Omega} + \xi_2^T \tau_{j,e} + \xi_2^T \tau_d - \xi_2^T \mathcal{F}(\dot{q}_{j,e}) \end{aligned} \tag{4.27}$$

Considering Assumption (A) (4.4) and employing the Young inequality, the last term on the right-hand side of the Equation 4.27 can be articulated as below:

$$\begin{aligned} \xi_2^T \tau_d &\leq \frac{1}{2}\xi_2^T \xi_2 + \frac{1}{2}\tau_d^T \tau_d \\ &\leq \frac{1}{2}\xi_2^T \xi_2 + \frac{1}{2}\bar{\tau}_d^2 \end{aligned} \tag{4.28}$$

Thereafter, the derivative of the Lyapunov function fulfills the inequality equation as follows:

$$\dot{V} = -\xi_1^T \epsilon_1 \xi_1 + \xi_1^T \xi_2 + \xi_2^T \Phi\hat{\Omega} + \xi_2^T \tau_{j,e} - \xi_2^T \mathcal{F}(\dot{q}_{j,e}) + \frac{1}{2}\xi_2^T \xi_2 + \frac{1}{2}\bar{\tau}_d^2 \tag{4.29}$$

The trajectory tracking control law can be designed as:

$$\tau_{j,e} = -\epsilon_2 \xi_2 - \xi_1 - \Phi\hat{\Omega} - \frac{1}{2}\xi_2 + \mathcal{F}(\dot{q}_{j,e}) \tag{4.30}$$

where, ϵ_2 denotes another diagonal matrix of positive value. Furthermore, after placing the position control law from 4.30 to 4.29, the derivative of the Lyapunov function can be reworked as:

$$\dot{V} \leq -\xi_1^T \epsilon_1 \xi_1 - \xi_2^T \epsilon_2 \xi_2 + \frac{1}{2}\bar{\tau}_d^2 \tag{4.31}$$

It is evident from Equation 4.31 the derivative of the Lyapunov function can be expressed in the following form of inequality,

$$\dot{V} \leq -\mho V + \rho_d \tag{4.32}$$

where,

$$\mho = \min\left(2\lambda_{\min}(\epsilon_1), \frac{2\lambda_{\min}(\epsilon_2)}{\lambda_{\max}(\mathcal{M}_{h,e}(q_{j,e}))}\right) \text{ and } \quad \rho_d = \frac{1}{2}\bar{\tau}_d{}^2 \tag{4.33}$$

where ρ_d belongs to a class of κ functions and $\lambda_{min}(.), \lambda_{max}(.)$ are the minimum and maximum eigenvalues of $(.)$, respectively.

Multiplying both sides of Equation 4.32 by an exponent term $e^{\mho t}$, and integrating over $t = [0, t]$ yields the following equation:

$$0 \leq V \leq \left(V(0) - \frac{\rho_d}{\mho}\right) e^{-\mho t} + \frac{\rho_d}{\mho} \tag{4.34}$$

By defining $\widehat{V} = \max\left\{V(0), \frac{\rho_d}{\mho}\right\}$, the following inequalities scan be obtained:

$$\|\xi_1\| \leq \sqrt{2\widehat{V}}, \text{ and } \quad \|\xi_2\| \leq \sqrt{\frac{2\widehat{V}}{\lambda_{\max}(\mathcal{M}_{h,e}(q_{j,e}))}} \tag{4.35}$$

It is observed from Equation 4.34 and Equation 4.35 that increasing the $\mho$ and decreasing ρ_d can ensure the error signals $||\xi_1||$ and $||\xi_2||$ to converge to small values. Consequently, when the controller gains ϵ_1 and ϵ_2 are increased, the tracking performance can be improved with reduced positional errors. On the other hand, increasing the adaptation gain $\sqcap$ confirms the fast convergence of the estimated parameters to the actual values. However, in a real-case scenario, the controller parameters cannot be selected as very large to avoid the noise and high frequency, which degrade the system performance.

The above set of equations confirms the characterization of input to state stability (ISS), where input is regarded as the bounded external disturbances τ_d, and the proposed control strategy eventually guarantees all the signals to be bounded [169, 216, 217]. In addition, the convergence of even small tracking errors for the coupled human-exoskeleton system can be ensured with the proper selection of control law parameters. The complete design architecture of the robust adaptive backstepping control for the lower limb exoskeleton system is shown in Figure 4.1. In the closed-loop control, the actual signals from the dynamics can be recorded by using feedback sensors.

In the parametric strict feedback system, the 'overparameterization' problem persists due to the number of parameters' estimates greater than the number of unknown parameters. The reason behind this condition is the presence of unknown parameter estimates in each design step of the adaptive backstepping. However, in the present work, the first design step is free from any unknown parameters estimation and generically postponed to the last design step; therefore, avoiding the 'overparameterization' phenomena (refer to Step 2). Furthermore, the 'explosion of terms' is another well-known complexity that appears from the presence of inertial, centrifugal, and gravity matrices while differentiating the virtual control. However, the proposed design in this work avoids this complexity due to the non-existence of such dynamical matrices (refer to Equation 4.15).

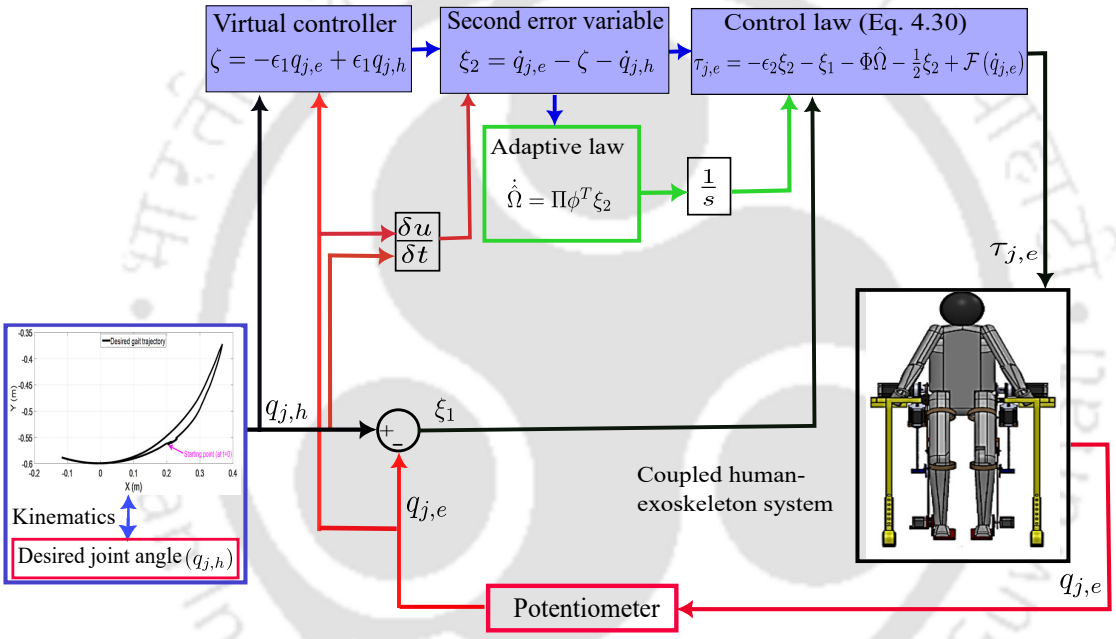

FIGURE 4.1: RABS Control Architecture

4.4 Results and Discussions

In this section, the simulation and experimental results regarding the performance of the robust adaptive backstepping control are discussed for the pediatric exoskeleton system. The considered exoskeleton is LLES$v2$ and subject is of age 12 years (male), body mass 40 kg, body height 132 cm. The desired joint angles with the subject's gait trajectory are estimated using a wireless Kinect-LabView motion capture setup. The effectiveness of the designed control strategy is validated with

the previously designed NF-CPID control as a contrast control scheme. The simulation and experimental runs in this chapter are carried out in MATLAB/Simulink R2020b (ode45 solver with variable step and non-adaptive zero crossing algorithm).

4.4.1 Simulation Results

The proposed control strategy is exploited to track the desired gait trajectory during passive-assist gait rehabilitation in the presence of model uncertainties and external disturbances. In order to validate the robustness of the proposed RABS control, the parametric perturbations are considered by increasing the lower-limb masses of the coupled pediatric-exoskeleton as $30\%, 20\%$, and 10% ($m'_{1h,e} = m_{1h,e} + 0.3m_{1h,e}, m'_{2h,e} = m_{2h,e} + 0.2m_{2h,e}, m'_{3h,e} = m_{3h,e} + 0.1m_{3h,e}$) respectively. Moreover, external disturbances are added as $\tau_{d1} = 6\sin(4\pi t), \tau_{d2} = 5\sin(3\pi t), \tau_{d3} = 3\sin(2\pi t)$. The Coulomb friction, and viscous velocity factor are selected as $C_f = [0.8, 0.8, 0.8]^T, \sigma_v = [1.2, 1.2, 1.2]^T$. As the exoskeleton setup changes from LLES$v1$ to LLES$v2$, the proportional, integral, and derivative gain values in NF-CPID control are $K_p = 180, K_i = 7, K_d = 32$ for hip joint, $K_p = 179, K_i = 4, K_d = 41$ for knee joint and $K_p = 152, K_i = 4, K_d = 23$ for ankle joint. The centre distance parameter matrix is selected as $c_j = (-5, -4, -3, -2, -1, 0, 1, 2, 3, 4, 5)_{9\times11}$ and curve width for the Gaussian function is taken as $\sigma_{wj} = 4$. The positive constant in adaptive law is selected as $\kappa_p = 17$. After performing numerical iterations, the RABS control law parameters are selected as $\epsilon_1 = \text{diag}(175), \epsilon_2 = \text{diag}(70)$, and $\sqcap = \text{diag}(0.06)$.

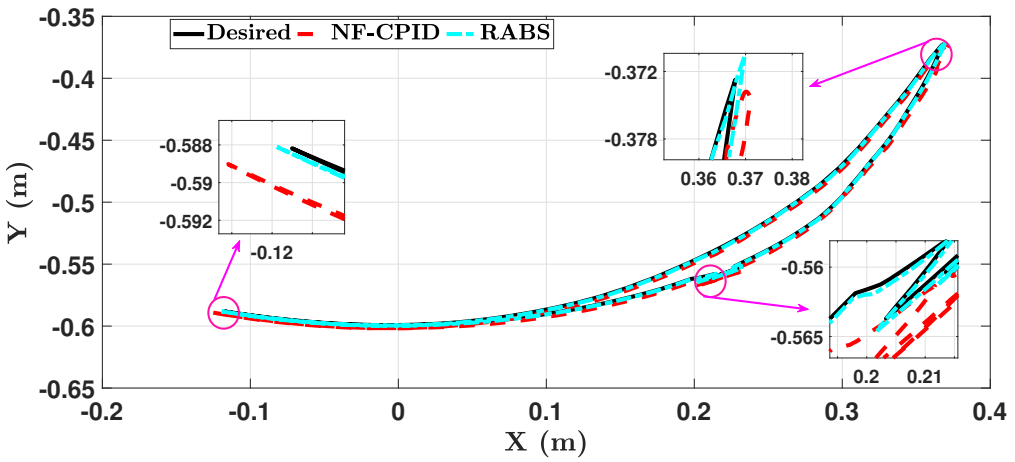

FIGURE 4.2: Cartesian gait tracking for perturbed mass values and periodic disturbances with RABS and NF-CIPD control

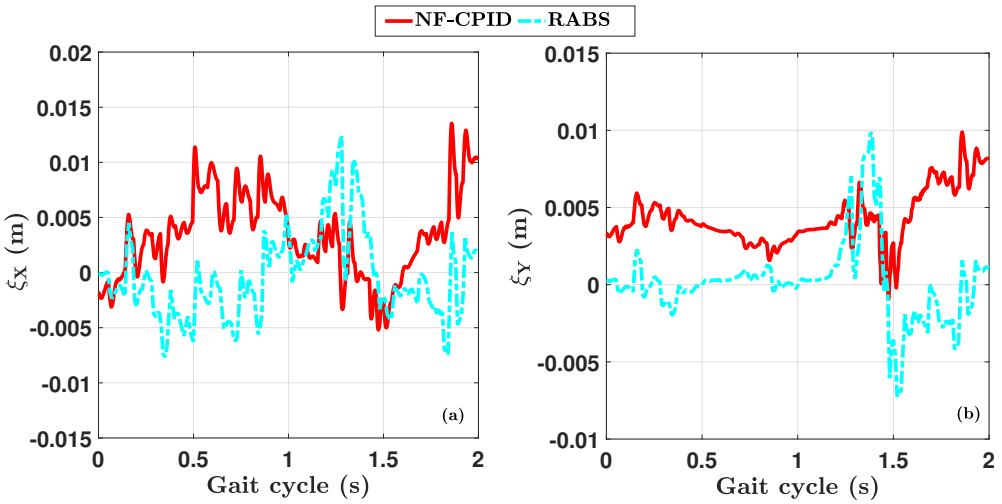

FIGURE 4.3: Gait tracking error in (a) X-direction and (b) Y-direction for perturbed mass values and external disturbances with RABS and NF-CIPD control

By incorporating control law parameters in the robust adaptive backstepping control with dynamic uncertainties, the trajectory tracking of the desired gait is presented in Figure 4.2. The black line represents the desired trajectory starting with (X: 0.23m, Y : −0.56m). The actual trajectories after applying the proposed control (RABS) and contrast control (NF-CPID) are shown by the dotted cyan line and the red line, respectively. Three zoomed-in view are shown to demonstrate the effectiveness of the proposed control while tracking the desired gait trajectory. The position error in X- and Y-direction (ξ_X and ξ_Y) is shown in Figures 4.3(a) and 4.3(b). The proposed RABS control outperforms the contrast one in both directions. The maximum absolute deviation in X-direction ($|\xi_X|$) is 0.012 m and 0.014 m for RABS control and for NF-CPID control, respectively. In Y-direction, although the maximum absolute deviation ($|\xi_Y|$) is quite similar, the deviation for the contrast control is found to be higher from the beginning of the gait cycle which ensures the lower performance of the contrast control as compared to the proposed one.

4.4.2 Experimental Results

In this section, experimental results are discussed for the coupled subject-exoskeleton system, where LLES$v2$ is considered along with the pediatric subject of age 12 years, body mass 40 kg, body height 132 cm (C12 from Table 2.7). The subject has post-effects of paraplegic CP with with no sign of pain and discomfort, and

having FMA ordinal score 1. As per the hospital, the subject's record was maintained under the GMFCS-III with flexion deformities of 1.75° hip, 7.92° knee, and 0.95° of the ankles. Although the subject can walk short distances without any assistance; however, can not apply significant force from his side which is beneficial for the control experiments in the passive-assist mode. The real-time control architecture for the coupled subject-exoskeleton system is shown in Figure 4.4. Although the hardware configuration and feedback units (multiturn potentiometers) are modified for the subject-LLES$v2$, the working principle is similar to the coupled dummy-LLES$v1$ as mentioned in Section 2.4 of the Chapter 2.

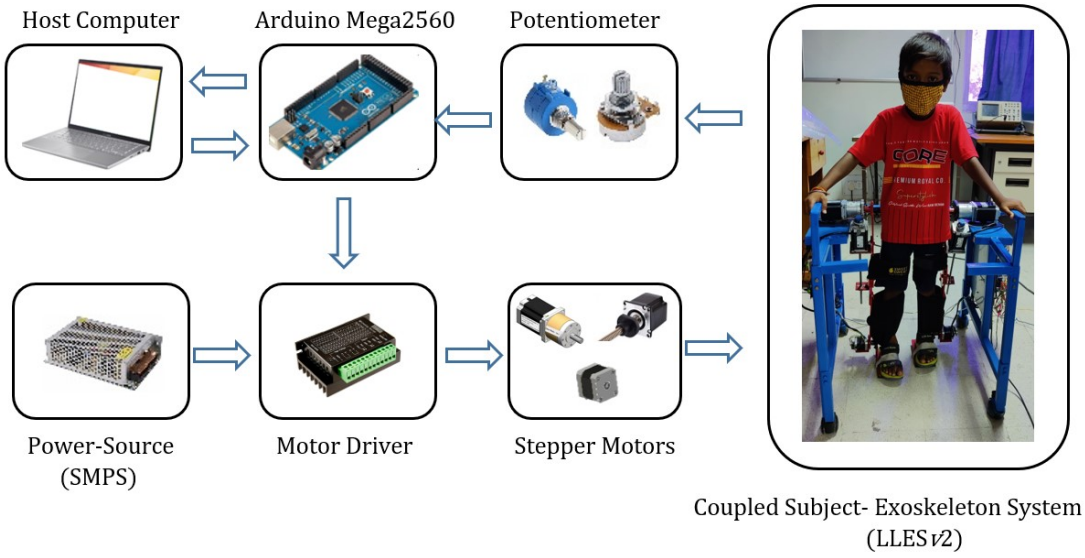

FIGURE 4.4: Real-time control architecture of LLES$v2$ with a pediatric subject (GMFCS-Level III)

After applying the proposed (RABS) and contrast (NF-CPID) control in real-time, the tracking of the desired gait trajectory by the coupled system is shown in Figure 4.6. The proportional, integral, and derivative gain values in NF-CPID control are $K_p = 0.61, K_i = 0.0007, K_d = 0.02$ for hip joint, $K_p = 0.43, K_i = 0.0006, K_d = 0.03$ for knee joint and $K_p = 0.12, K_i = 0.01, K_d = 0.02$ for ankle joint. The centre distance parameter matrix is selected as $c_j = (-5, -4, -3, -2, -1, 0, 1, 2, 3, 4, 5)_{9\times 11}$ and curve width for the Gaussian function is taken as $\sigma_{wj} = 4$. The positive constant in adaptive law is selected as $\kappa_p = 1.5$. After performing numerical iterations, the RABS control law parameters are selected as $\epsilon_1 = \text{diag}(1.55), \epsilon_2 = \text{diag}(0.9)$, and $\sqcap = \text{diag}(0.004)$. Three zoomed-in view are shown to demonstrate the effectiveness of the proposed control while tracking the desired gait trajectory. Moreover, as shown in Figure 4.5, the functional characterization of the coupled system is carried out where the real-time movements of foot trajectory is recorded at different phases of a gait cycle.

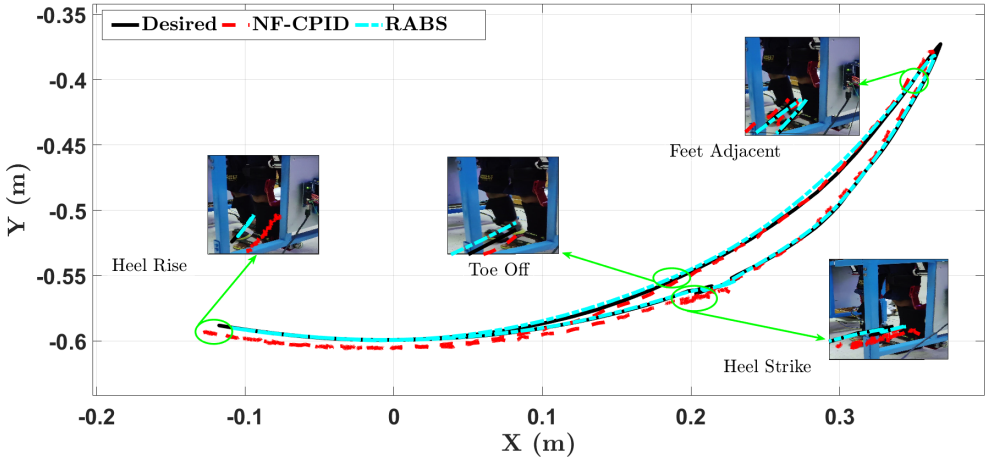

FIGURE 4.5: Functional characterization of the coupled system while tracking Cartesian gait tracking with RABS and NF-CIPD control

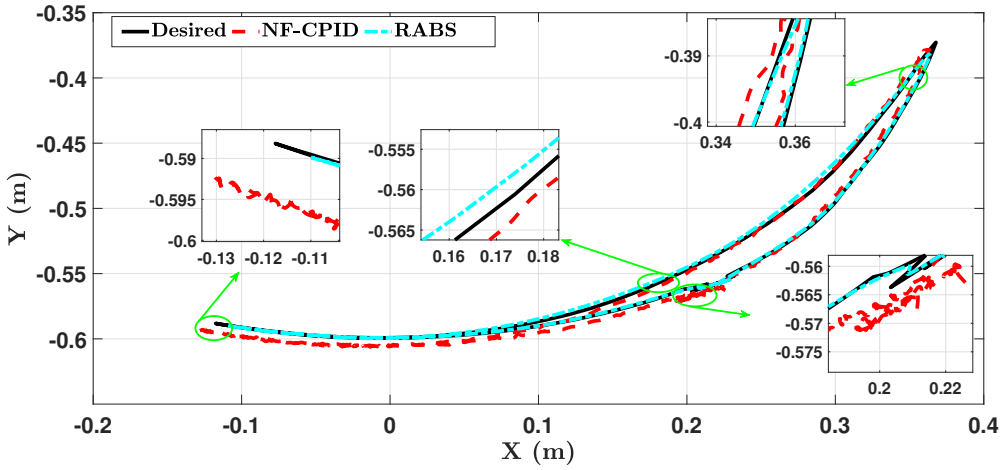

FIGURE 4.6: Cartesian gait tracking for subject-LLES$v2$ with RABS and NF-CIPD control

It can be observed from Figure 4.5 and 4.6, the proposed control outperforms the contrast control for tracking the desired gait trajectory. Moreover, from the Cartesian error in X- and Y-direction shown in Figure 4.7(a) and Figure 4.7(b), it is found that there is a significant difference between the performance of RABS control and NF-CPID control throughout the gait cycle except at the initial swing phase. The maximum absolute error in X-direction ($|\xi_X|$) is 0.007 m and 0.015 m for RABS control and for NF-CPID control, respectively. In Y-direction, the respective deviation ($|\xi_Y|$) is 0.004 m and 0.006 m for RABS control and for NF-CPID control. It is pertinent to mention that the experimental results for the contrast control are quantitatively similar to the simulation results; however, the noise increases for the former one. On the other hand, the the performance of

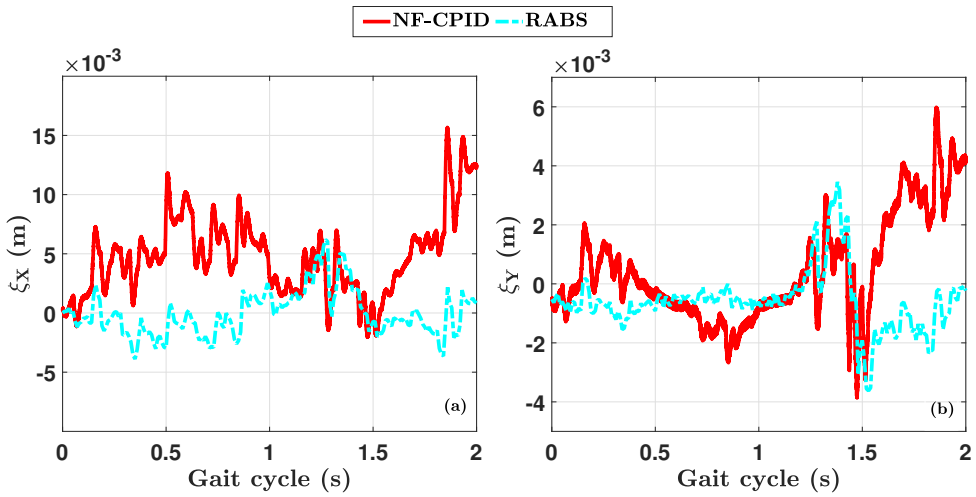

FIGURE 4.7: Gait tracking error in (a) X-direction and (b) Y-direction for subject-LLES$v2$ with RABS and NF-CIPD control

RABS control is improved in experimental results as compared to the simulation ones which ensures less uncertainties and disturbances in the real-time coupled system.

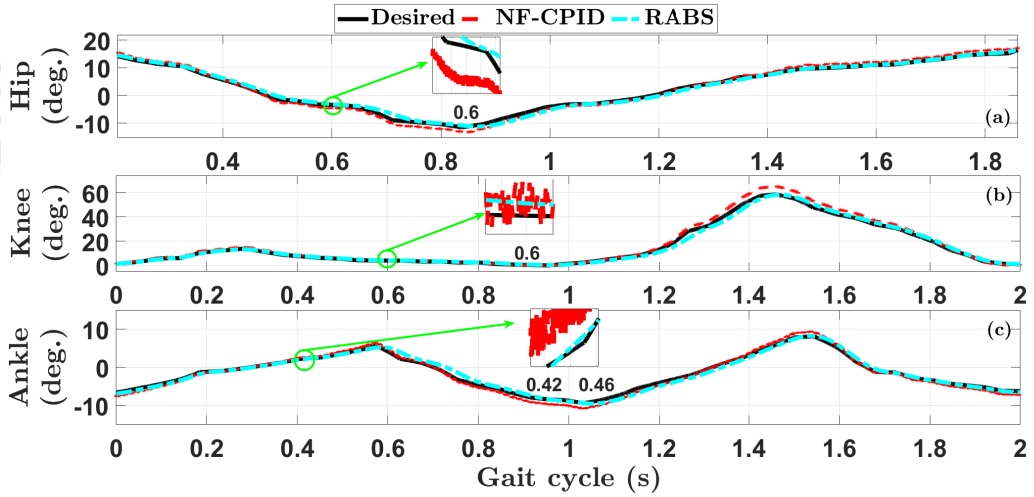

FIGURE 4.8: (a) Hip, (b) knee, and (c) ankle joint tracking for subject-LLES$v2$ with RABS and NF-CIPD control

Moving further, the tracking of desired joint angles of the lower limb is shown in Figures 4.8(a), 4.8(b), and 4.8(c). A zoom-in view is illustrated for each joint to visualize the difference between performance of both the controllers. Figure 4.9(a), 4.9(b), and 4.9(c) represents the error (ξ_1) between desired and actual joint trajectory. In case of hip joint, the RMSE for NF-CPID and RABS control scheme is 0.79° and 0.353°. For knee joint, the respective RMSE is 2.471° and 1.468°. The respective RMSE for the ankle joint is 0.951° and 0.334°. The PI is

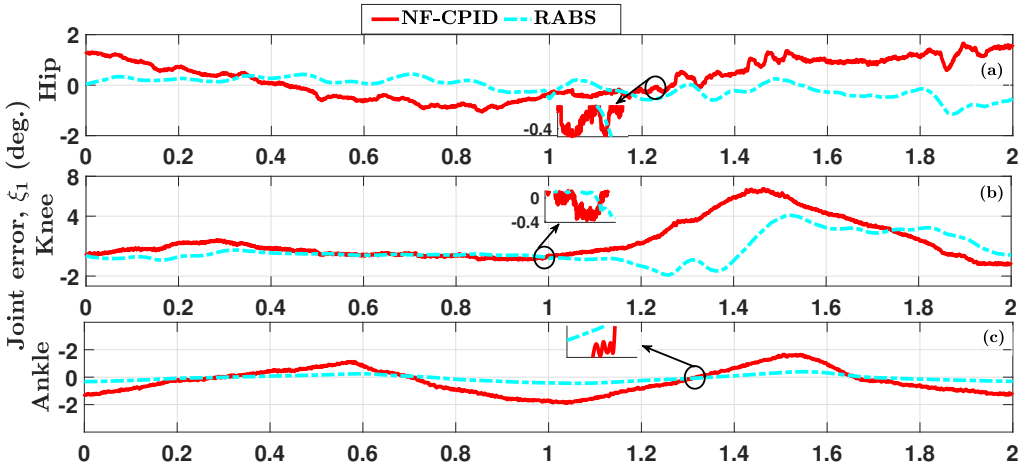

FIGURE 4.9: (a) Hip, (b) knee, and (c) ankle joint tracking error for subject-LLES$v2$ with RABS and NF-CIPD control

evaluated as 55.32%, 40.59%, 64.88% for hip, knee, and ankle joint which shows the potential of proposed control for the passive-assist gait tracking by the coupled subject-exoskeleton system.

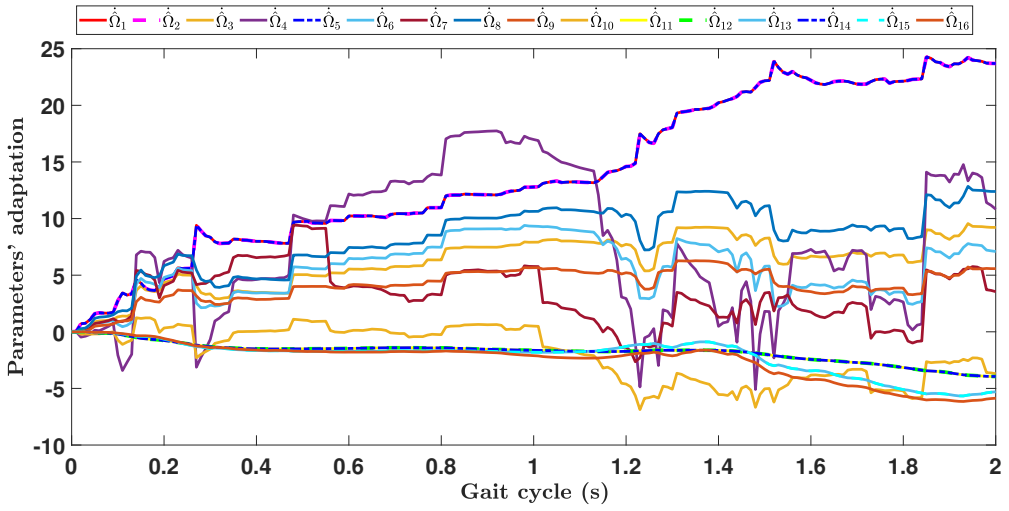

FIGURE 4.10: Parameter adaptation of Ω for subject-LLES$v2$ with RABS

Following the adaptation law (Eq. 4.26), the estimation of the unknown parameters for the coupled exoskeleton system with proposed RABS control is shown in Figure 4.10. Although, the estimated parameters are bounded and converged to preserve the stability of the closed-loop process with promising gait tracking performance; however, confluence of these parameters to their true values is not compulsorily possible. Furthermore, it can be noted from the results of both cases that estimation of $1^{st}, 2^{nd}$, and 5^{th} parameters $(\dot{\hat{\Omega}}_1, \dot{\hat{\Omega}}_2, \dot{\hat{\Omega}}_5)$ follow same adaptation over the gait cycle. Likewise, the $11^{th}, 12^{th}$, and 14^{th} parameters $(\dot{\hat{\Omega}}_{11}, \dot{\hat{\Omega}}_{12}, \dot{\hat{\Omega}}_{14})$ are

estimated with same adaptation values. Moreover, the 13^{th} estimated parameter ($\dot{\hat{\Omega}}_{13}$) converge with the same values as of 15^{th} parameter ($\dot{\hat{\Omega}}_{15}$). These observations show that the number of parameter estimates ($n_{\dot{\hat{\Omega}}} = 11$) are less than the number of unknown parameters ($n_{\Omega} = 16$) which further supports the avoidance 'overparameterization' phenomena.

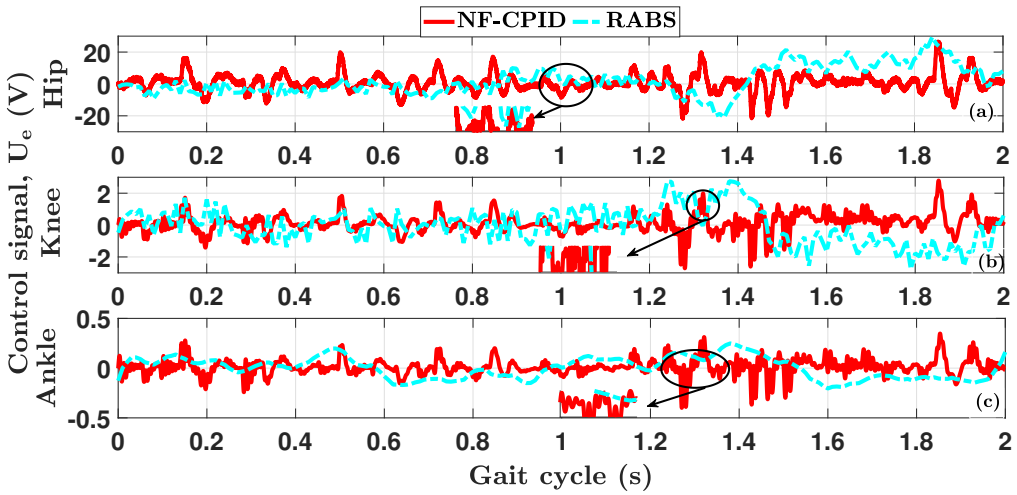

FIGURE 4.11: (a) Hip, (b) knee, and (c) ankle joint torque for coupled subject-LLES$v2$ system with NF-CPID and RABS

While tracking the desired gait trajectory during passive-assist gait rehabilitation, the control evolution (U_e) for both the controllers shown in Figure 4.11(a), 4.11(b), and 4.11(c). In case of contrast NF-CPID control, the RMSV for hip, knee, and ankle joints are generated as 5.65 V, 0.59 V, and 0.08 V. On the other hand, the respective control voltage for the proposed RABS control are computed as 8.25V, 0.94 V, and 0.13 V which is marginally higher than the contrast control. It can be observed that proposed RABS scheme requires higher control signals to track the desired trajectory in swing phase as compared to stance phase. However, the chattering index is found to be significantly lower for proposed RABS control (CI_{hip} : 1350.98, CI_{knee} : 172.74, and CI_{ankle} : 82.45) compared to the contrast NF-CPID control scheme (CI_{hip} : 2750, CI_{knee} : 667.64, and CI_{ankle} : 11.23) during PA gait tracking by coupled system.

The implication of the proposed control can be effectively appreciated in the case of post-stroke subjects with pathological gait. The potential end-users of the control-aided rehabilitation experiment could be the pediatric subjects, the age range of 8-12 years (25-40kg and 115-125cm), suffering from paraplegic gait post-CP with no sign of pain and discomfort (GMFCS-Level III and FMA ordinal scale 1). Based on the disparity between joint angles with and without exoskeletons

and the subject's feedback, the tuning of the designed controller can be carried out for the end-users.

4.5 Summary

This chapter presented a robust adaptive backstepping control for the pediatric gait exoskeleton system. The dynamic modeling of a coupled human-exoskeleton system is presented for passive-assist gait rehabilitation of pediatric subjects. The proposed control scheme is designed with a virtual adaptation law to dealt PPED. The Lyapunov theory is formulated to ensure the system's stability during walking. The well-known complexities of the classical backstepping control, i.e., overparameterization and explosion of terms are avoided by postponing the parameters' estimation to last design step and absence of inertial, centrifugal, and gravity derivatives in the virtual control law, respectively. The proposed RABS control has been tested with an experimental setup of LLES$v2$ coupled with a pediatric subject of GMFCS-Level III. The performance is improved by 55.32%, 40.59%, 64.88% for hip, knee, and ankle joint, respectively as compared to NF-CPID control. From the experimental results, it can be easily perceived that the proposed control strategy shows improved performance for tracking the desired trajectory during passive-assist gait rehabilitation. However, the controller in passive-assist mode is incompetent to appreciate the interaction of the subject during gait rehabilitation. Therefore, in the next chapter, a subject-cooperative control scheme is proposed to include the active participation of the subject during active-assist mode.

Chapter 5

Robust Adaptive Backstepping Sliding Mode Subject-Cooperative Control for Active-Assist Gait Tracking of the Pediatric Exoskeleton

5.1 Introduction

The passive-assist rehabilitation mode with a fixed desired trajectory neglects the subject's active participation and degrades the therapeutic performance in case of partial muscle strength. Therefore, this chapter proposes a novel subject-cooperative control (SCC) based on a variable admittance control scheme and a robust position control scheme for the pediatric lower-limb exoskeleton system. At first, the dynamic modeling of the coupled subject-exoskeleton system in active-assist mode is presented in Section 5.2 with PPED. A neural-fuzzy-based variable admittance control (VAC) is designed in Section 5.3 to incorporate a realistic subject-exoskeleton interaction and consider the active participation of the subject. Thereafter, a robust adaptive backstepping sliding mode control (ABSMC) with rapid reaching law (RRL) is presented in Section 5.4 to deal with PPED. The stability of the proposed position control is addressed using a stepwise selection of appropriate Lyapunov candidate functions. In Section 5.5, the effectiveness of the

proposed adaptive backstepping sliding mode-variable admittance control (ABSM-VAC) scheme is compared with an adaptive backstepping-fixed admittance control (AB-FAC) for two different cases. In the first case, the regular active-assist rehabilitation mode is considered, while the second case corresponds to the active-assist mode with the effect of sudden reflex. Based on the several simulation runs, the proposed cooperative controller has shown a promising tracking behavior, appropriate compliant interaction, and safety aspects for the subject in active-assist gait training. Finally, the outcomes of applying the proposed cooperative control are summarized in Section 5.6.

5.2 Dynamic modeling

In general, two major characteristics of the exoskeleton robot are the synchronization of joint movements and physical interaction with the human. In dynamic modeling of the LEER, researchers have usually addressed the problem of syncing the robot's joint movements with the human; however, they ignored the aspects of physical human-robot interaction (pHRI). In this work, the dynamic model of the coupled subject-exoskeleton is considered with the effects of pHRI. Furthermore, it is pertinent to mention that there is always an inconsistency between between the actual exoskeleton robot and its mathematical model due to parametric perturbations and external disturbances. Therefore, taking such disparities into account, the dynamic relation of the exoskeleton robot Equation (2.15) can be modified as:

$$\begin{aligned}\tau_{j,e} - \tau_{j,int} + \tau_d = &\big(\mathcal{M}_{oe}(q_{j,e}) + \delta_s \mathcal{M}_e(q_{j,e})\big)\ddot{q}_{j,e} \\ &+ \big(\mathcal{C}_{oe}(q_{j,e}, \dot{q}_{j,e}) + \delta_s \mathcal{C}_e(q_{j,e}, \dot{q}_{j,e})\big)\dot{q}_{j,e} \\ &+ \big(\mathcal{G}_{oe}(q_{j,e}) + \delta_s \mathcal{G}(q_{j,e})\big) + \mathcal{F}(\dot{q}_{j,e})\end{aligned} \tag{5.1}$$

where, $\tau_d \in \mathbb{R}^3$ is the disturbance vector; $\mathcal{M}_{oe} \in \mathbb{R}^{3\times3}$, $\mathcal{C}_{oe} \in \mathbb{R}^{3\times3}$, and $\mathcal{G}_{oe} \in \mathbb{R}^3$ is the normal value of inertia, Coriolis, gravity matrix, respectively; 'δ_s' indicates the uncertain scaling factor; and $\mathcal{F}(\dot{q}_{j,e}) \in \mathbb{R}^3$ denotes the friction model as represented in Equation 3.36.

Rearranging Equation 5.1, one can get

$$\tau_{j,e} - \tau_{j,int} + \rho = \mathcal{M}_{oe}(q_{j,e})\ddot{q}_{j,e} + \mathcal{C}_{oe}(q_{j,e}, \dot{q}_{j,e})\dot{q}_{j,e} + \mathcal{G}_{oe}(q_{j,e}) \tag{5.2}$$

with

$$\rho = \tau_d - \mathcal{F}(\dot{q}_{j,e}) - \delta_s\big(\mathcal{M}(q_{j,e})\ddot{q}_{j,e} + \mathcal{C}(q_{j,e}, \dot{q}_{j,e}) + \mathcal{G}(q_{j,e})\big) \tag{5.3}$$

where ρ denotes the lumped form of parametric uncertainties and external disturbances.

5.3 ANFIS-based Variable Admittance Control

5.3.1 Admittance control

The admittance control allows the exoskeleton robot to alter its desired trajectory based on the interaction force applied by the subject. The modified trajectory is compliant with the subject-exoskeleton interaction force, which depends upon the deviation between the original human trajectory and the actual exoskeleton trajectory. The tracking of modified reference trajectory by the exoskeleton is dealt with using a low-level controller. If the desired (original human) gait trajectory is $q_{j,h}$ and the reference (modified) gait trajectory is $q_{j,\alpha}$, then the admittance model can be designed as

$$M_a(\ddot{q}_{j,h} - \ddot{q}_{j,\alpha}) + C_a(\dot{q}_{j,h} - \dot{q}_{j,\alpha}) + K_a(q_h - q_{j,\alpha}) = \tau_{j,int} \tag{5.4}$$

$$\ddot{q}_{j,\alpha} = \ddot{q}_{j,h} - M_a^{-1}\big\{C_a(\dot{q}_{j,h} - \dot{q}_{j,\alpha}) + K_a(q_{j,h} - q_{j,\alpha}) - \tau_{j,int}\big\} \tag{5.5}$$

where M_a, C_a, K_a denotes the inertia, damping and stiffness admittance parameters. It is evident from Equation 5.4 and 5.5 that if interaction torque is negligible then $q_{j,\alpha} = q_{j,h}$ which represents the case of PA training mode. Furthermore, in real scenario where the subject's movement is significantly less due to the insufficient muscle strength, the acceleration term with inertial coefficient (M_a) could be ignored. On the other hand, the damping (C_a) and stiffness (K_a) parameters should be varying to attain the biological movement of exoskeleton robot in real-time. Therefore, in the next section, a novel adaptive neuro-fuzzy inference system (ANFIS)-based approach is proposed to vary the admittance parameters in real-time.

5.3.2 ANFIS adaptation of admittance parameters

In active-assist rehabilitation settings, the damping and stiffness parameters of the exoskeleton robot need to be altered in agreement with the interaction torques generated by the active participation of the subject. The variation in admittance parameter should be characterized by two crucial aspects, i.e., flexibility and safety of the subject. If the interaction torque increases, the damping admittance parameter should be increased to compensate for any oscillations. On the other hand, if the interaction torque rises, the stiffness parameter should be decreased at first to allow the subject to participate cooperatively. After a certain point of time, when interaction torque starts exceeding a considerable limit, the stiffness parameter must be increased to make the exoskeleton rigid for the subject's safety. The robot should adequately comply with the human limbs in all such scenarios. However, the range of damping and stiffness parameters pronounces their effect in the admittance control.

Following the above-mentioned logic, in this work, the behavior of the interaction torques, damping admittance parameters, and stiffness admittance parameters are selected as follows:

$$\acute{\tau}_{j,int} = \mathbb{m} t_g \tag{5.6}$$

$$\acute{C}_a = \mathbb{n} t_g \tag{5.7}$$

$$\acute{K}_a = \mathbb{o} {t_g}^2 + \mathbb{b} t_g + \mathbb{c} \tag{5.8}$$

where slope constant $\mathbb{m}$ depends on the upper and lower limits of the interaction torques obtained from the robust ABSM control with fixed admittance parameters; $\mathbb{m}$ depends on the heuristic selection of upper and lower bounds of C_a; $\mathbb{o}$, $\mathbb{b}$, and $\mathbb{c}$ are decided according to the heuristic selection of upper and lower bounds of K_a. The above formulations (Equations 5.6-5.8) are further used as training dataset in the neural-fuzzy architecture shown in Figure 3.1. In this work, the two input-output datasets are prepared as follows:

$$\begin{bmatrix} \acute{\tau}_{1,int} & \acute{\tau}_{2,int} & \acute{\tau}_{3,int} & \acute{C}_a \end{bmatrix} \tag{5.9}$$

$$\begin{bmatrix} \acute{\tau}_{1,int} & \acute{\tau}_{2,int} & \acute{\tau}_{3,int} & \acute{K}_a \end{bmatrix} \tag{5.10}$$

where $\acute{\tau}_{1,int}, \acute{\tau}_{2,int}$ and $\acute{\tau}_{3,int}$ denote the input vectors as hip, knee, and ankle joint interaction torque; $\acute{C}_a$ and $\acute{K}_a$ are the output vectors as damping and stiffness admittance parameters.

5.4 Robust ABSM-RRL Position Control

In this section, the concept of the sliding surface is combined with an adaptive backstepping approach to design a robust architecture of gait tracking control for the pediatric lower-extremity exoskeleton robot during active-assist training mode. At first, the sliding surface is selected based on the error states and virtual control law from the backstepping process. Thereafter, an improved power reaching law is proposed with Lyapunov stability for rapid convergence of error states to the sliding surface. Finally, the robust ABSM-RRL control scheme is proposed for the exoskeleton robot having the lumped effect of model uncertainties and external disturbances. Inherently, the asymptotic stability of the exoskeleton system is guaranteed using Lyapunov theory. The dynamic model of a simplified 3-joint lower limb robotic exoskeleton in parametric-based strict-feedback representation can be expressed below.

$$r_{1a} = q_{j,e}, r_{2a} = \dot{q}_{j,e}, r = [r_{1a}, r_{2a}]^T \tag{5.11}$$

$$\begin{cases} \dot{r}_{1a} & = r_{2a} \\ \dot{r}_{2a} & = {\mathcal{M}_{oe}}^{-1}(q_{j,e})\big(\tau_{j,e} - \tau_{j,int} + \rho - \mathcal{C}_{oe}(q_{j,e}, \dot{q}_{j,e})\dot{q}_{j,e} - \mathcal{G}_{oe}(q_{j,e})\big) \end{cases} \tag{5.12}$$

where $r_{1a} \in \mathbb{R}^3, r_{2a} \in \mathbb{R}^3$ are the state vectors of the exoskeleton robot.

The gait tracking error variables can be selected as

$$\xi_{1a} = q_{j,e} - q_{j,\alpha} \tag{5.13}$$

$$\xi_{2a} = \dot{\xi}_{1a} - \zeta_a = r_{2a} - \dot{q}_{j,\alpha} - \zeta_a \tag{5.14}$$

where, ζ_a denotes the virtual control law to be selected in backstepping approach for stabilizing the dynamical system.

Taking the Equation 5.13 and Equation 5.14 into account, the sliding surface could be selected to ensure equilibrium condition of error variables as follows

$$s = \lambda_p \xi_{1a} + \xi_{2a} \tag{5.15}$$

where $\lambda_p \in \mathbb{R}^{3\times3}$ denotes positive definite diagonal matrix.

Furthermore, in this work, a rapid reaching law with varying power terms is proposed as below for faster convergence of error states to the sliding surface.

$$\dot{s} = -\kappa_1 |s|^{\beta_1(s)} sgn(s) - \kappa_2 |s|^{\beta_2(s)} sgn(s) \tag{5.16}$$

with

$$\beta_1(s) = \varepsilon_0 + \varepsilon_1 tanh(s^{\mu}) - \varepsilon_2 tanh\left(\eta s^2\right) \tag{5.17}$$

$$\beta_2(s) = \begin{cases} \varepsilon & \text{if } |s| \geq 1 \\ 1 & \text{if } |s| < 1 \end{cases} \tag{5.18}$$

where $\kappa_1 > 0, \kappa_2 > 0, 0 < \varepsilon_0 > \varepsilon_2 > 1, \varepsilon_1 > 1, \eta > 0, \varepsilon = \varepsilon_0 + \varepsilon_1 - \varepsilon_2 > 1$, and μ is a positive even number.

In Equation 5.16, two variable power terms offer impressive adaptability features where the former one ($\beta_1(s)$) is a designed non-linear function and the latter one ($\beta_2(s)$) represents a piecewise-defined function. By choosing suitable values of μ and η, Equation 5.16 can be further expressed as

$$\dot{s} = \begin{cases} -\kappa_1 |s|^{\varepsilon} sgn(s) - \kappa_2 |s|^{\varepsilon} sgn(s), & |s| \geq 1 \\ -\kappa_1 |s|^{\varepsilon_0 - \varepsilon_2} sgn(s) - \kappa_2 s, & 0 < |s| < 1 \\ -\kappa_1 |s|^{\varepsilon_0} sgn(s) - \kappa_2 s, & |s| \to 0 \end{cases} \tag{5.19}$$

Given the dynamic model in Equation 5.12 with state vectors (r_{1a}, r_{2a}) in Equation 5.11, the state variables $\left(\xi_{1a}, \xi_{2a}\right)$ in Equations 5.13-5.14 can rapidly converge to the sliding surface (s) selected as Equation 5.15 via improved reaching law ($\dot{s}$) defined in Equation 5.16.

Selecting a Lyapunov candidate function as follows:

$$V = \frac{1}{2} s^T s \tag{5.20}$$

Exploiting Equation 5.16, the derivative of the above function can be formulated as

$$\begin{aligned} \dot{V} &= s\dot{s} \\ &= -\kappa_1 |s|^{(\beta_1+1)(s)} sgn(s) - \kappa_2 |s|^{(\beta_2+1)(s)} sgn(s) < 0 \end{aligned} \tag{5.21}$$

Interpreting Equation 5.20 and Equation 5.21 for $V > 0$ and $\dot{V} < 0$ prove that the state variables can access the sliding surface in an approaching time t_a.

The approaching time can be approximately computed as below in two phases for $|s(0)| > 1$; phase 1: If $s(0) \rightarrow |s| = 1$, then $\beta_1(s) = \beta_2(s) = \varepsilon$ and phase 2: If $|s| = 1 \rightarrow s = 0$, then $\beta_1(s) = \varepsilon_0 - \varepsilon_2, \beta_2(s) = 1$.

$$t_a \approx \frac{1 - |s(0)|^{1-\varepsilon}}{(\kappa_1 + \kappa_2)(\varepsilon - 1)} + \frac{1}{\kappa_1(1 - \varepsilon_0 + \varepsilon_2)} ln\left(1 + \frac{\kappa_1}{\kappa_2}\right) \tag{5.22}$$

Given the dynamic model in Equation 5.12 and sliding surface (s) in Equation 5.15 with rapid reaching law ($\dot{s}$) in Equation 5.16, if the control law can be selected as

$$\begin{aligned} \tau_{j,e} = \tau_{j,int} + \mathcal{M}_{oe}(q_{j,e})\big[&- \lambda_p(\xi_{2a} - \nu\xi_{1a}) + \ddot{q}_{j,\alpha} - \nu\dot{\xi}_{1a} - hs\big] \\ &+ \mathcal{C}_{oe}(q_{j,e}, \dot{q}_{j,e}) + \mathcal{G}_{oe}(q_{j,e}) - \hat{\rho} \\ &- \mathcal{M}_{oe}(q_{j,e}) h\big(\kappa_1 |s|^{\beta_1(s)} + \kappa_2 |s|^{\beta_2(s)}\big) sgn(s) \end{aligned} \tag{5.23}$$

where $\nu \in \mathbb{R}^{3\times3}, h \in \mathbb{R}^{3\times3}$ are positive definite diagonal matrices and $\hat{\rho}$ is the estimation of ρ which can be modeled with an adaptive law as

$$\dot{\hat{\rho}} = \Gamma_c \big({\mathcal{M}_{oe}}^{-1}(q_{j,e})\big)^T s \tag{5.24}$$

to compensate the model uncertainties and external disturbances, then the error states asymptotically converges to equilibrium point, i.e., $\xi_{1a}, \xi_{2a} \rightarrow 0$ when time $t \rightarrow \infty$.

Considering the virtual control law as follows

$$\zeta_a = -\nu\xi_{1a} \tag{5.25}$$

Substituting Equation 5.25 into Equation 5.14, the second error variable can be written as

$$\xi_{2a} = \dot{\xi}_{1a} - \zeta_a = r_{2a} - \dot{q}_{j,\alpha} + \nu\xi_{1a} \tag{5.26}$$

Step 1:

Selecting the Lyapunov candidate function as

$$V_1 = \frac{1}{2} {\xi_{1a}}^T \xi_{1a} \tag{5.27}$$

Differentiating the above equation, one can get

$$\dot{V}_1 = {\xi_{1a}}^T \dot{\xi}_1 = {\xi_{1a}}^T \big(\xi_{2a} - \nu\xi_{1a}\big) = {\xi_{1a}}^T \xi_{2a} - {\xi_{1a}}^T \nu\xi_{1a} \tag{5.28}$$

Referring Equation 5.28, the $\dot{V}_1 < 0$ for $\xi_{2a} = 0$, the first subsystem of the coupled human-exoskeleton system in AA mode is stable.

Step 2:

Further differentiating Equation 5.26 as

$$\dot{\xi}_{2a} = \ddot{\xi}_{1a} - \dot{\zeta}_a = \dot{r}_{2a} - \ddot{q}_{j,\alpha} + \nu\dot{\xi}_{1a} \tag{5.29}$$

Another Lyapunov candidate function can be selected as

$$V_2 = V_1 + \frac{1}{2}s^T s \tag{5.30}$$

where s denotes for sliding surface given in Equation 5.15.

Differentiating Equation 5.30 and using Equations 5.26, 5.29, and 5.12 will result into

$$\begin{aligned}
\dot{V}_2 &= {\xi_{1a}}^T\xi_{2a} - {\xi_{1a}}^T\nu\xi_{1a} + s^T\left(\lambda_p\dot{\xi}_{1a} + \dot{\xi}_2\right) \\
&= {\xi_{1a}}^T\xi_{2a} - {\xi_{1a}}^T\nu\xi_{1a} + s^T\left[\lambda_p\left(\xi_{2a} - \nu\xi_{1a}\right) + \dot{r}_{2a} - \ddot{q}_{j,\alpha} + \nu\dot{\xi}_{1a}\right] \\
&= {\xi_{1a}}^T\xi_{2a} - {\xi_{1a}}^T\nu\xi_{1a} + s^T\left[\lambda_p\left(\xi_{2a} - \nu\xi_{1a}\right) + {\mathcal{M}_{oe}}^{-1}(q_{j,e})\right. \\
&\quad \left(\tau_{j,e} - \tau_{j,int} + \rho - \mathcal{C}_{oe}(q_{j,e}, \dot{q}_{j,e})\dot{q}_{j,e} - \mathcal{G}_{oe}(q_{j,e})\right) \\
&\quad \left. - \ddot{q}_{j,\alpha} + \nu\dot{\xi}_{1a}\right]
\end{aligned} \tag{5.31}$$

In the above equation, determining ρ is difficult in actual control architecture. Therefore, an adaptive law based on ABSM control is proposed in further steps to avoid the need to define the upper limits of ρ.

Step 3:

Design

$$\tilde{\rho} = \rho - \hat{\rho} \tag{5.32}$$

where $\hat{\rho}$ is the estimation of ρ and $\tilde{\rho}$ is the estimation error. Differentiating above equation, one can get

$$\dot{\tilde{\rho}} = \dot{\rho} - \dot{\hat{\rho}} = -\dot{\hat{\rho}} \tag{5.33}$$

Now, the third Lyapunov candidate function can be selected as

$$V_3 = V_2 + \frac{1}{2\Gamma_c}\tilde{\rho}^T\tilde{\rho} \tag{5.34}$$

where Γ_c is a positive constant. Further, differentiating the above equation for

$$\begin{aligned}\dot{V}_3 &= \dot{V}_2 - \frac{1}{\Gamma_c}\tilde{\rho}^T\dot{\hat{\rho}} \\ &= {\xi_{1a}}^T\xi_{2a} - {\xi_{1a}}^T\nu\xi_{1a} + s^T\Big[\lambda_p\big(\xi_{2a} - \nu\xi_{1a}\big) + {\mathcal{M}_{oe}}^{-1}(q_{j,e}) \\ &\quad \big(\tau_{j,e} - \tau_{j,int} + \hat{\rho} - \mathcal{C}_{oe}(q_{j,e},\dot{q}_{j,e})\dot{q}_{j,e} - \mathcal{G}_{oe}(q_{j,e})\big) \\ &\quad - \ddot{q}_{j,\alpha} + \nu\dot{\xi}_{1a}\Big] - \frac{1}{\Gamma_c}\tilde{\rho}^T\left(\dot{\hat{\rho}} - \Gamma_c\big({\mathcal{M}_{oe}}^{-1}(q_{j,e})\big)^T s\right)\end{aligned} \tag{5.35}$$

Substituting proposed control law ($\tau_{j,e}$) and adaptive algorithm ($\dot{\hat{\rho}}$) selected as Equation 5.23 and Equation 5.24 into Equation 5.35,

$$\begin{aligned}\dot{V}_3 &= {\xi_{1a}}^T\xi_{2a} - {\xi_{1a}}^T\nu\xi_{1a} - s^T hs \\ &\quad - s^T h\big(\kappa_1|s|^{\beta_1(s)} + \kappa_2|s|^{\beta_2(s)}\big)sgn(s) \\ &\leq {\xi_{1a}}^T\xi_{2a} - {\xi_{1a}}^T\nu\xi_{1a} - s^T hs \\ &\leq -\big({\xi_{1a}}^T\nu\xi_{1a} - {\xi_{1a}}^T\xi_{2a} + s^T hs\big) \\ &\leq -\big({\xi_{1a}}^T\nu\xi_{1a} - {\xi_{1a}}^T\xi_{2a} + (\lambda_p\xi_{1a} + \xi_{2a})^T h(\lambda_p\xi_{1a} + \xi_{2a})\big) \\ &\leq -\big({\xi_{1a}}^T\nu\xi_{1a} + \lambda_p^T\lambda_p h{\xi_{1a}}^T\xi_{1a} + \lambda_p^T{\xi_{1a}}^T h\xi_{2a} - \frac{I}{2}{\xi_{1a}}^T\xi_{2a} \\ &\quad + {\xi_{2a}}^T h\lambda_p\xi_{1a} - \frac{I}{2}{\xi_{1a}}^T\xi_{2a} + {\xi_{2a}}^T h\xi_{2a}\big) \\ &\leq -\begin{bmatrix}\xi_{1a} & \xi_{2a}\end{bmatrix}\begin{bmatrix}\nu + \lambda_p^T h\lambda_p & h\lambda_p - \frac{I}{2} \\ h\lambda_p - \frac{I}{2} & h\end{bmatrix}\begin{bmatrix}\xi_{1a} \\ \xi_{2a}\end{bmatrix}\end{aligned} \tag{5.36}$$

Therefore, Equation 5.36 can be expressed as

$$\dot{V}_3 \leq -\begin{bmatrix}\xi_{1a} & \xi_{2a}\end{bmatrix}^T\psi\begin{bmatrix}\xi_{1a} \\ \xi_{2a}\end{bmatrix} \tag{5.37}$$

where

$$\psi = \begin{bmatrix}\nu + \lambda_p^T h\lambda_p & h\lambda_p - \frac{I}{2} \\ h\lambda_p - \frac{I}{2} & h\end{bmatrix} \tag{5.38}$$

It is evident from above relation that the ψ can be positive definite with the proper selection of h, ν, and λ_p. Therefore, Equation 5.37 satisfies

$$\dot{V}_3 \leq 0 \tag{5.39}$$

Finally, interpreting Equation 5.39, the asymptotic convergence of error variables is ensured for desired gait tracking, which proves the stability of the coupled human-exoskeleton robot in cooperative training mode. The complete architecture of the

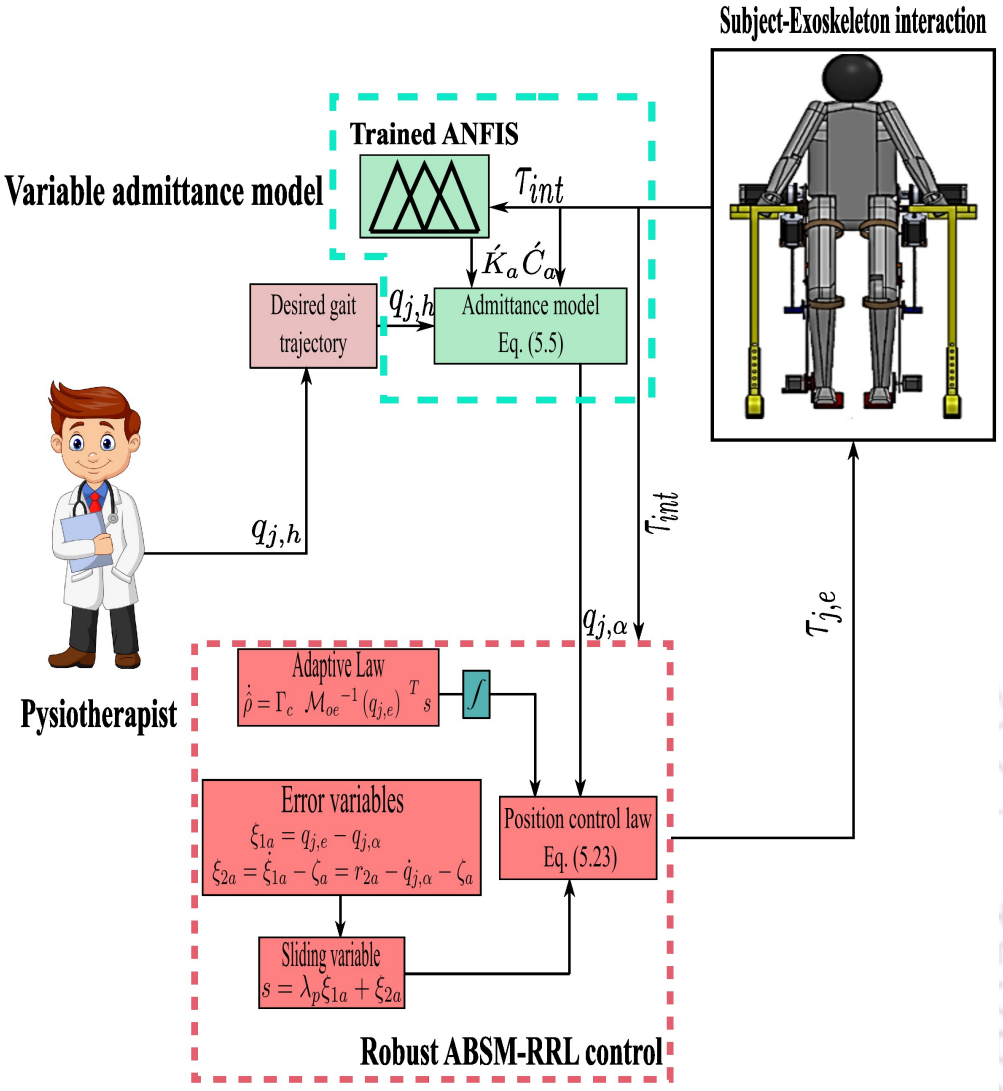

FIGURE 5.1: ABSM-SCC control architecture

proposed cooperative control is shown in Figure 5.1.

5.5 Results and Discussions

This section examines the performance of the proposed subject-cooperative control (ABSM-VAC) using various simulation runs where LLESv2 is considered along with the pediatric subject of age 08 years, body mass 34 kg kg, body height 128 cm (C6 from Table 2.7). The simulation runs in this chapter are carried out in MATLAB/Simulink R2020b (ode45 solver with variable step and non-adaptive zero crossing algorithm) The results are compared to the contrast control (AB-FAC) for two different cases, i.e., regular active-assist training mode and active-assist

training mode with sudden interaction reflex. The uncertain model parameter, external disturbances, Coulomb friction, and viscous velocity factor are considered as $\delta = 0.2, \tau_d = \big[\big(3sin(2t) + 2 \times random(1)\big), \big(2sin(2t) + random(1)\big), \big(sin(2t) + t\big)\big]^T, C_f = [0.8, 0.8, 0.8]^T, \sigma = [1.2, 1.2, 1.2]^T$ to validate the robustness of the inner loop position control. The control parameters in ABSM with RRL are as follows: $\lambda_p = 8, h = 26, \nu = diag(100, 60, 60), \Gamma_c = diag(0.1, 0.1, 0.1), \kappa_1 = 22, \kappa_2 = 38, \varepsilon_0 = 0.2, \varepsilon_1 = 0.6, \varepsilon_2 = 0.05, \mu = 6$, and $\eta = 1.5$. The fixed admittance parameters in the contrast control are $C_a = diag(2, 2, 2)$ and $K_a = diag(100, 100, 100)$. These admittance values are further used in the ABSM cooperative control to compute the minimum and maximum limit of the interaction torques. In Equation 2.16, the damping and spring coefficients for the bracing straps are selected as $c = [10, 10, 2]^T$ and $k = [200, 200, 20]^T$. The limits of admittance parameters are selected based on the numerical iterations around the fixed admittance values. Thereafter, two network architectures ($anfis1.fis$ and $anfis2.fis$) are formed based on input-output training dataset as per Equations 5.6-5.8 and 5.9-5.10. The details of the input-output dataset used for training of ANFIS architecture are given in Table 5.1.

TABLE 5.1: Input and output training range of ANFIS architectures

	Interaction torques (Nm)			Admittance parameters	
	Hip	Knee	Ankle	Damping (Nm/deg.)	Stiffness (Nm-s/deg.)
	$\acute{\tau}_{1,int}$	$\acute{\tau}_{2,int}$	$\acute{\tau}_{3,int}$	$\acute{C}_a$	$\acute{K}_a$
Minimum	-12.55	-28.44	-5.71	1	50
Maximum	11.75	24.60	6.52	3	150

Furthermore, to select the ANFIS training parameters, several simulation runs are carried out by altering the number of MF $(1 - 20)$ and epochs $(1 - 30)$ till the specified error tolerance is achieved between the desired and target output vectors. Conventionally, the ANFIS technique exploits two optimization models, backpropagation and hybrid, to build the learning characteristics between the input and output vectors. In the hybrid approach, a least square algorithm and the gradient descent model are exploited to modulate the errors. This work uses the hybrid method with both datasets while training the network architectures. The complete details of training parameters are provided in Table 5.2. The co-simulation results for different cases are discussed using two performance metrics

TABLE 5.2: Training parameters used in ANFIS architectures

Training Parameters	$anfis1.fis$	$anfis2.fis$
MF type	Gaussian	Gaussian
Number of MF	5	6
Number of Epochs	10	15
Error tolerance	0.0001	0.001
Learning model	Hybrid	Hybrid

as, root mean square (RMS) and performance index (PI), defined as follows:

$$RMS(P) = \sqrt{\frac{1}{N}\sum_{v=1}^{N} {p_v}^2} \tag{5.40}$$

$$PI = \frac{RMS(P)_{AB-FAC} - RMS(P)_{ABSM-VAC}}{RMS(P)_{ABSM-FAC}} \times 100\% \tag{5.41}$$

where p_v denotes the performance value such that if p_v: joint angular error (ξ_{1a}, i.e., $q_{j,\alpha}$), then $RMS(P)$ denotes the root mean square error ($RMSE$) and if p: joint torque (T), then $RMS(P)$ refers to the root mean square torque ($RMST$); N represents the total number of data points.

5.5.1 Case 1: Active-assist training mode

As mentioned earlier, the AA training mode is beneficial for such cases where subjects have restored partial motor strength after the onset of neurological disease. As subjects apply their recovered muscle strength of lower-limbs for desired movement, the exoskeleton robot need to comply with them using the proposed cooperative control. After employing the control parameters and relevant admittance values, the tracking of joint variables for the contrast and proposed control is shown in Figures 6.2 and 6.3. It can be observed from Figures 6.2(a), 6.3(a), and 6.4(a), the deviation between actual (q_e) and reference (modified) (q_α) hip joint trajectory is less in case of proposed variable admittance-based cooperative control ($RMSE_{ABSM-VAC}$: 0.193° as compared to the contrast control ($RMSE_{AB-FAC}$: 0.247°). From Figures 6.2(b), 6.3(b), and 6.4(b), a similar trend of joint error ($q_{j,\alpha}$) is noted for knee joint ($RMSE_{ABSM-VAC}$: 0.489°, $RMSE_{AB-FAC}$: 0.535°). In case of ankle joint (Figures 6.2(c), 6.3(c), and 6.4(c)), although the trend is similar

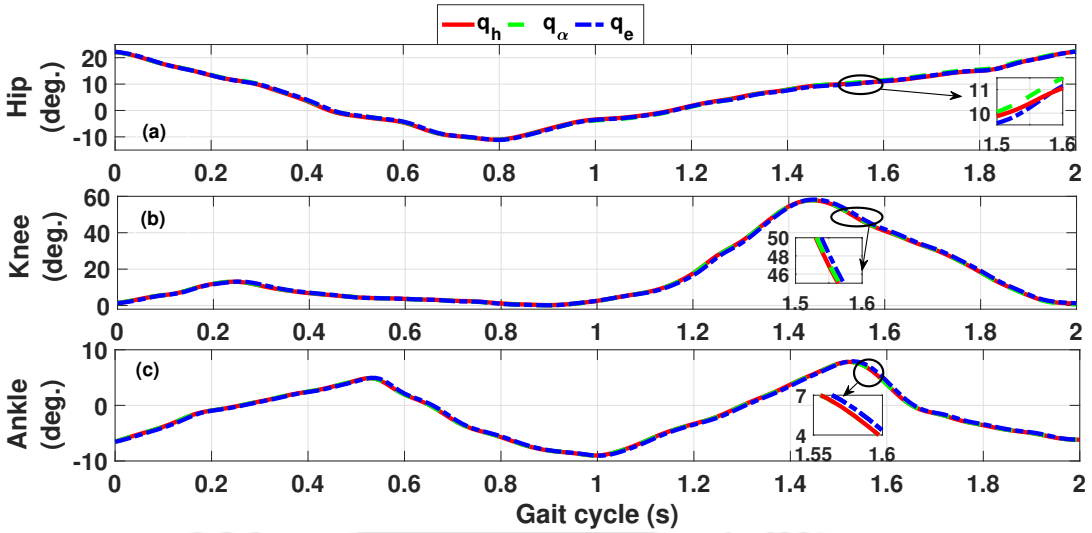

FIGURE 5.2: Trajectory tracking for (a) hip, (b) knee, and (c) ankle joint using contrast control (AB-FAC)

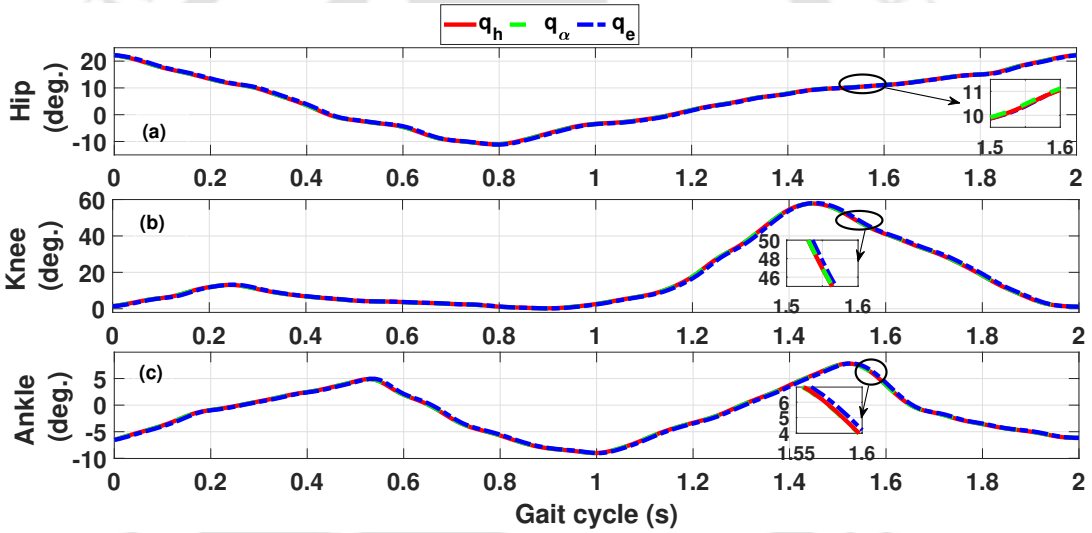

FIGURE 5.3: Trajectory tracking for (a) hip, (b) knee, and (c) ankle joint using proposed control (ABSM-VAC)

to hip and knee joint, there is a marginal difference between joint error of proposed ($RMSE_{ABSM-VAC}$: 0.166° and contrast control $RMSE_{AB-FAC}$: 0.187°). The tracking performance is summarized in Table 5.3.

The sliding surfaces (s) for hip, knee, and ankle joint in the proposed control (ABSM-VAC) are shown in Figure 5.5(a). It can be inferred from the plots of sliding surfaces that the tracking error converges asymptotically and reaches the settling phase at 1.97 s, 1.96 s, and 1.96 s for hip, knee, and ankle joints, respectively. Furthermore, Figure 5.5(b) presents the root mean square error (RMSE) of lumped parameter estimation ($\hat{\rho}$) with the value of 0.1×10^{-3} at starting and

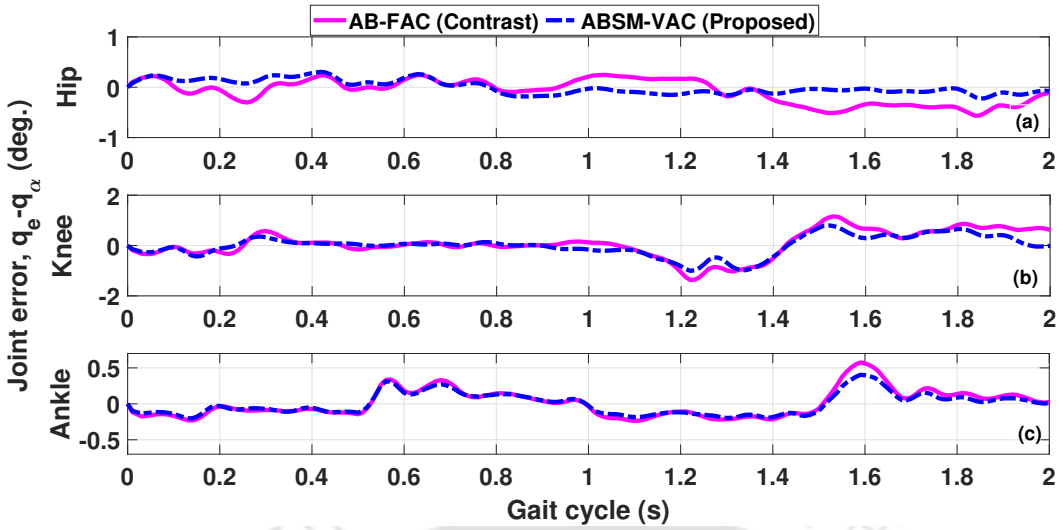

FIGURE 5.4: Trajectory tracking error for (a) hip, (b) knee, and (c) ankle joint using contrast and proposed control

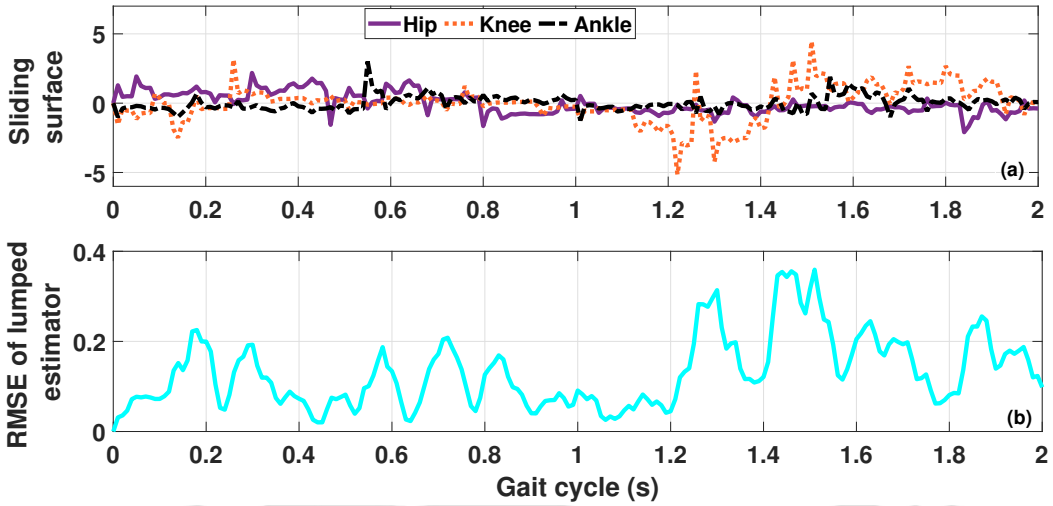

FIGURE 5.5: Plot of (a)sliding variable and (b) root mean square of lumped estimation error using proposed control (ABSM-VAC)

0.1 at end of the gait cycle. It is evident that the adaptive law in 5.24 estimates the uncertainties and disturbances in the system quite precisely.

Invoking the joint trajectory results in the Cartesian space, the actual gait trajectory followed by the exoskeleton is shown in Figure 5.6 for contrast control and proposed control. It can be easily interpreted that, for AB-FAC, the robot allows the subject to move the lower limb more flexibly throughout the gait cycle. However, when considering the real-time scenario where admittance parameters change every moment, the proposed control (ABSM-VAC) allows flexibility and rigidity based on trained ANFIS architecture. For instance, for zoom-in views illustrated

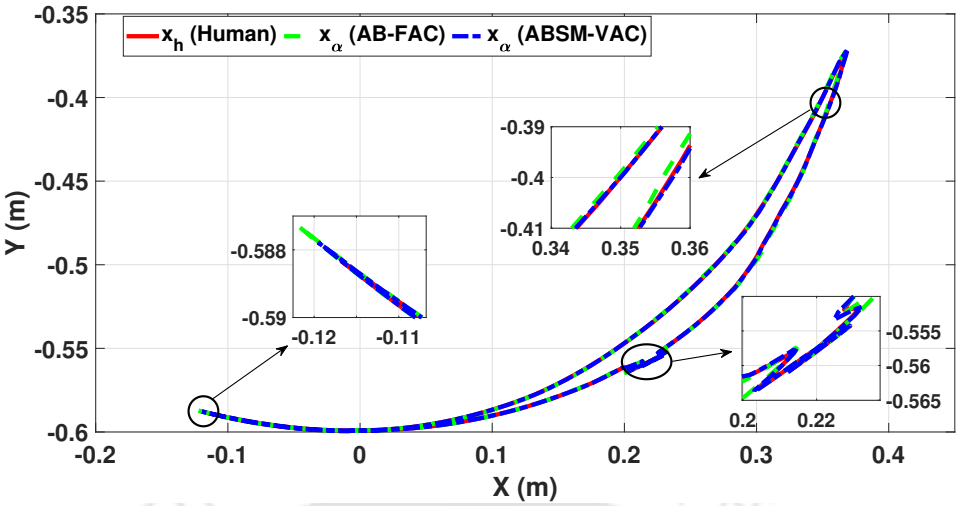

FIGURE 5.6: Reference gait trajectory (Cartesian) using contrast and proposed control

in Figure 5.6, the proposed control allows less flexibility (more rigidity) compared to most of the other segments in the trajectory.

Moving further with the results in Figure 6.7, it can be easily perceived that lesser interaction torques are generated with the proposed control (ABSM-VAC) as compared to the contrast control (AB-FAC). For the hip joint, as shown in Figure 6.7(a), the proposed control offers less active participation of the subject in early stance ($0-0.4$ s) and initial swing ($1.1-1.5$ s) phase of the gait cycle and allows more active participation in other phases of the gait cycle with marginally lower values than the contrast control. Figures 6.7(b) and 6.7(c) also show the heterogeneous nature of the knee and ankle joint interaction torque over the gait cycle; however, within different gait phases. This heterogeneous nature is due to the logic considered in 5.6-5.8 and inputted in ANFIS architecture. The real-time variation in the admittance parameter over the gait cycle is shown in Figure 5.8 where left and right $x-$axis represents the damping and stiffness parameter, respectively.

The results of joint torques are presented in Figure 6.8. From Figure 6.7 and 6.8, it can be easily noticed that for very similar values of interaction torques with both control approaches ($0.41-0.85$ s for hip, $0.3-0.6$ s for knee, and $0.28-0.58$ s for ankle), the proposed control requires less amount of torque. Moreover, referring Figure 6.8(a), 6.8(b), and 6.8(c) as an overall, less joint torques are produced using proposed control ($RMST_{ABSM-VAC}$: 31.62 Nm for hip, 14.22 Nm for knee, and 0.91 Nm for ankle) as compared to the contrast control ($RMST_{AB-FAC}$: 42.99 Nm for hip, 15.47 Nm for knee, and 1.18 Nm for ankle). The overall torque

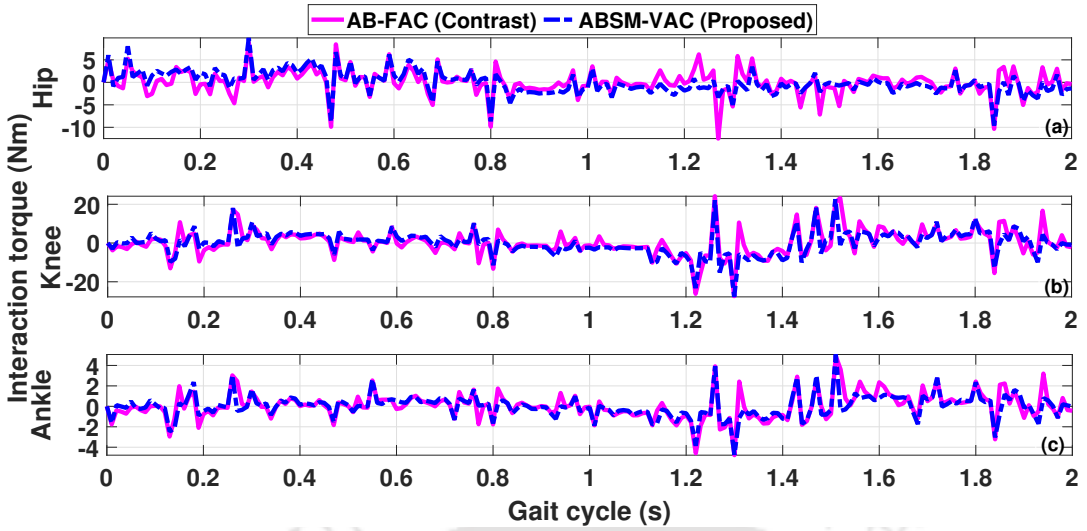

FIGURE 5.7: Interaction torques for (a) hip, (b) knee, and (c) ankle joint using contrast and proposed control

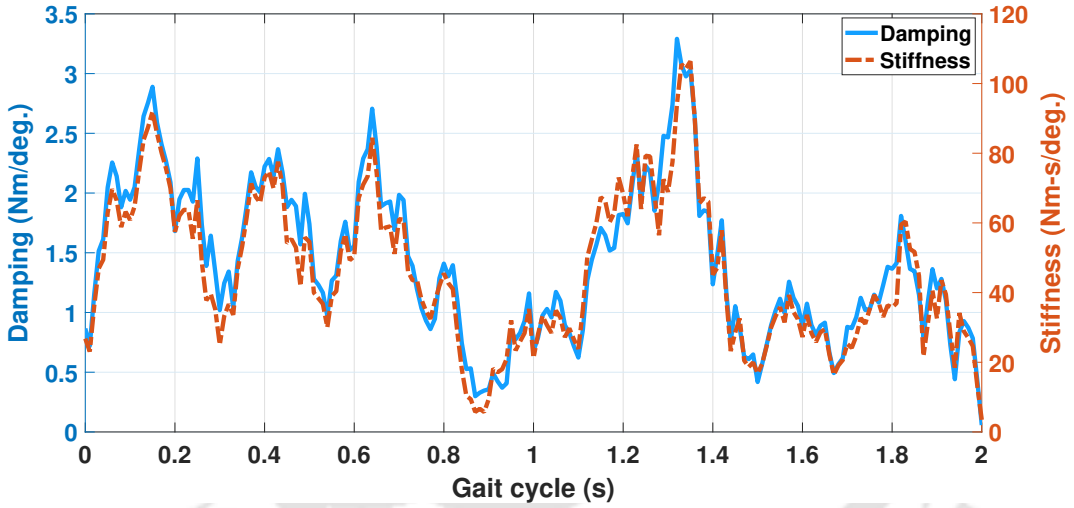

FIGURE 5.8: Variable damping and stiffness admittance parameters over a gait cycle

performance is compiled in Table 5.3. Therefore, it can be concluded that the proposed cooperative control generates lesser amount of joint torques to precisely track the reference gait trajectory as compared to contrast control, irrespective of the subject's active participation. The sudden peaks in joint torques are also predominant in case of contrast control, especially, in case of ankle joint (Figure 6.8(c)).

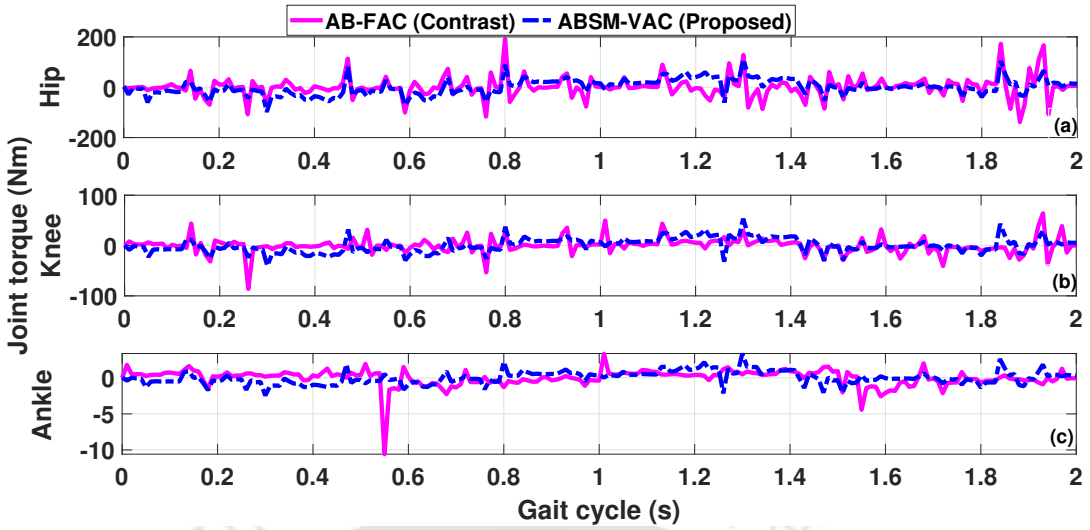

FIGURE 5.9: Joint torques for (a) hip, (b) knee, and (c) ankle using contrast and proposed control

TABLE 5.3: Comparative performance analysis of the proposed control over the contrast control during the active-assist rehabilitation

Joint	Tracking Performance (RMSE, °)		PI (%)	Torque Performance (RMST, Nm)		PI (%)
	Contrast Control (AB-FAC)	Proposed Control (ABSM-VAC)		Contrast Control (AB-FAC)	Proposed Control (ABSM-VAC)	
Hip	0.247	0.193	21.86	42.94	31.62	26.36
Knee	0.535	0.489	8.59	15.47	14.22	8.08
Ankle	0.187	0.166	11.23	1.18	0.91	22.88

5.5.2 Case II: Active-assist training mode with sudden reflex

To investigate the potential of robust trajectory control and variable admittance model of the proposed cooperative control, another case of active-assist rehabilitation is considered with the inclusion of sudden reflex. The reflex is defined as an interaction torque $\left(\tau_s^{int}\right)$ generated due to an equivalent interaction force $\left(F_{eq}^{int}\right)$ at the ankle. The equivalent interaction force is modeled as a pulse function that appears at certain time intervals and is expressed as follows [218]:

$$F_{eq}^{int}(t) = \begin{cases} A_{int}, & \text{if } t_{int}^{s} \leq t \leq t_{int}^{e} \\ 0, & \text{otherwise} \end{cases} \tag{5.42}$$

where $A_{int} = 40$N is the amplitude of the modeled reflex and $t_{int}^{s} = 0.5$s, $t_{int}^{e} = 0.6$s represent the starting and ending time intervals for the sudden forces, respectively.

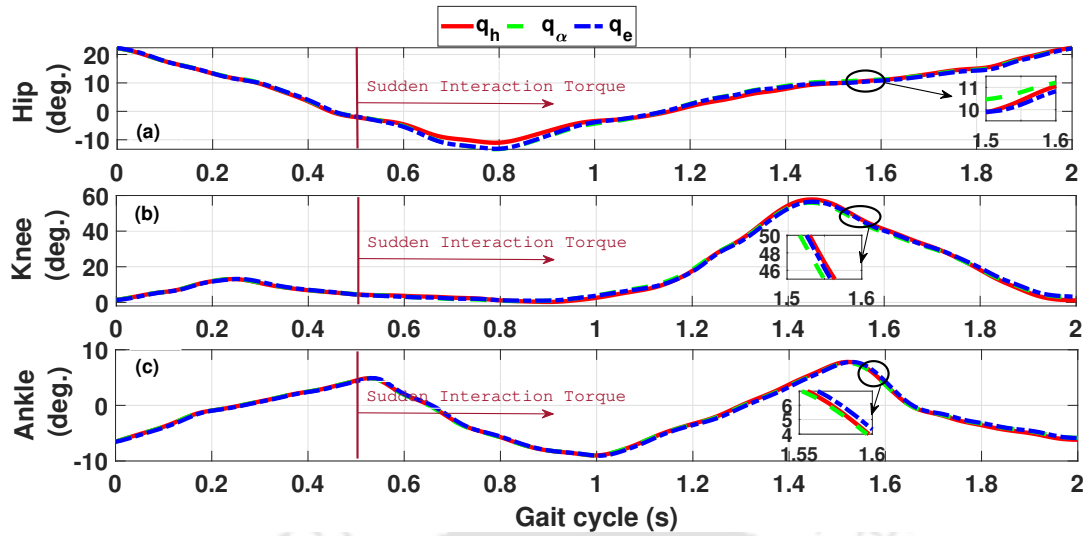

FIGURE 5.10: Trajectory tracking for (a) hip, (b) knee, and (c) ankle joint using contrast control (AB-FAC) under the effect of sudden reflex

The joint trajectory tracking for the contrast and proposed control using the appropriate control gains and admittance values is shown in Figures 5.10 and 5.11. Referring Figures 5.10(a), 5.11(a), and 5.12(a), the difference between actual (q_e) and reference (q_α) hip trajectory is significantly higher for contrast control ($RMSE_{AB-FAC}$: 0.269°), especially, after application of sudden reflex. However, the proposed control offers promising tracking of reference hip joint with $RMSE_{ABSM-VAC}$ of 0.202°. For knee joint (Figures 5.10(b), 5.11(b), and 5.12(b)), the proposed control fell little short with $RMSE_{ABSM-VAC}$ of 0.724° as compared to the contrast control ($RMSE_{AB-FAC}$: 0.679°). This reverse trend shows high flexibility levels at a certain period due to the simultaneous effect of sudden reflex and variable admittance model. In case of ankle joint (Figures 5.10(c), 5.11(c), and 5.12(c)), the proposed control ($RMSE_{ABSM-VAC}$: 0.189°) outperforms the contrast control ($RMSE_{AB-FAC}$: 0.20°) marginally for the joint error ($q_{j,\alpha}$). The tracking performance is enlisted in Table 5.4.

Similar to Case I, the sliding surfaces (s) in Figure 5.13(a) show the asymptotic convergence of error states for hip, knee, and ankle joints using the proposed control (ABSM-VAC). However, the tracking error reached the settling period at 1.98 s, 1.99 s, and 1.97 s, which is slightly higher due to the sudden incoming reflex. Furthermore, as shown in Figure 5.13(b), the root mean square (RMS) of lumped parameter estimation error ($\bar{\rho}$), with the value of 0.1×10^{-3} at starting and 0.45 at end of the gait cycle, ensures that the adaptive law in 5.24 is able to estimate the uncertainties and disturbances in the system very well. The sudden

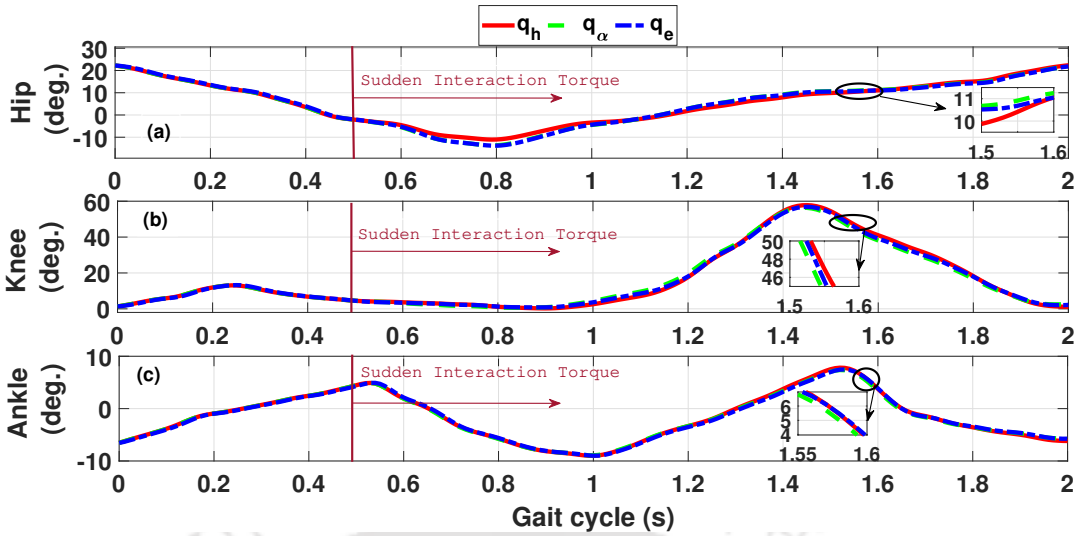

FIGURE 5.11: Trajectory tracking for (a) hip, (b) knee, and (c) ankle joint using proposed control (ABSM-VAC) under the effect of sudden reflex

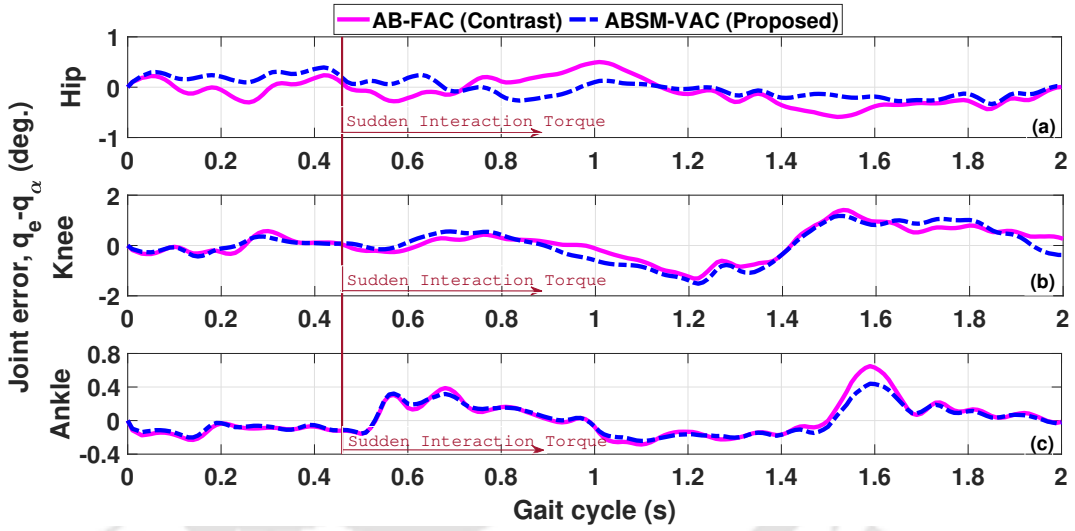

FIGURE 5.12: Trajectory tracking error for (a) hip, (b) knee, and (c) ankle joint using contrast and proposed control under the effect of sudden reflex

rise in the RMS value can be seen due to the exertion of sudden interaction force at 0.5 s.

The results of the actual gait trajectory in Cartesian space are shown in Figure 5.14 using the contrast and proposed control. It is evident from the left and right zoom-in view that, unlike the contrast control (AB-FAC), the proposed control (ABSM-VAC) offers added flexibility to the robot under the presence of sudden reflex, which ensures the safety of the subject. Moreover, the third zoom-in view (at $X, Y : 0.2, -0.565 : 0.24, -0.0.55$) depicts that the proposed control can stiffen the robot during the start and end of the gait trajectory for effective tracking.

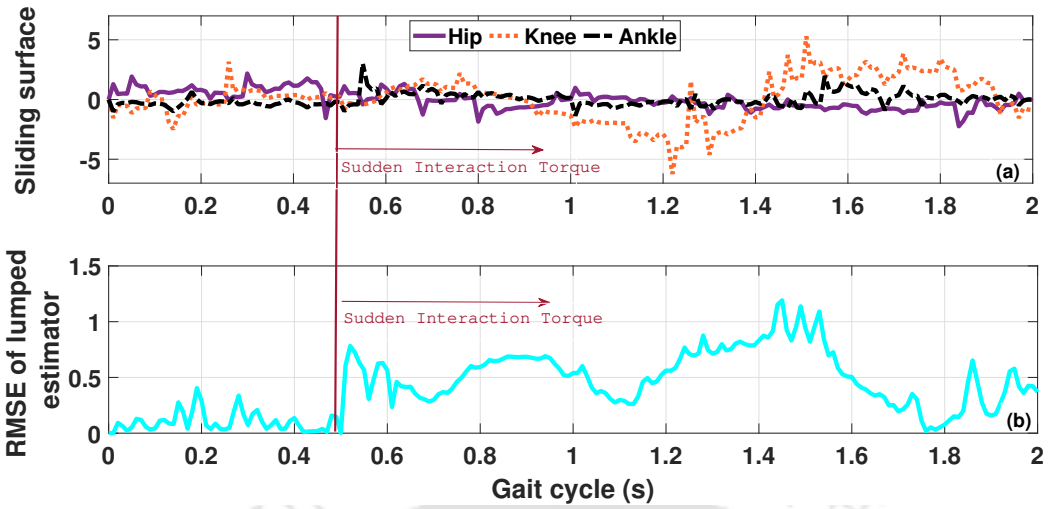

FIGURE 5.13: Plot of (a)sliding variable and (b) root mean square of lumped estimation error using proposed control (ABSM-VAC) under the effect of sudden reflex

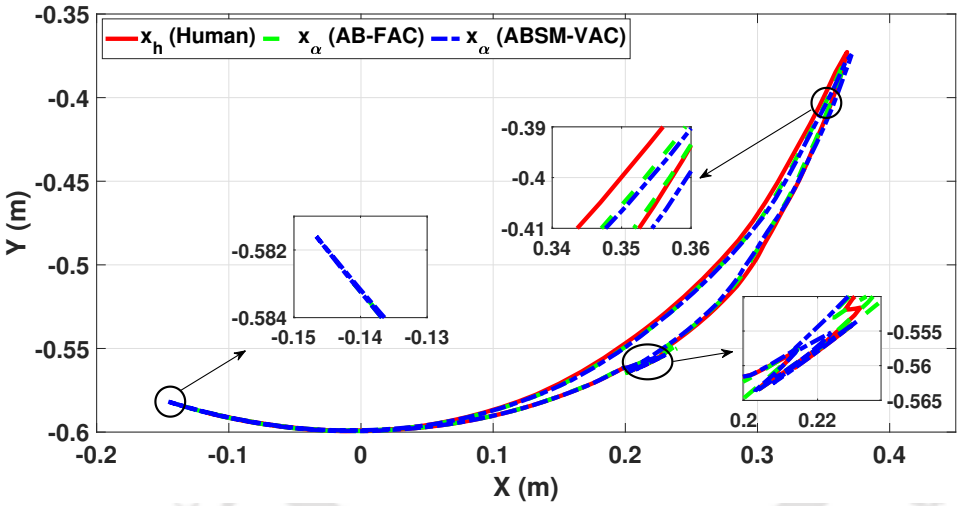

FIGURE 5.14: Reference gait trajectory (Cartesian) using contrast and proposed control under the effect of sudden reflex

This effectiveness is guaranteed with the effect of real-time changing admittance parameters using trained ANFIS architecture.

Figure 5.15 illustrates that similar interaction torques are generated for contrast control (AB-FAC) and proposed control (ABSM-VAC). The effect of applying sudden reflex after 0.5 s can be visible for the hip joint, knee, and ankle joint, as shown in Figures 5.15(a), 5.15(b), and 5.15(c), respectively. Moreover, it is pertinent to mention that the effect of applying sudden reflex is more dominant in the case of hip and ankle joints than the knee joint. Furthermore, the real-time variation in the admittance parameter over the gait cycle is shown in Figure

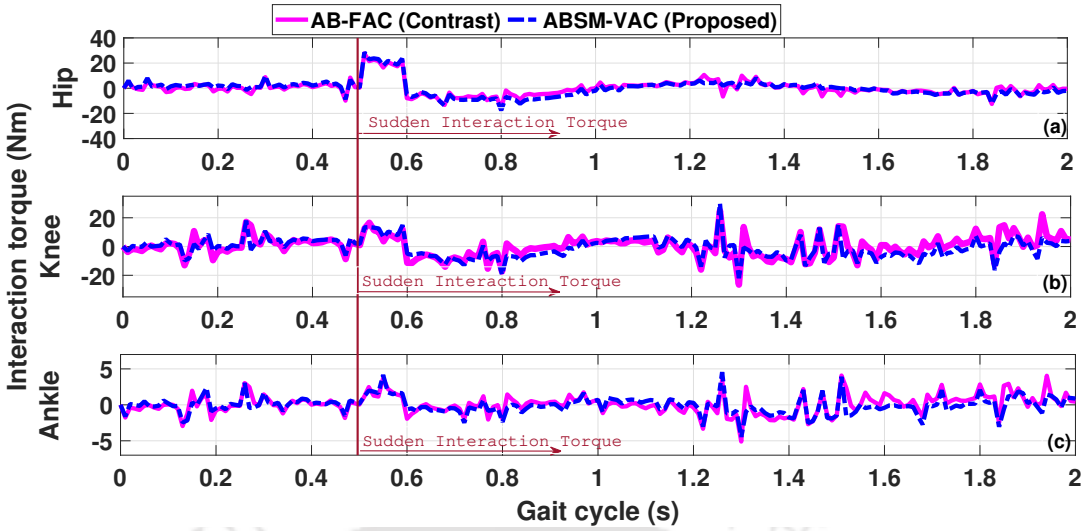

FIGURE 5.15: Interaction torques for (a) hip, (b) knee, and (c) ankle joint using contrast and proposed control under the effect of sudden reflex

5.16 where left and right $x-$axis represents the damping and stiffness parameter, respectively. The sudden fall in the admittance parameters between $0.5 - 0.6$ s represents the effect of sudden interaction force. The decreased stiffness allows flexibility to the robot and the safety of the subject eventually in case of sudden reflex. On the other hand, the lesser value of the damping parameter inherits the vibratory motion; however, it affects the system minimally due to the small range.

Interpreting the results of Figures 5.15 and 5.17, it is evident that for very similar values of the interaction torques with both control approaches, the proposed (ABSM-VAC) control requires less amount of torque ($RMST_{ABSM-VAC}$: 31.05 Nm for hip, 14.2 Nm for knee, and 0.95 Nm for ankle) as compared to the contrast control ($RMST_{AB-FAC}$: 39.9 Nm for hip, 14.94 Nm for knee, and 1.17 Nm for ankle). Figures 5.17(a), 5.17(b), and 5.17(c) present the joint torques for hip, knee, and ankle using both control approaches. The overall torque performance is outlined in Table 5.4. It is important to indicate that the effect of sudden reflex is negligible due to the small value of equivalent interaction torque in comparison with large values of joint torques. Furthermore, like Case I, it can be concluded that the proposed cooperative control generates a lesser amount of joint torques to precisely track the reference gait trajectory as compared to contrast control, even with the inclusion of considerable sudden reflex. The sharp peak in ankle joint torque is still high in the case of contrast control, as shown in Figure 5.17(c).

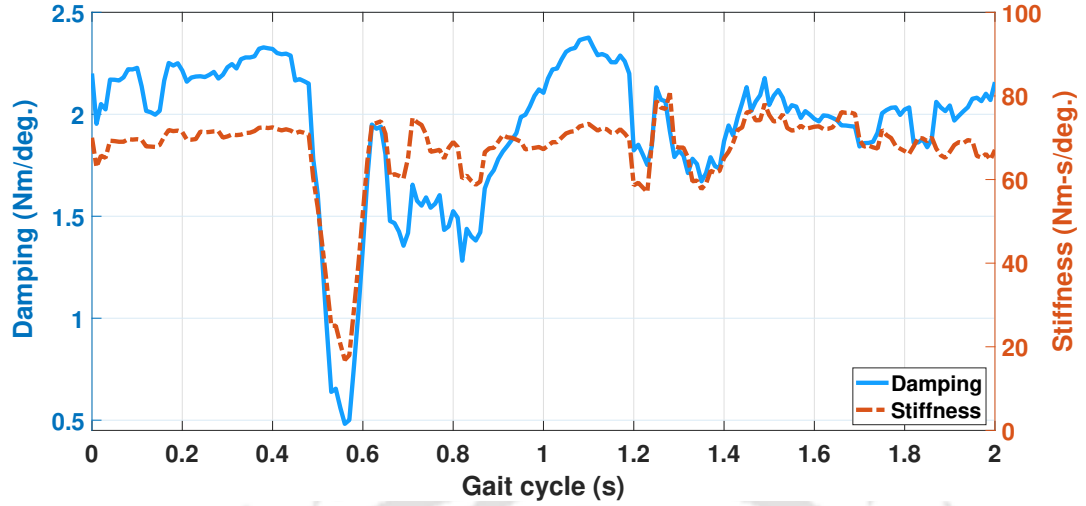

FIGURE 5.16: Variable damping and stiffness admittance parameters over a gait cycle under the effect of sudden reflex

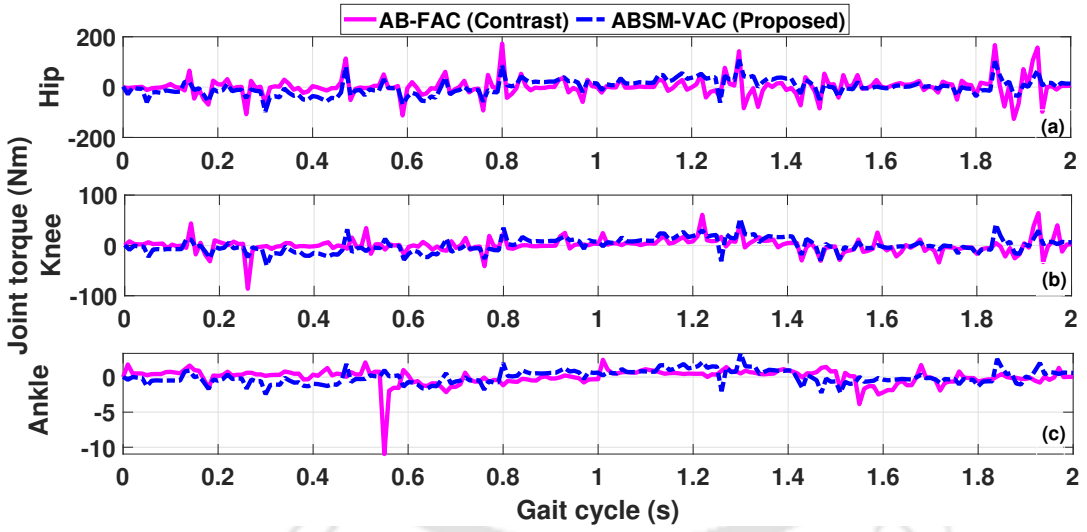

FIGURE 5.17: Joint torques for (a) hip, (b) knee, and (c) ankle using contrast and proposed control under the effect of sudden reflex

TABLE 5.4: Comparative performance analysis of the proposed control over the contrast control during the active-assist rehabilitation

Joint	Tracking Performance (RMSE, °)		PI (%)	Torque Performance (RMST, Nm)		PI (%)
	Contrast Control (AB-FAC)	Proposed Control (ABSM-VAC)		Contrast Control (AB-FAC)	Proposed Control (ABSM-VAC)	
Hip	0.269	0.202	24.90	39.90	31.05	22.18
Knee	0.679	0.724	-6.62	14.94	14.2	4.95
Ankle	0.200	0.189	5.5	1.17	0.95	18.8

5.6 Summary

This work proposes an adaptive backstepping sliding mode-based subject cooperative control scheme for a pediatric lower-extremity exoskeleton robot. The dynamic modeling of the coupled subject-exoskeleton system is briefly presented, considering PPED in a lumped form. A variable admittance model is introduced using the ANFIS approach to mimic the complaint subject-exoskeleton interaction more effectively. A robust adaptive backstepping sliding mode control with rapid reaching law is presented using Lyapunov theory to follow the reference gait trajectory under dynamic uncertainties. Finally, the performance of the proposed control is compared with the ABC with fixed admittance parameters for two different therapeutic cases. In case of active-assist mode with sudden reflex, the performance of the proposed ABSM-VAC has been found better by 26.9% and 5.7% for tracking the reference hip and ankle joint, respectively as compared to the AB-FAC. However, in case of knee joint, the proposed control underperformed marginally with PI of 6.6% due to the simultaneous effect of sudden reflex and variable admittance model. The proposed cooperative control has outperformed the contrast control for safe human-robot interaction, efficacious active participation, precise gait tracking, and less chattering. However, in the proposed control, error states obtained from reference and actual trajectory have been converged to specified tolerance level near the end of the gait cycle due to active participation of the subject. Therefore, another human-in-the-loop subject-cooperative control is introduced In the next chapter for finite-time convergence of the tracking error states.

Chapter 6

Adaptive Backstepping Integral Singularity-Free Fast Terminal Sliding Mode Subject Cooperative Control for Active-Assist Gait Tracking of the Pediatric Exoskeleton

6.1 Introduction

In this chapter, the previously designed ABSM-SCC is improved for the finite time convergence of the error states to the origin on the sliding surface. At first, an admittance model with fixed parameters is briefly presented in Section 6.2. Thereafter, an integral singularity-free fast terminal sliding mode (ISFFTSM) surface is selected and involved with the adaptation law of the backstepping process in Section 6.3. As the proposed approach exploits the ISFFTSM and ABC and can be redefined similarly to the high order sliding mode control (HOSMC), it can preserve the caliber of the ABC, integral terminal sliding mode control (ITSMC), singularity-free fast terminal sliding mode control (SFFTSMC), and high order sliding mode (HOSM), simultaneously [219–221]. The results of the proposed control are compared with ABSM-SCC and discussed in Section 6.4. The proposed approach guarantees finite time convergence while avoiding singularity issues, fast

transient response, better tracking performance, and minimal chattering. Section 6.5 summarizes the concluding remarks of the chapter.

6.2 Admittance Model

If the desired (original human) gait trajectory is $q_{j,h}$ and the reference (modified) gait trajectory is $q_{j,\alpha}$, then the admittance model can be designed as

$$M_a\left(\ddot{q}_{j,h}-\ddot{q}_{j,\alpha}\right)+C_a\left(\dot{q}_{j,h}-\dot{q}_{j,\alpha}\right)+K_a\left(q_h-q_{j,\alpha}\right)=\tau_{j,int} \tag{6.1}$$

$$\ddot{q}_{j,\alpha}=\ddot{q}_{j,h}-M_a^{-1}\left\{C_a\left(\dot{q}_{j,h}-\dot{q}_{j,\alpha}\right)+K_a\left(q_{j,h}-q_{j,\alpha}\right)-\tau_{j,int}\right\} \tag{6.2}$$

where M_a, C_a, K_a denotes the inertia, damping and stiffness admittance parameters. Furthermore, in a real scenario where the subject's movement is significantly less due to insufficient muscle strength, the acceleration term with inertial coefficient (M_a) could be ignored. In low-level admittance, the parameters are decreased to attain flexibility, while in high-level admittance, the parameters are increased for the user's safety. However, in this work, to reduce the computational complexity of the proposed ABISFFTSM-SCC control, the fixed admittance model is selected instead of the variable admittance model.

6.3 Adaptive Backstepping ISFFTSM Position Control

In this section, the concept of the finite-time sliding surface is combined with a backstepping approach and adaptive law to design a robust architecture of gait tracking control for the pediatric gait exoskeleton robot during active-assist training mode. At first, an integral singularity-free fast terminal sliding (ISFFTS) surface is considered based on the error states to achieve a fast transient response and finite-time convergence without singularity phenomena. Moreover, an improved power reaching law from Section 5.4 is used for rapid convergence of error states to the sliding surface. Finally, the robust ABISSFFTSM control scheme is proposed for the exoskeleton robot having the lumped effect of model uncertainties and external disturbances. Inherently, the stability of the proposed control is ensured through the Lyapunov-based stepwise backstepping design process, which includes the first, second, and third order of the sliding surface.

The ISFFTS surface is inspired by [222] and can be expressed as follows:

$$s_1 = \int \left(\xi_a + k_{1m}{\xi_a}^{[l_o]} + k_{2m}\dot{\xi}_a^{[p_o/q_o]}\right) \tag{6.3}$$

where, ξ_a denotes the tracking error between actual $(q_{j,e})$ and reference $(q_{j,\alpha})$ trajectory; k_{1m}, k_{2m} are the positive definite diagonal matrices; p_o and q_o are positive odd numbers satisfying the relation $1 < p_o/q_o < 2$ and $l_o > p_o/q_o$.

Similar to the ABSM control scheme in Chapter 5, this work also exploits the rapid reaching law (Equation 5.15) with approaching time t_a (Equation 5.19) to move the error state to the sliding surface. Moreover, as the sliding surface in Equation 6.3 converges to zero with ξ_a being the terminal attractor. The finite time t_c taken by the error state to slide from time $\xi_a\,(t_a) \neq 0$ to time $\xi_a\,(t_a + t_c) = 0$ is expressed as [222].

$$t_c = \frac{\frac{p_o}{q_o}\left|r_{1a}\,(t_a)\right|^{1-\frac{q_o}{p_o}}}{k_{1m}\left(\frac{p_o}{q_o}-1\right)} \cdot \aleph\left(\frac{q_o}{p_o}, \frac{\frac{p_o}{q_o}-1}{(l_o-1)\frac{p_o}{q_o}}; 1 + \frac{\frac{p_o}{q_o}-1}{(l_o-1)\frac{p_o}{q_o}}; -k_{1m}\left|r_{1a}\,(t_a)\right|^{l_o-1}\right) \tag{6.4}$$

where $\aleph$ denotes Gauss' hypergeometric function. Differentiating the sliding surface for the first and second derivative as follows:

$$\dot{s}_1 = \xi_a + k_{1m}\xi_a^{[l_o]} + k_{2m}\dot{\xi}_a^{\,[p_o/q_o]} \tag{6.5}$$

$$\ddot{s}_1 = \dot{\xi}_a + k_{1m}l_o|\xi_a|^{l_o-1}\cdot\dot{\xi}_a + k_{2m}\frac{p_o}{q_o}|\dot{\xi}_a|^{(p_o/q_o)-1}\cdot\ddot{\xi}_a \tag{6.6}$$

Employing the Equations 5.12, 6.5, and 6.6, the second-order state space form of the coupled subject-exoskeleton system can be converted into a third-order state space form based on the error state and sliding surface as

$$\begin{aligned}
\dot{s}_1 &= s_2\\
\dot{s}_2 &= s_3\\
\dot{s}_3 &= \frac{d}{dt}\begin{pmatrix} \dot{\xi}_a + k_{1m}l_o|\xi_a|^{l_o-1}\cdot\dot{\xi}_a + k_{2m}\frac{p_o}{q_o}|\dot{\xi}_a|^{(p_o/q_o)-1} \times {\mathcal{M}_{oe}}^{-1}(q_{j,e}) \\ \left(\tau_{j,e} - \tau_{j,int} + \rho - \mathcal{C}_{oe}(q_{j,e},\dot{q}_{j,e})\dot{q}_{j,e} - \mathcal{G}_{oe}(q_{j,e}) - \mathcal{M}_{oe}(q_{j,e})\ddot{q}_{j,\alpha}\right)\end{pmatrix}\\
&= \frac{d}{dt}\Big(\mathbb{X}(\xi_a,\dot{\xi}_a) + \mathbb{Y}(\dot{\xi}_a) \times \left({\mathcal{M}_{oe}}^{-1}(q_{j,e})\left(\tau_{j,e} - \tau_{j,int}\right) + \nabla + f(r_{1a}, r_{2a}) - \ddot{q}_{j,\alpha}\right)\Big)
\end{aligned} \tag{6.7}$$

where $\mathbb{X}(\xi_a,\dot{\xi}_a) = \dot{\xi}_a + k_{1m}l_o\left|\xi_a\right|^{l_o-1}\cdot\dot{\xi}_a$, $\mathbb{Y}(\dot{\xi}_a) = k_{2m}\left(\frac{p_o}{q_o}\right)\left|\dot{\xi}_a\right|^{(p_o/q_o)-1}$, $\nabla = {\mathcal{M}_{oe}}^{-1}\rho$ and $f(r_{1a}, r_{2a}) = {\mathcal{M}_{oe}}^{-1}\big(-\mathcal{C}_{oe}(q_{j,e},\dot{q}_{j,e})\dot{q}_{j,e} - \mathcal{G}_{oe}(q_{j,e})\big)$.

Given the cooperative pediatric-exoskeleton dynamic model in Equation 5.12 and third-order state space form of sliding surface in Equation 6.7 with rapid reaching law ($\dot{s}$) in Equation 5.19, if the control law can be selected as

$$\tau_{j,e} = \tau_{j,int} + \Upsilon(\dot{\xi}_a)^{-1}\mathcal{M}_{oe}\left(q_{j,e}\right)\left(\tau_s(t) - \tau_{ap}(t)\right) \tag{6.8}$$

where

$$\tau_s(t) = -\Upsilon(\dot{\xi}_a)\left(f\left(r_{1a}, r_{2a}\right) - \ddot{q}_{j,\alpha}\right) - \aleph(\xi_a, \dot{\xi}_a) + \mathfrak{o}_2 - \int\left(\S_3\vartheta_3 + \vartheta_2\right) \tag{6.9}$$

$$\tau_{ap}(t) = \int\left(\dot{\hat{\mathfrak{r}}} + \kappa_1|\vartheta_3|^{\beta_1(\vartheta_3)} + \kappa_2|\vartheta_3|^{\beta_2(\vartheta_3)}\right)\mathrm{sgn}\left(\vartheta_3\right) \tag{6.10}$$

$$\vartheta_2 = s_2 + \S_1\vartheta_1 \tag{6.11}$$

$$\vartheta_3 = \aleph\left(\xi_a, \dot{\xi}_a\right) + \Upsilon\left(\dot{\xi}_a\right)\ddot{\xi}_a - \mathfrak{o}_2 \tag{6.12}$$

$$\mathfrak{o}_2 = \left(\S_2\vartheta_2 - \vartheta_1 - \S_1 s_2\right) \tag{6.13}$$

where $\S_1, \S_2, \S_3$ are positive design parameter, and $\hat{\mathfrak{r}}$ is the upper bound estimation of $\mathfrak{r}$ which holds the relation $\left|(d/dt)(\Upsilon(\dot{\xi}_a)\nabla)\right| \leq \mathfrak{r}$ and can be modeled with an adaptive law as

$$\dot{\hat{\mathfrak{r}}} = \frac{1}{d_c}\left|\vartheta_3\right|; \quad d_c: \quad \text{user defined constant} \tag{6.14}$$

to deal with parametric perturbations and external disturbances, then the error state (ξ_a) rapidly converges to equilibrium point in finite time.

A stepwise backstepping design is exploited to obtain the required control input of the cooperative system (Equation 6.7). The following modified coordinates are considered:

$$\vartheta_1(t) = s_1(t) \tag{6.15}$$

$$\vartheta_2(t) = s_2(t) - \mathfrak{o}_1 \tag{6.16}$$

$$\vartheta_3(t) = s_3(t) - \mathfrak{o}_2 \tag{6.17}$$

where $\mathfrak{o}_i (i = 1, 2)$ denotes the virtual control law in the ith step.

Step 1:

Considering a Lyapunov candidate function as

$$V_1 = (1/2){\vartheta_1}^T\vartheta_1 \tag{6.18}$$

Differentiating Equation 6.18 over time and using Equations 6.15 and 6.16, one can get

$$\dot{V}_1 = \vartheta_1 \left(\vartheta_2 + \mathfrak{a}_1\right) \tag{6.19}$$

Selecting the virtual control law $\mathfrak{a}_1$ as follows

$$\mathfrak{a}_1(t) = -\S_1 \vartheta_1(t) \tag{6.20}$$

where $\S_1$ is a positive design parameter.

Substituting Equation 6.20 into Equation 6.18,

$$\dot{V}_1 = -\S_1 \left|\vartheta_1\right|^2 + \vartheta_1 \vartheta_2 \tag{6.21}$$

It can be observed from Equation 6.21 that $\dot{V}_1 = -\S_1 \left|\vartheta_1\right|^2$ when $\vartheta_2 = 0$, and therefore, ϑ_1 will be asymptotically stable.

Step 2:

Considering another Lyapunov candidate function based on first one as follows:

$$V_2 = V_1 + \frac{1}{2}\vartheta_2^2 \tag{6.22}$$

Differentiating the above Equation 6.22 with respect to time and using Equations 6.16 and 6.7 , one can get

$$\dot{V}_2 = \dot{V}_1 + \vartheta_2 \dot{\vartheta}_2 \tag{6.23}$$

$$= \dot{V}_1 + \vartheta_2 (\dot{s}_2 - \dot{\mathfrak{a}}_1) \tag{6.24}$$

$$= \dot{V}_1 + \vartheta_2 (\vartheta_3 + \mathfrak{a}_2 + \S_1 s_2) \tag{6.25}$$

Now, selecting the second virtual control law as

$$\mathfrak{a}_2(t) = -\S_2 \vartheta_2 - \vartheta_1 - \S_1 s_2. \tag{6.26}$$

where, $\S_2$ is another design parameter.

Substituting the Equation 6.26 into Equation 6.23,

$$\begin{aligned} \dot{V}_2 &= -\S_1 \left|\vartheta_1\right|^2 + \vartheta_1 \vartheta_2 + \vartheta_2 \left(\vartheta_3 - \S_2 \vartheta_2 - \vartheta_1\right) \\ &= -\S_1 \left|\vartheta_1\right|^2 - \S_2 \left|\vartheta_2\right|^2 + \vartheta_2 \vartheta_3 \end{aligned} \tag{6.27}$$

It can be observed from Equation 6.27 that $\dot{V}_2 = -\S_1 |\vartheta_1|^2 - \S_2 |\vartheta_2|^2$ when $\vartheta_3 = 0$, and therefore, ϑ_1 and ϑ_2 will be asymptotically stable.

Step 3:

Considering the third Lyapunov candidate function based on the second one as follows:

$$V_3 = V_2 + \frac{1}{2}\vartheta_3^2 + \frac{1}{2}d_c\tilde{\mathbb{r}}^2 \tag{6.28}$$

where $\tilde{\mathbb{r}} = \mathbb{r} - \hat{\mathbb{r}}$ is the estimation error.

Differentiating the above Equation 6.28 with respect to time and using Equations 6.17 and 6.7, one can get

$$\begin{aligned}
\dot{V}_3 &= \dot{V}_2 + \vartheta_3\dot{\vartheta}_3 + d_c(\hat{\mathbb{r}} - \mathbb{r})\dot{\hat{\mathbb{r}}} \\
&= -\S_1 |\vartheta_1|^2 - \S_2 |\vartheta_2|^2 + \vartheta_2\vartheta_3 + \vartheta_3\Bigg(\frac{d}{dt}\Big(\mathbb{X}(\xi_a, \dot{\xi}_a) + \mathbb{Y}(\dot{\xi}_a)\times \\
&\quad \big(\mathcal{M}_{oe}{}^{-1}(q_{j,e})\big(\tau_{j,e} - \tau_{j,int}\big) + \nabla + f(r_{1a}, r_{2a}) - \ddot{q}_{j,\alpha}\big)\Big) - \dot{\Phi}_2\Bigg) + d_c(\hat{\mathbb{r}} - \mathbb{r})\dot{\hat{\mathbb{r}}}
\end{aligned} \tag{6.29}$$

Now, incorporating the proposed control law from Equation 6.8 and adaptive law from Equation 6.14 to the above Equation 6.29,

$$\begin{aligned}
\dot{V}_3 &= -\S_1 |\vartheta_1|^2 - \S_2 |\vartheta_2|^2 - \xi_3 |\vartheta_3|^2 + \vartheta_3\frac{d}{dt}\Big(-\tau_{ap} + \mathbb{Y}(\dot{\xi}_a)\nabla\Big) + d_c(\hat{\mathbb{r}} - \mathbb{r})\dot{\hat{\mathbb{r}}} \\
&= -\S_1 |\vartheta_1|^2 - \S_2 |\vartheta_2|^2 - \S_3 |\vartheta_3|^2 + d_c(\hat{\mathbb{r}} - \mathbb{r})\dot{\hat{\mathbb{r}}} \\
&\quad + \vartheta_3\Big(-\big(\dot{\hat{\mathbb{r}}} + \kappa_1|\vartheta_3|^{\beta_1(\vartheta_3)} + \kappa_2|\vartheta_3|^{\beta_2(\vartheta_3)}\big)\,\mathrm{sign}\,(\vartheta_3) + \frac{d}{dt}\big(\mathbb{Y}(\dot{\xi}_a)\nabla\big)\Big) \\
&\leq -\S_1 |\vartheta_1|^2 - \S_2 |\vartheta_2|^2 - \S_3 |\vartheta_3|^2 - \big(\mathbb{r} + \kappa_1|\vartheta_3|^{\beta_1(\vartheta_3)} + \kappa_2|\vartheta_3|^{\beta_2(\vartheta_3)}\big)\,|\vartheta_3| \\
&\quad + \frac{d}{dt}\big(\mathbb{Y}(\dot{\xi}_a)\nabla\big)\,|\vartheta_3| \\
&\leq -\S_1 |\vartheta_1|^2 - \S_2 |\vartheta_2|^2 - \S_3 |\vartheta_3|^2
\end{aligned} \tag{6.30}$$

Following above Equation 6.30, it is found that $\dot{V}_3 \leq 0$ and negative semidefinite, which proves that $\vartheta_1(t), \vartheta_2(t)$, and $\vartheta_3(t)$ converges to zero in a finite time. Therefore, in cooperative active-assist mode, it can be concluded that the gait tracking error (ξ_a) rapidly converges to the origin in finite time under parametric perturbations and external disturbances using the proposed ABISFFTSM-based subject cooperative control scheme. The complete architecture of the proposed controller is shown in Figure 6.1.

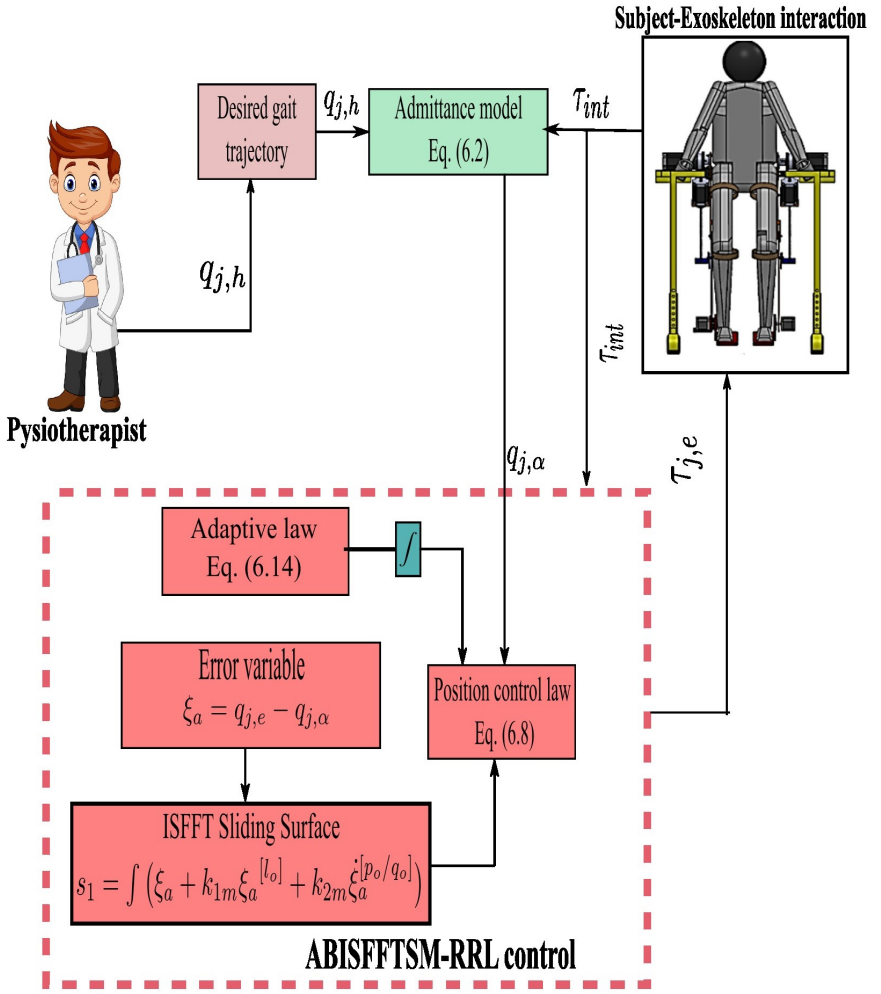

FIGURE 6.1: ABISFFTSM-SCC control architecture

6.4 Results and Discussions

In this section, the performance of the proposed ABISFFTSM-SCC control is examined using various simulation runs while comparing it to the contrast control (ABSM-SCC). The LLESv 2 is considered along with the pediatric subject of age 08 years, body mass 34 kg, body height 128 cm (C6 from Table 2.7). The simulation runs in this chapter are carried out in MATLAB/Simulink R2020b (ode45 solver with variable step and adaptive zero crossing algorithm). The uncertain model parameter, external disturbances, Coulomb friction, and viscous velocity factor are considered as $\delta = 0.2, \tau_d = \big[\big(3sin(2t) + 2 \times random(1)\big), \big(2sin(2t) + random(1)\big), \big(sin(2t) + t\big)\big]^T, C_f = [0.8, 0.8, 0.8]^T, \sigma = [1.2, 1.2, 1.2]^T$ to validate the robustness of the inner loop position control. The control parameters in AB-ISFFTSM control and ABSM control with RRL are given in Table 6.1. The fixed admittance parameters in the proposed and contrast control are $M_a =$

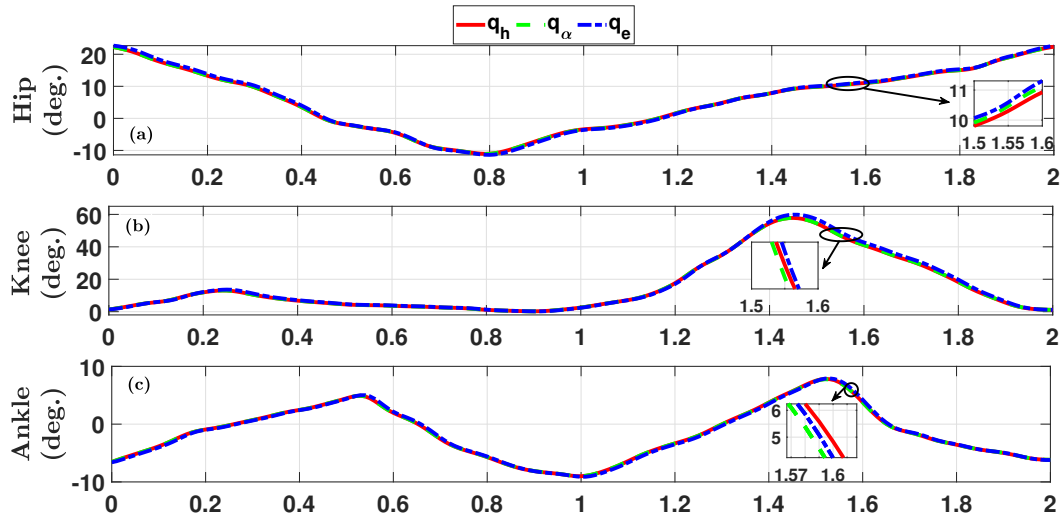

FIGURE 6.2: Trajectory tracking for (a) hip, (b) knee, and (c) ankle joint using contrast control (ABSM-SCC)

$diag(15, 15, 12)$, $C_a = diag(5, 5, 5)$ and $K_a = diag(200, 200, 200)$. In Eq. 2.16, the damping and spring coefficients for the bracing straps are selected as $c = [10, 10, 2]^T$ and $k = [200, 200, 20]^T$. The limits of admittance parameters are selected based on the numerical iterations around the fixed admittance values.

TABLE 6.1: Control Parameters

Control Scheme	Parameter value
ABISFFTSM with RRL	$\kappa_{1m} = diag(10, 10, 10), \kappa_{2m} = diag(5, 5, 5)$, $l_o = 1.8, p_o = 9, q_o = 7$, $\S_1 = diag(250, 250, 250), \S_2 = diag(100, 100, 100)$, $\S_3 = diag(10, 10, 10), d_c = 0.5$, $\kappa_1 = 18, \kappa_2 = 32$, $\varepsilon_0 = 0.25, \varepsilon_1 = 0.8, \varepsilon_2 = 0.06, \mu = 5, \eta = 1.4$
ABSM with RRL	$\lambda_p = 10, h = 22, \nu = diag(120, 66, 65)$, $\Gamma_c = diag(0.1, 0.1, 0.1), \kappa_1 = 20, \kappa_2 = 32$, $\varepsilon_0 = 0.15, \varepsilon_1 = 0.6, \varepsilon_2 = 0.05, \mu = 5$, and $\eta = 1.5$.

Following the AA training mode, subjects exert the recovered/residual muscle energy of their lower-limbs for the desired movement, and the exoskeleton needs to follow the same as quickly as possible via the proposed cooperative control. The tracking of joint variables for the contrast and proposed control using the relevant control parameters and admittance values is shown in Figures 6.2 and 6.3. From Figures 6.2(a), 6.3(a), and 6.4(a), the deviation between actual (q_e) and reference (modified) (q_α) hip joint trajectory is found to less in case of proposed cooperative control ($RMSE_{ABISFFTSM-SCC} : 0.131°$) as compared to the contrast control ($RMSE_{ABSM-SCC} : 0.214°$). From Figures 6.2(b), 6.3(b), and 6.4(b), a

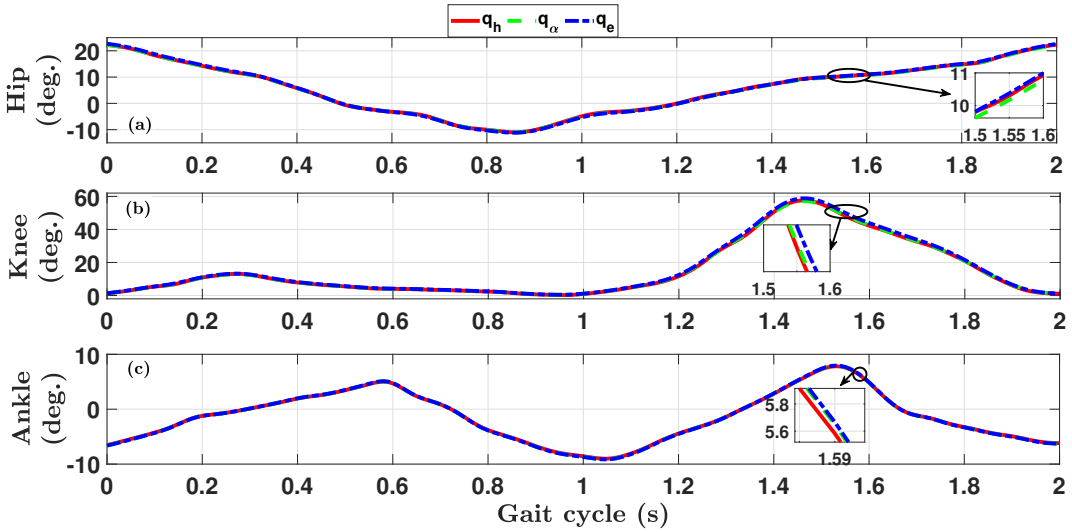

FIGURE 6.3: Trajectory tracking for (a) hip, (b) knee, and (c) ankle joint using proposed control (ABISFFTSM-SCC)

similar trend of joint error ($q_{j,\alpha}$) is noted for knee joint ($RMSE_{ABISFFTSM-SCC}$: 0.291°, $RMSE_{ABSM-SCC}$: 0.592°). In case of ankle joint (Figures 6.2(c), 6.3(c), and 6.4(c)), although the trend is similar to hip and knee joint, there is a substantial difference between joint error of proposed ($RMSE_{ABISFFTSM-SCC}$: 0.026° and contrast control $RMSE_{ABSM-SCC}$: 0.134°). The tracking performance is summarized in Table 6.2.

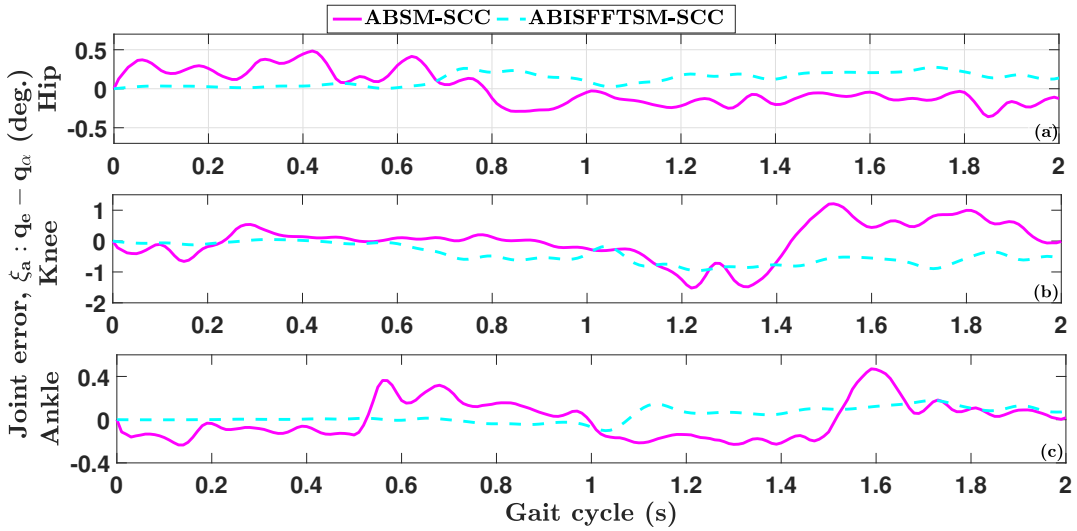

FIGURE 6.4: Trajectory tracking error for (a) hip, (b) knee, and (c) ankle joint using contrast and proposed control

The sliding function (s) for hip, knee, and ankle joints is plotted in Figure 6.5(a)-(c) to understand the convergence behavior of both controllers. It is clearly evident that the function value is rapidly converging within the finite time for the proposed

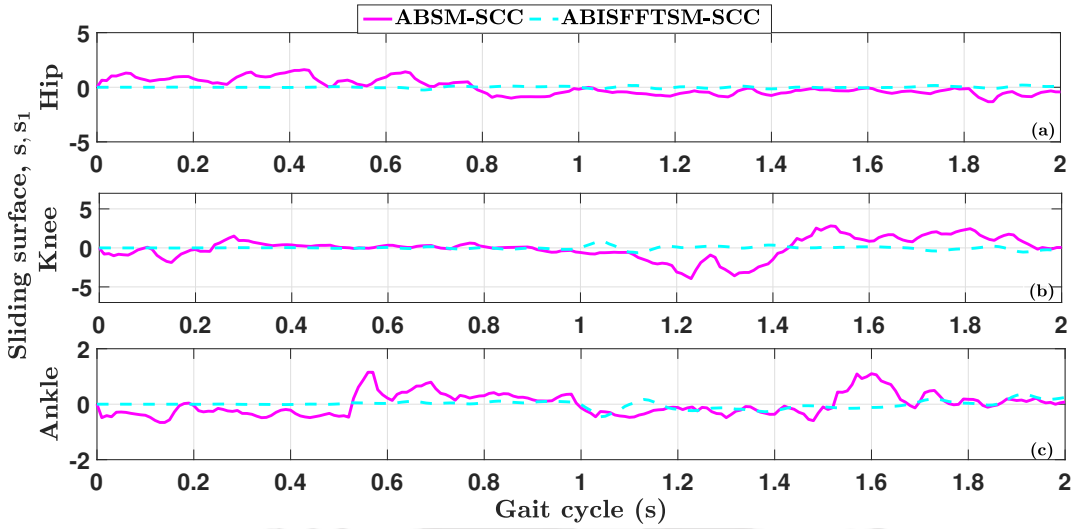

FIGURE 6.5: Plot of sliding variable for contrast (ABSM-SCC) and proposed control (ABISFFTSM-SCC)

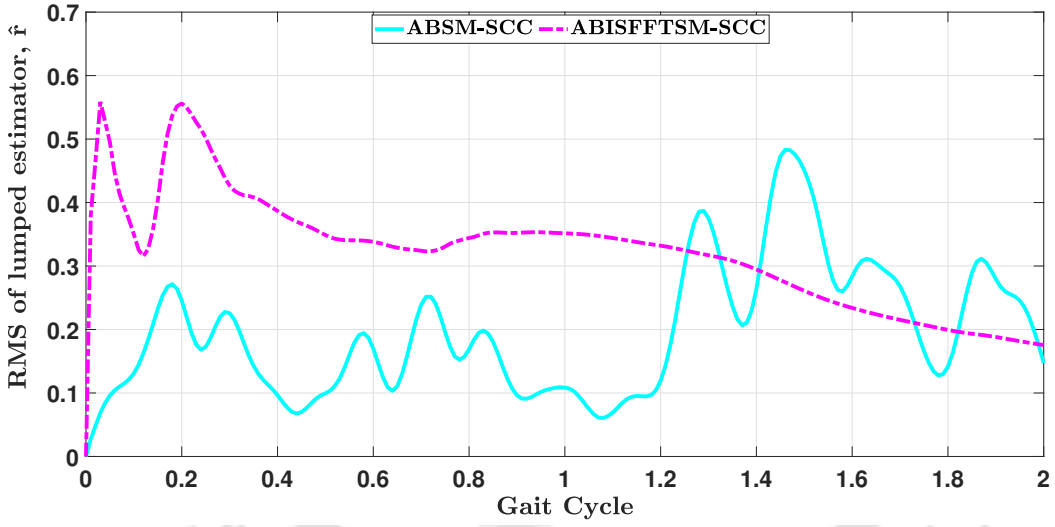

FIGURE 6.6: Plot of root mean square error of lumped parameter estimation for contrast (ABSM-SCC) and proposed control (ABISFFTSM-SCC)

controller and enters the settling phase from the beginning of the gait cycle. On the other hand, the sliding function delays the convergence process in the case of contrast control scheme and reaches the settling phase at 1.97 s, 1.95 s, and 1.94 s for hip, knee, and ankle joints, respectively. Furthermore, Figure 6.6(presents the root mean square error (RMSE) of lumped parameter estimation ($\hat{r}$) for both the controllers. Starting with the error value of 0.0012 and ending with the error value of 0.18, the estimation for the parametric perturbations and external disturbances is found to be more accurate and congregating for the proposed ABISFFTSM-SCC control. However, the contrast control can estimate the uncertainties and disturbances randomly, starting With a value of 0.011 at starting and 0.16 at

the end of the gait cycle. For the next gait cycle, similar observations are found due to the same control action applied on the healthy gait trajectory for another two seconds. Therefore, the plots are presented for a single gait cycle to avoid repetitive results.

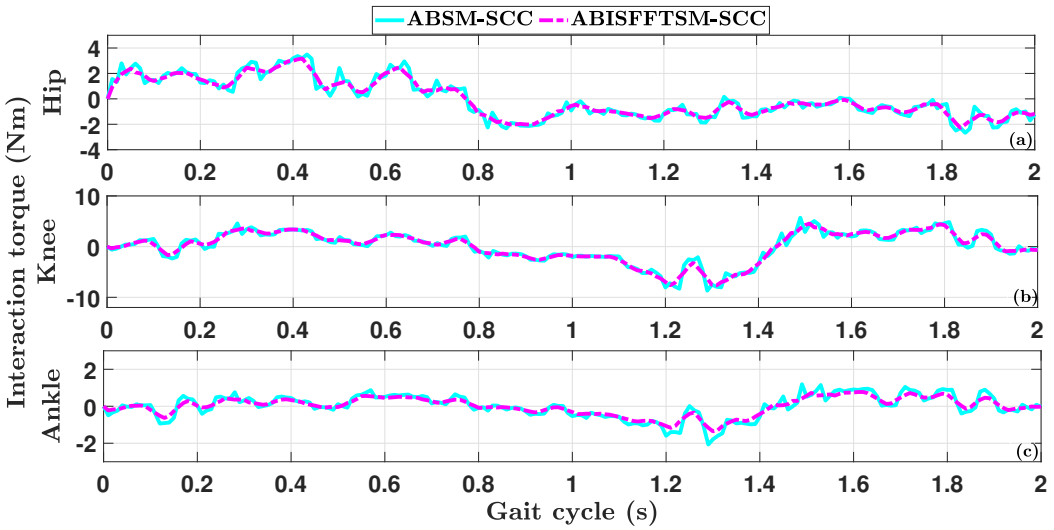

FIGURE 6.7: Interaction torques for (a) hip, (b) knee, and (c) ankle joint using contrast and proposed control

Figure 6.7(a)-(c) presents the interaction torques produced due to the subject active participation in AA rehabilitation mode. It can be deduced that interaction torques are marginally less generated with the proposed control (ABISFFTSM-SCC) as compared to the contrast control (ABSM-SCC). More specifically, in the stance phase, the proposed control offers less active participation to the subject's hip joint than the knee and ankle joints.

From Figure 6.7 and 6.8, it is worth-noted that for similar values of interaction torques with both control approaches, the proposed control require less amount of torques. Inferring Figure 6.8(a), 6.8(b), and 6.8(c), lesser joint torques are produced using proposed control ($RMST_{ABISFFTSM-SCC}$: 49.51 Nm for hip, 16.69 Nm for knee, and 0.47 Nm for ankle) as compared to the contrast control ($RMST_{ABSM-SCC}$: 52.04 Nm for hip, 17.53 Nm for knee, and 0.51 Nm for ankle). The overall torque performance is compiled in Table 6.2. Therefore, it can be concluded that the very precise tracking of reference gait trajectory is possible with the lesser amount of joint torques of the proposed cooperative control, irrespective of the subject's active participation.

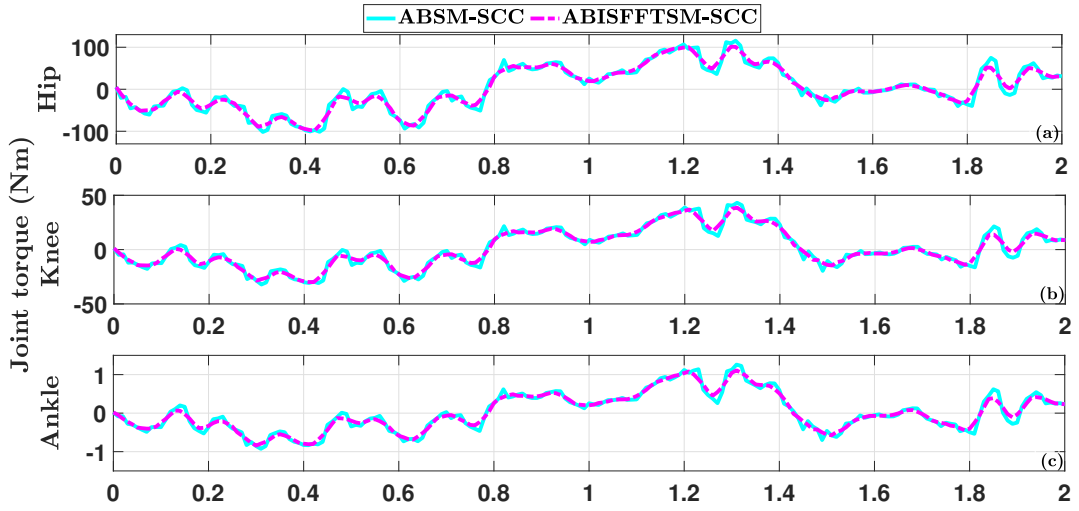

FIGURE 6.8: Joint torques for (a) hip, (b) knee, and (c) ankle using contrast and proposed control

TABLE 6.2: Comparative performance analysis of the proposed control over the contrast control during the active-assist rehabilitation

Joint	Tracking Performance (RMSE, °)		PI (%)	Torque Performance (RMST, Nm)		PI (%)
	Contrast Control (ABSM-SCC)	Proposed Control (ABISFFTSM-SCC)		Contrast Control (ABSM-SCC)	Proposed Control (ABISFFTSM-SCC)	
Hip	0.214	0.131	38.78	52.04	49.51	4.86
Knee	0.592	0.291	50.84	17.53	16.69	4.79
Ankle	0.134	0.026	80.59	0.51	0.47	7.84

6.5 Summary

In this chapter, an adaptive backstepping approach is augmented with an integral singularity-free fast terminal sliding mode control scheme to attain the finite time convergence of error states in active-assist mode. A fixed admittance model is considered in the outer loop to regulate the interaction forces based on the subject's active participation. It has been observed from the simulation runs that the proposed ABISFFTSM-SCC outperformed the contrast ABSM-SCC by 38.78%, 50.84%, 80.59% for hip, knee, and ankle joint tracking, respectively. Moreover, the proposed control requires less coupled joint torque than contrast control. Overall, the proposed control has been found to be effective in achieving fast and finite-time convergence of the error states to the origin, along with minimal chattering in the active-assist mode of gait rehabilitation.

Chapter 7

Conclusion and Future Work

7.1 Introduction

In this chapter, the general and specific conclusions on the different designs of robust control schemes for the newly developed lower-limb exoskeleton systems (LLES$v1$ and LLES$v2$) in passive-assist and active-assist mode are presented extensively. At first, the concluding remarks on the design and development of the pediatric exoskeletons are enlisted. The critical observations on the design of passive-assist gait tracking control schemes are pointed out. Thereafter, conclusions are made on the active-assist subject-cooperative gait tracking control schemes. Finally, the scope of future work is also highlighted in the chapter.

7.2 Conclusions

7.2.1 Design, Modeling, and Prototype Development of Pediatric Gait Exoskeleton

- A new stand-aided lower-limb exoskeleton system has been designed in two stages (LLES$v1$ and LLES$v2$) for the gait rehabilitation and motion assistance of pediatric population (8-12 years) in sagittal plane.
- A MS Kinect-Labview experimental motion capture setup has been established to identify the healthy joint angles of the subjects.

- The dynamic modeling of the exoskeleton has been carried out for passive- and active-assist rehabilitation mode.
- A proof-of-concept exoskeleton prototype has been developed with estimated actuators and hardware components.

7.2.2 Robust Intelligent Control Techniques for Passive-Assist Gait Tracking of the Pediatric Exoskeleton

- A robust LQR-NF control scheme is introduced for the exoskeleton system to track the desired gait in passive-assist mode. An input-output linearization approach has been employed to transform the non-linear model to linear one before applying LQR control.
- The performance of the proposed control has been found better by 65.5%, 44.5%, and 23.52% while perturbation the system's masses by 30% and compared to the ERL-SMC contrast control.
- Another intelligent controller, NF-CPID, has been proposed to deal with external disturbances along with PP. An online adaptation of weights has been incorporated to compensate the PPED.
- It has been observed that NF-CPID control performs less effectively in case of PP only as compared to contrast control (RLQR-NF), especially in the swing phase of the gait cycle. However, in case of PPED, a significant improvement is noted for the NF-CPID control (PI_{hip}: 43.03%, PI_{Knee}: 33.37%, PI_{ankle}: 12.28%).
- An experimental validation has been carried out for LLES$v1$ coupled with a child dummy. The proposed NF-CPID has been found effective by 71.8%, 59.5%, and 32.15% for the respective lower-limb joint tracking.
- Although less than the contrast control, a considerable noise has been observed in the experimental results with NF-CPID control. Moreover, the computational complexity augments due to the iterative tuning and selection of neural-fuzzy hyperparameters.

7.2.3 Robust Adaptive Backstepping Control for the Passive-Assist Gait Exoskeleton with Model Uncertainties and External Disturbances

- An implicit Lyapunov-based adaptive backstepping control approach has been presented for precise gait tracking, lessen the computational complexity and reducing the noise in the presence of PPED. The implicit Lyapunov-based design approach ensures the uniform boundedness of the closed-loop signals under PPED.
- The well-known complexities of the classical backstepping control, i.e., over-parameterization and explosion of terms have been avoided by postponing the parameters' estimation to last design step and absence of inertial, centrifugal, and gravity derivatives in the virtual control law, respectively.
- The proposed RABS control has been tested with an experimental setup of LLES$v2$ coupled with a pediatric subject of GMFCS-Level III. The performance has been improved by 55.32%, 40.59%, 64.88% for hip, knee, and ankle joint, respectively as compared to NF-CPID control.
- The number of parameter estimates ($n_{\hat{\Omega}} = 11$) has been found less than the number of unknown parameters ($n_{\hat{\Omega}}$=16) which supports the avoidance of 'overparameterization' phenomena.

7.2.4 Robust Adaptive Backstepping Sliding Mode Subject-Cooperative Control for a Pediatric Lower- Extremity Exoskeleton Robot

- A human-in-the-loop cooperative control based on trajectory tracking and subject-exoskeleton interaction has been proposed where ANFIS-based variable admittance model has been considered to regulate the subject's participation. For admittance-modified gait tracking, a robust adaptive backstepping sliding mode with rapid reaching law has been proposed.
- The co-simulation results have been presented for active-assist mode aided with sudden reflex. The performance of the proposed ABSM-VAC has been found better by 26.9% and 5.7% for tracking the reference hip and ankle joint, respectively as compared to the AB-FAC. However, in case of knee

joint, the proposed control underperformed marginally with PI of 6.6% due to the simultaneous effect of sudden reflex and variable admittance model.

- The results of the reference gait trajectory have shown that the proposed ABSM-VAC can stiffen the robot during the start and end of the gait trajectory for effective tracking.
- The decreased stiffness parameter has allowed flexibility to the robot and the safety of the subject in case of sudden reflex.

7.2.5 Adaptive Backstepping Integral Singularity-Free Fast Terminal Sliding Mode-based Subject Cooperative Control for the Pediatric Gait Exoskeleton Device

- An ABISFFTSM-based subject cooperative control has been designed for the exoskeleton system to achieve the finite-time convergence of error states and improve the tracking performance of ABSM with fixed admittance values.
- This proposed approach has exploited the merits of integral terminal sliding mode and higher order sliding mode control with adaptive backstepping control. A fixed admittance model has been considered in the outer loop control to regulate the interaction forces.
- The proposed ABISFFTSM-SCC has outperformed the ABSM-SCC by 30.84%, 10.47%, and 56.89% for tracking the reference hip, knee, and ankle joint, respectively.
- The sliding function has shown the potential of proposed cooperative control to converge the error states in finite-time as compared to ABSM-SCC.

7.3 Scope of the Future Work

In this work, a 3-DOFs LLES has been designed for the gait rehabilitation of pediatric subjects in the sagittal plane. Thereafter, few robust control schemes have been designed for a pediatric exoskeleton system in passive-and active-assist modes. However, simulation and experimental investigations are limited to the passive-assist control of the pediatric exoskeleton due to the unavailability of the required subject and time constraints. Therefore, the present work can be extended as follows:

- The design, modeling, and control can be extended to incorporate the remaining two planes, i.e., transverse and frontal plane in passive-and active-assist modes.
- The experimental validations may be carried out for the proposed cooperative control schemes to understand the subject's contribution more clearly.
- Electromyography signals (EMGs)-based supervisory control can be explored for estimating the muscle's interaction of the subject to the exoskeleton.
- The clinical trials with the unhealthy subject can be conducted to test the efficacy of the proposed control schemes.

Appendix A

The element-wise expression of coupled inertia matrix ($M_{(h,e)}$), Coriolis/centrifugal matrix ($C_{(h,e)}$), and gravity matrix ($G_{(h,e)}$) are as follows:

$$M_{(h,e)}(q_{j,e}) = \begin{bmatrix} M_{11(h,e)} & M_{12(h,e)} & M_{13(h,e)} \\ M_{21(h,e)} & M_{22(h,e)} & M_{23(h,e)} \\ M_{31(h,e)} & M_{32(h,e)} & M_{33(h,e)} \end{bmatrix},$$

$$C_{(h,e)}(q_{j,e}\dot{q}_{j,e}) = \begin{bmatrix} C_{11(h,e)} & C_{12(h,e)} & C_{13(h,e)} \\ C_{21(h,e)} & C_{22(h,e)} & C_{23(h,e)} \\ C_{31(h,e)} & C_{32(h,e)} & C_{33(h,e)} \end{bmatrix}, G_{(h,e)}(q_{j,e}) = \begin{bmatrix} G_{1(h,e)} \\ G_{2(h,e)} \\ G_{3(h,e)} \end{bmatrix}$$

$$\begin{aligned}
M_{11(h,e)} =& m_{1(h,e)} l_{c1(h,e)}^2 + I_{1(h,e)} + m_{2(h,e)} \Big(l_{1(h,e)}^2 + l_{c2(h,e)}^2 + 2 l_{1(h,e)} l_{c2(h,e)} \mathbb{C}_2 \Big) \\
& + I_{2(h,e)} + m_{3(h,e)} \Big(l_{1(h,e)}^2 + l_{2(h,e)}^2 + l_{c3(h,e)}^2 + 2 l_{1(h,e)} l_{2(h,e)} \mathbb{C}_2 \\
& + 2 l_{1(h,e)} l_{c3(h,e)} \mathbb{C}_{23} \Big) + I_{3(h,e)} \\
M_{12(h,e)} =& m_{2(h,e)} \Big(l_{c2(h,e)}^2 + l_{1(h,e)} l_{c2(h,e)} \mathbb{C}_2 \Big) + I_{2(h,e)} + m_{3(h,e)} \Big(l_{2(h,e)}^2 + l_{c3(h,e)}^2 \\
& + l_{1(h,e)} l_{2(h,e)} \mathbb{C}_2 + l_{1(h,e)} l_{c3(h,e)} \mathbb{C}_{23} + 2 l_{2(h,e)} l_{c3(h,e)} \mathbb{C}_3 \Big) + I_{3(h,e)} \\
M_{13(h,e)} =& m_{3(h,e)} \Big(l_{c3(h,e)}^2 + l_{1(h,e)} l_{c3(h,e)} \mathbb{C}_{23} + l_{2(h,e)} l_{c3(h,e)} \mathbb{C}_3 \Big) + I_{3(h,e)} \\
M_{22(h,e)} =& m_{2(h,e)} l_{c2(h,e)}^2 + I_{2(h,e)} + m_{3(h,e)} \Big(l_{2(h,e)}^2 + l_{c3(h,e)}^2 + 2 l_{2(h,e)} l_{c3(h,e)} \mathbb{C}_3 \Big) \\
& + I_{3(h,e)} \\
M_{23(h,e)} =& m_{3(h,e)} \Big(l_{c3(h,e)}^2 + l_{2(h,e)} l_{c3(h,e)} \mathbb{C}_3 \Big) + I_{3(h,e)} \\
M_{33(h,e)} =& m_{3(h,e)} l_{c3(h,e)}^2 + I_{3(h,e)} \\
M_{21(h,e)} =& M_{12(h,e)}, M_{13(h,e)} = M_{31(h,e)}, M_{23(h,e)} = M_{32(h,e)}
\end{aligned} \tag{A.1}$$

$$
\begin{aligned}
C_{11(h,e)} =& -2m_{2(h,e)}l_{1(h,e)}l_{c2(h,e)}S_2\dot{q}_{2,e} - 2m_{3(h,e)}l_{1(h,e)}l_{2(h,e)}S_2\dot{q}_{2,e} \\
& - 2m_{3(h,e)}l_{1(h,e)}l_{c3(h,e)}S_{23}\Big(\dot{q}_{2,e}+\dot{q}_{3,e}\Big) - 2m_{3(h,e)}l_{2(h,e)}l_{c3(h,e)}S_3\dot{q}_{3,e} \\
C_{12(h,e)} =& -m_{2(h,e)}l_{1(h,e)}l_{c2(h,e)}S_2\Big(2\dot{q}_{1,e}+\dot{q}_{2,e}\Big) - m_{3(h,e)}l_{1(h,e)}l_{2(h,e)}S_2\Big(2\dot{q}_{1,e}+\dot{q}_{2,e}\Big) \\
& - m_{3(h,e)}l_{1(h,e)}l_{c3(h,e)}S_{23}\Big(2\dot{q}_{1,e}+\dot{q}_{2,e}+\dot{q}_{3,e}\Big) \\
C_{13(h,e)} =& -m_{3(h,e)}l_{1(h,e)}l_{c3(h,e)}S_{23}\Big(2\dot{q}_{1,e}+2\dot{q}_{2,e}+\dot{q}_{3,e}\Big) \\
C_{21(h,e)} =& -2m_{3(h,e)}l_{2(h,e)}l_{c3(h,e)}S_3\dot{q}_{3,e} + \Big(m_{2(h,e)}l_{1(h,e)}l_{c2(h,e)}S_2 \\
& + m_{3(h,e)}\big(l_{1(h,e)}l_{2(h,e)}S_2 + l_{1(h,e)}l_{c3(h,e)}S_{23}\big)\Big)\dot{q}_{1,e} \\
C_{22(h,e)} =& -2m_{3(h,e)}l_{2(h,e)}l_{c3(h,e)}S_3\dot{q}_{3,e} \\
C_{23(h,e)} =& -m_{3(h,e)}l_{2(h,e)}l_{c3(h,e)}S_{3(h,e)}\Big(2\dot{q}_{1,e}+2\dot{q}_{2,e}+\dot{q}_{3,e}\Big) \\
C_{31(h,e)} =& m_{3(h,e)}l_{1(h,e)}l_{c3(h,e)}S_{23}\dot{q}_{1,e} + m_{3(h,e)}l_{2(h,e)}l_{c3(h,e)}S_3\Big(\dot{q}_{1,e}+2\dot{q}_{2,e}\Big) \\
C_{32(h,e)} =& m_{3(h,e)}l_{2(h,e)}l_{c3(h,e)}S_3\Big(2\dot{q}_{1,e}+\dot{q}_{2,e}\Big) \\
C_{33(h,e)} =& 0
\end{aligned}
\tag{A.2}
$$

$$
\begin{aligned}
G_{1(h,e)} =& m_{1(h,e)}gl_{c1(h,e)}S_1 + m_{2(h,e)}g\Big(l_{1(h,e)}S_1 + l_{c2(h,e)}S_{12}\Big) \\
& + m_{3(h,e)}g\Big(l_{1(h,e)}S_1 + l_{2(h,e)}S_{12} + l_{c3(h,e)}S_{123}\Big) \\
G_{2(h,e)} =& m_{2(h,e)}gl_{c2(h,e)}S_{12} + m_{3(h,e)}g\Big(l_{2(h,e)}S_{12} + l_{c3(h,e)}S_{123}\Big) \\
G_{3(h,e)} =& m_{3(h,e)}gl_{c3(h,e)}S_{123}
\end{aligned}
\tag{A.3}
$$

In above expressions,

$S_j = sin(q_{j,e}), S_{jj} = sin(q_{j,e}+q_{j,e})$, and $S_{jjj} = sin(q_{j,e}+q_{j,e}+q_{j,e}) \quad \forall j = 1,2,3$

$\mathbb{C}_j = cos(q_{j,e}), \mathbb{C}_{jj} = cos(q_{j,e}+q_{j,e})$, and $\mathbb{C}_{jjj} = cos(q_{j,e}+q_{j,e}+q_{j,e}) \quad \forall j = 1,2,3.$

Appendix B

The elements of the state-weight factor matrices $(\mathcal{A}, \mathcal{B})$ can be evaluated using following derived formulations. For $\mathcal{A}$ matrix,

$$\begin{aligned}
\alpha_{41} =& -12l_{1(h,e)}l_{2(h,e)}l_{3(h,e)}g\Big(2m^2_{2(h,e)} + 4m_{1(h,e)}m_{2(h,e)} + 3m_{1(h,e)}m_{3(h,e)} \\
&+ 2m_{2(h,e)}m_{3(h,e)}\Big) \\
\tilde{\alpha}_{41} =& 2l_{2(h,e)}l_{3(h,e)}\Big(12l^2_{1(h,e)}m^2_{2(h,e)} + 12l^2_{1(h,e)}m_{2(h,e)}m_{3(h,e)} + 16l^2_{1(h,e)}m_{1(h,e)}m_{2(h,e)} \\
&+ 12l^2_{1(h,e)}m_{1(h,e)}m_{3(h,e)} - 48l_{2(h,e)}l_{3(h,e)}m_{2(h,e)}m_{3(h,e)} - 36l_{2(h,e)}l_{3(h,e)}m^2_{3(h,e)}\Big) \\
\alpha_{42} =& 72l_{1(h,e)}l_{2(h,e)}l_{3(h,e)}g\Big(m^2_{2(h,e)} + m^2_{3(h,e)} + 2m_{2(h,e)}m_{3(h,e)}\Big) \\
\tilde{\alpha}_{42} =& \tilde{\alpha}_{41} \\
\alpha_{43} =& -18gl_{1(h,e)}m_{2(h,e)}m_{3(h,e)} \\
\tilde{\alpha}_{43} =& \frac{\widetilde{\alpha}_{41}}{2l_{2(h,e)}l_{3(h,e)}} \\
\alpha_{51} =& 12g\Big(6l_{1(h,e)}m_{2(h,e)} + 3l_{1(h,e)}m_{3(h,e)} + 4l_{2(h,e)}m_{2(h,e)} + 3l_{2(h,e)}m_{3(h,e)}\Big) \\
&\Big(l_{1(h,e)}m_{2(h,e)} + l_{1(h,e)}m_{3(h,e)} + l_{2(h,e)}m_{3(h,e)} + \frac{l_{1(h,e)}m_{1(h,e)}}{2} \\
&+ \frac{l_{2(h,e)}m_{2(h,e)}}{2} + \frac{l_{3(h,e)}m_{3(h,e)}}{2}\Big) \\
\tilde{\alpha}_{51} =& \tilde{\alpha}_{51''} = \tilde{\alpha}_{52'} = \tilde{\alpha}_{52''} = \tilde{\alpha}_{53} = \tilde{\alpha}_{53''} = \tilde{\alpha}_{63} = \tilde{\alpha}_{52} = \tilde{\alpha}_{53'} = \tilde{\alpha}_{63''} = \frac{\tilde{\alpha}_{41}}{2l_{3(h,e)}} \\
\alpha_{51'} =& 6g\Big(l_{2(h,e)}m_{2(h,e)} + 2l_{2(h,e)}m_{3(h,e)} + l_{3(h,e)}m_{3(h,e)}\Big) \\
&\Big(4l^2_{1(h,e)}m_{1(h,e)} + 12l^2_{1(h,e)}m_{2(h,e)} + 3l^2_{1(h,e)}m_{3(h,e)} + 4l^2_{2(h,e)}m_{2(h,e)} + 3l^2_{2(h,e)}m_{3(h,e)} \\
&+ 12l_{1(h,e)}l_{2(h,e)}m_{2(h,e)} + 6l_{1(h,e)}l_{2(h,e)}m_{3(h,e)} - 12l_{2(h,e)}l_{3(h,e)}m_{3(h,e)}\Big)
\end{aligned}$$

$$\tilde{\alpha}_{51'} = \frac{l_{2(h,e)}\tilde{\alpha}_{41}}{2l_{3(h,e)}}$$

$$\begin{aligned}\alpha_{51''} =& 6gm_{3(h,e)}\Big(6l^2_{1(h,e)}l_{2(h,e)}m_{1(h,e)} + 3l^2_{2(h,e)}l_{1(h,e)}m_{2(h,e)} + 9l^2_{1(h,e)}l_{2(h,e)}m_{2(h,e)} \\ &+ 4l^2_{1(h,e)}l_{3(h,e)}m_{1(h,e)} + 12l^2_{1(h,e)}l_{3(h,e)}m_{2(h,e)} + 3l^2_{1(h,e)}l_{3(h,e)}m_{3(h,e)} \\ &- 12l^2_{3(h,e)}l_{2(h,e)}m_{3(h,e)} - 18l^2_{2(h,e)}l_{3(h,e)}m_{3(h,e)} + 6l_{1(h,e)}l_{2(h,e)}l_{3(h,e)}m_{2(h,e)} \\ &+ 3l_{1(h,e)}l_{2(h,e)}l_{3(h,e)}m_{3(h,e)}\Big)\end{aligned}$$

$$\begin{aligned}\alpha_{52} =& 6g\Big(l_{2(h,e)}m_{2(h,e)} + 2l_{2(h,e)}m_{3(h,e)} + l_{3(h,e)}m_{3(h,e)}\Big) \\ &\Big(6l_{1(h,e)}m_{2(h,e)} + 3l_{1(h,e)}m_{3(h,e)} + 4l_{2(h,e)}m_{2(h,e)} + 3l_{2(h,e)}m_{3(h,e)}\Big)\end{aligned}$$

$$\begin{aligned}\alpha_{52'} =& 6g\Big(l_{2(h,e)}m_{2(h,e)} + 2l_{2(h,e)}m_{3(h,e)} + l_{3(h,e)}m_{3(h,e)}\Big) \\ &\Big(4l^2_{1(h,e)}m_{1(h,e)} + 12l^2_{1(h,e)}m_{2(h,e)} + 3l^2_{1(h,e)}m_{3(h,e)} + 4l^2_{2(h,e)}m_{2(h,e)} + 3l^2_{2(h,e)}m_{3(h,e)} + \\ &12l_{1(h,e)}l_{2(h,e)}m_{2(h,e)} + 6l_{1(h,e)}l_{2(h,e)}m_{3(h,e)} - 12l_{2(h,e)}l_{3(h,e)}m_{3(h,e)}\Big)\end{aligned}$$

$$\alpha_{52''} = \alpha_{51''} = \alpha_{53} = \alpha_{63}$$

$$\alpha_{53'} = 6gl_{3(h,e)}m_{3(h,e)}\Big(6l_{1(h,e)}m_{2(h,e)} + 3l_{1(h,e)}m_{3(h,e)} + 4l_{2(h,e)}m_{2(h,e)} + 3l_{2(h,e)}m_{3(h,e)}\Big)$$

$$\begin{aligned}\alpha_{53''} =& 6gl_{3(h,e)}m_{3(h,e)}\Big(4l^2_{1(h,e)}m_{1(h,e)} + 12l^2_{1(h,e)}m_{2(h,e)} + 3l^2_{1(h,e)}m_{3(h,e)} \\ &+ 4l^2_{2(h,e)}m_{2(h,e)} + 3l^2_{2(h,e)}m_{3(h,e)} + 12l_{1(h,e)}l_{2(h,e)}m_{2(h,e)} + 6l_{1(h,e)}l_{2(h,e)}m_{3(h,e)} - \\ &12l_{2(h,e)}l_{3(h,e)}m_{3(h,e)}\Big)\end{aligned}$$

$$\begin{aligned}\alpha_{61} =& 6g\Big(l_{2(h,e)}m_{2(h,e)} + 2l_{2(h,e)}m_{3(h,e)} + l_{3(h,e)}m_{3(h,e)}\Big) \\ &\Big(6l^2_{1(h,e)}l_{2(h,e)}m_{1(h,e)} + 3l^2_{2(h,e)}l_{1(h,e)}m_{2(h,e)} + 9l^2_{1(h,e)}l_{2(h,e)}m_{2(h,e)} \\ &+ 4l^2_{1(h,e)}l_{3(h,e)}m_{1(h,e)} + 12l^2_{1(h,e)}l_{3(h,e)}m_{2(h,e)} + 3l^2_{1(h,e)}l_{3(h,e)}m_{3(h,e)} \\ &- 12l^2_{3(h,e)}l_{2(h,e)}m_{3(h,e)} - 18l^2_{2(h,e)}l_{3(h,e)}m_{3(h,e)} \\ &+ 6l_{1(h,e)}l_{2(h,e)}l_{3(h,e)}m_{2(h,e)} + 3l_{1(h,e)}l_{2(h,e)}l_{3(h,e)}m_{3(h,e)}\Big)\end{aligned}$$

$$\tilde{\alpha}_{61} = \tilde{\alpha}_{61'} = \tilde{\alpha}_{62} = \tilde{\alpha}_{62'} = \tilde{\alpha}_{63'} = \frac{l_{2(h,e)}\tilde{\alpha}_{41}}{2}$$

$$
\begin{aligned}
\alpha_{61'} =& 6g\Big(3l_{1(h,e)}^2 l_{2(h,e)}^2 m_{2(h,e)}^2 + 12l_{1(h,e)}^2 l_{2(h,e)}^2 m_{2(h,e)} m_{3(h,e)} + 4l_{1(h,e)}^2 l_{2(h,e)}^2 m_{1(h,e)} m_{2(h,e)} \\
&+ 12l_{1(h,e)}^2 l_{2(h,e)}^2 m_{1(h,e)} m_{3(h,e)} + 18l_{1(h,e)}^2 l_{2(h,e)} l_{3(h,e)} m_{2(h,e)} m_{3(h,e)} \\
&+ 12l_{1(h,e)}^2 l_{2(h,e)} l_{3(h,e)} m_{1(h,e)} m_{3(h,e)} + 12l_{1(h,e)}^2 l_{3(h,e)}^2 m_{2(h,e)} m_{3(h,e)} \\
&+ 3l_{1(h,e)}^2 l_{3(h,e)}^2 m_{3(h,e)}^2 + 4l_{1(h,e)}^2 l_{3(h,e)}^2 m_{1(h,e)} m_{3(h,e)} - 12l_{2(h,e)}^3 l_{3(h,e)} m_{2(h,e)} m_{3(h,e)} \\
&- 36l_{2(h,e)}^3 l_{3(h,e)} m_{3(h,e)}^2 - 36l_{2(h,e)}^2 l_{3(h,e)}^2 m_{3(h,e)}^2 - 12l_{3(h,e)}^3 l_{2(h,e)} m_{3(h,e)}^2\Big) \\
\alpha_{61''} =& 36g l_{1(h,e)}\Big(l_{2(h,e)} m_{2(h,e)} + 2l_{3(h,e)} m_{2(h,e)} + l_{3(h,e)} m_{3(h,e)}\Big) \\
&\Big(l_{1(h,e)} m_{2(h,e)} + l_{1(h,e)} m_{3(h,e)} + l_{2(h,e)} m_{3(h,e)} \\
&+ \frac{l_{1(h,e)} m_{1(h,e)}}{2} + \frac{l_{2(h,e)} m_{2(h,e)}}{2} + \frac{l_{3(h,e)} m_{3(h,e)}}{2}\Big) \\
\alpha_{62} =& \alpha_{61} \\
\alpha_{62'} =& \alpha_{61'} = \alpha_{63'} \\
\alpha_{62''} =& 36g l_{1(h,e)}\Big(l_{2(h,e)} m_{2(h,e)} + 2l_{3(h,e)} m_{2(h,e)} + l_{3(h,e)} m_{3(h,e)}\Big) \\
&\Big(l_{2(h,e)} m_{3(h,e)} + \frac{l_{2(h,e)} m_{2(h,e)}}{2} + \frac{l_{3(h,e)} m_{3(h,e)}}{2}\Big) \\
\alpha_{63''} =& 18g l_{1(h,e)} m_{3(h,e)}\Big(l_{2(h,e)} m_{2(h,e)} + 2l_{3(h,e)} m_{2(h,e)} + l_{3(h,e)} m_{3(h,e)}\Big)
\end{aligned} \tag{B.1}
$$

For $\mathcal{B}$ matrix,

$$
\begin{aligned}
\beta_{41} =& 96l_{2(h,e)} l_{3(h,e)} m_{2(h,e)} + 72l_{2(h,e)} l_{3(h,e)} m_{3(h,e)} \\
\tilde{\beta}_{41} =& \tilde{\alpha}_{41} \\
\beta_{42} =& -\Big(144l_{1(h,e)} l_{3(h,e)} m_{2(h,e)} + 72l_{1(h,e)} l_{3(h,e)} m_{3(h,e)} + 96l_{2(h,e)} l_{3(h,e)} m_{2(h,e)} \\
&+ 72l_{2(h,e)} l_{3(h,e)} m_{3(h,e)}\Big) \\
\tilde{\beta}_{42} =& \tilde{\beta}_{43} = \tilde{\beta}_{41} \\
\beta_{43} =& 72l_{1(h,e)} l_{2(h,e)} m_{2(h,e)} + 144l_{1(h,e)} l_{3(h,e)} m_{2(h,e)} + 72l_{1(h,e)} l_{3(h,e)} m_{3(h,e)} \\
\beta_{51} =& -\Big(72l_{1(h,e)} m_{2(h,e)} + 36l_{1(h,e)} m_{3(h,e)} + 48l_{2(h,e)} m_{2(h,e)} + 36l_{2(h,e)} m_{3(h,e)}\Big) \\
\tilde{\beta}_{51} =& \frac{\tilde{\beta}_{41}}{2l_{3(h,e)}}
\end{aligned}
$$

for

$$
\begin{aligned}
\beta_{52} =& 48l^2_{1(h,e)}m_{1(h,e)} + 144l^2_{1(h,e)}m_{2(h,e)} + 36l^2_{1(h,e)}m_{3(h,e)} + 48l^2_{2(h,e)}m_{2(h,e)} \\
&+ 36l^2_{2(h,e)}m_{3(h,e)} + 144l_{1(h,e)}l_{2(h,e)}m_{2(h,e)} + 72l_{1(h,e)}l_{2(h,e)}m_{3(h,e)} - \\
&144l_{2(h,e)}l_{3(h,e)}m_{3(h,e)} \\
\tilde{\beta}_{52} =& \frac{l_{2(h,e)}\tilde{\beta}_{41}}{2l_{3(h,e)}} \\
\beta_{53} =& -\Big(72l^2_{1(h,e)}l_{2(h,e)}m_{1(h,e)} + 36l^2_{2(h,e)}l_{1(h,e)}m_{2(h,e)} + 108l^2_{1(h,e)}l_{2(h,e)}m_{2(h,e)} \\
&+ 48l^2_{1(h,e)}l_{3(h,e)}m_{1(h,e)} + 144l^2_{1(h,e)}l_{3(h,e)}m_{2(h,e)} + 36l^2_{1(h,e)}l_{3(h,e)}m_{3(h,e)} \\
&- 144l^2_{3(h,e)}l_{2(h,e)}m_{3(h,e)} - 216l^2_{2(h,e)}l_{3(h,e)}m_{3(h,e)} + 72l_{1(h,e)}l_{2(h,e)}l_{3(h,e)}m_{2(h,e)} \\
&+ 36l_{1(h,e)}l_{2(h,e)}l_{3(h,e)}m_{3(h,e)}\Big) \\
\tilde{\beta}_{53} =& \frac{l_{2(h,e)}\widetilde{\beta}_{41}}{2} \\
\beta_{61} =& 36l_{1(h,e)}\Big(l_{2(h,e)}m_{2(h,e)} + 2l_{3(h,e)}m_{2(h,e)} + l_{3(h,e)}m_{3(h,e)}\Big) \\
\tilde{\beta}_{61} =& \frac{\widetilde{\beta}_{41}}{2} \\
\beta_{62} =& \beta_{53} \\
\tilde{\beta}_{62} =& \tilde{\beta}_{53} \\
\beta_{63} =& 36l^2_{1(h,e)}l^2_{2(h,e)}m^2_{2(h,e)} + 144l^2_{1(h,e)}l^2_{2(h,e)}m_{2(h,e)}m_{3(h,e)} \\
&+ 48l^2_{1(h,e)}l^2_{2(h,e)}m_{1(h,e)}m_{2(h,e)} + 144l^2_{1(h,e)}l^2_{2(h,e)}m_{1(h,e)}m_{3(h,e)} \\
&+ 216l^2_{1(h,e)}l_{2(h,e)}l_{3(h,e)}m_{2(h,e)}m_{3(h,e)} + 144l^2_{1(h,e)}l_{2(h,e)}l_{3(h,e)}m_{1(h,e)}m_{3(h,e)} \\
&+ 144l^2_{1(h,e)}l^2_{3(h,e)}m_{2(h,e)}m_{3(h,e)} + 36l^2_{1(h,e)}l^2_{3(h,e)}m^2_{3(h,e)} \\
&+ 48l^2_{1(h,e)}l^2_{3(h,e)}m_{1(h,e)}m_{3(h,e)} - 144l^3_{2(h,e)}l_{3(h,e)}m_{2(h,e)}m_{3(h,e)} \\
&- 432l^3_{2(h,e)}l_{3(h,e)}m^2_{3(h,e)} - 432l^2_{2(h,e)}l^2_{3(h,e)}m^2_{3(h,e)} - 144l^3_{3(h,e)}l_{2(h,e)}m^2_{3(h,e)} \\
\tilde{\beta}_{63} =& \frac{l_{2(h,e)}l_{3(h,e)}m_{3(h,e)}\widetilde{\beta}_{41}}{2}
\end{aligned}
\tag{B.2}
$$

Appendix C

The elements of the regression matrix ($\Phi \in \mathbb{R}^{3\times 16}$) and the vector of unknown parameters ($\Omega \in \mathbb{R}^{16\times 1}$) are as follows:

$$
\begin{aligned}
&\Phi(1,1) = \Phi(1,2) = \Phi(1,5) = \ddot{q}_{1,e}\\
&\Phi(1,3) = \ddot{q}_{1,e}\mathbb{C}_2 + \frac{\mathbb{C}_2}{2}\ddot{q}_{2,e} - \dot{q}_{2,e}\dot{q}_{1,e}S_2 - S_2\dot{q}_{2,e}\left(\dot{q}_{1,e} + \frac{\dot{q}_{2,e}}{2}\right)\\
&\Phi(1,4) = \ddot{q}_{1,e} + 4\ddot{q}_{2,e}, \quad \Phi(1,6) = \ddot{q}_{1,e} + \ddot{q}_{2,e},\\
&\Phi(1,7) = \ddot{q}_{1,e} + \ddot{q}_{2,e} + \ddot{q}_{3,e}\\
&\Phi(1,8) = 2\mathbb{C}_2\ddot{q}_{1,e} + \mathbb{C}_2\ddot{q}_{2,e} - 4S_2\dot{q}_{2,e}\dot{q}_{1,e} - S_2(\dot{q}_{2,e})^2\\
&\Phi(1,9) = \mathbb{C}_{23}\ddot{q}_{1,e} + \frac{\mathbb{C}_{23}}{2}\ddot{q}_{2,e} + \frac{\mathbb{C}_{23}}{2}\ddot{q}_{3,e} - 2S_{23}\dot{q}_{2,e}\dot{q}_{1,e} - 3\frac{S_{23}}{2}\dot{q}_{3,e}\dot{q}_{2,e}\\
&\qquad - 2S_{23}\dot{q}_{1,e}\dot{q}_{3,e} - \frac{S_{23}}{2}(\dot{q}_{2,e})^2 - \frac{(S_{23})}{2}(\dot{q}_{3,e})^2\\
&\Phi(1,10) = \mathbb{C}_3\ddot{q}_{2,e} + \frac{\mathbb{C}_3}{2}\ddot{q}_{3,e}, \quad \Phi(1,11) = \Phi(1,12) = \Phi(1,14) = gS_1\\
&\Phi(1,13) = \Phi(1,15) = gS_{12}, \quad \Phi(1,16) = gS_{123}\\
&\Phi(2,1) = \Phi(2,2) = \Phi(2,5) = \Phi(2,11) = \Phi(2,12) = \Phi(2,14) = 0\\
&\Phi(2,3) = \frac{S_2}{2}(\dot{q}_{1,e})^2, \quad \Phi(2,4) = 4\ddot{q}_{2,e}, \quad \Phi(2,6) = \frac{\ddot{q}_{2,e}}{2}\\
&\Phi(2,7) = \ddot{q}_{2,e} + \ddot{q}_{2,e} \quad \Phi(2,8) = S_2(\dot{q}_{1,e})^2, \quad \Phi(2,9) = \frac{S_{23}}{2}(\dot{q}_{1,e})^2\\
&\Phi(2,10) = \mathbb{C}_3(\ddot{q}_{2,e} + \ddot{q}_{3,e}) - 2S_3\dot{q}_{3,e}(\dot{q}_{1,e} + \dot{q}_{2,e}) - \frac{S_3}{2}(\dot{q}_{3,e})^2\\
&\Phi(2,13) = \Phi(2,15) = gS_{12}, \quad \Phi(2,16) = gS_{123}\\
&\Phi(3,1) = \Phi(3,2) = \Phi(3,3) = \Phi(3,4) = \Phi(3,5) = \Phi(3,6) = \Phi(3,8) = \Phi(3,11)\\
&\qquad = \Phi(3,12) = \Phi(3,13) = \Phi(3,14) = \Phi(3,15) = 0\\
&\Phi(3,7) = \ddot{q}_{3,e}, \quad \Phi(3,9) = \frac{(S_{23})}{2}(\dot{q}_{1,e})^2,\\
&\Phi(3,10) = S_3\left(\frac{\dot{q}_{1,e}}{2} + \dot{q}_{3,e}\right)\dot{q}_{1,e} + \frac{S_3}{2}(2\dot{q}_{1,e} + \dot{q}_{2,e})\dot{q}_{2,e}, \quad \Phi(3,16) = gS_{123}
\end{aligned}
\tag{C.1}
$$

$$\Omega_1 = \frac{m_{1(h,e)}{l_{1(h,e)}}^2}{3}, \quad \Omega_2 = \frac{5m_{2(h,e)}{l_{1(h,e)}}^2}{4}, \quad \Omega_3 = m_{2(h,e)}l_{1(h,e)}l_{2(h,e)},$$
$$\Omega_4 = \frac{m_{2(h,e)}{l_{2(h,e)}}^2}{12}, \quad \Omega_5 = m_{3(h,e)}{l_{1(h,e)}}^2, \quad \Omega_6 = m_{3(h,e)}{l_{2(h,e)}}^2,$$
$$\Omega_7 = \frac{m_{3(h,e)}{l_{3(h,e)}}^2}{3}, \quad \Omega_8 = m_{3(h,e)}l_{1(h,e)}l_{2(h,e)}, \quad \Omega_9 = m_{3(h,e)}l_{1(h,e)}l_{3(h,e)},$$
$$\Omega_{10} = m_{3(h,e)}l_{2(h,e)}l_{3(h,e)}, \quad \Omega_{11} = \frac{m_{2(h,e)}l_{1(h,e)}}{2}, \quad \Omega_{12} = m_{2(h,e)}l_{1(h,e)},$$
$$\Omega_{13} = \frac{m_{2(h,e)}l_{2(h,e)}}{2}, \quad \Omega_{14} = m_{3(h,e)}l_{1(h,e)}, \quad \Omega_{15} = m_{3(h,e)}l_{2(h,e)}, \quad \Omega_{16} = \frac{m_{3(h,e)}l_{3(h,e)}}{2} \tag{C.2}$$

In above expressions,

$$S_j = sin(q_{j,e}), S_{jj} = sin(q_{j,e} + q_{j,e}), \text{ and } S_{jjj} = sin(q_{j,e} + q_{j,e} + q_{j,e}) \quad \forall j = 1, 2, 3$$

$$\mathbb{C}_j = cos(q_{j,e}), \mathbb{C}_{jj} = cos(q_{j,e} + q_{j,e}), \text{ and } \mathbb{C}_{jjj} = cos(q_{j,e} + q_{j,e} + q_{j,e}) \quad \forall j = 1, 2, 3.$$

Bibliography

[1] W. Mathiyakom and J. L. McNitt-Gray, "Regulation of angular impulse during fall recovery," *J Rehabil Res Dev*, vol. 45, no. 8, pp. 1237–1248, 2008.

[2] W. H. Organization, "Disability and health," Online, 2021, last accessed: July 2022. [Online]. Available: http://www.minimalbeispiel.de/mini-en.html

[3] W. Johnson, O. Onuma, M. Owolabi, and S. Sachdev, "Stroke: a global response is needed," *Bulletin of the World Health Organization*, vol. 94, no. 9, p. 634, 2016.

[4] E. Bárbara-Bataller, J. L. Méndez-Suárez, C. Alemán-Sánchez, J. Sánchez-Enríquez, and M. Sosa-Henríquez, "Change in the profile of traumatic spinal cord injury over 15 years in spain," *Scandinavian journal of trauma, resuscitation and emergency medicine*, vol. 26, no. 1, pp. 1–8, 2018.

[5] S. Meyer, M. Poryo, M. Flotats-Bastardas, D. Ebrahimi-Fakhari, and U. Yilmaz, "Schlaganfall bei kindern und jugendlichen," *Der Radiologe*, vol. 57, no. 7, pp. 569–576, 2017.

[6] A. Chauhan, M. Singh, N. Jaiswal, A. Agarwal, J. K. Sahu, and M. Singh, "Prevalence of cerebral palsy in indian children: a systematic review and meta-analysis," *The Indian Journal of Pediatrics*, vol. 86, no. 12, pp. 1124–1130, 2019.

[7] I. Kopyta, A. Dobrucka-Głowacka, A. Cebula, and B. Sarecka-Hujar, "Does the occurrence of particular symptoms and outcomes of arterial ischemic stroke depend on sex in pediatric patients?—a pilot study," *Brain Sciences*, vol. 10, no. 11, p. 881, 2020.

[8] N. Smania, P. Bonetti, M. Gandolfi, A. Cosentino, A. Waldner, S. Hesse, C. Werner, G. Bisoffi, C. Geroin, and D. Munari, "Improved gait after repetitive locomotor training in children with cerebral palsy," *American journal of physical medicine & rehabilitation*, vol. 90, no. 2, pp. 137–149, 2011.

[9] D. G. de Sousa, L. A. Harvey, S. Dorsch, and J. V. Glinsky, "Interventions involving repetitive practice improve strength after stroke: a systematic review," *Journal of physiotherapy*, vol. 64, no. 4, pp. 210–221, 2018.

[10] C. C. Johnson, "The benefits of physical activity for youth with developmental disabilities: a systematic review," *American journal of health promotion*, vol. 23, no. 3, pp. 157–167, 2009.

[11] T. Yan, M. Cempini, C. M. Oddo, and N. Vitiello, "Review of assistive strategies in powered lower-limb orthoses and exoskeletons," *Robotics and Autonomous Systems*, vol. 64, pp. 120–136, 2015.

[12] B. S. Rupal, S. Rafique, A. Singla, E. Singla, M. Isaksson, and G. S. Virk, "Lower-limb exoskeletons: Research trends and regulatory guidelines in medical and non-medical applications," *International Journal of Advanced Robotic Systems*, vol. 14, no. 6, p. 1729881417743554, 2017.

[13] J. C. Moreno, J. Figueiredo, and J. L. Pons, "Exoskeletons for lower-limb rehabilitation," in *Rehabilitation Robotics*. Elsevier, 2018, pp. 89–99.

[14] M. Sarajchi, M. K. Al-Hares, and K. Sirlantzis, "Wearable lower-limb exoskeleton for children with cerebral palsy: A systematic review of mechanical design, actuation type, control strategy, and clinical evaluation," *IEEE Transactions on Neural Systems and Rehabilitation Engineering*, 2021.

[15] P. K. Jamwal, S. Hussain, and M. H. Ghayesh, "Robotic orthoses for gait rehabilitation: an overview of mechanical design and control strategies," *Proceedings of the Institution of Mechanical Engineers, Part H: Journal of Engineering in Medicine*, vol. 234, no. 5, pp. 444–457, 2020.

[16] W. Huo, S. Mohammed, J. C. Moreno, and Y. Amirat, "Lower limb wearable robots for assistance and rehabilitation: A state of the art," *IEEE systems Journal*, vol. 10, no. 3, pp. 1068–1081, 2014.

[17] A. M. Dollar and H. Herr, "Lower extremity exoskeletons and active orthoses: Challenges and state-of-the-art," *IEEE Transactions on robotics*, vol. 24, no. 1, pp. 144–158, 2008.

[18] H. Herr, "Exoskeletons and orthoses: classification, design challenges and future directions," *Journal of neuroengineering and rehabilitation*, vol. 6, no. 1, pp. 1–9, 2009.

[19] J. L. Pons, "Rehabilitation exoskeletal robotics," *IEEE Engineering in Medicine and Biology Magazine*, vol. 29, no. 3, pp. 57–63, 2010.

[20] H. Kazerooni and R. Steger, "The berkeley lower extremity exoskeleton," 2006.

[21] E. Guizzo and H. Goldstein, "The rise of the body bots [robotic exoskeletons]," *IEEE spectrum*, vol. 42, no. 10, pp. 50–56, 2005.

[22] C. J. Walsh, K. Endo, and H. Herr, "A quasi-passive leg exoskeleton for load-carrying augmentation," *International Journal of Humanoid Robotics*, vol. 4, no. 03, pp. 487–506, 2007.

[23] Y. Sankai, "Hal: Hybrid assistive limb based on cybernics," in *Robotics research*. Springer, 2010, pp. 25–34.

[24] T. Nakamura, K. Saito, and K. Kosuge, "Control of wearable walking support system based on human-model and grf," in *Proceedings of the 2005 IEEE international conference on robotics and automation*. IEEE, 2005, pp. 4394–4399.

[25] J. F. Veneman, R. Kruidhof, E. E. Hekman, R. Ekkelenkamp, E. H. Van Asseldonk, and H. Van Der Kooij, "Design and evaluation of the lopes exoskeleton robot for interactive gait rehabilitation," *IEEE Transactions on neural systems and rehabilitation engineering*, vol. 15, no. 3, pp. 379–386, 2007.

[26] S. Mohan, J. Mohanta, S. Kurtenbach, J. Paris, B. Corves, and M. Huesing, "Design, development and control of a 2prp-2ppr planar parallel manipulator for lower limb rehabilitation therapies," *Mechanism and Machine Theory*, vol. 112, pp. 272–294, 2017.

[27] D. Sanz-Merodio, M. Cestari, J. C. Arevalo, X. A. Carrillo, and E. Garcia, "Generation and control of adaptive gaits in lower-limb exoskeletons for motion assistance," *Advanced Robotics*, vol. 28, no. 5, pp. 329–338, 2014.

[28] R. M. Andrade, S. Sapienza, and P. Bonato, "Development of a "transparent operation mode" for a lower-limb exoskeleton designed for children with cerebral palsy," in *2019 IEEE 16th international conference on rehabilitation robotics (ICORR)*. IEEE, 2019, pp. 512–517.

[29] P. W. Duncan, R. Zorowitz, B. Bates, J. Y. Choi, J. J. Glasberg, G. D. Graham, R. C. Katz, K. Lamberty, and D. Reker, "Management of adult stroke rehabilitation care: a clinical practice guideline," *stroke*, vol. 36, no. 9, pp. e100–e143, 2005.

[30] MayoClinic, "Spinal cord injury," Online, 2018, last accessed: July 2022. [Online]. Available: http://www.mayoclinic.com/health/spinal-cord-injury/DS00460

[31] L. Vogel and C. Anderson, "Spinal cord injuries in children and adolescents: a review," *The Journal of Spinal Cord Medicine*, vol. 26, no. 3, pp. 193–203, 2003.

[32] M. L. Aisen, D. Kerkovich, J. Mast, S. Mulroy, T. A. Wren, R. M. Kay, and S. A. Rethlefsen, "Cerebral palsy: clinical care and neurological rehabilitation," *The Lancet Neurology*, vol. 10, no. 9, pp. 844–852, 2011.

[33] S. McIntyre, C. Morgan, K. Walker, and I. Novak, "Cerebral palsy—don't delay," *Developmental disabilities research reviews*, vol. 17, no. 2, pp. 114–129, 2011.

[34] N. Peterson and R. Walton, "Ambulant cerebral palsy," *Orthopaedics and Trauma*, vol. 30, no. 6, pp. 525–538, 2016.

[35] J. Howard, B. Soo, H. K. Graham, R. N. Boyd, S. Reid, A. Lanigan, R. Wolfe, and D. S. Reddihough, "Cerebral palsy in victoria: motor types, topography and gross motor function," *Journal of paediatrics and child health*, vol. 41, no. 9-10, pp. 479–483, 2005.

[36] P. Rosenbaum, N. Paneth, A. Leviton, M. Goldstein, M. Bax, D. Damiano, B. Dan, B. Jacobsson *et al.*, "A report: the definition and classification of cerebral palsy april 2006," *Dev Med Child Neurol Suppl*, vol. 109, no. suppl 109, pp. 8–14, 2007.

[37] C. Cans, "Surveillance of cerebral palsy in europe: a collaboration of cerebral palsy surveys and registers," *Developmental Medicine & Child Neurology*, vol. 42, no. 12, pp. 816–824, 2000.

[38] G. Bialik and U. Givon, "Cerebral palsy: classification and etiology," *Acta orthopaedica et traumatologica turcica*, vol. 43, no. 2, pp. 77–80, 2009.

[39] R. Palisano, P. Rosenbaum, S. Walter, D. Russell, E. Wood, and B. Galuppi, "Development and reliability of a system to classify gross motor function in

children with cerebral palsy," *Developmental medicine & child neurology*, vol. 39, no. 4, pp. 214–223, 1997.

[40] S. Lefmann, R. Russo, and S. Hillier, "The effectiveness of robotic-assisted gait training for paediatric gait disorders: systematic review," *Journal of neuroengineering and rehabilitation*, vol. 14, no. 1, pp. 1–10, 2017.

[41] S. Armand, G. Decoulon, and A. Bonnefoy-Mazure, "Gait analysis in children with cerebral palsy," *EFORT open reviews*, vol. 1, no. 12, pp. 448–460, 2016.

[42] J. Rodda and H. Graham, "Classification of gait patterns in spastic hemiplegia and spastic diplegia: a basis for a management algorithm," *European journal of neurology*, vol. 8, pp. 98–108, 2001.

[43] A. Theadom, M. Rodrigues, R. Roxburgh, S. Balalla, C. Higgins, R. Bhattacharjee, K. Jones, R. Krishnamurthi, and V. Feigin, "Prevalence of muscular dystrophies: a systematic literature review," *Neuroepidemiology*, vol. 43, no. 3-4, pp. 259–268, 2014.

[44] M. W. Whittle, *Gait analysis: an introduction*. Butterworth-Heinemann, 2014.

[45] M. S. Nixon, T. Tan, and R. Chellappa, *Human identification based on gait*. Springer Science & Business Media, 2010, vol. 4.

[46] K. K. Biswas and S. K. Basu, "Gesture recognition using microsoft kinect®," in *The 5th international conference on automation, robotics and applications*. IEEE, 2011, pp. 100–103.

[47] H. Haggag, M. Hossny, S. Nahavandi, and D. Creighton, "Real time ergonomic assessment for assembly operations using kinect," in *2013 UKSim 15th International Conference on Computer Modelling and Simulation*. IEEE, 2013, pp. 495–500.

[48] C.-Y. Chang, B. Lange, M. Zhang, S. Koenig, P. Requejo, N. Somboon, A. A. Sawchuk, and A. A. Rizzo, "Towards pervasive physical rehabilitation using microsoft kinect," in *2012 6th international conference on pervasive computing technologies for healthcare (PervasiveHealth) and workshops*. IEEE, 2012, pp. 159–162.

[49] R. Tanaka, H. Takimoto, T. Yamasaki, and A. Higashi, "Validity of time series kinematical data as measured by a markerless motion capture system

on a flatland for gait assessment," *Journal of biomechanics*, vol. 71, pp. 281–285, 2018.

[50] Y. Ma, K. Mithraratne, N. C. Wilson, X. Wang, Y. Ma, and Y. Zhang, "The validity and reliability of a kinect v2-based gait analysis system for children with cerebral palsy," *Sensors*, vol. 19, no. 7, p. 1660, 2019.

[51] X. Xu, R. W. McGorry, L.-S. Chou, J.-h. Lin, and C.-c. Chang, "Accuracy of the microsoft kinect™ for measuring gait parameters during treadmill walking," *Gait & posture*, vol. 42, no. 2, pp. 145–151, 2015.

[52] M. Eltoukhy, J. Oh, C. Kuenze, and J. Signorile, "Improved kinect-based spatiotemporal and kinematic treadmill gait assessment," *Gait & posture*, vol. 51, pp. 77–83, 2017.

[53] T. B. Rodrigues, D. P. Salgado, C. Ó. Catháin, N. O'Connor, and N. Murray, "Human gait assessment using a 3d marker-less multimodal motion capture system," *Multimedia Tools and Applications*, vol. 79, no. 3, pp. 2629–2651, 2020.

[54] G. Roy, T. Jacob, D. Bhatia, and S. Bhaumik, "Optical marker-and vision-based human gait biomechanical analysis," in *Hybrid Machine Intelligence for Medical Image Analysis*. Springer, 2020, pp. 275–291.

[55] D. Regazzoni, A. Vitali, F. Colombo Zefinetti, and C. Rizzi, "Gait analysis in the assessment of patients undergoing a total hip replacement," in *ASME International Mechanical Engineering Congress and Exposition*, vol. 83518. American Society of Mechanical Engineers, 2019, p. V014T14A003.

[56] B. Chen, H. Ma, L.-Y. Qin, X. Guan, K.-M. Chan, S.-W. Law, L. Qin, and W.-H. Liao, "Design of a lower extremity exoskeleton for motion assistance in paralyzed individuals," in *2015 IEEE International Conference on Robotics and Biomimetics (ROBIO)*. IEEE, 2015, pp. 144–149.

[57] D.-X. Liu, W. Du, X. Wu, C. Wang, and Y. Qiao, "Deep rehabilitation gait learning for modeling knee joints of lower-limb exoskeleton," in *2016 IEEE International Conference on Robotics and Biomimetics (ROBIO)*. IEEE, 2016, pp. 1058–1063.

[58] H. Kim, Y. J. Shin, and J. Kim, "Design and locomotion control of a hydraulic lower extremity exoskeleton for mobility augmentation," *Mechatronics*, vol. 46, pp. 32–45, 2017.

[59] B. Fournier, "Model and characterization of a passive biomimetic ankle for lower extremity powered exoskeleton," Ph.D. dissertation, Université d'Ottawa/University of Ottawa, 2018.

[60] S. Sahoo, M. Saboo, D. K. Pratihar, and S. Mukhopadhyay, "Real-time detection of actual and early gait events during level-ground and ramp walking," *IEEE Sensors Journal*, vol. 20, no. 14, pp. 8128–8136, 2020.

[61] S. Sahoo, S. K. Panda, D. K. Pratihar, and S. Mukhopadhyay, "Prediction of step length using neuro-fuzzy approach suitable for prosthesis control," *IEEE Transactions on Instrumentation and Measurement*, vol. 69, no. 8, pp. 5658–5665, 2020.

[62] K. N. Winfree, P. Stegall, and S. K. Agrawal, "Design of a minimally constraining, passively supported gait training exoskeleton: Alex ii," in *2011 IEEE international conference on rehabilitation robotics*. IEEE, 2011, pp. 1–6.

[63] P. Stegall, K. Winfree, D. Zanotto, and S. K. Agrawal, "Rehabilitation exoskeleton design: Exploring the effect of the anterior lunge degree of freedom," *IEEE Transactions on Robotics*, vol. 29, no. 4, pp. 838–846, 2013.

[64] T. Lenzi, M. C. Carrozza, and S. K. Agrawal, "Powered hip exoskeletons can reduce the user's hip and ankle muscle activations during walking," *IEEE Transactions on Neural Systems and Rehabilitation Engineering*, vol. 21, no. 6, pp. 938–948, 2013.

[65] R. Ronsse, B. Koopman, N. Vitiello, T. Lenzi, S. M. M. De Rossi, J. Van Den Kieboom, E. Van Asseldonk, M. C. Carrozza, H. Van Der Kooij, and A. J. Ijspeert, "Oscillator-based walking assistance: A model-free approach," in *2011 IEEE international conference on rehabilitation robotics*. IEEE, 2011, pp. 1–6.

[66] C. L. Lewis and D. P. Ferris, "Invariant hip moment pattern while walking with a robotic hip exoskeleton," *Journal of biomechanics*, vol. 44, no. 5, pp. 789–793, 2011.

[67] N. d'Elia, F. Vanetti, M. Cempini, G. Pasquini, A. Parri, M. Rabuffetti, M. Ferrarin, R. Molino Lova, and N. Vitiello, "Physical human-robot interaction of an active pelvis orthosis: toward ergonomic assessment of wearable robots," *Journal of neuroengineering and rehabilitation*, vol. 14, no. 1, pp. 1–14, 2017.

[68] K. Junius, N. Lefeber, E. Swinnen, B. Vanderborght, and D. Lefeber, "Metabolic effects induced by a kinematically compatible hip exoskeleton during sts," *IEEE Transactions on Biomedical Engineering*, vol. 65, no. 6, pp. 1399–1409, 2017.

[69] C. Fleischer and G. Hommel, "A human–exoskeleton interface utilizing electromyography," *IEEE Transactions on Robotics*, vol. 24, no. 4, pp. 872–882, 2008.

[70] G. Aguirre-Ollinger, J. E. Colgate, M. A. Peshkin, and A. Goswami, "Inertia compensation control of a one-degree-of-freedom exoskeleton for lower-limb assistance: Initial experiments," *IEEE transactions on neural systems and rehabilitation engineering*, vol. 20, no. 1, pp. 68–77, 2012.

[71] K. Kim, C.-H. Yu, G.-Y. Jeong, M. Heo, and T.-K. Kwon, "Analysis of the assistance characteristics for the knee extension motion of knee orthosis using muscular stiffness force feedback," *Journal of Mechanical Science and Technology*, vol. 27, no. 10, pp. 3161–3169, 2013.

[72] K. I. Sherwani, N. Kumar, A. Chemori, M. Khan, and S. Mohammed, "Rise-based adaptive control for eicosi exoskeleton to assist knee joint mobility," *Robotics and Autonomous Systems*, vol. 124, p. 103354, 2020.

[73] M. Khamar and M. Edrisi, "Designing a backstepping sliding mode controller for an assistant human knee exoskeleton based on nonlinear disturbance observer," *Mechatronics*, vol. 54, pp. 121–132, 2018.

[74] Z. F. Lerner, D. L. Damiano, H.-S. Park, A. J. Gravunder, and T. C. Bulea, "A robotic exoskeleton for treatment of crouch gait in children with cerebral palsy: Design and initial application," *IEEE Transactions on Neural Systems and Rehabilitation Engineering*, vol. 25, no. 6, pp. 650–659, 2016.

[75] T. Yamada, H. Kadone, Y. Shimizu, and K. Suzuki, "An exoskeleton brake unit for children with crouch gait supporting the knee joint during stance," in *2018 International symposium on micro-nanomechatronics and human science (MHS)*. IEEE, 2018, pp. 1–7.

[76] J. Chen, J. Hochstein, C. Kim, D. Damiano, and T. Bulea, "Design advancements toward a wearable pediatric robotic knee exoskeleton for overground gait rehabilitation," in *2018 7th IEEE International Conference on Biomedical Robotics and Biomechatronics (Biorob)*. IEEE, 2018, pp. 37–42.

[77] E. P. Washabaugh and C. Krishnan, "A wearable resistive robot facilitates locomotor adaptations during gait," *Restorative neurology and neuroscience*, vol. 36, no. 2, pp. 215–223, 2018.

[78] M. A. H. Mohd Adib, S. Y. Han, P. R. Ramani, L. J. You, L. M. Yan, I. Mat Sahat, and N. H. Mohd Hasni, "Restoration of kids leg function using exoskeleton robotic leg (exroleg) device," in *Proceedings of the 10th National Technical Seminar on Underwater System Technology 2018*. Springer, 2019, pp. 335–342.

[79] P.-C. Kao, C. L. Lewis, and D. P. Ferris, "Invariant ankle moment patterns when walking with and without a robotic ankle exoskeleton," *Journal of biomechanics*, vol. 43, no. 2, pp. 203–209, 2010.

[80] K. Kim, J.-J. Kim, S.-R. Kang, G.-Y. Jeong, and T.-K. Kwon, "Analysis of the assistance characteristics for the plantarflexion torque in elderly adults wearing the powered ankle exoskeleton," in *ICCAS 2010*. IEEE, 2010, pp. 576–579.

[81] P. Malcolm, W. Derave, S. Galle, and D. De Clercq, "A simple exoskeleton that assists plantarflexion can reduce the metabolic cost of human walking," *PloS one*, vol. 8, no. 2, p. e56137, 2013.

[82] G. Chen, Z. Zhou, B. Vanderborght, N. Wang, and Q. Wang, "Proxy-based sliding mode control of a robotic ankle-foot system for post-stroke rehabilitation," *Advanced Robotics*, vol. 30, no. 15, pp. 992–1003, 2016.

[83] A. Erdogan, B. Celebi, A. C. Satici, and V. Patoglu, "Assist on-ankle: a reconfigurable ankle exoskeleton with series-elastic actuation," *Autonomous Robots*, vol. 41, no. 3, pp. 743–758, 2017.

[84] Z. F. Lerner, G. M. Gasparri, M. O. Bair, J. L. Lawson, J. Luque, T. A. Harvey, and A. T. Lerner, "An untethered ankle exoskeleton improves walking economy in a pilot study of individuals with cerebral palsy," *IEEE Transactions on Neural Systems and Rehabilitation Engineering*, vol. 26, no. 10, pp. 1985–1993, 2018.

[85] Marsi-Bionics, "Atlas 2030," Online, 2019, last accessed: June 2022. [Online]. Available: https://www.marsibionics.com/en/atlas-pediatricexo-product-detail/

[86] C. Bayón, S. Lerma, O. Ramírez, J. I. Serrano, M. Del Castillo, R. Raya, J. M. Belda-Lois, I. Martínez, and E. Rocon, "Locomotor training through a novel robotic platform for gait rehabilitation in pediatric population," *Journal of neuroengineering and rehabilitation*, vol. 13, no. 1, pp. 1–6, 2016.

[87] D. Eguren, M. Cestari, T. P. Luu, A. Kilicarslan, A. Steele, and J. L. Contreras-Vidal, "Design of a customizable, modular pediatric exoskeleton for rehabilitation and mobility," in *2019 IEEE international conference on systems, man and cybernetics (SMC)*. IEEE, 2019, pp. 2411–2416.

[88] M. Canela, A. J. d. Ama, and J. L. Pons, "Design of a pediatric exoskeleton for the rehabilitation of the physical disabilities caused by cerebral palsy," in *Converging Clinical and Engineering Research on Neurorehabilitation*. Springer, 2013, pp. 255–258.

[89] C. A. Laubscher, R. J. Farris, and J. T. Sawicki, "Design and preliminary evaluation of a powered pediatric lower limb orthosis," in *International Design Engineering Technical Conferences and Computers and Information in Engineering Conference*, vol. 58172. American Society of Mechanical Engineers, 2017, p. V05AT08A061.

[90] H. Kawamoto, S. Taal, H. Niniss, T. Hayashi, K. Kamibayashi, K. Eguchi, and Y. Sankai, "Voluntary motion support control of robot suit hal triggered by bioelectrical signal for hemiplegia," in *2010 Annual international conference of the IEEE engineering in medicine and biology*. IEEE, 2010, pp. 462–466.

[91] M. Maggu, R. Udasi, and D. Nikitina, "Designing exoskeletons for children: Overcoming challenge associated with weight-bearing and risk of injury," in *Companion of the 2018 ACM/IEEE International Conference on Human-Robot Interaction*, 2018, pp. 39–39.

[92] F. Patané, S. Rossi, F. Del Sette, J. Taborri, and P. Cappa, "Wake-up exoskeleton to assist children with cerebral palsy: design and preliminary evaluation in level walking," *IEEE Transactions on Neural Systems and Rehabilitation Engineering*, vol. 25, no. 7, pp. 906–916, 2017.

[93] Y. Long, Z. Du, C. Chen, W. Wang, L. He, X. Mao, G. Xu, G. Zhao, X. Li, and W. Dong, "Development and analysis of an electrically actuated lower extremity assistive exoskeleton," *Journal of Bionic Engineering*, vol. 14, no. 2, pp. 272–283, 2017.

[94] B. Chen, C.-H. Zhong, X. Zhao, H. Ma, X. Guan, X. Li, F.-Y. Liang, J. C. Y. Cheng, L. Qin, S.-W. Law *et al.*, "A wearable exoskeleton suit for motion assistance to paralysed patients," *Journal of orthopaedic translation*, vol. 11, pp. 7–18, 2017.

[95] X. Jin, S. Zhu, X. Zhu, Q. Chen, and X. Zhang, "Single-input adaptive fuzzy sliding mode control of the lower extremity exoskeleton based on human–robot interaction," *Advances in Mechanical Engineering*, vol. 9, no. 2, p. 1687814016686665, 2017.

[96] M. Vasanthakumar, B. Vinod, J. K. Mohanta, and S. Mohan, "Design and robust motion control of a planar 1p-2p rp hybrid manipulator for lower limb rehabilitation applications," *Journal of Intelligent & Robotic Systems*, vol. 96, no. 1, pp. 17–30, 2019.

[97] O. Baser, H. Kizilhan, and E. Kilic, "Biomimetic compliant lower limb exoskeleton (biocomex) and its experimental evaluation," *Journal of the Brazilian Society of Mechanical Sciences and Engineering*, vol. 41, no. 5, pp. 1–15, 2019.

[98] J. Sancho-Pérez, M. Pérez, E. García, D. Sanz-Merodio, A. Plaza, and M. Cestari, "Mechanical description of atlas 2020, a 10-dof paediatric exoskeleton," in *Advances in Cooperative Robotics*. World Scientific, 2017, pp. 814–822.

[99] T. Nakamura, K. Saito, Z. Wang, and K. Kosuge, "Realizing model-based wearable antigravity muscles support with dynamics terms," in *2005 IEEE/RSJ International Conference on Intelligent Robots and Systems*. IEEE, 2005, pp. 2694–2699.

[100] H. He and K. Kiguchi, "A study on emg-based control of exoskeleton robots for human lower-limb motion assist," in *2007 6th International special topic conference on information technology applications in biomedicine*. IEEE, 2007, pp. 292–295.

[101] M. Bortole, A. Venkatakrishnan, F. Zhu, J. C. Moreno, G. E. Francisco, J. L. Pons, and J. L. Contreras-Vidal, "The h2 robotic exoskeleton for gait rehabilitation after stroke: early findings from a clinical study," *Journal of neuroengineering and rehabilitation*, vol. 12, no. 1, pp. 1–14, 2015.

[102] J. Wu, J. Gao, R. Song, R. Li, Y. Li, and L. Jiang, "The design and control of a 3dof lower limb rehabilitation robot," *Mechatronics*, vol. 33, pp. 13–22, 2016.

[103] Y. Yang, D. Huang, and X. Dong, "Robust repetitive learning control of lower limb exoskeleton with hybrid electro-hydraulic system," in *2018 IEEE 7th Data Driven Control and Learning Systems Conference (DDCLS)*. IEEE, 2018, pp. 718–723.

[104] Y. Tu, A. Zhu, J. Song, H. Shen, Z. Shen, X. Zhang, and G. Cao, "An adaptive sliding mode variable admittance control method for lower limb rehabilitation exoskeleton robot," *Applied Sciences*, vol. 10, no. 7, p. 2536, 2020.

[105] M. Sanchez-Manchola, D. Gómez-Vargas, D. Casas-Bocanegra, M. Munera, and C. A. Cifuentes, "Development of a robotic lower-limb exoskeleton for gait rehabilitation: Agora exoskeleton," in *2018 IEEE ANDESCON*. IEEE, 2018, pp. 1–6.

[106] A. Cullell, J. C. Moreno, E. Rocon, A. Forner-Cordero, and J. L. Pons, "Biologically based design of an actuator system for a knee–ankle–foot orthosis," *Mechanism and Machine Theory*, vol. 44, no. 4, pp. 860–872, 2009.

[107] L. Chen, C. Wang, X. Song, J. Wang, T. Zhang, and X. Li, "Dynamic trajectory adjustment of lower limb exoskeleton in swing phase based on impedance control strategy," *Proceedings of the Institution of Mechanical Engineers, Part I: Journal of Systems and Control Engineering*, vol. 234, no. 10, pp. 1120–1132, 2020.

[108] G. Belforte, L. Gastaldi, and M. Sorli, "Pneumatic active gait orthosis," *Mechatronics*, vol. 11, no. 3, pp. 301–323, 2001.

[109] K. Kong and D. Jeon, "Design and control of an exoskeleton for the elderly and patients," *IEEE/ASME Transactions on mechatronics*, vol. 11, no. 4, pp. 428–432, 2006.

[110] N. L. Tagliamonte, F. Sergi, G. Carpino, D. Accoto, and E. Guglielmelli, "Human-robot interaction tests on a novel robot for gait assistance," in *2013 IEEE 13th international conference on rehabilitation robotics (ICORR)*. IEEE, 2013, pp. 1–6.

[111] Y. Mori, J. Okada, and K. Takayama, "Development of a standing style transfer system" able" for disabled lower limbs," *IEEE/ASME Transactions on Mechatronics*, vol. 11, no. 4, pp. 372–380, 2006.

[112] X. Jin, A. Prado, and S. K. Agrawal, "Retraining of human gait-are lightweight cable-driven leg exoskeleton designs effective?" *IEEE Transactions on Neural Systems and Rehabilitation Engineering*, vol. 26, no. 4, pp. 847–855, 2018.

[113] Y. Long, Z.-j. Du, W.-d. Wang, and W. Dong, "Robust sliding mode control based on ga optimization and cmac compensation for lower limb exoskeleton," *Applied bionics and biomechanics*, vol. 2016, 2016.

[114] T.-J. Yeh, M.-J. Wu, T.-J. Lu, F.-K. Wu, and C.-R. Huang, "Control of mckibben pneumatic muscles for a power-assist, lower-limb orthosis," *Mechatronics*, vol. 20, no. 6, pp. 686–697, 2010.

[115] G. S. Sawicki and D. P. Ferris, "A pneumatically powered knee-ankle-foot orthosis (kafo) with myoelectric activation and inhibition," *Journal of neuroengineering and rehabilitation*, vol. 6, no. 1, pp. 1–16, 2009.

[116] B. Ding, J. Qian, L. Shen, and Y. Zhang, "Finite element analysis and optimized design of exoskeleton for lower extremity rehabilitation training," in *2012 IEEE International Conference on Robotics and Biomimetics (ROBIO)*. IEEE, 2012, pp. 1397–1402.

[117] L. Pan, C. He, and Q. Li, "Structural static characteristic analysis of lower limb exoskeleton based on finite element modeling," in *2015 3rd International Conference on Mechanical Engineering and Intelligent Systems*. Atlantis Press, 2015, pp. 104–109.

[118] C. Huang, W. Chen, J. Liu, and J. Zhang, "Design of a compliant joint actuator for lower-limb exoskeleton robot," in *2017 12th IEEE Conference on Industrial Electronics and Applications (ICIEA)*. IEEE, 2017, pp. 1522–1527.

[119] J. Wang, Y. Pang, X. Chang, W. Chen, and J. Zhang, "Mechanical design and optimization on lower limb exoskeleton for rehabilitation," in *2019 14th IEEE Conference on Industrial Electronics and Applications (ICIEA)*. IEEE, 2019, pp. 137–142.

[120] A. Nithyaa, S. Poonguzhali, and N. Vigneshwari, "Three-dimensional modelling of wheelchair contrived with lower limb exoskeleton for right hemiplegic dysfunction," *Proceedings of the Institution of Mechanical Engineers, Part H: Journal of Engineering in Medicine*, vol. 234, no. 7, pp. 651–659, 2020.

[121] V. Varma, R. Yogeshwar Rao, P. Vundavilli, M. Pandit, and P. Budarapu, "A machine learning-based approach for the design of lower limb exoskeleton," *International Journal of Computational Methods*, p. 2142012, 2022.

[122] D. A. Winter, *Biomechanics and motor control of human gait: normal, elderly and pathological*, 1991.

[123] Z. F. Lerner, T. A. Harvey, and J. L. Lawson, "A battery-powered ankle exoskeleton improves gait mechanics in a feasibility study of individuals with cerebral palsy," *Annals of biomedical engineering*, vol. 47, no. 6, pp. 1345–1356, 2019.

[124] S. L. Delp, F. C. Anderson, A. S. Arnold, P. Loan, A. Habib, C. T. John, E. Guendelman, and D. G. Thelen, "Opensim: open-source software to create and analyze dynamic simulations of movement," *IEEE transactions on biomedical engineering*, vol. 54, no. 11, pp. 1940–1950, 2007.

[125] X. Yang, H. She, H. Lu, T. Fukuda, and Y. Shen, "State of the art: bipedal robots for lower limb rehabilitation," *Applied Sciences*, vol. 7, no. 11, p. 1182, 2017.

[126] E. Added, H. Gritli, and S. Belghith, "Modeling and analysis of the dynamic walking of a biped robot with knees," in *2021 18th International Multi-Conference on Systems, Signals & Devices (SSD)*. IEEE, 2021, pp. 179–185.

[127] W. Znegui, H. Gritli, and S. Belghith, "Design of an explicit expression of the poincaré map for the passive dynamic walking of the compass-gait biped model," *Chaos, Solitons & Fractals*, vol. 130, p. 109436, 2020.

[128] M. Iribe, R. Hirouji, D. Ura, K. Osuka, and T. Kinugasa, "Experimental verification of the characteristic behaviors in passive dynamic walking," *Artificial Life and Robotics*, vol. 26, no. 2, pp. 187–194, 2021.

[129] W. Znegui, H. Gritli, and S. Belghith, "Stabilization of the passive walking dynamics of the compass-gait biped robot by developing the analytical

expression of the controlled poincaré map," *Nonlinear Dynamics*, vol. 101, no. 2, pp. 1061–1091, 2020.

[130] S. H. Collins, M. B. Wiggin, and G. S. Sawicki, "Reducing the energy cost of human walking using an unpowered exoskeleton," *Nature*, vol. 522, no. 7555, pp. 212–215, 2015.

[131] C. Di Natali, A. Sadeghi, A. Mondini, E. Bottenberg, B. Hartigan, A. De Eyto, L. O'Sullivan, E. Rocon, K. Stadler, B. Mazzolai *et al.*, "Pneumatic quasi-passive actuation for soft assistive lower limbs exoskeleton," *Frontiers in neurorobotics*, p. 31, 2020.

[132] S. Glowinski, M. Obst, S. Majdanik, and B. Potocka-Banaś, "Dynamic model of a humanoid exoskeleton of a lower limb with hydraulic actuators," *Sensors*, vol. 21, no. 10, p. 3432, 2021.

[133] A. B. Zoss, H. Kazerooni, and A. Chu, "Biomechanical design of the berkeley lower extremity exoskeleton (bleex)," *IEEE/ASME Transactions on mechatronics*, vol. 11, no. 2, pp. 128–138, 2006.

[134] B. Kalita and S. Dwivedy, "Dynamic analysis of pneumatic artificial muscle (pam) actuator for rehabilitation with principal parametric resonance condition," *Nonlinear Dynamics*, vol. 97, no. 4, pp. 2271–2289, 2019.

[135] B. Kalita and S. K. Dwivedy, "Nonlinear dynamic response of pneumatic artificial muscle: A theoretical and experimental study," *International Journal of Non-Linear Mechanics*, vol. 125, p. 103544, 2020.

[136] ——, "Numerical investigation of nonlinear dynamics of a pneumatic artificial muscle with hard excitation," *Journal of Computational and Nonlinear Dynamics*, vol. 15, no. 4, p. 041003, 2020.

[137] D. Sanz-Merodio, M. Cestari, J. C. Arevalo, and E. Garcia, "Control motion approach of a lower limb orthosis to reduce energy consumption," *International journal of advanced robotic systems*, vol. 9, no. 6, p. 232, 2012.

[138] K. Suzuki, G. Mito, H. Kawamoto, Y. Hasegawa, and Y. Sankai, "Intention-based walking support for paraplegia patients with robot suit hal," *Advanced Robotics*, vol. 21, no. 12, pp. 1441–1469, 2007.

[139] D. Shi, W. Zhang, W. Zhang, and X. Ding, "A review on lower limb rehabilitation exoskeleton robots," *Chinese Journal of Mechanical Engineering*, vol. 32, no. 1, pp. 1–11, 2019.

[140] C. Bayon, O. Ramírez, M. D. Del Castillo, J. I. Serrano, R. Raya, J. M. Belda-Lois, R. Poveda, F. Mollà, T. Martin, I. Martínez *et al.*, "Cpwalker: Robotic platform for gait rehabilitation in patients with cerebral palsy," in *2016 IEEE International Conference on Robotics and Automation (ICRA)*. IEEE, 2016, pp. 3736–3741.

[141] C. Chen, S. Zhang, X. Zhu, J. Shen, and Z. Xu, "Disturbance observer-based patient-cooperative control of a lower extremity rehabilitation exoskeleton," *International Journal of Precision Engineering and Manufacturing*, vol. 21, no. 5, pp. 957–968, 2020.

[142] A. Taherifar, G. Vossoughi, and A. S. Ghafari, "Variable admittance control of the exoskeleton for gait rehabilitation based on a novel strength metric," *Robotica*, vol. 36, no. 3, pp. 427–447, 2018.

[143] R. Luo, S. Sun, X. Zhao, Y. Zhang, and Y. Tang, "Adaptive cpg-based impedance control for assistive lower limb exoskeleton," in *2018 IEEE International Conference on Robotics and Biomimetics (ROBIO)*. IEEE, 2018, pp. 685–690.

[144] J. Chen, J. Hochstein, C. Kim, L. Tucker, L. E. Hammel, D. L. Damiano, and T. C. Bulea, "A pediatric knee exoskeleton with real-time adaptive control for overground walking in ambulatory individuals with cerebral palsy," *Frontiers in Robotics and AI*, vol. 8, p. 173, 2021.

[145] W. Hassani, S. Mohammed, H. Rifaï, and Y. Amirat, "Powered orthosis for lower limb movements assistance and rehabilitation," *Control Engineering Practice*, vol. 26, pp. 245–253, 2014.

[146] M. K. Shepherd and E. J. Rouse, "Design and validation of a torque-controllable knee exoskeleton for sit-to-stand assistance," *IEEE/ASME Transactions on Mechatronics*, vol. 22, no. 4, pp. 1695–1704, 2017.

[147] C.-F. Chen, Z.-J. Du, L. He, J.-Q. Wang, D.-M. Wu, and W. Dong, "Active disturbance rejection with fast terminal sliding mode control for a lower limb exoskeleton in swing phase," *IEEE Access*, vol. 7, pp. 72 343–72 357, 2019.

[148] P. Yang, G. Zhang, J. Wang, X. Wang, L. Zhang, and L. Chen, "Command filter backstepping sliding model control for lower-limb exoskeleton," *Mathematical Problems in Engineering*, vol. 2017, 2017.

[149] W. Sun, J.-W. Lin, S.-F. Su, N. Wang, and M. J. Er, "Reduced adaptive fuzzy decoupling control for lower limb exoskeleton," *IEEE transactions on cybernetics*, vol. 51, no. 3, pp. 1099–1109, 2020.

[150] S. K. Hasan and A. K. Dhingra, "Development of a model reference computed torque controller for a human lower extremity exoskeleton robot," *Proceedings of the Institution of Mechanical Engineers, Part I: Journal of Systems and Control Engineering*, vol. 235, no. 9, pp. 1615–1637, 2021.

[151] S. Ahmed, H. Wang, and Y. Tian, "Robust adaptive fractional-order terminal sliding mode control for lower-limb exoskeleton," *Asian Journal of Control*, vol. 21, no. 1, pp. 473–482, 2019.

[152] M. H. Samaei, S. Sheikh Ahmadi, M. Naderi Soorki, and S. S. Amini, "Comment on s. ahmed, h. wang, and y. tian,"robust adaptive fractional-order terminal sliding mode control for lower-limb exoskeleton," asian j. control, vol. 21, no. 1, pp. 1–10 (2019)," *Asian Journal of Control*, 2022.

[153] J. Liu, Y. Zhang, J. Wang, and W. Chen, "Adaptive sliding mode control for a lower-limb exoskeleton rehabilitation robot," in *2018 13th IEEE Conference on Industrial Electronics and Applications (ICIEA)*. IEEE, 2018, pp. 1481–1486.

[154] S. Han, H. Wang, and Y. Tian, "Model-free based adaptive nonsingular fast terminal sliding mode control with time-delay estimation for a 12 dof multifunctional lower limb exoskeleton," *Advances in Engineering Software*, vol. 119, pp. 38–47, 2018.

[155] S. Ahmed, H. Wang, and Y. Tian, "Model-free control using time delay estimation and fractional-order nonsingular fast terminal sliding mode for uncertain lower-limb exoskeleton," *Journal of Vibration and Control*, vol. 24, no. 22, pp. 5273–5290, 2018.

[156] S. Hasan and A. K. Dhingra, "Biomechanical design and control of an eight dof human lower extremity rehabilitation exoskeleton robot," *Results in Control and Optimization*, vol. 7, p. 100107, 2022.

[157] X. Zhang, H. Wang, Y. Tian, L. Peyrodie, and X. Wang, "Model-free based neural network control with time-delay estimation for lower extremity exoskeleton," *Neurocomputing*, vol. 272, pp. 178–188, 2018.

[158] P. Zhang, J. Zhang, and Z. Zhang, "Design of rbfnn-based adaptive sliding mode control strategy for active rehabilitation robot," *IEEE Access*, vol. 8, pp. 155 538–155 547, 2020.

[159] S. Han, H. Wang, Y. Tian, and N. Christov, "Time-delay estimation based computed torque control with robust adaptive rbf neural network compensator for a rehabilitation exoskeleton," *ISA transactions*, vol. 97, pp. 171–181, 2020.

[160] J. Wang, J. Liu, G. Zhang, and S. Guo, "Periodic event-triggered sliding mode control for lower limb exoskeleton based on human–robot cooperation," *ISA transactions*, vol. 123, pp. 87–97, 2022.

[161] R. Nataraj and A. J. van den Bogert, "Simulation analysis of linear quadratic regulator control of sagittal-plane human walking—implications for exoskeletons," *Journal of biomechanical engineering*, vol. 139, no. 10, 2017.

[162] N. Ajjanaromvat and M. Parnichkun, "Trajectory tracking using online learning lqr with adaptive learning control of a leg-exoskeleton for disorder gait rehabilitation," *Mechatronics*, vol. 51, pp. 85–96, 2018.

[163] D. L. Castro, C.-H. Zhong, F. Braghin, and W.-H. Liao, "Lower limb exoskeleton control via linear quadratic regulator and disturbance observer," in *2018 IEEE International Conference on Robotics and Biomimetics (ROBIO)*. IEEE, 2018, pp. 1743–1748.

[164] Z. Shen, Y. Zhuang, J. Zhou, J. Gao, and R. Song, "Design and test of admittance control with inner adaptive robust position control for a lower limb rehabilitation robot," *International Journal of Control, Automation and Systems*, vol. 18, no. 1, pp. 134–142, 2020.

[165] K. Almaghout, B. Tarvirdizadeh, K. Alipour, and A. Hadi, "Design and control of a lower limb rehabilitation robot considering undesirable torques of the patient's limb," *Proceedings of the Institution of Mechanical Engineers, Part H: Journal of Engineering in Medicine*, vol. 234, no. 12, pp. 1457–1471, 2020.

[166] M. Mokhtari, M. Taghizadeh, and M. Mazare, "Optimal adaptive high-order super twisting sliding mode control of a lower limb exoskeleton robot," *Modares Mechanical Engineering*, vol. 19, no. 3, pp. 777–787, 2019.

[167] A. Estrada, L. Fridman, and R. Iriarte, "Combined backstepping and hosm control design for a class of nonlinear mimo systems," *International Journal of Robust and Nonlinear Control*, vol. 27, no. 4, pp. 566–581, 2017.

[168] J. Zhou and C. Wen, *Adaptive backstepping control of uncertain systems: Nonsmooth nonlinearities, interactions or time-variations*. Springer, 2008.

[169] M. Abbas, S. Al Issa, and S. K. Dwivedy, "Event-triggered adaptive hybrid position-force control for robot-assisted ultrasonic examination system," *Journal of Intelligent & Robotic Systems*, vol. 102, no. 4, pp. 1–19, 2021.

[170] C.-Y. Li, W.-X. Jing, and C.-S. Gao, "Adaptive backstepping-based flight control system using integral filters," *Aerospace Science and Technology*, vol. 13, no. 2-3, pp. 105–113, 2009.

[171] F. Wang, Q. Zou, and Q. Zong, "Robust adaptive backstepping control for an uncertain nonlinear system with input constraint based on lyapunov redesign," *International Journal of Control, Automation and Systems*, vol. 15, no. 1, pp. 212–225, 2017.

[172] N. Adhikary and C. Mahanta, "Backstepping sliding mode controller for a co-ordinated links (cool) robot arm," in *2014 13th International Workshop on Variable Structure Systems (VSS)*. IEEE, 2014, pp. 1–5.

[173] Q. Guo, Y. Zhang, B. G. Celler, and S. W. Su, "Neural adaptive backstepping control of a robotic manipulator with prescribed performance constraint," *IEEE transactions on neural networks and learning systems*, vol. 30, no. 12, pp. 3572–3583, 2018.

[174] M. Abbas and S. K. Dwivedy, "Adaptive control for networked uncertain cooperative dual-arm manipulators: an event-triggered approach," *Robotica*, vol. 40, no. 6, pp. 1951–1978, 2022.

[175] R. Coban, "Adaptive backstepping sliding mode control with tuning functions for nonlinear uncertain systems," *International Journal of Systems Science*, vol. 50, no. 8, pp. 1517–1529, 2019.

[176] Z. F. Lerner, D. L. Damiano, and T. C. Bulea, "Estimating the mechanical behavior of the knee joint during crouch gait: Implications for real-time motor control of robotic knee orthoses," *IEEE Transactions on Neural Systems and Rehabilitation Engineering*, vol. 24, no. 6, pp. 621–629, 2016.

[177] N. Aliman, R. Ramli, and S. M. Haris, "Design and development of lower limb exoskeletons: A survey," *Robotics and Autonomous Systems*, vol. 95, pp. 102–116, 2017.

[178] Ü. Önen, F. M. Botsalı, M. Kalyoncu, M. Tınkır, N. Yılmaz, and Y. Şahin, "Design and actuator selection of a lower extremity exoskeleton," *IEEE/ASME Transactions on mechatronics*, vol. 19, no. 2, pp. 623–632, 2013.

[179] A. Rodriguez-Martinez, B. Zhou, M. K. Sophiea, J. Bentham, C. J. Paciorek, M. L. Iurilli, R. M. Carrillo-Larco, J. E. Bennett, M. Di Cesare, C. Taddei *et al.*, "Height and body-mass index trajectories of school-aged children and adolescents from 1985 to 2019 in 200 countries and territories: a pooled analysis of 2181 population-based studies with 65 million participants," *The Lancet*, vol. 396, no. 10261, pp. 1511–1524, 2020.

[180] S. Vispute, V. Khadilkar, A. Khadilkar, V. Ekbote, N. Singh, and S. Chiplonkar, "Inter-regional differences in body proportions in indian children and adolescents—a cross-sectional multicentric study," *Annals of Human Biology*, vol. 47, no. 1, pp. 1–9, 2020.

[181] S. Massardi, D. Rodriguez-Cianca, D. Pinto-Fernandez, J. C. Moreno, M. Lancini, and D. Torricelli, "Characterization and evaluation of human–exoskeleton interaction dynamics: A review," *Sensors*, vol. 22, no. 11, p. 3993, 2022.

[182] C. J. Arellano, C. S. Layne, D. P. O'CONNOR, M. Scott-Pandorf, and M. J. Kurz, "Does load carrying influence sagittal plane locomotive stability?" *Medicine & Science in Sports & Exercise*, vol. 41, no. 3, pp. 620–627, 2009.

[183] Y. Zou, N. Wang, X. Wang, H. Ma, and K. Liu, "Design and experimental research of movable cable-driven lower limb rehabilitation robot," *IEEE Access*, vol. 7, pp. 2315–2326, 2018.

[184] M. d. C. Sanchez-Villamañan, J. Gonzalez-Vargas, D. Torricelli, J. C. Moreno, and J. L. Pons, "Compliant lower limb exoskeletons: a comprehensive review on mechanical design principles," *Journal of neuroengineering and rehabilitation*, vol. 16, no. 1, pp. 1–16, 2019.

[185] K. A. Witte and S. H. Collins, "Design of lower-limb exoskeletons and emulator systems," in *Wearable robotics*. Elsevier, 2020, pp. 251–274.

[186] J. Narayan, A. Kalani, and S. K. Dwivedy, *Lower Extremity Exoskeleton Device for Motion Assistance and GaitRehabilitation: Design Considerations*. Springer International Publishing, Cham, 2020, pp. 1–18.

[187] D. O. Abrahamyan, A. Gazarian, and P. M. Braillon, "Estimation of stature and length of limb segments in children and adolescents from whole-body dual-energy x-ray absorptiometry scans," *Pediatric Radiology*, vol. 38, no. 3, pp. 311–315, 2008.

[188] A. Huseynov, C. P. Zollikofer, W. Coudyzer, D. Gascho, C. Kellenberger, R. Hinzpeter, and M. S. Ponce de León, "Developmental evidence for obstetric adaptation of the human female pelvis," *Proceedings of the National Academy of Sciences*, vol. 113, no. 19, pp. 5227–5232, 2016.

[189] M. M. Martins, C. P. Santos, A. Frizera-Neto, and R. Ceres, "Assistive mobility devices focusing on smart walkers: Classification and review," *Robotics and Autonomous Systems*, vol. 60, no. 4, pp. 548–562, 2012.

[190] A. J. Young and D. P. Ferris, "State of the art and future directions for lower limb robotic exoskeletons," *IEEE Transactions on Neural Systems and Rehabilitation Engineering*, vol. 25, no. 2, pp. 171–182, 2016.

[191] C. Elliott, V. Vijayakumar, W. Zink, and R. Hansen, "National instruments labview: a programming environment for laboratory automation and measurement," *JALA: Journal of the Association for Laboratory Automation*, vol. 12, no. 1, pp. 17–24, 2007.

[192] V. L. Chester, M. Tingley, and E. N. Biden, "A comparison of kinetic gait parameters for 3–13 year olds," *Clinical Biomechanics*, vol. 21, no. 7, pp. 726–732, 2006.

[193] B. S. Cigali, E. Uluçam, and C. Bozer, "3d motion analysis of hip, knee and ankle joints of children aged between 7-11 years during gait," *Balkan Medical Journal*, vol. 2011, no. 2, pp. 197–201, 2011.

[194] S. M. Kung, P. W. Fink, P. Hume, and S. P. Shultz, "Kinematic and kinetic differences between barefoot and shod walking in children," *Footwear Science*, vol. 7, no. 2, pp. 95–105, 2015.

[195] A. J. van den Bogert, L. Read, and B. M. Nigg, "An analysis of hip joint loading during walking, running, and skiing." *Medicine and science in sports and exercise*, vol. 31, no. 1, pp. 131–142, 1999.

[196] J. T. Weinhandl, B. S. Irmischer, and Z. A. Sievert, "Effects of gait speed of femoroacetabular joint forces," *Applied Bionics and Biomechanics*, vol. 2017, 2017.

[197] H. D. Kim, J.-G. Kim, D.-M. Jeon, M.-H. Shin, N. Han, M.-J. Eom, and G.-Y. Jo, "Analysis of vertical ground reaction force variables using foot scans in hemiplegic patients," *Annals of Rehabilitation Medicine*, vol. 39, no. 3, pp. 409–415, 2015.

[198] S. H. Hwang, D. I. Sun, J. Han, and W.-S. Kim, "Gait pattern generation algorithm for lower-extremity rehabilitation–exoskeleton robot considering wearer's condition," *Intelligent Service Robotics*, vol. 14, no. 3, pp. 345–355, 2021.

[199] I. D. Geonea and D. Tarnita, "Design and evaluation of a new exoskeleton for gait rehabilitation," *Mechanical Sciences*, vol. 8, no. 2, pp. 307–321, 2017.

[200] F. Wang, L. Yan, J. Xiao, and L. Fan, "Design and simulation analysis of an improved wearable power knee exoskeleton," *Journal of Vibroengineering*, vol. 21, no. 5, pp. 1472–1482, 2019.

[201] T. Lee, I. Kim, and S.-H. Lee, "Estimation of the continuous walking angle of knee and ankle (talocrural joint, subtalar joint) of a lower-limb exoskeleton robot using a neural network," *Sensors*, vol. 21, no. 8, p. 2807, 2021.

[202] Q.-T. Dao, M.-L. Nguyen, and S.-i. Yamamoto, "Discrete-time fractional order integral sliding mode control of an antagonistic actuator driven by pneumatic artificial muscles," *Applied Sciences*, vol. 9, no. 12, p. 2503, 2019.

[203] J.-J. E. Slotine and J. Karl Hedrick, "Robust input-output feedback linearization," *International Journal of control*, vol. 57, no. 5, pp. 1133–1139, 1993.

[204] M. W. Spong, S. Hutchinson, and M. Vidyasagar, *Robot modeling and control*. John Wiley & Sons, 2020.

[205] M. A. Henson and D. E. Seborg, "Input-output linearization of general nonlinear processes," *AIChE Journal*, vol. 36, no. 11, pp. 1753–1757, 1990.

[206] Y.-n. Fei and Q.-h. Wu, "Tracking control of robot manipulators via output feedback linearization," *Frontiers of Mechanical Engineering in China*, vol. 1, no. 3, pp. 329–335, 2006.

[207] J.-S. Jang and C.-T. Sun, "Neuro-fuzzy modeling and control," *Proceedings of the IEEE*, vol. 83, no. 3, pp. 378–406, 1995.

[208] T. Takagi and M. Sugeno, "Derivation of fuzzy control rules from human operator's control actions," *IFAC Proceedings Volumes*, vol. 16, no. 13, pp. 55–60, 1983.

[209] A. Singla, J. Narayan, and H. Arora, "Investigating the potential of redundant manipulators in narrow channels," *Proceedings of the Institution of Mechanical Engineers, Part C: Journal of Mechanical Engineering Science*, vol. 235, no. 18, pp. 3723–3736, 2021.

[210] S. S. Roy and D. K. Pratihar, "Adaptive neuro-fuzzy expert systems for predicting specific energy consumption and energy stability margin in crab walking of six-legged robots," *Journal of Intelligent & Fuzzy Systems*, vol. 24, no. 3, pp. 467–482, 2013.

[211] P. Benner, "Control theory," *Handbook of Linear Algebra*, 2006.

[212] I. Chawla and A. Singla, "Real-time control of a rotary inverted pendulum using robust lqr-based anfis controller," *International Journal of Nonlinear Sciences and Numerical Simulation*, vol. 19, no. 3-4, pp. 379–389, 2018.

[213] C.-S. Chen, "Dynamic structure adaptive neural fuzzy control for mimo uncertain nonlinear systems," *Information Sciences*, vol. 179, no. 15, pp. 2676–2688, 2009.

[214] B. Farkas and S.-A. Wegner, "Variations on barbălat's lemma," *The American Mathematical Monthly*, vol. 123, no. 8, pp. 825–830, 2016.

[215] M. H. Rahman, M. Saad, J.-P. Kenné, and P. S. Archambault, "Control of an exoskeleton robot arm with sliding mode exponential reaching law," *International Journal of Control, Automation and Systems*, vol. 11, no. 1, pp. 92–104, 2013.

[216] M. Krstic, P. V. Kokotovic, and I. Kanellakopoulos, *Nonlinear and adaptive control design*. John Wiley & Sons, Inc., 1995.

[217] H. Gritli and S. Belghith, "Lmi-based synthesis of a robust saturated controller for an underactuated mechanical system subject to motion constraints," *European Journal of Control*, vol. 57, pp. 179–193, 2021.

[218] M. Torabi, M. Sharifi, and G. Vossoughi, "Robust adaptive sliding mode admittance control of exoskeleton rehabilitation robots," *Scientia Iranica*, vol. 25, no. 5, pp. 2628–2642, 2018.

[219] C.-S. Chiu, "Derivative and integral terminal sliding mode control for a class of mimo nonlinear systems," *Automatica*, vol. 48, no. 2, pp. 316–326, 2012.

[220] Y. Feng, X. Yu, and Z. Man, "Non-singular terminal sliding mode control of rigid manipulators," *Automatica*, vol. 38, no. 12, pp. 2159–2167, 2002.

[221] M. Bhave, S. Janardhanan, and L. Dewan, "An efficient control of rigid robotic manipulator with uncertainties using higher order sliding mode control," *International Journal of Modelling, Identification and Control*, vol. 19, no. 2, pp. 179–185, 2013.

[222] M. Van, X. P. Do, and M. Mavrovouniotis, "Self-tuning fuzzy pid-nonsingular fast terminal sliding mode control for robust fault tolerant control of robot manipulators," *ISA transactions*, vol. 96, pp. 60–68, 2020.

Publications (From Thesis)

Journal publication

1. **Narayan, J.**, Abbas, M. and Dwivedy, S.K., 2022. Robust Adaptive Backstepping Sliding Mode Subject-Cooperative Control for a Pediatric Lower-Extremity Exoskeleton Robot. **International Journal of Control, Automation and Systems**, [**Revision Submitted**].

2. **Narayan, J.** Abbas, M. and Dwivedy, S.K., 2022. Robust Adaptive Backstepping Control for a Lower-Limb Exoskeleton System with Model Uncertainties and External Disturbances. **Automatika**, 64(1), 145-161.

3. **Narayan, J.** and Dwivedy, S.K., 2022. Biomechanical Study and Prediction of Lower Extremity Joint Movements Using Bayesian Regularization-Based Backpropagation Neural Network. **ASME Journal of Computing and Information Science in Engineering**, 22(1).

4. **Narayan, J.** and Dwivedy, S.K., 2021. Robust LQR-based neural-fuzzy tracking control for a lower limb exoskeleton system with parametric uncertainties and external disturbances. **Applied Bionics and Biomechanics**, 2021.

5. **Narayan, J.** and Dwivedy, S.K., 2020. Towards neuro-fuzzy compensated pid control of lower extremity exoskeleton system for passive gait rehabilitation. **IETE Journal of Research**, 69(2).

6. **Narayan, J.** and Dwivedy, S.K., 2021. Preliminary design and development of a low-cost lower-limb exoskeleton system for paediatric rehabilitation. **Proceedings of the Institution of Mechanical Engineers, Part H: Journal of Engineering in Medicine**, 235(5), pp.530-545.

7. **Narayan, J.**, Kalita, B. and Dwivedy, S.K., 2022. Adaptive Backstepping Human-Cooperative Control of a Gait Exoskeleton System with High and Low Level Admittance. **Proceedings of the Institution of Mechanical Engineers, Part I: Journal of Systems and Control Engineering**, [**Revision Submitted**].

8. **Narayan, J.** and Dwivedy, S.K., 2022. A Robust Human-in-the-Loop Adaptive Backstepping Integral Singularity-Free Fast Terminal Sliding Mode

Active-Assist Control for the Pediatric Gait Exoskeleton Robot. **IEEE Transactions on Mechatronics**, [**Submitted**].

9. **Narayan, J.**, Abbas, M., Patel, B., and Dwivedy, S.K., 2022. Adaptive RBF Neural Network-Computed Torque Control for a Pediatric Gait Exoskeleton System: An Experimental Study. **Intelligent Service Robotics**, [**Submitted**].

10. Kalita, B., **Narayan, J.** and Dwivedy, S.K., 2021. Development of active lower limb robotic-based orthosis and exoskeleton devices: a systematic review. **International Journal of Social Robotics**, 13(4), pp.775-793.

Conference publications

1. **Narayan, J.**, Patel, B., Abbas, M., Shivhare, G. and Dwivedy, S.K., 2022, April. Cooperative Control of a Pediatric Exoskeleton System for Active-Assist Gait Rehabilitation. In 2022 **8th IEEE International Conference on Electronics, Computing and Communication Technologies, (CONECCT), Bangalore, India**, [**Accepted**][**Best Paper Award**]

2. **Narayan, J.**, Abbas, M., Patel, B. and Dwivedy, S.K., 2022, March. A Singularity-Free Terminal Sliding Mode Control of an Uncertain Paediatric Exoskeleton System. In 2022 **5th IEEE International Conference on Advanced Systems and Emergent Technologies (IC_ASET), Hammamet, Tunisia**, (pp. 198-203), IEEE.

3. **Narayan, J.**, Bharti, R. R., and Dwivedy, S.K., 2022, March. Robust Sliding Mode Control with Reaching Laws for a Pediatric Lower-Limb Exoskeleton System. In 2022 2nd **International Conference on Power, Control and Computing Technologies (ICPC2T), Raipur, India**, (pp. 1-6), IEEE. **[Best Paper Award]**

4. **Narayan, J.**, Bhoir, A.A., Borgohain, A. and Dwivedy, S.K., 2021, December. Design and Analysis of a Stand-aided Lower-Limb Exoskeleton System for Pediatric Rehabilitation. In 2021 **International Conference on Computational Performance Evaluation (ComPE), Meghalaya, India**, (pp. 950-955). IEEE. **[Best Paper Award]**

5. **Narayan, J.**, Pardasani, A. and Dwivedy, S.K., 2020, July. Comparative gait analysis of healthy young male and female adults using Kinect-Labview

setup. In 2020 **International Conference on Computational Performance Evaluation (ComPE), Meghalaya, India**, (pp. 688-693). IEEE.

6. **Narayan, J.**, Kalani, A. and Dwivedy, S.K., 2019, October. Reference trajectory based Jacobian transpose control of a novel lower limb exoskeleton system for children. In 2019 5th **International conference on signal processing, computing and control (ISPCC), Solan, India**, (pp. 102-107). IEEE.

Book Chapters

1. **Narayan, J.**, Jhunjhunwala, S., Mishra, S. and Dwivedy, S.K., 2022. A comparative performance analysis of backpropagation training optimizers to estimate clinical gait mechanics. **Predictive Modeling in Biomedical Data Mining and Analysis**, p.83.

2. Gupta, M., **Narayan, J.** and Dwivedy, S.K., 2020. Modeling of a novel lower limb exoskeleton system for paraplegic patients. In **Advances in Fluid Mechanics and Solid Mechanics** (pp. 199-210). Springer, Singapore.

Publications (Related to Thesis)

Journal publication

1. **Narayan, J.**, Abbas, M. and Dwivedy, S.K., 2021. Adaptive iterative learning-based gait tracking control for paediatric exoskeleton during passive-assist rehabilitation. **International Journal of Intelligent Engineering Informatics**, 9(6), pp.507-532.

2. **Narayan, J.**, Kalita, B. and Dwivedy, S.K., 2021. Development of robot-based upper limb devices for rehabilitation purposes: a systematic review. **Augmented Human Research**, 6(1), pp.1-33.

3. Abbas, M., **Narayan, J.** and Dwivedy, S.K., 2022. Event-triggered adaptive control for upper-limb robot-assisted passive rehabilitation exercises with input delay. **Proceedings of the Institution of Mechanical Engineers, Part I: Journal of Systems and Control Engineering**, 236(4), pp.832-845.

4. Abbas, M., **Narayan, J.** and Dwivedy, S.K., 2022. Event-Triggered Adaptive Control for Upper-Extremity Therapeutic Robot in Active-Assist Mode. **Proceedings of the Institution of Mechanical Engineers, Part H: Journal of Engineering in Medicine [Under Review]**

Book Chapters

1. Patil, V., **Narayan, J.**, Sandhu, K. and Dwivedy, S.K., 2022. Integration of Virtual Reality and Augmented Reality in Physical Rehabilitation: A State-of-the-Art Review. **Revolutions in Product Design for Healthcare**, pp.177-205. Springer, Cham.

2. Kundu, K., Shivhare, G., Patil, V., **Narayan, J.** and Dwivedy, S.K., 2022. Heel-End-and Toe-End-Based Gait Kinematics of Female Young Adults: Implications of Therapeutic Intervention. **In Assistive Technology Intervention in Healthcare** (pp. 137-158). CRC Press.

3. **Narayan, J.**, Abbas, M. and Dwivedy, S.K., 2022. Transpose Jacobian Control of Flexible Joint Upper Limb Exoskeleton System. **In Machines, Mechanism and Robotics** (pp. 401-411). Springer, Singapore.